LUDWIG-MAXIMILIANS-UNIVERSITY
MUNICH

DOCTORAL THESIS

Searches for supersymmetric particles decaying to W and Higgs bosons in events with an isolated lepton with the ATLAS detector

AUTHOR: DANIJELA BOGAVAC

April 19, 2018

Searches for supersymmetric particles decaying to W and Higgs bosons in events with an isolated lepton with the ATLAS detector

Dissertation an der Fakultät für Physik
der Ludwig-Maximilians-Universität München
vorgelegt von

DANIJELA BOGAVAC
aus Kragujevac

München, 19. April 2018

Erstgutachter: Prof. Dr. Dorothee Schaile

Zweitgutachter: Prof. Dr. Martin Faessler

Tag der mündlichen Prüfung: 11. Juni 2018

"I know you're living in my mind
It's not the same as being alive
Supersymmetry,
Supersymmetry..."

Arcade Fire

Zusammenfassung

Das Standardmodell (SM) der Teilchenphysik ist eine Theorie, die über Beschreibungen aller bekannten Elementarteilchen und deren Wechselwirkungen untereinander, mit Ausnahme von gravitativen Wechselwirkungen, verfügt. Es gibt jedoch offene Fragen, die nicht vom SM erklärt werden können. Supersymmetrie (SUSY), welche weitere Teilchen vorhersagt und einige der ungelösten Fragestellungen erklären kann, ist eine mögliche Erweiterung des SMs. Der Schwerpunkt dieser Arbeit liegt auf zwei Suchen nach supersymmetrischen Teilchen in Daten von Proton-Proton Kollisionen am Large Hadron Collider (LHC), die vom ATLAS Detektor in den Jahren 2015 und 2016 aufgezeichnet wurden.

Die erste Suche basiert auf einem vereinfachten SUSY Modell, welches die Paarerzeugung von Squarks und Gluinos durch starke Wechselwirkungen in LHC Kollisionen erlaubt. Motiviert durch die Entdeckung des Higgs-Bosons 2012 betrachtet das Modell Higgs-, W- und Z-Bosonen in der Zerfallskette. Der Endzustand setzt sich aus einem Lepton (Elektron oder Myon), Jets und fehlendem Transversalimpuls zusammen. Die Analyse verwendet drei Signalregionen, die die unterschiedlichen kinematischen Eigenschaften der Squark- und Gluinozerfälle berücksichtigen. Die Ergebnisse werden auch mit einer Reinterpretation einer bereits publizierten Analyse, die auf ein geringfügig unterschiedliches supersymmetrisches Modell abzielt, verglichen.

Die zweite Suche untersucht ein weiteres vereinfachtes SUSY Modell, welches elektroschwache Paarerzeugung vom Charginos ($\tilde{\chi}_i^{\pm}$) und Neutralinos ($\tilde{\chi}_j^0$) animmt und in dem das leichteste Chargino ($\tilde{\chi}_1^{\pm}$) zu W- und das zweitleichteste Neutralino ($\tilde{\chi}_2^0$) zu Higgs-Bosonen zerfällt. Der Enzustand mit einem Lepton (Elektron oder Myon), zwei b-Jets aus dem Higgs Boson Zerfall und fehlendem Transversalimpuls, wurde mittels dreier statistisch orthogonaler Signalregionen untersucht. Die Daten stimmen in jeder der Signalregionen mit den Vorhersagen des SMs überein.

Abstract

The Standard Model (SM) of particle physics is a theory that provides a description of all known elementary particles and their interactions except gravitational interactions. Nevertheless, there are a few open issues which cannot be explained by the SM. Supersymmetry (SUSY) is a well motivated extension of the SM which solves some of its shortcomings and predicts the existence of new particles. This thesis presents two searches for supersymmetric particles in proton-proton collisions delivered by the Large Hadron Collider (LHC) and recorded by the ATLAS detector in 2015 and 2016.

The first search considers a simplified SUSY model in which squarks and gluinos are pair-produced by the strong interactions in LHC collisions. Inspired by the discovery of the Higgs boson in 2012, this model includes Higgs bosons in the decay chain as well as W and Z bosons. The final state considered consists of one lepton (electron or muon), jets and missing transverse momentum. The analysis uses three signal regions which are designed to target the wide range of kinematics expected from squark or gluino decays. The obtained sensitivity has been compared with a reinterpretation of a published analysis which targets a slightly different supersymmetric model.

The second search explores a simplified SUSY model of electroweak pair production of charginos ($\tilde{\chi}_i^{\pm}$) and neutralinos ($\tilde{\chi}_j^0$) in which the lightest chargino ($\tilde{\chi}_1^{\pm}$) and next-to-lightest neutralino ($\tilde{\chi}_2^0$) decay to W and Higgs bosons, respectively. A final state with one lepton (electron or muon), two b-jets from the Higgs boson decay, and missing transverse momentum is explored using three statistically orthogonal signal regions. The data are found to be compatible with the SM predictions in all signal regions.

Contents

List of Abbreviations

ALFA	**A**bsolute **L**uminosity **F**or **A**TLAS
ALICE	**A** **L**arge **I**on **C**ollider **E**xperiment: a particle detector designed to study the quark-gluion plasma.
ATLAS	**A** **T**oroidal **L**HC **A**pparatu**S**: one of two general-purpose particle detectors installed at the Large Hadron Collider ring.
BR	**B**ranching **R**atio
CERN	**C**onseil **E**uropéen pour la **R**echerche **N**ucléaire
CMS	**C**ompact **M**uon–**S**olenoid: one of two general-purpose particle detectors installed at the Large Hadron Collider ring.
CR	**C**ontrol **R**egion: a part of parameter space with a high background contribution and a low signal contamination.
CSC	**C**athode-**S**trip **C**hamber: the part of the MS used for a precise measurement of the track coordinates.
CTP	**C**entral **T**rigger **P**rocessors: part of the Level-1 trigger, responsible for making a final decision at the Level-1.
DM	**D**ark **M**atter
EMCal	**E**lectro**M**agnetic **Cal**orimeter: calorimeter that measures energies of electrons and photons.
eV	**e**lectron**V**olt
FCal	LAr **F**orward **Cal**orimeter
GRL	**G**ood **R**un **L**ist: list of good events obtained by applying data quality criteria.
HEC	LAr **H**adronic **E**nd-cap **C**alorimeter
HLT	**H**igh **L**evel **T**rigger: second level of trigger, responsible for reducing the output rate of the Level-1 to 1 kHz.
IBL	**I**nsertable **B**-**L**ayer: component of the Pixel detector.
ID	**I**nner **D**etector: the innermost of the ATLAS detecor, responsible for particle tracking.
JER	**Jet** **E**nergy **R**esolution: the uncertainty on the energy resolution of jets.
JES	**Jet** **E**nergy **S**cale: the uncertainty on jet kinematic measurements.
JVT	**J**et **V**ertex **T**agger: an algorithm used to reject reconstructed jets from pile-up vertices.
LAr	Lead-**L**iquid **Ar**gon: the active material used in the electromagnetic calorimeter.

LCG	**L**HC **C**omputing **G**rid
LEP	**L**arge **E**lectron–**P**ositron Collider: an electron-proton collider at CERN closed in 2000.
LHC	**L**arge **H**adron **C**ollider
LHCb	**L**arge **H**adron **C**ollider **b**eauty: a particle detector designed to study B-physics.
LHCf	**L**arge **H**adron **C**ollider **f**orward: a special-purpose detector for astroparticle (cosmic ray) physics.
LINAC 2	**LIN**ear **AC**celerator 2: a linear accelerator at CERN.
LSP	**L**ightest **S**upersymmetric **P**article
LUCID	**LU**minosity measurement using **C**erenkov **I**ntegrating **D**etector
L1	**L**evel-1: first level of trigger, responsible for reducing the initial event rate to less than 100 kHz.
L1Calo	**L1 Calo**rimeter trigger system: part of the Level-1 trigger used to identify of all physics objects except muons.
L1Muon	**L1 Muon** trigger system: part of the Level-1 trigger used for muon candidates.
L1Topo	**L1 To**pological trigger modules: part of the Level-1 trigger used to calculate event topological quantities between Level-1 objects.
MC	**M**onte **C**arlo simulation
MDT	**M**onitored **D**rift **T**ube: subdetector of the MS designed to provide precision measurements of muons.
MoEDAL	**Mo**nopole and **E**xotics **D**etector **A**t the **L**HC: a special-purpose detector designed to search for hypothetical particles such as magnetic monopoles.
MS	**M**uon **S**pectrometer: the outermost part of the ATLAS detector which identifies and measures the momenta of muons.
MSSM	**M**inimal **S**upersymmetry **S**tandard **M**odel: a supersymmetric extension of the SM with the minimum number of additional particles.
Pixel	Silicon **Pixel** Detector: layer of the ATLAS Inner detector.
PS	**P**roton **S**ynchrotron: a 600m-long circular accelerator at CERN.
PSB	**P**roton **S**ynchrotron **B**ooster: a circular accelerator at CERN.
PV	**P**rimary **V**ertex: the vertex of the hard scattering.
QCD	**Q**uantum **C**hromo**d**ynamics
RoI	**R**egion **o**f **I**nterest: a geometrical region which contains candidates for the high trigger level.
RPC	**R**esistive **P**late **C**hambers: a system for triggering in the MS.
SCT	**S**emi**C**onductor **T**racker: part of the ATLAS Inner detector.
SM	**S**tandard **M**odel
SPS	**S**uper **P**roton **S**ynchrotron: the second largest accelerator at CERN.
SR	**S**ignal **R**egion: a part of parameter space with a high signal acceptance and a low background contamination.
SRB	**S**ignal **R**egion **B**oosted: used in the search for squarks and gluinos decaying to W/Z/h bosons to cover boosted scenarios.
SRC	**S**ignal **R**egion **C**ompressed: used in the search for squarks and gluinos decaying to W/Z/h bosons to cover compressed scenarios.
SRHM	**S**ignal **R**egion **H**igh **M**ass: used in the search for $\tilde{\chi}_1^{\pm}\tilde{\chi}_2^0$ to cover scenarios with high mass differences between $\tilde{\chi}_1^{\pm}/\tilde{\chi}_2^0$ and $\tilde{\chi}_1^0$.

SRI	**S**ignal **R**egion **I**ntermediate: used in the search for squarks and gluinos decaying to W/Z/h bosons to cover intermediate scenarios.
SRLM	**S**ignal **R**egion **L**ow **M**ass: used in the search for $\tilde{\chi}_1^{\pm}\tilde{\chi}_2^0$ to cover scenarios with small mass differences between $\tilde{\chi}_1^{\pm}/\tilde{\chi}_2^0$ and $\tilde{\chi}_1^0$.
SRMM	**S**ignal **R**egion **M**edium **M**ass: used in the search for $\tilde{\chi}_1^{\pm}\tilde{\chi}_2^0$ to cover scenarios with medium mass differences between $\tilde{\chi}_1^{\pm}/\tilde{\chi}_2^0$ and $\tilde{\chi}_1^0$.
SUSY	**S**uper**s**ymmetry
SV	**S**econdary **V**ertex: vertex in the decay of an unstable particle.
TCRHM	**T**op **C**ontrol **R**egion **H**igh **M**ass: used in the search for $\tilde{\chi}_1^{\pm}\tilde{\chi}_2^0$ to estimate the $t\bar{t}$ background. It is defined to have the same m_T criterion as the SRHM.
TCRLM	**T**op **C**ontrol **R**egion **L**ow **M**ass: used in the search for $\tilde{\chi}_1^{\pm}\tilde{\chi}_2^0$ to estimate the $t\bar{t}$ background. It is defined to have the same m_T criterion as the SRLM.
TCRMM	**T**op **C**ontrol **R**egion **M**edium **M**ass: used in the search for $\tilde{\chi}_1^{\pm}\tilde{\chi}_2^0$ to estimate the $t\bar{t}$ background. It is defined to have the same m_T criterion as the SRMM.
TGC	**T**hin **G**ap **C**hambers: a system for triggering in the MS.
TOTEM	**TOT**al **E**lastic and diffractive cross-section **M**easurement: a special-purpose detector which measures the total proton-proton cross-section and studies the elastic and diffractive scattering.
TRT	**T**ransition **R**adiation **T**racker: component of the ATLAS Inner detector.
VEV	**V**acuum **E**xpectation **V**alue: the minimum of the Higgs potential.
VR	**V**alidation **R**egion: a part of parameter space used to validate SM background estimates.
$VRHM_{OFF}$	**V**alidation **R**egion **H**igh **M**ass **OFF**: used in the search for $\tilde{\chi}_1^{\pm}\tilde{\chi}_2^0$ to validate the SM estimates. Its definition includes the whole range of m_{bb} except signal peak with its width and the same m_T criterion as the SRHM.
$VRHM_{ON}$	**V**alidation **R**egion **H**igh **M**ass **ON**: used in the search for $\tilde{\chi}_1^{\pm}\tilde{\chi}_2^0$ to validate the SM estimates. Its definition includes the signal peak with its width in m_{bb} and the same m_T criterion as the SRHM.
$VRLM_{OFF}$	**V**alidation **R**egion **L**ow **M**ass **OFF**: used in the search for $\tilde{\chi}_1^{\pm}\tilde{\chi}_2^0$ to validate the SM estimates. Its definition includes the whole range of m_{bb} except signal peak with its width and the same m_T criterion as the SRLM.
$VRLM_{ON}$	**V**alidation **R**egion **L**ow **M**ass **ON**: used in the search for $\tilde{\chi}_1^{\pm}\tilde{\chi}_2^0$ to validate the SM estimates. Its definition includes the signal peak with its width in m_{bb} and the same m_T criterion as the SRLM.
$VRMM_{OFF}$	**V**alidation **R**egion **M**edium **M**ass **OFF**: used in the search for $\tilde{\chi}_1^{\pm}\tilde{\chi}_2^0$ to validate the SM estimates. Its definition includes the whole range of m_{bb} except signal peak with its width and the same m_T criterion as the SRMM.
$VRMM_{ON}$	**V**alidation **R**egion **M**edium **M**ass **ON**: used in the search for $\tilde{\chi}_1^{\pm}\tilde{\chi}_2^0$ to validate the SM estimates. Its definition includes the signal peak with its width in m_{bb} and the same m_T criterion as the SRMM.
ZDC	**Z**ero-**D**egree **C**alorimeter

TO MY FAMILY

Chapter 1

Introduction

The Standard Model of particle physics provides a description of all known fundamental particles and three interactions between them. Only gravitational interactions are not included. The Standard Model has been extremely successful in describing physics at the lower energy scale. With the discovery of the Higgs boson at CERN (the European Organization for Nuclear Research) in 2012, the Standard Model is completed. However, there are still some issues which are not explained by the Standard Model.

Several astronomical observations have shown the presence of dark matter which seems to have no interactions with ordinary matter except via the weak and gravitational interactions. The Standard Model does not provide candidates for dark matter. Only 5% of the energy density in the universe consists of particles described by the Standard Model.

One issue of the Standard Model is associated with the radiative corrections to the Higgs boson mass. This problem is known as the hierarchy problem and also requests an explanation.

Many theories have been developed to solve these issues. One of them is supersymmetry which introduces a new symmetry between fermions, particles with half-integer spin and bosons, particles with integer spin. In supersymmetry, each Standard Model particle has a partner particle with the same properties except for the spin which differs by half a unit. The theory gives new supersymmetric particles, but unfortunately none of these particles have been observed so far. This implies that supersymmetry is broken and supersymmetric particles have to be heavier than their Standard Model partners.

Searches for supersymmetric particles with different signal scenarios and final states at the Large Hadron Collider have been performed for many years. The ATLAS detector is one of the seven detectors at CERN which record collisions delivered by the Large Hadron Collider. This thesis focuses on two searches for supersymmetric particles in proton-proton collisions recorded by the ATLAS detector.

Outline of the thesis

This thesis is organized as follows:

Chapter 2 gives the theoretical framework in which this thesis is done. It covers the theory of the Standard Model of particle physics and describes its shortcomings. The second part of this chapter introduces a new theory known as supersymmetry and explains how supersymmetry can solve some shortcomings of the Standard Model. At the end of the chapter, supersymmetric signals on which this thesis is based are described.

Chapter 3 describes the Large Hadron Collider and the ATLAS detector. The Monte Carlo simulation including an overview of generators used in this thesis is given. The last part of this chapter describes the CERN grid computing as necessary tool for processing and storing the collected data.

Chapter 4 explains the algorithms and techniques used in ATLAS for the reconstruction, identification and isolation of particles produced in proton-proton collisions.

Chapter 5 details the Standard Model processes which have a similar final state as the considered supersymmetric signals in this thesis.

Chapter 6 describes the kinematic variables used to discriminate the supersymmetric signals from the Standard Model backgrounds and shows their discriminating power.

Chapter 7 provides the general analysis strategy used in many searches for supersymmetric particles in the ATLAS experiment, including both of the searches presented in this thesis.

Chapter 8 gives the mathematical background of the statistical tool used to obtain the background normalization factors and to check if any potential excess of observed events over the Standard Model predictions is statistically significant.

Chapter 9 describes a search for squarks and gluinos decaying via the lightest chargino ($\tilde{\chi}_1^{\pm}$) or the next-to-lightest neutralino ($\tilde{\chi}_2^0$) to W/Z/h bosons and the lightest supersymmetric particle. The lightest supersymmetric particle is the lightest neutralino ($\tilde{\chi}_1^0$). The final state consists of one lepton (electron or muon), jets and missing transverse momentum. The number of jets including jets from b-quarks depends on the decay of the W/Z/h boson.

Chapter 10 presents a search for charginos and neutralinos in which the lightest chargino ($\tilde{\chi}_1^{\pm}$) decays to a W boson and the lightest supersymmetric particles and the next-to-lightest neutralino ($\tilde{\chi}_2^0$) decays to a Higgs boson and the lightest supersymmetric particle. The lightest supersymmetric particle is the lightest neutralino as in the previous search. The final state considered here is one lepton (electron or muon) from the W boson, two b-jets from the Higgs boson and missing transverse momentum from neutrino and neutralinos.

Chapter 2

Theory overview

This chapter discusses the theoretical background necessary to understand the work presented in this thesis. The Standard Model of particle physics describes elementary particles and their interactions except gravitational interactions. Although it has experimentally been confirmed up to the TeV scale showing remarkably successful results, some hints exist which point to new physics beyond the Standard Model. Several theories have been developed to address these hints. Supersymmetry is one of the most popular extensions of the Standard Model and can elegantly address the open questions, as discussed at the end of this chapter. This thesis presents two searches for supersymmetric particles.

2.1 The Standard Model

The Standard Model (SM) of particle physics was developed in the late 1960s and early 1970s and is the theory that provides a description of all known elementary particles [1, 2]. It successfully models three fundamental forces in nature: the strong force, the weak force and the electromagnetic force. The gravitational force is not described by the SM.
The SM is a gauge invariant quantum field theory with the symmetry group:

$$SU(3)_C \otimes SU(2)_L \otimes U(1)_Y$$

where $SU(3)_C$ is the component of the Quantum Chromodynamics and C indicates the color charge. $SU(2)_L \otimes U(1)_Y$ corresponds to the electroweak theory, in which the weak force and the electromagnetic force are unified. L refers to left-handed fields, and Y is the quantum number for hypercharge, connected to the charge Q and the third component of the weak isospin T_3 by $Y=2(Q-T_3)$.
The SM theory is experimentally well verified and with the discovery of the Higgs boson at the Large Hadron Collider in 2012 all particles predicted by

this theory have been observed [3, 4]. Figure 2.1 shows all particles described by the SM with their masses[1], charges and spins.

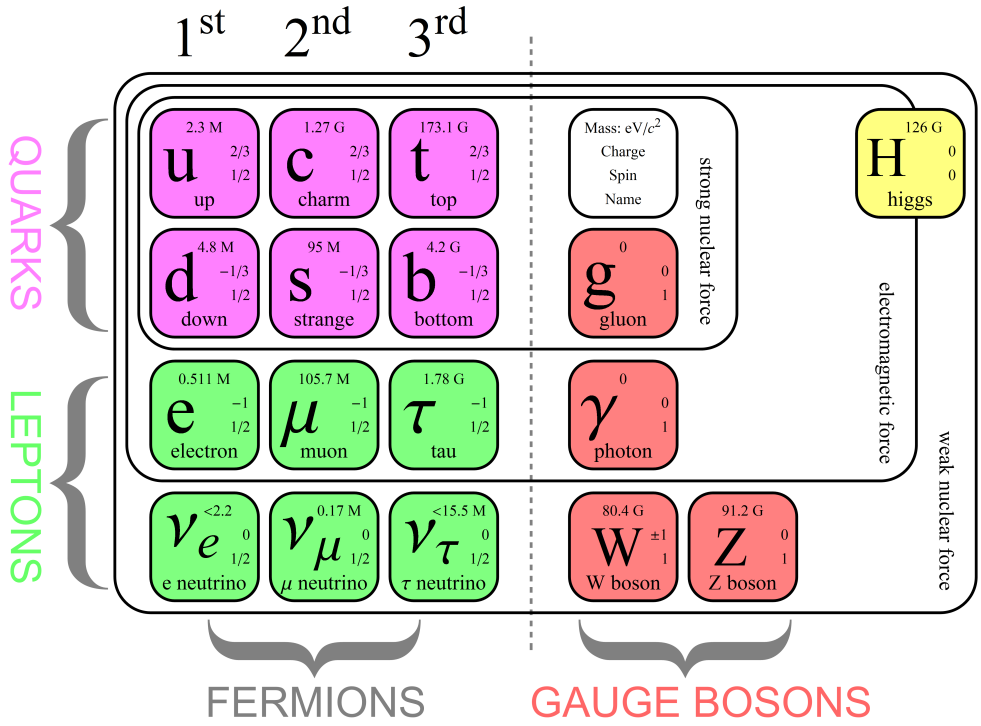

FIGURE 2.1: The Standard Model particles and their masses, charges and spins [5].

2.1.1 Particle content of the Standard Model

The SM particles are divided into two groups depending on the value of their spin. Fermions are particles with spin of $1/2\ \hbar$. In the SM, there are 12 fermions which are divided into leptons and quarks. The leptons interact through the electromagnetic interaction (charged leptons) and the weak interaction, while the quarks interact also through the strong interaction. The fermions are grouped into three families or generations, made of SU(2) doublets. The particles of the higher generation have heavier masses:

$$\begin{pmatrix} \nu_e \\ e^- \end{pmatrix}, \begin{pmatrix} \nu_\mu \\ \mu^- \end{pmatrix}, \begin{pmatrix} \nu_\tau \\ \tau^- \end{pmatrix}; \qquad \begin{pmatrix} u \\ d \end{pmatrix}, \begin{pmatrix} c \\ s \end{pmatrix}, \begin{pmatrix} t \\ b \end{pmatrix}$$

Each generation of leptons has one of the three quantum lepton numbers: the electron L_e, muon L_μ or tau L_τ.

[1] Natural units where $c = \hbar = 1$ are used in this thesis. Masses, energy and momenta are expressed in electrovolts (eV) where 1 eV corresponds to the energy a single electron gained or lost when moving through an electric potential difference of one volt.

Quarks have fractional electric charges. Up quarks have + 2/3 e, while the down quarks are charged - 1/3 e. Quarks also have an additional property called color charge. This charge is characterized by colors: red, blue and green.

Bosons are particles with integer spin detailed in Table 2.1. The gluon is massless and electrically neutral, but carries color charge. It is the mediator of the strong force. The photon is a massless and electrically neutral gauge boson. It is the mediator of the electromagnetic force. Four further bosons are massive: the charged W^+ and W^-, the electrically neutral Z^0 and H^0 bosons. The $W^\pm$ and Z^0 are mediators of the weak force, the H^0 boson has spin 0 and is a key to generating in particular W and Z masses.

Name	Mass [GeV]	Spin	Force of mechanism
Gluon	0	1	strong interaction
Photon	0	1	electroweak interaction
$W^\pm$	80.39	1	
Z	91.19	1	
H	125	0	mass generation

TABLE 2.1: The SM bosons listed with their electrical charge and arranged with increasing masses, expressed in GeV [6].

2.1.2 Quantum chromodynamics

Quantum chromodynamics (QCD) [7] is a non-Abelian gauge theory based on the local group $SU(3)_C$, which describes the strong interactions. The $SU(3)_C$ group has eight generators which correspond to eight real and independent gluon gauge fields. They are defined by a linear combination of color and anti-color.
The strong coupling constant α_s, that gives the strength of the strong interaction is defined as:

$$\alpha_s \equiv \frac{g_s}{4\pi} \tag{2.1}$$

A value of the α_s depends on the momentum transfer Q^2. At lower values of Q^2 which correspond to distances of $> \mathcal{O}$ (10^{-15} m), the value of α_s gets large. This leads to a phenomenon called color confinement. Due to color confinement, quarks cannot be directly observed or be found in isolation. Instead, quarks create bound states called hadrons. There are two types of hadrons: mesons and baryons. The mesons consist of one quark and one anti-quark with opposite color charges, while the baryons consist of three-particle bound states of quarks or anti-quarks with three different color charges. For

example, protons and neutrons are baryons. The proton is the stable and the lightest color state containing only quarks: u, u and d.
If the values of Q^2 are larger, corresponding to distances of $< \mathcal{O}(10^{-15}$ m) then α_s gets smaller. This leads to a phenomenon called asymptotic. Due to this phenomena, gluons can behave as free particles.

2.1.3 Electroweak interactions

In the 1960s Glashow, Salam and Weinberg proposed the $SU(2)_L \otimes U(1)_Y$ group aiming at the unification of the electromagnetic and weak interactions, as mentioned earlier. The $SU(2)_L$ is the gauge symmetry group of the weak isospin and has three massive gauge bosons labeled as $W^1_\mu, W^2_\mu, W^3_\mu$. On the other hand, the $U(1)_Y$ is the symmetry group with one neutral gauge boson labeled as B_μ.
Mass for fermions and bosons when added by hand to the Glashow-Salam-Weinberg theory would violate gauge symmetry. In order to solve this problem, the Brout-Englert-Higgs mechanism of electroweak spontaneous breaking was introduced [1, 8]. In this mechanism, masses can be generated by introducing a scalar Higgs field with a very specific potential. The shape of the Higgs potential looks like a Mexican hat (Figure 2.2) and it has a minimum which is not at zero. The Higgs field acquires a vacuum expectation value (VEV) which is responsible for generating masses of the weak bosons (as well as fermions).

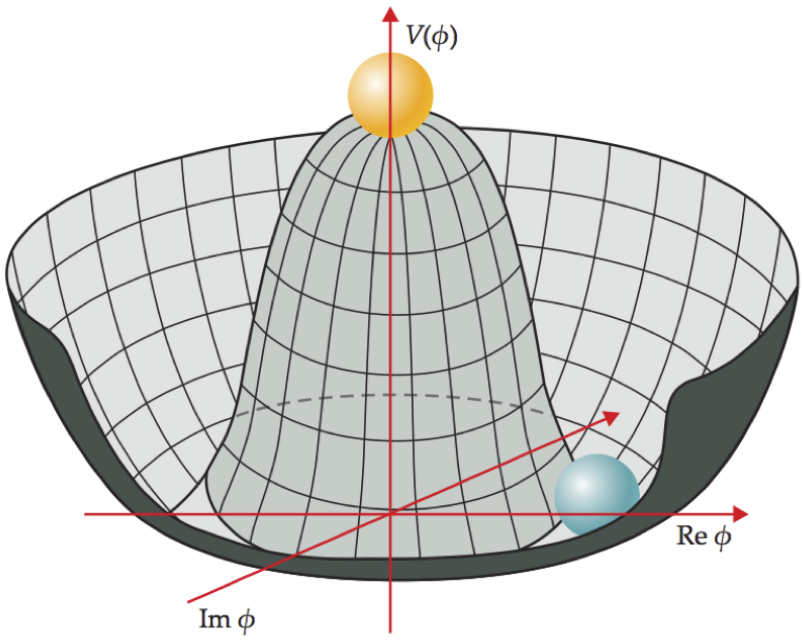

FIGURE 2.2: The potential of the scalar Higgs field [9].

The $W^1_\mu, W^2_\mu, W^3_\mu$ and B_μ bosons mix to form the physical states:

$$W^\pm_\mu = \frac{1}{\sqrt{2}}\left(W^1_\mu \mp iW^2_\mu\right) \tag{2.2}$$

$$Z_\mu = -B_\mu \sin\theta_W + W^3_\mu \cos\theta_W \tag{2.3}$$

$$A_\mu = B_\mu \cos\theta_W + W^3_\mu \sin\theta_W \tag{2.4}$$

where the mixing angle θ_W is called Weinberg angle and is defined as:

$$\sin\theta_W = g' / \sqrt{g'^2 + g^2} \tag{2.5}$$

The corresponding $SU(2)_L$ and $U(1)_Y$ coupling constants g and g' are related to the electric charge e:

$$e = g \cdot \sin\theta_W = g' \cdot \cos\theta_W \tag{2.6}$$

Since the masses of W and Z bosons are known and given in Table 2.1, the VEV can be calculated as $v \approx 246$ GeV [8].
This mechanism has only been validated in 2012, with the observation of a spin 0 boson with mass of 126.0±0.4(stat.)±0.4(sys) GeV by the ATLAS collaboration [3] and of 125.3±0.4(stat.)±0.5(sys) GeV by the CMS collaboration [4].

2.2 Problems in the Standard Model

The SM is a very successful theory which has been tested to remarkable precision over the past decades. Figure 2.3 shows several SM total production cross-sections measured by ATLAS and compared to theoretical expectations at 7 TeV, 8 TeV and 13 TeV. Nevertheless, there are still open questions that lead to a search for physics beyond the SM. Some of them are described in the following.

2.2.1 Hierarchy problem

One reason to extend the SM is known as the hierarchy problem which comes from the difference between the electroweak scale $M_{EW} \sim 10^2$ GeV and the Planck scale $M_{Pl} \sim 10^{19}$ GeV [11]. This difference affects the Higgs boson mass calculation. The mass of the Higgs boson is much lighter in comparison to the Planck mass. The Higgs mass squared m^2_H can be written as:

$$m^2_H = m^2_{H_0} + \triangle m^2_H \tag{2.7}$$

where m_{H_0} is the Higgs bare mass and $\triangle m_H$ are the quantum corrections of the Higgs boson mass. These corrections include the quantum loops from the interactions between particles and the Higgs boson and may be as large as the Planck mass.

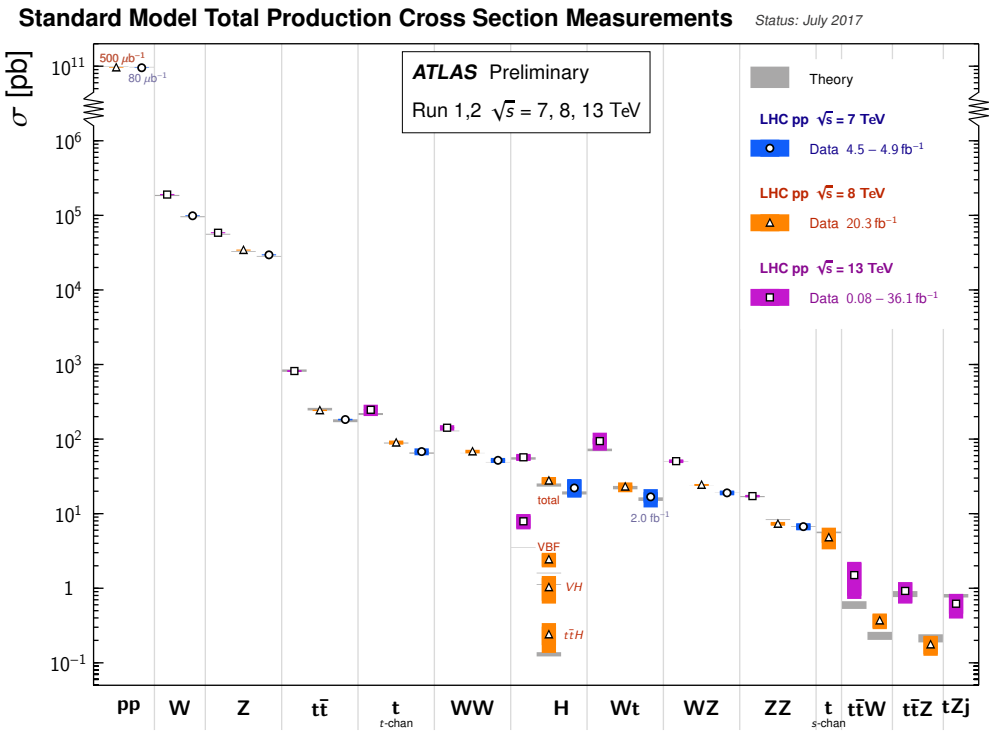

FIGURE 2.3: SM total production cross-sections of several processes including leptonic branching fraction corrections. The theoretical expectations are also shown [10].

2.2.2 Dark Matter

Several astrophysical observations have indicated that the universe contains more matter than can be explained by the SM. This matter is called Dark Matter (DM) and its composition and origin are unknown. DM can interact with the normal matter via the weak and gravitational interactions. According to the different astrophysical results, only about 4.9% of the universe is the normal matter, while DM and dark energy contribute about 26.8% and 68.3%, respectively [12]. The SM does not provide candidates for DM.

2.2.3 Gauge Couplings Unification

One weakness of the SM comes from the separation of forces. Extrapolating electroweak and strong couplings to high energy they do not meet at one energy, as one would expect if all interactions become unified.

2.3 Supersymmetry

Supersymmetry (SUSY) [11] is a theory that predicts a new type of symmetry between fermions and bosons. Such transformations are allowed by the operator Q:

$$Q\,|\,\text{Boson}\rangle = |\,\text{Fermion}\rangle, \quad Q\,|\,\text{Fermion}\rangle = |\,\text{Boson}\rangle \tag{2.8}$$

Each SM particle has a sypersymmetric partner whose spin differs by the value of 1/2, implying SM bosons have fermionic superpartners and vice versa. In SUSY, fields which describe bosons and fermions are grouped together into supermultiplets. Each supermultiplet consists of fermions and bosons, which are superpartners of each other. There are two types of supermultiplets. The first supermultiplet is called a chiral or matter or scalar supermultiplet. It has a Weyl fermion and a complex scalar field. All SM fermions (leptons and quarks) have to be members of chiral supermultiplets, and their superpartners are sfermions (sleptons and squarks). The symbols for the sfermions are the same as for the corresponding fermions, but with an additional tilde in order to distinguish them from their SM partners. The second type of supermultiplet is known as a gauge or vector supermultiplet. It contains a vector boson. All bosons with spin 1 are grouped in gauge multiplets and their superpartners are called gauginos. These are fermions with spin 1/2.
The Higgs sector contains two Higgs supermultiplets[2] formed by two Higgs doublets, labeled as $H_u = (H_u^+, H^0)$ and $H_d = (H_d^0, H_d^-)$. The supersymmetric Higgs partners ($\tilde{H}_u = (\tilde{H}_u^+, \tilde{H}^0)$ and $\tilde{H}_d = (\tilde{H}_d^0, \tilde{H}_d^-)$) are called the Higgsinos. The two Higgs doublets carry eight degrees of freedom. While three degrees of freedom are given to W and Z bosons, the other five give rise to five Higgs bosons: two CP even neutral Higgs bosons (h^0 and H^0), one CP odd neutral Higgs boson (A^0) and two charged Higgs bosons (H^+ and H^-). Figure 2.4 shows supersymmetric particles, so-called sparticles, with the corresponding partners of the SM.

2.3.1 Minimal supersymmetric standard model

The Minimal Supersymmetric Standard Model (MSSM) is a supersymmetric extension to the SM with the minimum number of additional particles. Tables 2.2 and 2.3 show the particle content of the MSSM arranged in the chiral and gauge supermultiplets, respectively.

2.3.2 Soft supersymmetry breaking

One interesting fact is that none of the sparticles has been discovered at the mass scale of their SM partners. If SUSY was unbroken then the sparticles

[2]Two supermultiplets are requested in order to have the exact cancellation of gauge anomalies.

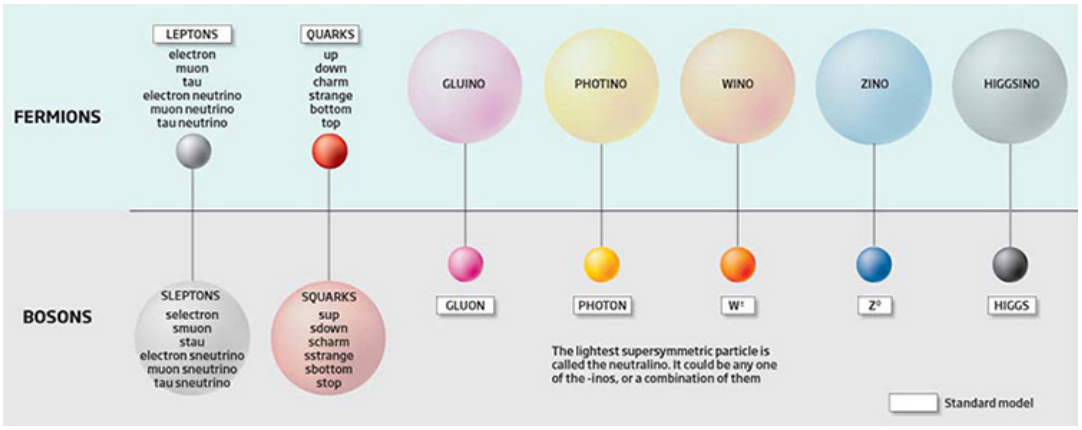

FIGURE 2.4: Schematic overview of spartciles with corresponding SM partners [13].

Names	Spin 0	Spin 1/2	$SU(3)_C$	$SU(2)_L$	$U(1)_Y$
Squarks / quarks	$(\tilde{u}_L\ \tilde{d}_L)$	$(u_L\ d_L)$	3	2	1/6
	$\tilde{u}_R$	u_R	$\overline{3}$	1	-2/3
($\times$ 3 families)	$\tilde{d}_R$	d_R	$\overline{3}$	1	1/3
Sleptons / leptons	$(\tilde{\nu}\ \tilde{e}_L)$	$(\nu\ e_L)$	1	2	-1/2
($\times$ 3 families)	$\tilde{e}_R$	e_R	1	1	1
Higgs / Higgsinos	$(H_u^+\ H_u^0)$	$(\tilde{H}_u^+\ \tilde{H}_u^0)$	1	2	+1/2
	$(H_d^0\ H_d^-)$	$(\tilde{H}_d^0\ \tilde{H}_d^-)$	1	2	-1/2

TABLE 2.2: Chiral supermultiplets in the MSSM. The first column shows the type of particles. The second and third columns contain the spin 0 and spin 1/2 components of each of these supermultiplets. The last three columns give quantum numbers [11].

must exactly have the same masses as their SM partners. Since the sparticles have not been discovered yet, it is clear that SUSY is a broken symmetry. An important consequence of SUSY breaking is the solution for the hierarchy problem. Unbroken supersymmetry allows that quadratic divergences in the scalar squared mass vanish to all orders in the perturbation theory. But if the symmetry is broken then the mechanism of symmetry breaking has to be soft. It means SUSY breaking must be done without introducing quadratic divergences. In this case, the broken symmetry still gives a solution to the hierarchy problem.

Names	Spin 1/2	Spin 1	$SU(3)_C$	$SU(2)_L$	$U(1)_Y$
Gluino / gluon	$\tilde{g}$	g	8	1	0
Winos / W bosons	$\tilde{W}^{\pm}$ $\tilde{W}^0$	$W^{\pm}$ W^0	1	3	0
Bino / B boson	$\tilde{B}^0$	B^0	1	1	0

TABLE 2.3: Gauge supermultiplets in the MSSM. The first column shows the type of particles. The second and third columns contain the spin 1/2 and spin 1 components of each of these supermultiplets. The last three columns give quantum numbers [11].

In case of soft supersymmetry breaking, the total Lagrangian can be written in the form:

$$\mathcal{L} = \mathcal{L}_{SUSY} + \mathcal{L}_{soft} \tag{2.9}$$

where $\mathcal{L}_{SUSY}$ contains the original SUSY parameters and $\mathcal{L}_{soft}$ contains all additional parameters.

The soft part of Lagrangian $\mathcal{L}_{soft}$ introduces many new parameters into the theory (105 in the MSSM).

2.3.3 Mass spectrum of the MSSM

The chiral and gauge supermultiplets given in Tables 2.2 and 2.3 make up the particle content of the MSSM. With $\mathcal{L}_{soft}$, new mass terms have been introduced, and they mix to form mass eigenstates of the sparticles. The neutral gauginos ($\tilde{W}^0$ and $\tilde{B}$) and the neutral higgsinos ($\tilde{H}_u^0$ and $\tilde{H}_d^0$) combine to form four mass eigenstates called neutralinos. They are denoted $\tilde{\chi}_j^0$ (j=1,2,3,4) with increasing mass.

The charged winos ($\tilde{W}^+$ and $\tilde{W}^-$) and the charged higgsinos ($\tilde{H}_u^+$ and $\tilde{H}_u^-$) mix to form two mass eigenstates with charge ± 1 called charginos. They are denoted as $\tilde{\chi}_i^{\pm}$ (i=1,2), again with increasing mass.

The gluino is a color octet fermion and does not mix with any other particles in the MSSM.

Mixing of the slepton and squark states is also present due to electroweak symmetry breaking effects. Usually, this is considered to be negligible except for the third generation sparticles. The $\tilde{\tau}_L$ and $\tilde{\tau}_R$ states mix to form the mass eigenstates $\tilde{\tau}_1$ and $\tilde{\tau}_2$. Similarly, the $\tilde{b}_L$ and $\tilde{b}_R$ states mix resulting in the mass eigenstates $\tilde{b}_1$ and $\tilde{b}_1$, and the $\tilde{t}_L$ and $\tilde{t}_R$ states give the mass eigenstates $\tilde{t}_1$ and $\tilde{t}_2$. They are denoted with increasing mass. From the Higgs sector, five mass eigenstates occur. Table 2.4 details all resulting mass eigenstates.

Names	Spin	Gauge eigenstates	Mass eigenstates
Higgs bosons	0	$H_u^0\ H_d^0\ H_u^+\ H_d^-$	$h^0\ H^0\ A^0\ H^\pm$
Squarks	0	$\tilde{u}_L\ \tilde{u}_R\ \tilde{d}_L\ \tilde{d}_R$ $\tilde{s}_L\ \tilde{s}_R\ \tilde{c}_L\ \tilde{c}_R$ $\tilde{t}_L\ \tilde{t}_R\ \tilde{b}_L\ \tilde{b}_R$	same same $\tilde{t}_1\ \tilde{t}_2\ \tilde{b}_1\ \tilde{b}_2$
Sleptons	0	$\tilde{e}_L\ \tilde{e}_R\ \tilde{\nu}_e$ $\tilde{\mu}_L\ \tilde{\mu}_R\ \tilde{\nu}_\mu$ $\tilde{\tau}_L\ \tilde{\tau}_R\ \tilde{\nu}_\tau$	same same $\tilde{\tau}_1\ \tilde{\tau}_2\ \tilde{\nu}_\tau$
Neutralinos	1/2	$\tilde{B}^0\ \tilde{W}^0\ \tilde{H}_u^0\ \tilde{H}_d^0$	$\tilde{\chi}_1^0\ \tilde{\chi}_2^0\tilde{\chi}_3^0\ \tilde{\chi}_4^0$
Charginos	1/2	$\tilde{W}^\pm\ \tilde{H}_u^+\ \tilde{H}_d^-$	$\tilde{\chi}_1^\pm\ \tilde{\chi}_2^\pm$
Gluino	1/2	$\tilde{g}$	same

TABLE 2.4: The particles in the MSSM with sfermion mixing for the first two families assumed to be negligible [11].

2.3.4 R-parity

According to proton decay experiments, the proton is stable. The Super-Kamiokande experiment sets a limit on the proton decay of 2.3 $\times 10^{33}$ years by using the $p \to K^+\bar{\nu}$ decay mode [14, 15]. This limit implies that if a process which allows the proton decay existed in nature, it has to be extremely rare. On the other hand, in the MSSM proton decays are allowed. In order to avoid proton decays, an additional number called R-parity is introduced as:

$$R = (-1)^{3(B-L)+2s} \tag{2.10}$$

where B and L are the baryon and lepton numbers, respectively and s is the spin of the particle. The SM particles have R=+1 while their supersymmetric partners have R=-1.
Important phenomenological consequences of R-parity are:

- sparticles have to be produced in pairs in particle colliders since the SM particles are used in the initial states.
- The lightest supersymmetric particle (LSP) has to be stable and is produced at the end of the decay chain. If it is electrically neutral, then it can only interact weakly or gravitationally with the normal matter.

2.4 Solutions to the SM problems

A strong argument in favour of SUSY is the solution of the SM problems discussed in Section 2.2. SUSY provides elegant solutions to these problems as discussed in the following.

2.4.1 Hierarchy problem

Two scalar bosons with a coupling of $\lambda_S = |\lambda_f|^2$ can compensate the contribution of the fermion and give the correction to the Higgs mass as [11]:

$$\Delta m_H^2 = \frac{\lambda_S}{16\pi^2}\left[\Lambda_{UV}^2 - 2m_S^2 \ln(\Lambda_{UV}/m_S) + \dots\right] \tag{2.11}$$

Because of an additional factor (-1) from Fermi statistics the contribution from the boson loops can cancel those from the fermion loops. Figure 2.5 shows two types of contributions. The first contribution is from the heavy Higgs boson and its superpartner (top), while the second contribution is from the heavy gauge boson (bottom left) and gaugino (bottom right). The green line presents the Higgs boson.

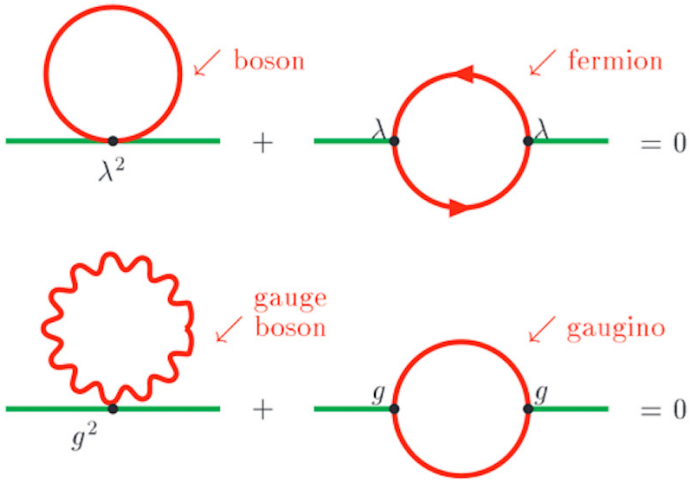

FIGURE 2.5: Cancellation of quadratic terms in the Higgs mass [16].

2.4.2 Dark matter

Several SUSY models provide a natural candidate for DM as consequence of R-parity conservation. The LSP has to be stable and electrically neutral [11]. It only interacts weakly with the normal matter and can be an excellent candidate for DM. In models described in this thesis, the lightest neutralino is the LSP.

2.4.3 Unification of gauge couplings

As discussed in the previous section 2.2, the electroweak and strong couplings do not meet at one energy as shown in Figure 2.6 (left). Introducing new particles predicted by the MSSM, a singular point at $\mathcal{O}(10^{16})$ GeV unites the coupling constants of all three forces as shown in Figure 2.6 (right).

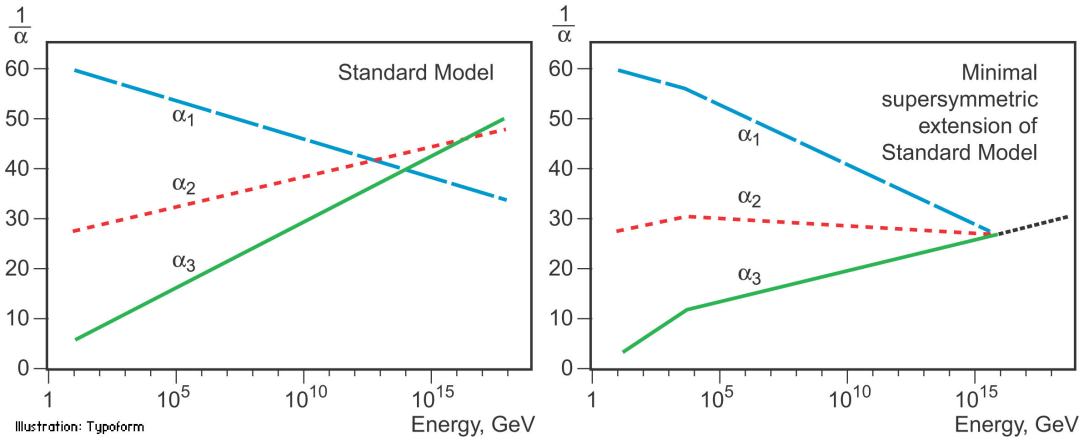

FIGURE 2.6: Running inverse coupling constants in the SM (left) and SUSY (right). In the SM, the three lines which show the inverse value of the coupling constant for the three fundamental forces, do not meet at one point. In SUSY, they do meet at one point [17].

2.5 Simplified models

The simplified models are defined by an effective Lagrangian describing a set of particles linked to observables such as particle masses and interactions, production cross-sections and branching ratios [18]. In the simplified models, only the production process for particles of interest is considered. The masses of all other particles which do not participate in the interaction are set to very high masses compared to the center-of-mass energy available.

In the simplified models, initial particles can decay directly or through an intermediate particle to a neutral and undetected particle, known as the LSP.

The signal scenarios considered in this thesis are all simplified models, and are discussed in the following.

2.5.1 Search for squarks and gluinos

In proton-proton collisions, the cross-section for the production of squarks and gluinos is expected to be larger than the cross-section for SUSY particles produced in the electroweak production. Figure 2.7 shows the cross-sections for various SUSY particles as a function of the average sparticle mass for proton-proton collisions at a centre-of-mass energy of 13 TeV.

In R-parity-conserving models, squarks and gluinos must be produced in pairs:

$$qq \rightarrow \tilde{q}_i\tilde{q}_j$$
$$q\bar{q} \rightarrow \tilde{g}\tilde{g},\ \tilde{q}_i\tilde{q}_j^*$$
$$gg \rightarrow \tilde{g}\tilde{g},\ \tilde{q}_i\tilde{q}_j^*$$

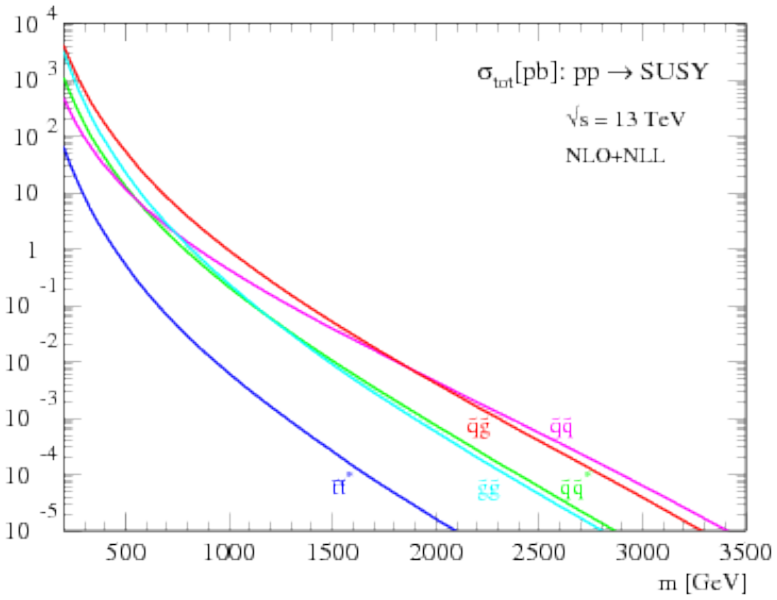

FIGURE 2.7: Next-to-leading order cross-section for the production of SUSY particles at the Large Hadron Collider [19].

If $m_{\tilde{q}} > m_{\tilde{g}}$, squarks decay to a quark and a gluino, $\tilde{q} \to q\tilde{g}$. If $m_{\tilde{q}} < m_{\tilde{g}}$, squarks decay to neutralinos ($\tilde{q} \to q\tilde{\chi}_j^0$) or charginos ($\tilde{q} \to q\tilde{\chi}_i^\pm$). The direct decay of squarks to the lightest neutralino and one SM quark, $\tilde{q} \to q\tilde{\chi}_1^0$, is kinematically favored. This is the simplest squark decay which results in a final state consisting of several jets and missing transverse momentum coming from the $\tilde{\chi}_1^0$. Since this thesis focuses on the searches with one lepton in a final state, a model in which a squark decays to either the lightest chargino and one SM quark $\tilde{q} \to q\tilde{\chi}_1^\pm$, or the next-to-lightest neutralino and one SM quark $\tilde{q} \to q\tilde{\chi}_2^0$ is considered. In this model, the chargino then decays to the lightest neutralino emitting a W boson $\tilde{\chi}_1^\pm \to W^\pm\tilde{\chi}_1^0$, while the next-to-lightest neutralino decays to either a Z boson and the lightest neutralino or a Higgs boson and the lightest neutralino, $\tilde{\chi}_2^0 \to Z/h\tilde{\chi}_1^0$. A Feynman diagram for such a decay is shown in Figure 2.8 (left).

On the other hand, gluinos can only decay via a squark, either on-shell or virtual. If $m_{\tilde{q}} < m_{\tilde{g}}$, then a two-body decay ($\tilde{g} \to q\bar{\tilde{q}}$) will be dominant. If $m_{\tilde{q}} > m_{\tilde{g}}$, gluinos can decay via off-shell squarks to neutralinos ($\tilde{g} \to q\bar{q}\tilde{\chi}_j^0$) or charginos ($\tilde{g} \to q\bar{q}\tilde{\chi}_i^\pm$). In the simplest decay mode, gluinos decay to the lightest neutralino and two SM quarks, $\tilde{g} \to q\bar{q}\tilde{\chi}_1^0$. This decay gives several jets and missing transverse momentum in a final state. Due to the one lepton requirement, in the model considered in this thesis, the gluino decays to either the lightest chargino and two SM quarks $\tilde{g} \to q\bar{q}\tilde{\chi}_1^\pm$ or the next-to-lightest neutralino and two SM quarks $\tilde{g} \to q\bar{q}\tilde{\chi}_2^0$, as shown in Figure 2.8 (right). The decay chains of the lightest chargino and the next-to-lightest neutralino are the same as for the squark production. In both productions, the LSP is assumed to be the lightest neutralino.

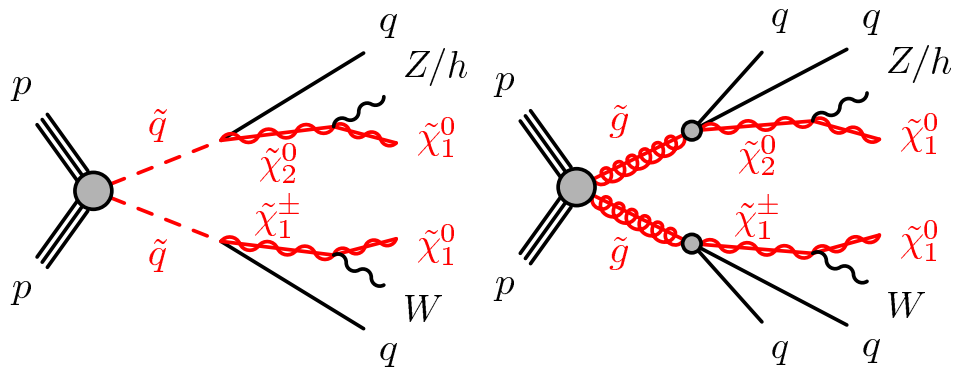

FIGURE 2.8: The decay topologies of the signal models considered in this thesis: squark production (left) and gluino production (right).

The final state considered here consists of exactly one lepton (electron or muon), different jet multiplicity depending on the decay chains of W, Z and h bosons and missing transverse momentum from neutrinos and neutralinos. This search is discussed in detail in Chapter 9.

2.5.2 Search for charginos and neutralinos

This section describes the process of direct pair production of the mass-degenerate $\tilde{\chi}_1^\pm\tilde{\chi}_2^0$, $pp \to \tilde{\chi}_1^\pm\tilde{\chi}_2^0$, which are assumed to be the lightest chargino and the next-to-lightest neutralino as shown in Figure 2.9. The $\tilde{\chi}_1^\pm\tilde{\chi}_2^0$ are generated to be wino-like, while the $\tilde{\chi}_1^0$ is bino-like. Masses of the $\tilde{\chi}_1^\pm\tilde{\chi}_2^0$ are set to be equal. Particles which are not involved in the decay chain are assumed to be massive and decoupled, while masses of the relevant particles ($\tilde{\chi}_1^\pm/\tilde{\chi}_2^0, \tilde{\chi}_1^0$) are varied independently to cover a large parameter space.

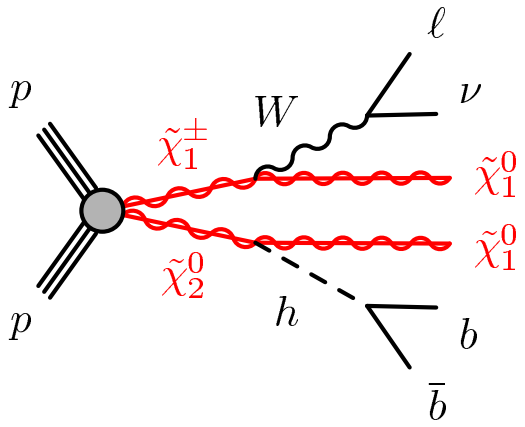

FIGURE 2.9: Diagram for the direct pair production of $\tilde{\chi}_1^\pm\tilde{\chi}_2^0$ considered in this thesis.

The lightest chargino decays to the lightest neutralino and a W boson with a 100% branching ratio, the $W^{\pm}$ boson then decays leptonically giving one charged lepton (electron or muon), $\tilde{\chi}_1^{\pm} \rightarrow \tilde{\chi}_1^0 W^{\pm} \rightarrow \tilde{\chi}_1^0 l^{\pm} \bar{\nu}$. On the other hand, the next-to-lightest neutralino decays to the lightest neutralino and a Higgs boson with the branching ratio of 100%. The Higgs boson mass is set to 125 GeV to be consistent with the measured value [3, 4] and its branching fractions are assumed to be the same as in the SM. However, only the Higgs decay chain to $b\bar{b}$ is considered due to the highest cross-section[3], $\tilde{\chi}_2^0 \rightarrow \tilde{\chi}_1^0 h \rightarrow \tilde{\chi}_1^0 b\bar{b}$. The final state considered for the search presented in this thesis has exactly one lepton (electron or muon) from the $W^{\pm}$ boson, two b-jets from the Higgs boson and missing transverse momentum from neutrino and neutralinos. This search is discussed in detail in Chapter 10.

[3] BR($H \rightarrow b\bar{b}$)=0.58 [20].

Chapter 3

Experimental overview

This chapter describes the design and working principles of the Large Hadron Collider and of the ATLAS detector which provide the dataset used in the searches presented in this thesis. Monte Carlo generators including the modelling of hard scattering, and an overview of different generators are detailed. The CERN Grid computing is also discussed since it provides significant resources to store, process and distribute data generated by the Large Hadron Collider.

3.1 The Large Hadron Collider

The Large Hadron Collider (LHC) is situated in a 26.7 km-long circular tunnel and at a depth of 45-170 m under the border of France and Switzerland as shown in Figure 3.1 [21]. This tunnel was originally constructed between 1984 and 1989 for the Large Electron Positron Collider (LEP) [21]. The LHC project was approved by the CERN Council in December 1994, while an approval to construct the 14 TeV machine in a single step came 2 years later [21]. The strong motivation for the LHC project was the existing LEP tunnel and a possibility to use the LEP injection chain. In 2000, the LEP was closed and its tunnel was used for the LHC [21]. The LHC started operation on 10th September 2008, but due to an incident the initial testing was delayed from 2008 to the end of 2009 [21, 22]. From 2010 to 2012 (LHC Run I) the LHC had very successful operations. An enormous success of the LHC Run I is the discovery of the Higgs boson, which had been the last undetected particle of the SM [3, 4].
After an upgrade phase of 2 years, the LHC resumed operations in 2015 and is now delivering two beams of protons accelerated to 6.5 TeV. A total collision energy is 13 TeV. This period of the LHC running is known as the LHC Run II.

Seven different experiments with their own detectors collect particles produced by collisions in the LHC [24]. The two biggest experiments are:

- ATLAS (**A** **T**oroidal **L**HC **A**pparatu**S**), and

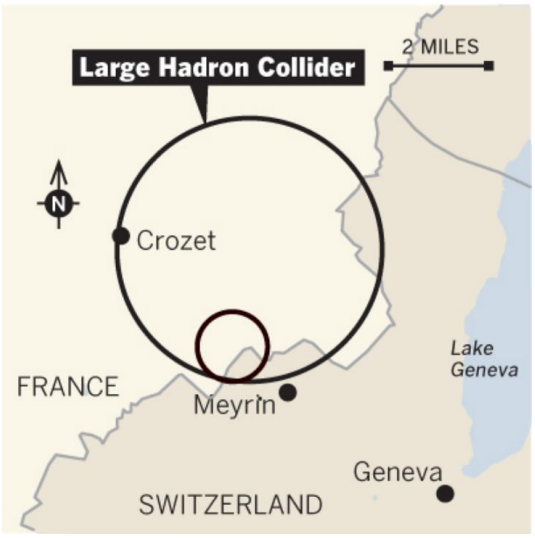

FIGURE 3.1: The geographical location of the LHC ring [23].

- CMS (**C**ompact **M**uon **S**olenoid) [25].

They use multi-purpose detectors to investigate the SM and beyond the SM theories. Since these two detectors are independent, results obtained from both of them are vital for the cross confirmation of any new discoveries. The other five experiments use detectors built for specialized purposes as described below.

- LHCb (**L**arge **H**adron **C**ollider **b**eauty) studies B-physics [26],
- ALICE (**A** **L**arge **I**on **C**ollider **E**xperiment) uses heavy-ion collisions to study the quark-gluion plasma [27],
- LHCf (**L**arge **H**adron **C**ollider **f**orward) uses particles produced at very small angles to the beam directions in LHC collisions to simulate cosmic rays [28],
- TOTEM (**TOT**al **e**lastic And diffractive cross section **M**easurement) measures the total proton-proton cross-section and studies the elastic and diffractive scattering [29], and
- MoEDAL (**Mo**nopole and **E**xotics **D**etector **A**t the **L**HC) searches for hypothetical particles such as magnetic monopoles and dyons [30].

Figure 3.2 shows the LHC ring and the position of four experiments: ATLAS, CMS, ALICE and LHCb that are installed around the points in which the beams collide.
The LHC has to accelerate a large number of protons which arrive in bunches. These bunches are prepared in the complex system of pre-accelerators.
Figure 3.3 shows the full CERN accelerator complex.

The protons are produced from hydrogen which has to pass through an electric field to stip off its electrons. Then the protons are passed through a

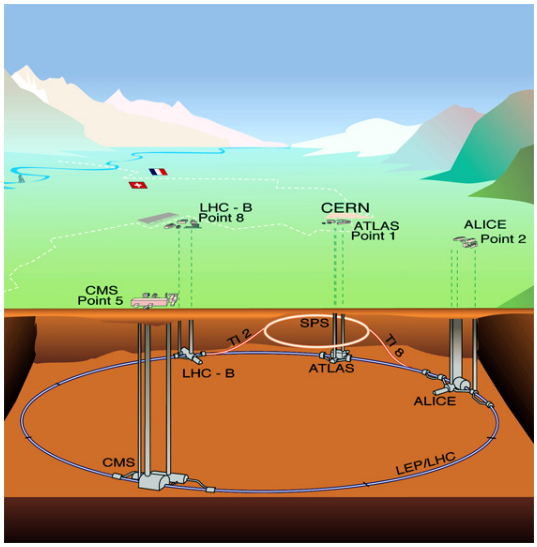

FIGURE 3.2: Overview of four LHC detectors installed in the LHC ring [31].

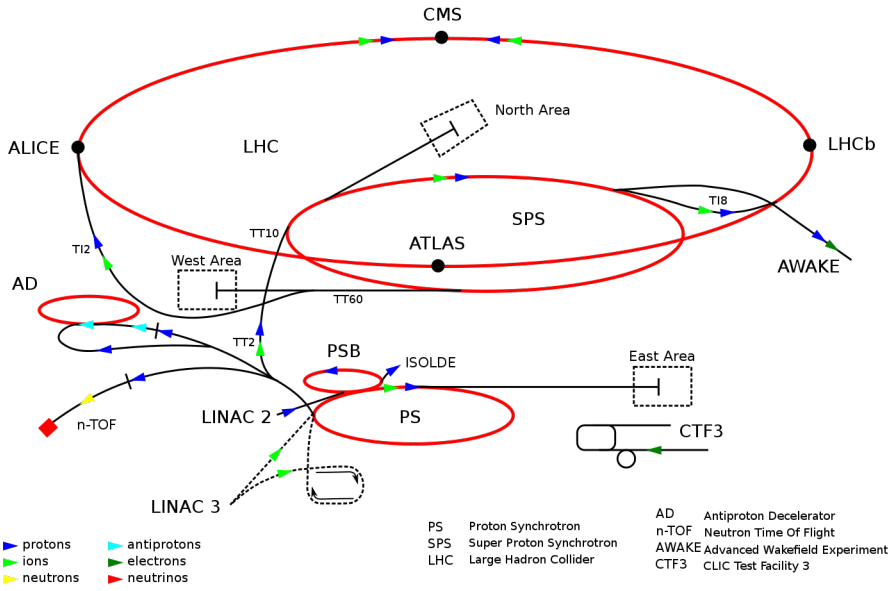

FIGURE 3.3: Map of the CERN accelerator complex [32].

series of systems that successively increase their energy before being injected into the main accelerator. The first system is the linear accelerator 2 (LINAC 2), which accelerates the protons to an energy of 50 MeV [33]. This accelerator uses positive and negative electric fields to push and pull particles through the accelerator. The protons are further injected into the first circular accelerator in the pre-accelerator complex called the Proton Synchrotron Booster (PSB). It is made up of four synchrotron rings that accelerate the protons up to 1.4 GeV and inject them into the Proton Synchrotron (PS) [33]. This 600

m long circular accelerator accelerates the protons up to 25 GeV by conventional room-temperature electromagnets [34]. The next step is the Super Proton Synchrotron (SPS), the second largest machine in the CERN accelerator complex with a 7 km long ring. The SPS uses conventional electromagnets to accelerate the protons to 450 GeV before they are injected into the LHC [33]. The last step is the final acceleration in the LHC. Here the proton bunches are accumulated and reach their maximum energy. Finally, they are circulated for 5 to 24 hours in the LHC ring, where collisions occur at four interaction points.

The LHC superconducting magnets produce a magnetic field of 8.3 T which bends beams and keeps them in their orbit at the high energy [33]. According to the design values, the LHC will collide beams consists of up to 2808 bunches with a 25 ns bunch spacing at the centre-of-mass energy of 14 TeV [35]. During operations in 2015 and 2016, the LHC collided beams consists of up to 2244 and 2076 bunches, respectively with a 25 ns bunch spacing at the centre-of-mass energy of 13 TeV [35].

3.1.1 Luminosity

The main goal of the ATLAS detector is to detect particles produced in different processes that originate from proton-proton collisions provided by the LHC. How many times a particular process will appear during collisions is a crucial information. The number of events, N, detected in a certain time, t, for the particular process expected after running an experiment can be calculated as:

$$\frac{dN}{dt} = \sigma \cdot L \tag{3.1}$$

where σ is the cross-section of the particular process and L is the luminosity [21, 36]. The cross-sections have different values for different processes as shown in Figure 2.3, where the cross-sections as a function of energy for different processes are given.

The instantaneous luminosity can be calculated from:

$$L = \frac{N_b^2 n_b f_{rev} \gamma_r}{4\pi \epsilon_n \beta^*} \cdot F \tag{3.2}$$

where N_b is the number of protons per bunch, n_b is the number of bunches per beam, f_{rev} is the revolution frequency, γ_r is the relativistic gamma factor, ϵ_n is the normalized transverse beam emittance, β^* is the β value at the interaction point and F is the reduction parameter introduced due to the geometry of the beam crossing defined as:

$$F = \left(1 + \left(\frac{\theta_c \sigma_z}{2\sigma^*}\right)^2\right)^{-1/2} \tag{3.3}$$

where θ_c is the crossing angle of the beams, σ_z is the root mean square of the bunch length in the z direction and σ^* is the same parameter but in the transverse direction [21, 36].

The integrated luminosity is the integral of the delivered luminosity over a period of time:

$$L_{int} = \int L dt \tag{3.4}$$

Usually, the cross-section is expressed in units of cm^{-2}. A second unit is barn, where 1 barn is $10^{-24} cm^2$. Integrated luminosities in ATLAS are usually reported in units of 1/pb or 1/fb. Figure 3.4 shows the total integrated luminosities delivered by the LHC and recorded by the ATLAS detector in 2015 and 2016.

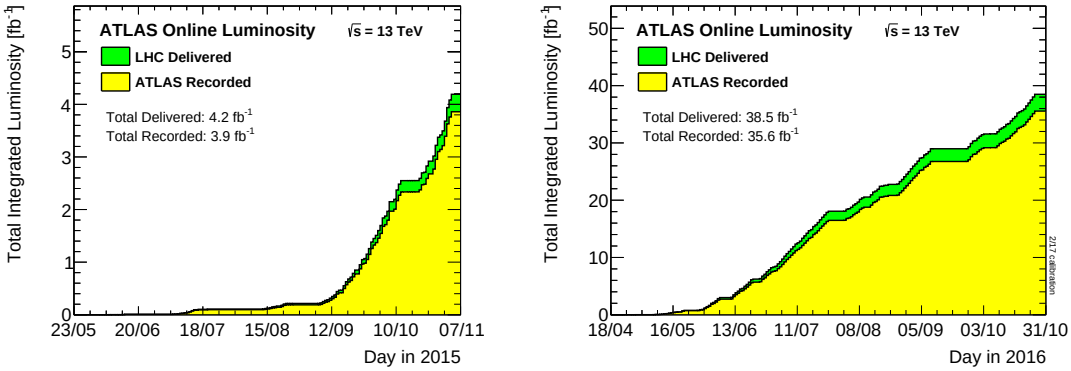

FIGURE 3.4: Total integrated luminosity versus time delivered by the LHC (green) and recorded by the ATLAS detector (yellow) during stable beams of proton-proton collisions at the centre-of-mass energy of 13 TeV in 2015 (left) and 2016 (right) [37].

3.1.2 Pile-up in proton-proton collisions

Due to the high instantaneous luminosity of the LHC, multiple proton-proton interactions, known as in-time pile-up occur within each bunch crossing. The expected value of pile-up (μ) is:

$$\mu = \frac{L \sigma_{inelastic}}{n_c f_{rev}} \tag{3.5}$$

where L is the luminosity defined in Equation 3.1, $\sigma_{inelastic}$ is the inelastic proton-proton cross-section, n_c is the number of colliding bunches in the LHC and f_{rev} is the revolution frequency with the value of 11.245 kHz [38]. If the luminosity in Equation 3.5 is measured by averaging over many bunch crossings, then this equation presents the average number of interactions per crossing. Figure 3.5 shows the average number of interactions per crossing for the data samples collected in 2015 and 2016, when the average number of

interactions per crossing had the values of 13.7 in 2015 and 24.9 in 2016 [37]. The in-time pile-up can also be accompanied by out-of-time pile-up that occurs when the detector and/or electronics integration time is significantly larger than the time between crossings.

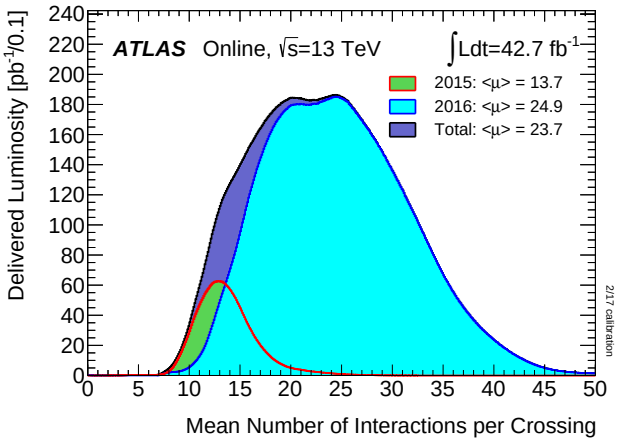

FIGURE 3.5: The average number of interactions per crossing as a function of recorded luminosity for the proton-proton data samples collected in 2015 and 2016 [37].

3.1.3 Operations in 2015 and 2016

This thesis uses only events collected by the ATLAS detector in 2015 and 2016 when the LHC delivered 42.7 fb^{-1} to ATLAS (4.2 fb^{-1} in 2015 and 38.5 fb^{-1} in 2016) [37]. Figure 3.6 shows the luminosity as a function of time delivered to ATLAS in 2015, 2016 and during the LHC Run I (2011 and 2012).

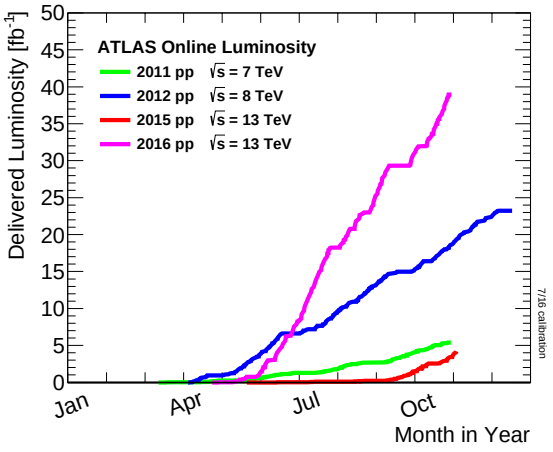

FIGURE 3.6: Integrated luminosities as a function of time recorded by the ATLAS detector [37].

3.2 The ATLAS detector

ATLAS is a general-purpose detector designed to precisely measure properties of all particles emerging from proton-proton collisions [39]. It has the shape of a cylinder as shown in Figure 3.7. With a length of 46 m, a diameter of 25 m and an overall weight of 7 000 tonnes, ATLAS presents the largest detector ever constructed for particle physics [39]. Its size is mainly determined by the Muon Spectrometer which gives the ATLAS detector its shape.

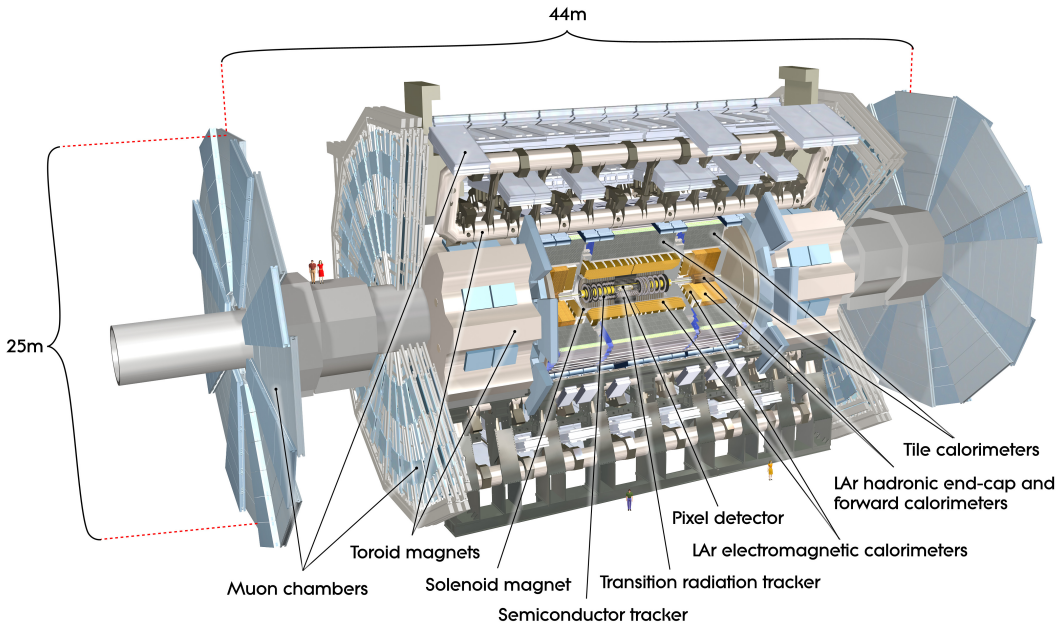

FIGURE 3.7: Schematic overview of the ATLAS detector installed in the LHC ring [39].

The ATLAS detector consists of four main components: the Inner Detector, the calorimeters, the Muon Spectrometer and the magnet system [39]. In addition, two systems are integrated with the detector components: the Trigger and Data Acquisition System which selects potentially interesting physics events, and the Computing System which provides software packages used to store and analyze large amounts of data recorded by the detector. All parts are discussed in the following starting from the ATLAS coordinate system.

3.2.1 ATLAS Coordinate System

The ATLAS coordinate system is a right-handed system that has its origin at the interaction point at the center of the detector. The direction of the beam line defines the z-axis, while the x-axis points to the center of the LHC ring and the y-axis points vertically upwards as shown in Figure 3.8. The half of the ATLAS detector at the positive z value is defined as the "A-side", the other half is referred to as the "C-side".

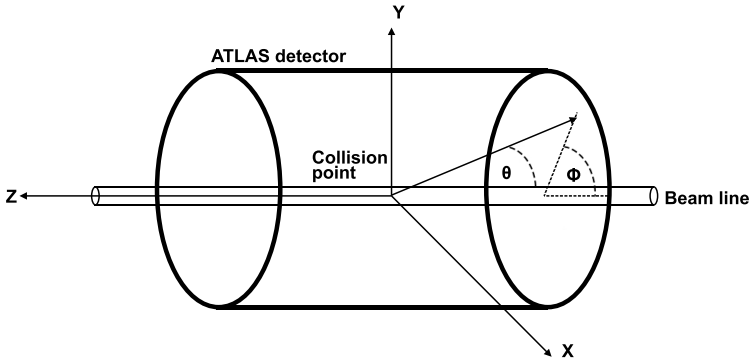

FIGURE 3.8: Illustration of the ATLAS coordinate system.

The azimuthal angle ϕ is measured around the beam line, while the polar angle θ is the angle from the beam line as illustrated in Figure 3.8. The rapidity is defined as [40]:

$$y = \frac{1}{2}\ln\left(\frac{E + p_z}{E - p_z}\right) \tag{3.6}$$

The pseudorapidity is the approximation of the rapidity for high-energy particles [40]:

$$\eta = -\ln\left(\tan\frac{\theta}{2}\right) \tag{3.7}$$

Figure 3.9 shows some values of the polar angle and the pseudorapidity for visualization the correspondence between them.

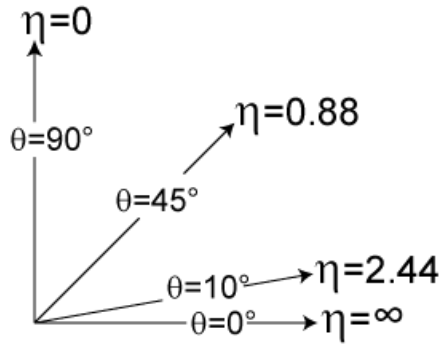

FIGURE 3.9: Values of the pseudorapidity as a function of the polar angles [41].

The geometrical distance between two particles in the pseudorapidity-azimuthal angle space is defined as:

$$\Delta R = \sqrt{\Delta\eta^2 + \Delta\phi^2} \tag{3.8}$$

The transverse momentum p_T and energy E_T are often used variables and are defined by their projection on the x-y plane:

$$E_T = E \times \sin\theta; \qquad p_T = p \times \sin\theta \tag{3.9}$$

3.2.2 Magnet system

The magnet system allows the measurement of particle momenta by bending charged particles. This bending is due to the Lorentz force:

$$\frac{d\vec{p}}{dt} = q(\vec{E} + \vec{v} \times \vec{B}) \tag{3.10}$$

where $\vec{p}$ is the particle 4-momentum, q is the charge of the particle, $\vec{E}$ is the electric field vector, $\vec{v}$ is the velocity vector of the charged particle and $\vec{B}$ is the magnetic field vector.
Figure 3.10 shows an overview of the magnet system which is 22 m long in diameter and 26 m in length [39].

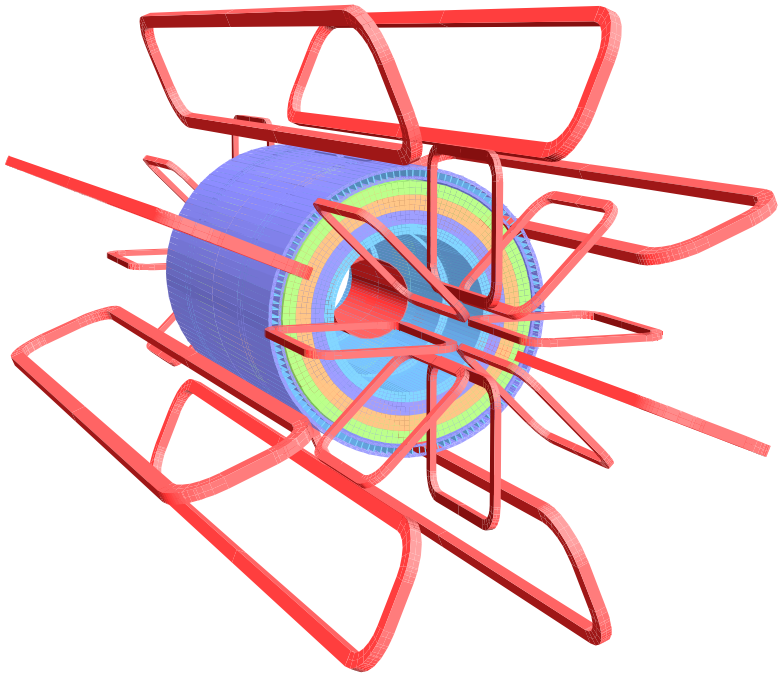

FIGURE 3.10: Schematic overview of the ATLAS magnet system. The solenoid is situated in the inner cylinder and provides an uniform magnetic field in the Inner Detector. The barrel and endcap toroids are outside and they provide a non-uniform magnetic field in the Muon Spectrometer [39].

The magnet system consists of four large superconducting magnets:

- **the central solenoid** is designed to provide a 2 T magnetic field. It is situated inside the calorimeters and surrounds the Inner Detector. The length of the solenoid is 5.8 m [39].

- **the barrel toroid** consists of eight separate coils and provides a magnetic field of 4 T [39]. It is situated outside the calorimeters. The length of the barrel toroid is 25.3 m [39].

- **two end-cap toroids** provide a magnetic field of 4 T and consist of eight independent coils which are located within the Muon Spectrometer [39]. The length of the end-cap toroids is 5.0 m [39].

3.2.3 Inner Detector

The ATLAS Inner Detector (ID) is situated at the center of the experiment. It is designed to measure the direction, momentum and charge of all electrically-charged particles produced by the LHC and to precisely determine the primary vertex (PV) and secondary vertex (SV). The ID has full coverage in ϕ and can measure particles with $|\eta| < 2.5$. Typical resolution is [39]:

$$\sigma_{p_T}/p_T = 0.05\% \cdot p_T \oplus 1\%$$

where the $\oplus$ symbol indicates a quadratic sum and p_T is measured in GeV. The ID has the geometry of a cylinder and consists of three individual detectors: the Silicon Pixel Tracker, the Semiconductor Tracker and the Transition Radiation Tracker as shown in Figure 3.11. The Silicon Pixel Tracker and the Semiconductor Tracker cover the region $|\eta| < 2.5$, while the Transition Radiation Tracker covers only $|\eta| < 2$. The length of the ID is 6.2 m, while its width is 2.1 m [39].
According to the design value, the detector should measure approximately 1000 charged particles every 25 ns [39].

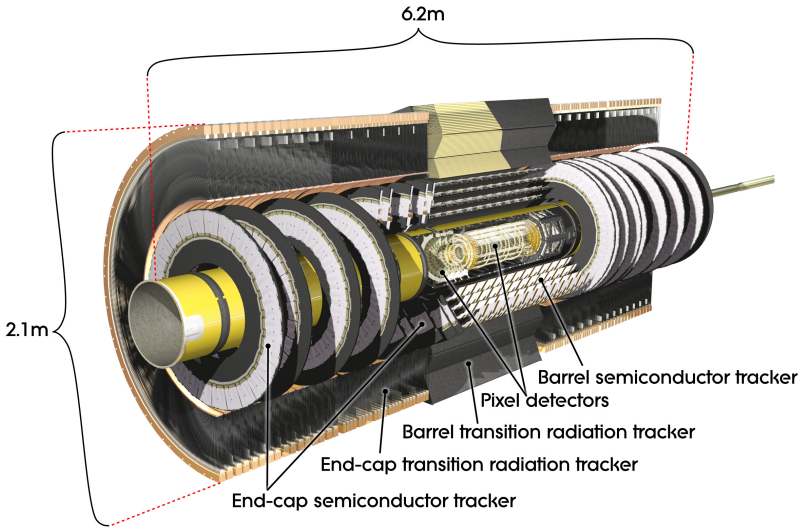

FIGURE 3.11: Individual components of the ATLAS Inner Detector [39].

Silicon Pixel Tracker

The Silicon Pixel Tracker (Pixel) is the detector situated closest to the beam line of the LHC and consists of four layers in the barrel and of two end-cap regions. The first three layers are labeled as Layer-0, Layer-1, and Layer-2, while the forth layer has been added for the 2015 data-taking and is called the Insertable B-Layer (IBL). The basic building element of the pixel detector is a set composed of silicon sensors and front-end electronics. All sensors are identical and consist of 47232 pixels [39]. Their nominal size in R – ϕ and z direction is 50 $\times$ 400 μm^2 in the barrel, respectively and 50 $\times$ 600 μm^2 in the end-cap regions in R – ϕ and R, respectively [39]. This detector is designed to provide the highest granularity used for the vertex reconstruction and the highest precision used for the measurement of impact parameters (IP's)[1] defined as the minimum distance between the track and the PV. In 2014, the IBL was added as the forth layer of the Pixel. This layer consists of 14 staves mounted directly on top of the beam pipe, inside the barrel Layer-0 as shown in Figure 3.12. The radius of the sensitive area is 33 mm from the interaction point. Because of this extremely close distance, the size of the pixel sensor is reduced to 50 $\times$ 250 μm leading to an improved impact parameter resolution. The IBL is especially useful for the identification of the SV. This can improve b-tagging, since the lifetime of b quarks allows them to travel a measurable distance before decaying.

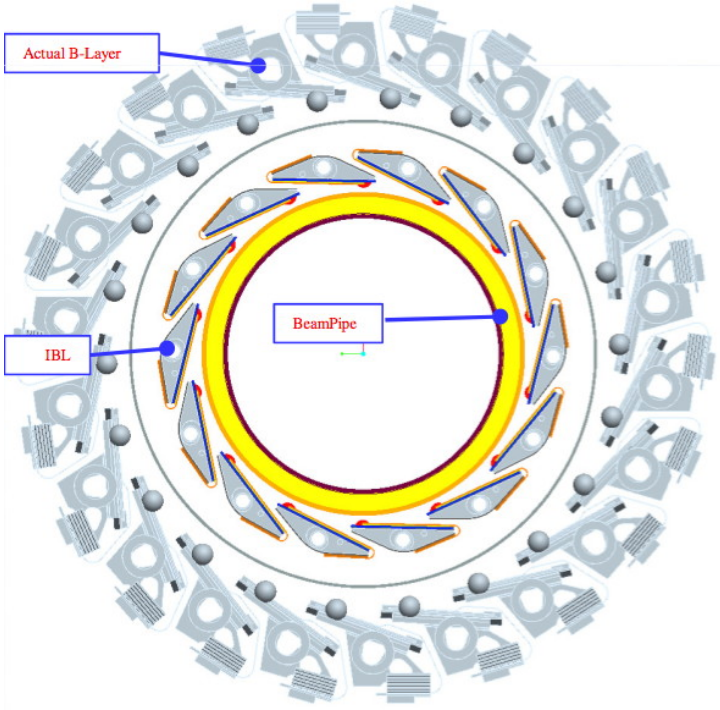

FIGURE 3.12: Schematic overview of the IBL in r – ϕ view [42].

[1] defined in more detail in Section 4.1.4.

Semiconductor Tracker

The Semiconductor Tracker (SCT) is the second subdetector which is located just outside the Pixel. It consists of four layers of silicon microstrip modules in the barrel and of two end-cap regions. The strips have a resolution of 17 $\times$ 580 in R – ϕ and z in the barrel, and 17 $\times$ 580 in R – ϕ and R in the end-cap regions, respectively [39].

Transition Radiation Tracker

The Transition Radiation Tracker (TRT) is the last component of the ID, situated just after the SCT. It consists of about 300000 gaseous tubes with a diameter of 4 mm [39]. The tubes are filled with a $Xe/CO_2/O_2$. The TRT provides only R – ϕ information with an accuracy of 130 μm per straw. It is used in the electron identification and contributes significantly to the momentum measurement.

3.2.4 Calorimeters

The ATLAS calorimeters lie outside of the ID and the solenoid and measure energies of particles produced in proton-proton collisions. They are designed to entirely stop most known particles except muons and neutrinos, which leave little or no energy in the calorimeters. The calorimeters cover a pseudorapidity range up to $|\eta| < 4.9$, but high granularity electromagnetic measurements are made in the range of $|\eta| < 2.5$ [39].

The main components of the calorimeter system are the electromagnetic calorimeter that measures energies of electrons and photons since they interact with the material and the hadronic calorimeters that measure energies of hadrons in their interactions with atomic nuclei. Figure 3.13 illustrates all parts of the calorimeters which are described in the following.

Electromagnetic calorimeter

The electromagnetic calorimeter (EMCal) is a lead-Liquid Argon (LAr) detector which consists of two main parts: a barrel and two end-caps. Both of them use liquid argon as the active material and lead as the passive layer. The barrel is built from 2048 so-called "accordion-shaped" absorbers, which are designed with the characteristic shape to reduce the drift time after a particle interaction [39]. This part covers a pseudorapidity range of $|\eta| < 1.475$ and is located between 2.8 m and 4 m from the beam line [39]. Depending on the η, three or four read-out layers are used. Figure 3.14 shows an illustration of the barrel module with different layers.

Each end-cap consists of inner and outer wheels and covers the range $1.375 < |\eta| < 3.2$ m from the interaction point [39]. The inner wheel is built of 256 absorbers and covers the region $2.5 < |\eta| < 3.2$, while the outer wheel is built of 768 absorbers and covers the rest of the range $1.375 < |\eta| < 2.5$ [39].

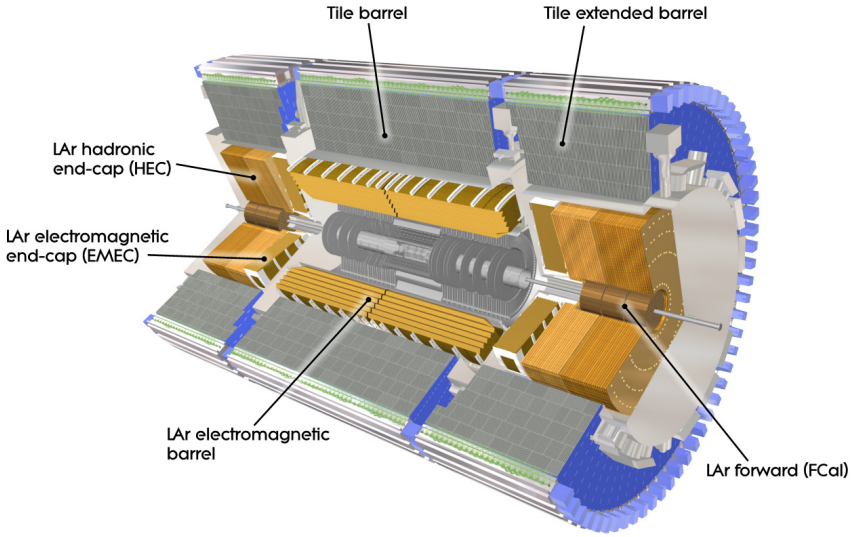

FIGURE 3.13: Schematic overview of the ATLAS calorimeter system [39].

Hadronic calorimeter

The hadronic calorimeter surrounds the EMCal and consists of the following three subdetectors:

- **The tile calorimeter** is a hadronic calorimeter which is located outside of the EMCal. It uses steel as the absorber and scintillation tiles as the active material. The Tile calorimeter consists of a barrel layer which covers the region $|\eta| < 1.0$ and two extended barrels for covering the region $0.8 < |\eta| < 1.7$ [39].

- **The LAr Hadronic End-cap Calorimeter** (HEC) consists of two wheels in each end-cap which are situated directly behind the end-cap of the EMCal. It uses liquid argon as the active material and copper plate as the absorbers. This calorimeter covers the region of $1.5 < |\eta| < 3.2$, overlapping with the forward detector and the tile calorimeter [39].

- **The LAr Forward Calorimeter** (FCal) is situated inside the inner radius of HEC wheels. This calorimeter provides electromagnetic and hadronic coverage in the region closest to the interaction point in the range $3.1 < |\eta| < 4.9$ [39]. It consists of three modules, where the first is used for electromagnetic measurements and is made of copper, while the other two are mainly used to measure energies of hadron interactions and are made of tungsten.

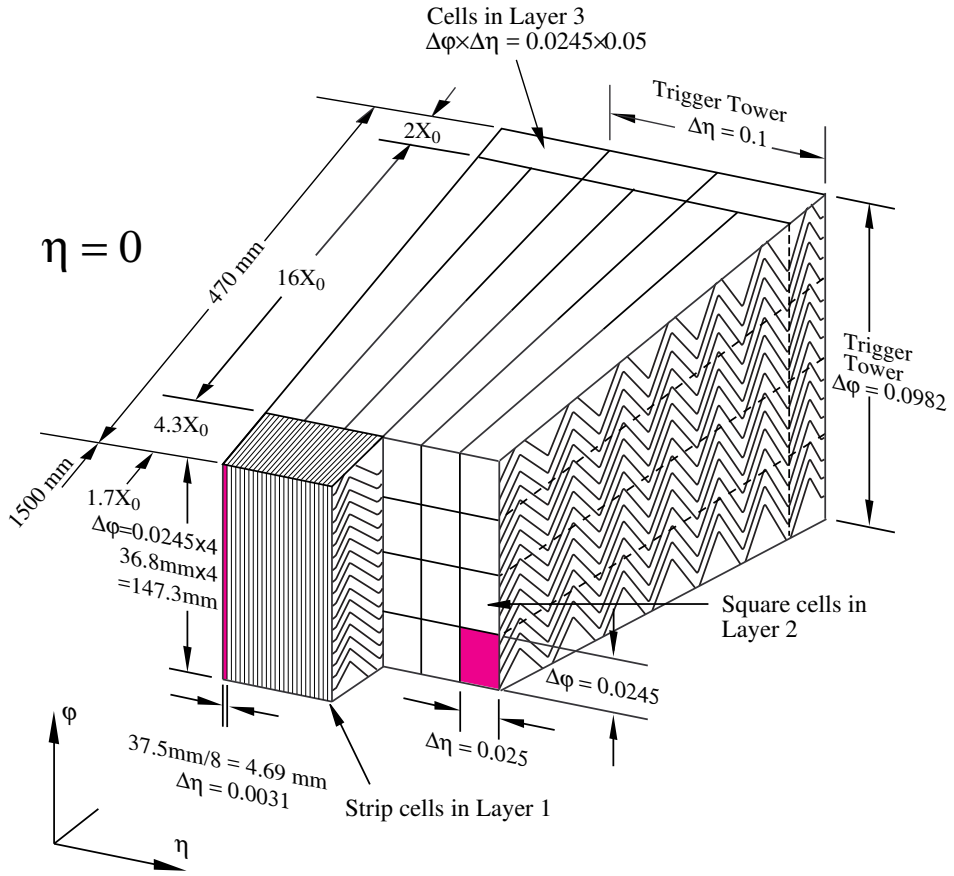

FIGURE 3.14: Readout granularity of the EMCal [39].

3.2.5 Muon Spectrometer

The ATLAS Muon Spectrometer (MS) is the outermost detector designed to reconstruct charged particles which pass through the ID and the calorimeters. It also provides an independent muon trigger. Muons can be measured in the range $|\eta| < 2.7$, and triggered in the range $|\eta| < 2.4$. The length of the entire MS is 40 m, while it is 24 m thick.

Figures 3.15 and 3.16 show the layout of the spectrometer which consists of four subdetectors. The largest subdetector of the MS is the Monitored Drift Tubes (MDT's) designed to provide precision measurements of charged particles. There are 1088 MDT's in the detector, arranged into three layers in the barrel and three wheels in the end-cap [39].

In the region $2 < |\eta| < 2.7$, Cathode Strip Chambers (CSC's) are used for a precise measurement of the track coordinates because of their high rate capability and time resolution. The CSC's are multiwire proportional chambers with two cathodes. Both cathodes are segmented, one with strips orthogonal to wires providing the precision coordinates and the other parallel to the wires providing the transverse coordinates. The typical resolution is 40 μm in R and 5 mm in ϕ.

Apart from the precision measurement systems, the MS also contains two

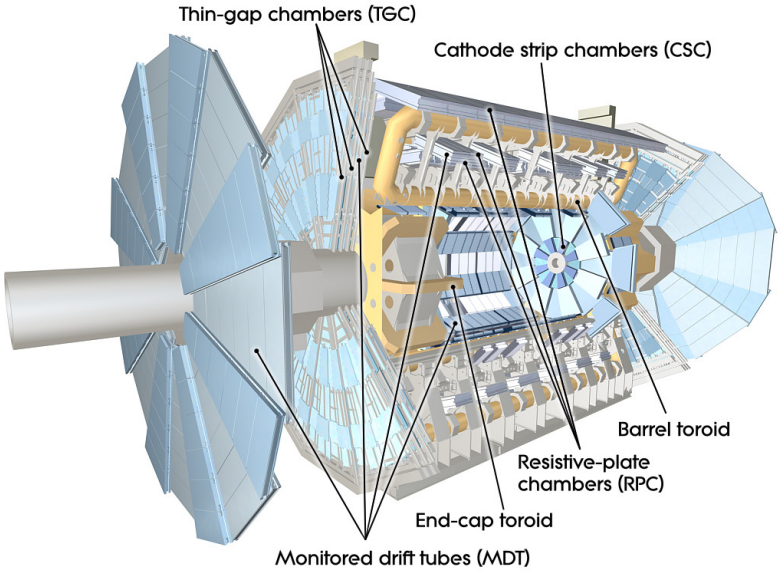

FIGURE 3.15: Main components of the Muon Spectrometer [39].

systems primarily for triggering. In the barrel region of ($|\eta| < 1.05$), Resistive Plate Chambers (RPC's) are used for this purpose, while in the end-cap ($1.05 < |\eta| < 2.4$) Thin Gap Chambers (TGC's) are used. The RPCs consist of two electrode plates with gas-filled gaps and their typical resolution is 10 mm in z and ϕ. The TGCs operate on the same principle as multi-wire proportional chambers and their typical resolution is from 2 to 6 mm in R and from 3 to 7 mm in ϕ.

3.2.6 Forward detectors

In addition, there are three smaller detectors that cover the ATLAS forward region called:

- LUCID (**LU**minosity measurement using **C**erenkov **I**ntegrating **D**etector),
- ALFA (**A**bsolute **L**uminosity **F**or **A**TLAS), and
- ZDC (**Z**ero-**D**egree **C**alorimeter).

The first two detectors are used to determine the luminosity delivered to ATLAS, while the third detector determines the centrality of heavy-ion collisions. These detectors are situated in the LHC ring at $\pm$17 m (LUCID), $\pm$240 m (ALFA) and $\pm$140 m (ZDC) from the interaction point [39].

3.3 ATLAS Trigger System

The LHC delivers proton-proton inelastic collisions at a frequency of 40 MHz, with a collision of proton-proton bunches in all interaction points every 25 ns

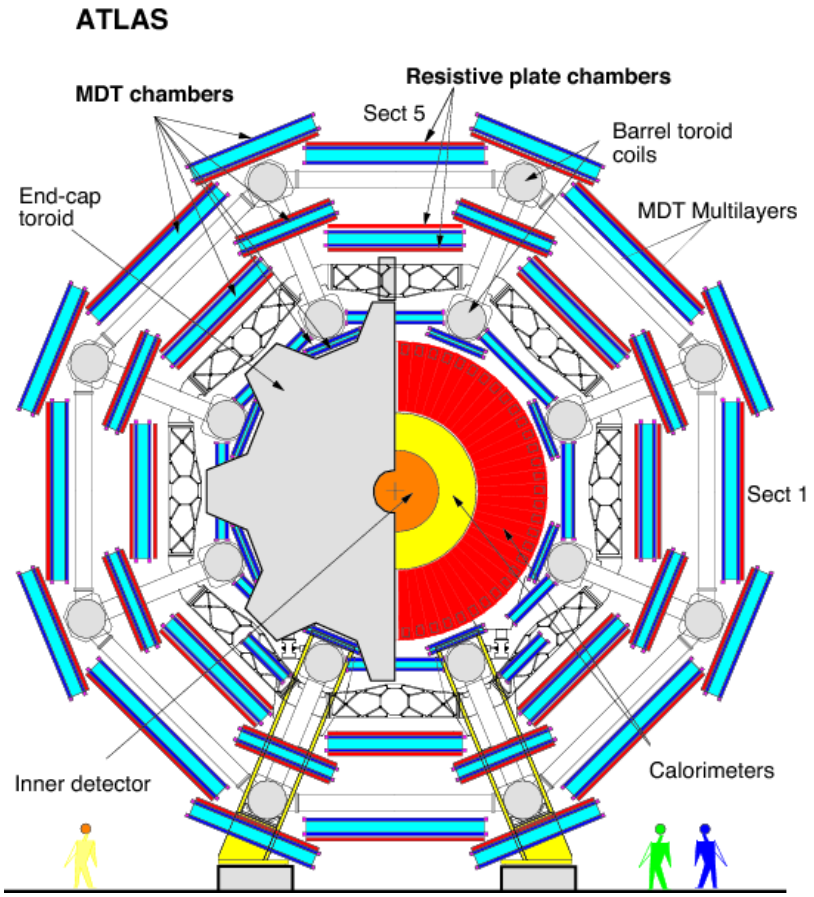

FIGURE 3.16: Illustration of the Muon Spectrometer in the x-y (top) and z-y (bottom) projections [39].

[39, 43]. In this manner, it is not possible to record every collision due to limited storage capacity. Instead, a trigger system is used to select potentially intere-sting events with a high efficiency and to reject a large rate of background events.

The ATLAS trigger system, shown in Figure 3.17 has two different types of event selection: the Level-1 and the High Level Trigger. The Level-1 provides a hardware-based trigger decision, while the High Level Trigger makes a trigger decision based on software algorithm. Each trigger level refines decisions made by the previous level applying new selection criteria. At the end, the 40 MHz frequency of the proton-proton collision data generated by the LHC is reduced to about 1 kHz recorded data with a data rate of approximately 1.5 GB/s [44–48].

3.3.1 Level-1

The Level-1 trigger (L1) is responsible for the first level of event selection reducing the initial event rate to less than 100 kHz. Its elements such as muon, jet, electromagnetic and tau clusters identify Regions of Interest (RoIs)

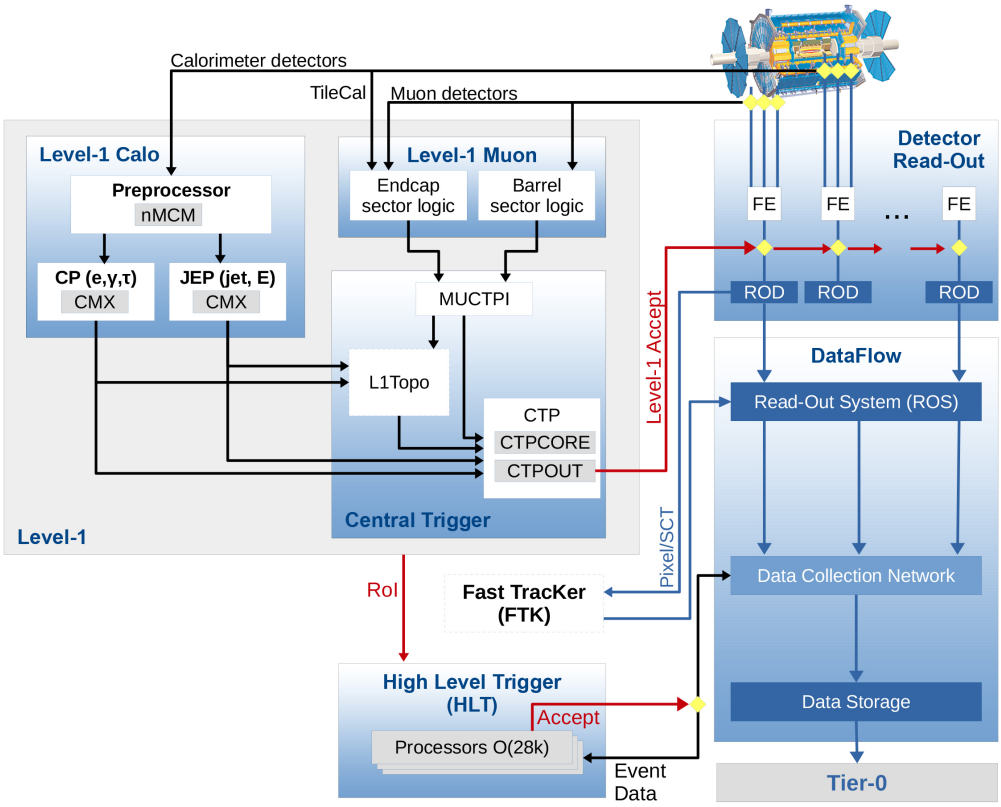

FIGURE 3.17: Schematic overview of the LHC Run II configuration of the Trigger and Data Acquisition System [43].

that seed further trigger decisions at the High Level Trigger. The fast custom-made electronics find the RoIs using coarse information from the fast read-out subdetectors: the calorimeters, the RPCs and TGCs within a latency of 2.5 μs.

The L1 system consists of the L1 calorimeter trigger system (L1Calo), the L1 muon trigger system (L1Muon), new L1 topological trigger modules (L1Topo) and the Central Trigger Processors (CTP).

The L1Calo uses input data from all calorimeters which comes from 7200 analog "trigger towers" built with a granularity of 0.1×0.1. The goal of the L1Calo is to identify all physics objects except muons.

The L1Muon uses input data from the RPC's and the TGC's. Multiplicities for different thresholds are measured using the logic provided by the Muon Central Trigger Processor Interface.

The L1Topo introduced in the LHC Run II calculates event topological quantities between L1 objects such as electron/photons, muons, jets, and taus. It uses trigger decisions made on information provided by the L1Calo and L1Muon streams and allows the CTP to perform L1 selections based on these quantities.

The CTP makes the trigger decision by applying different requirements

and prescale factors[2] specified in the trigger menu. After receiving a signal "Level-1 Accept", the L1 trigger decision is sent for further processing to the High Level Trigger with the coordinates in the η/ϕ-plane from each RoI.

3.3.2 High Level Trigger

The High Level Trigger (HLT) is implemented in software algorithms and reduces the output rate of the L1 to 1 kHz which corresponds to a data rate of 1.5 GB/s [44–48]. It uses the output data from RoIs and decides whether or not to keep an event. This process is performed based on its own trigger menu which also consists of the L1 thresholds. In order to make sure that all events that would pass the HLT requirements also passed the L1 requirements, the HLT thresholds are higher than their corresponding L1 thresholds.

All events that pass the HLT are written to trigger streams[3] and sent to the CERN Tier-0, defined in Section 3.5 for permanent storage.

3.3.3 Trigger streams

A trigger stream consists of related signatures (electron, γ, muon, jets, tau and missing transverse momentum) recorded in the same dataset. The ATLAS has four trigger streams:

1. **primary physics stream**, stores all potentially interesting events depending on which trigger fired,
2. **calibration stream**, as the name indicates it stores large data samples for detector calibrations,
3. **debug stream**, saves events which caused errors during online running for further investigation, and
4. **express stream**, designed to provide data quality information before the reconstruction of the primary physics stream starts.

3.3.4 Trigger menu

The trigger menu is defined as a full collection of L1 and HLT selection criteria and prescale factors. Typically, the trigger menu contains several hundred triggers which need to satisfy different physics goals at ATLAS, including a sufficient number of supporting triggers, alternative triggers, backup triggers and calibration triggers which are described below.

- Supporting triggers are used for monitoring or performance studies.
- Alternative triggers are used for comparison studies with the primary physics triggers.

[2] A prescale factor is a reduction factor to issue a trigger (e.g. a prescale factor on chain X of 5 means that every 5th event is accepted by the chain, while all others are discarded).

[3] defined in Section 3.3.3.

- Backup triggers are used in case of unexpected luminosity increases and have higher thresholds.
- Calibration triggers are used for the detector calibration.

The complete trigger menu of the ATLAS physics program for the LHC Run II includes the following triggers:

1. single and double lepton triggers,
2. jet triggers,
3. missing transverse momentum triggers,
4. tau triggers, and
5. b-jet triggers including muon-in-jet triggers.

3.3.5 Data quality

In 2015 and 2016 ATLAS had a high efficiency of data collection. Figure 3.18 shows the luminosity delivered by the LHC (in green) as a function of time, recorded by ATLAS (in yellow) and good for physics analyses (in blue) in 2015.

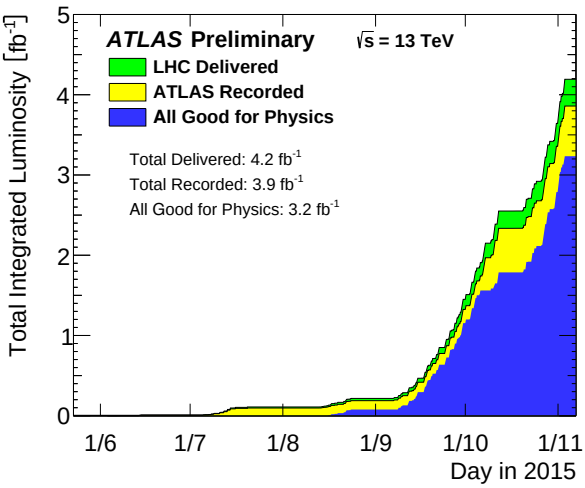

FIGURE 3.18: Cumulative luminosity versus time delivered to ATLAS (green), recorded by ATLAS (yellow) and good for physics (blue) [37].

Both analyses presented in this thesis use the 3.2 fb^{-1} and 32.9 fb^{-1} datasets, collected in 2015 and 2016, respectively.

3.4 Monte Carlo simulation

Samples obtained from the Monte Carlo (MC) simulation play a crucial role since they are used for many vital parts of analyses like the optimisation of signal regions and background estimations.
The simulation of proton-proton collisions and interactions of the produced particles with the detector are performed in several steps.

3.4.1 Simulation

The first step of the MC simulation is the generation of proton-proton collisions by event generators and it is independent of the detector. The MC simulation consists of several components, which are categorized according to scales of the momentum transfer involved. At the highest scales, the simulation starts with a hard process (hard scatter) in which incoming protons from collisions interact and produce a few outgoing particles such as the SM quarks, leptons, gauge or hypothetical new particles. The parton distribution functions which describe the momentum distribution of the incoming protons are used as input to generators. The matrix element of the hard process is calculated in perturbative QCD. This is illustrated in Figure 3.19, where a black blob presents the hard process.

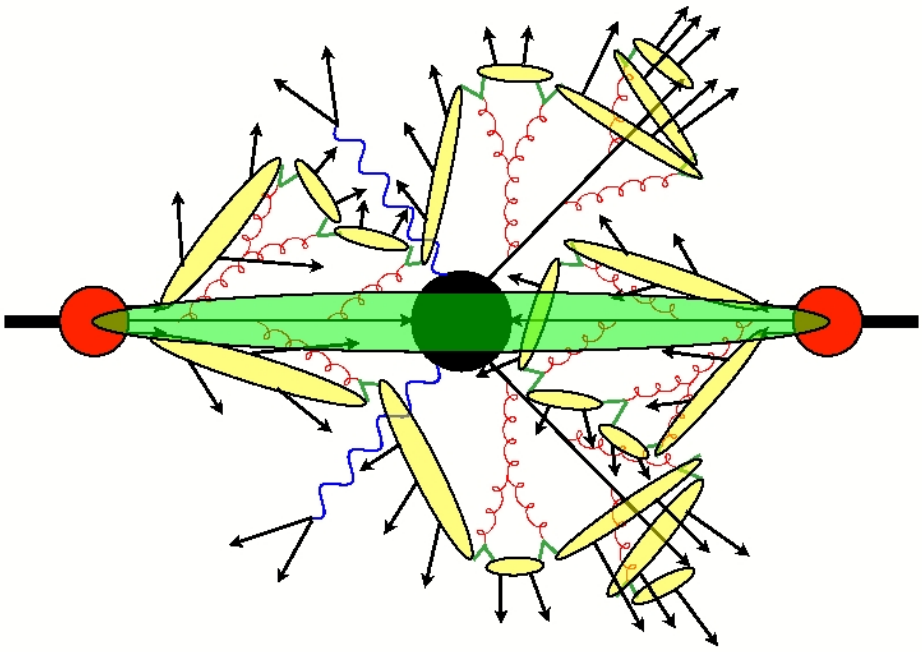

FIGURE 3.19: Illustration of a proton-proton collision simulated by a MC event generator [49].

Quarks, gluons and all other new particles with color can emit further gluons or quark-antiquark pairs. This leads to the formation of parton showers shown in red in Figure 3.19.

After parton showering the partons are bound into colorless hadrons, this process known as the process of hadronisation is shown in yellow in Figure 3.19.

In proton-proton collisions, the other constituents of the incoming protons can interact and produce the underlying event (UE) shown in green in Figure 3.19.

The MC simulation also includes Initial State Radiation (ISR) and Final State Radiation (FSR). ISR refers to particles radiated by incoming partons before the main interaction, while FSR occurs after the main interaction when outgoing partons radiate particles.

3.4.2 Overview of MC generators used in this thesis

The MC generators which generate particles from proton-proton collisions used in this thesis are:

- SHERPA[4] [50], is a multi-purpose generator designed to generate matrix elements, parton showers, hadronisation and the UE without interfacing with external packages. Matrix elements for $2 \rightarrow$ n (n=2,3,4,5,6) processes are calculated at the LO for many physics processes. A parton-shower model is used to describe the emission of additional QCD partons, while the UEs in hadron-hadron collisions are described by a simple model of multiple interactions.

- POWHEG[5]-Box [51–53], is a framework built based on POWHEG and can be used for some complex processes because it calculates matrix elements at the NLO. However, this framework has to be interfaced with another generator in order to describe any physics process beyond the hard scattering (it is not able to perform its own parton showering). For MC samples used in this thesis, it is done with PYTHIA[6] [54].

- MadGraph [55] is a MC event generator which can generate $2 \rightarrow$ N processes and decays. The initial and final state particles are specified by users. MadGraph generates all Feynman diagrams and gives a code for the matrix element evaluation.

[4]SHERPA is an acronym standing for "**S**imulation of **H**igh-**E**nergy **R**eactions of **PA**rticles".

[5]POWHEG is an acronym standing for " **P**ositive **W**eight **H**ardest **E**mission **G**enerator".

[6]PYTHIA is a general-purpose tool for the generation of high-energy collisions, which contains a coherent set of hard processes and physics models for parton showers, multiple interactions, string fragmentation and particle decays.

3.5 Computing system

Although the trigger system significantly reduces the number of events that need to be saved for further analyzing, still a huge amount of data needs to be stored. The processing of the data will necessitate efficient processing and large storage resources. Grid computing can address these needs since the main goal of its design is to distribute data to different sites all over the world.

The grid computing developed at CERN is called LHC Computing Grid (LCG) [56]. The main purpose of this project is to provide and maintain computing infrastructure for storage and analysis data which thousands of physicists from different parts of the world need to access and use. The LCG combines the computing and storage resources of more than 160 computing centers from 40 countries worldwide. The data produced by the LHC is distributed to these centers according to a hierarchical model illustrated in Figure 3.20. This model consists of sites organized in a four-tiered scheme as:

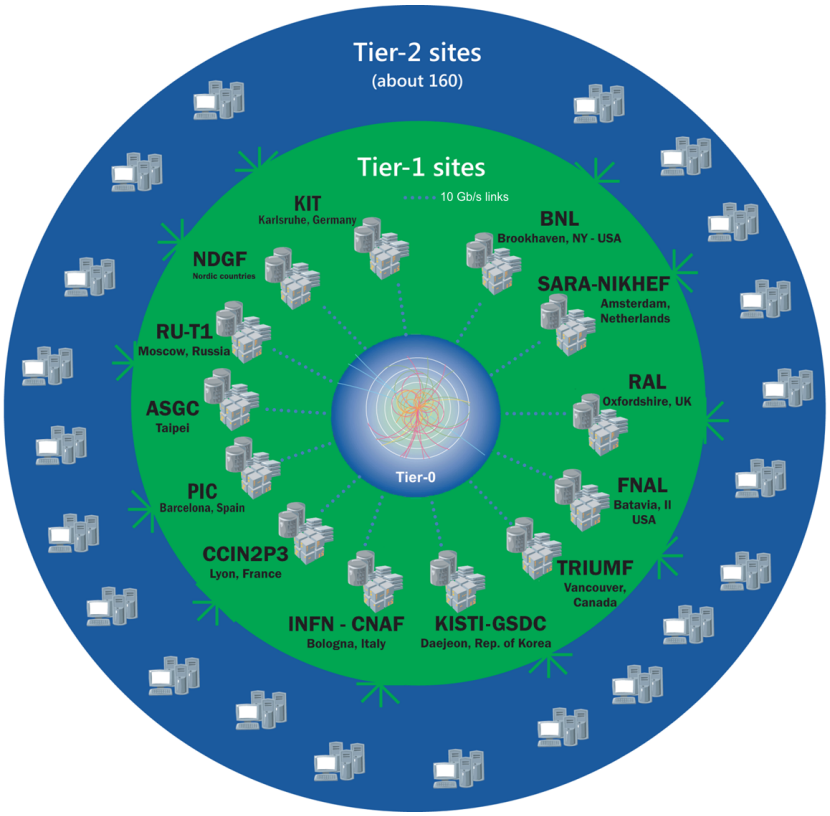

FIGURE 3.20: Schematic overview of the hierarchical model used in the LCG project [56].

- **Tier-0** is situated at CERN and provides storage resources for the original raw data that is output from the trigger system. Its responsibilities are to make a primary backup of the data and to send outputs to the Tier-1 sites.

- **Tier-1** consists of twelve computing centers based in different countries, but ATLAS uses only ten of them. Each center has to store raw and reconstructed data and provides computation capacity for processing data.
- **Tier-2s** are typically located at universities and scientific institutes. They provide storages and computation capacity for processing data and MC events.
- **Tier-3** consists of local clusters at universities and scientific institutes and provides other computing facilities needed for data analysis. It is outside of the LCG project.

Chapter 4

Object definitions

This chapter describes reconstruction and identification steps of objects such as electrons, muons, and jets. The reconstruction is a basic term used to describe steps of converting signals recorded by ATLAS into sets of measurements linked to particles produced in the detector. After the reconstruction step comes the identification step in which the quality of the objects needs be determined. This chapter also describes the reconstruction and calculation of missing transverse momentum.

4.1 Electrons

Electrons leave a track in the Inner Detector (ID) and initiate an electromagnetic shower in the electromagnetic calorimeter (EMCal). Figure 4.1 shows the signature of an electron.

4.1.1 Reconstruction

Electrons are reconstructed using energy deposits in the EMCal [48, 58], linked to a track of a charged particle in the ID. When an electron interacts with the EMCal, its energy is deposited in individual calorimeter cells. The clusters of calorimeter cells are reconstructed using a sliding-window algorithm with a window size of 3 x 0.025 units in η-space and 5 x 0.025 units in ϕ-space [48, 58]. This window is marked as "3x5". The unit size of 0.025 x 0.025 corresponds to the granularity of the middle layer of the EMCal [48, 58]. The reconstruction step is finished when at least one track is matched to the reconstructed cluster. After the track matching, the clusters of the electron candidates are rebuilt using a larger cluster size of 3x7 in the barrel and 5x5 in the end-cap [48, 58].
The electron energy is determined by summing the energy measured in the cluster and the energy deposit outside of the cluster window.

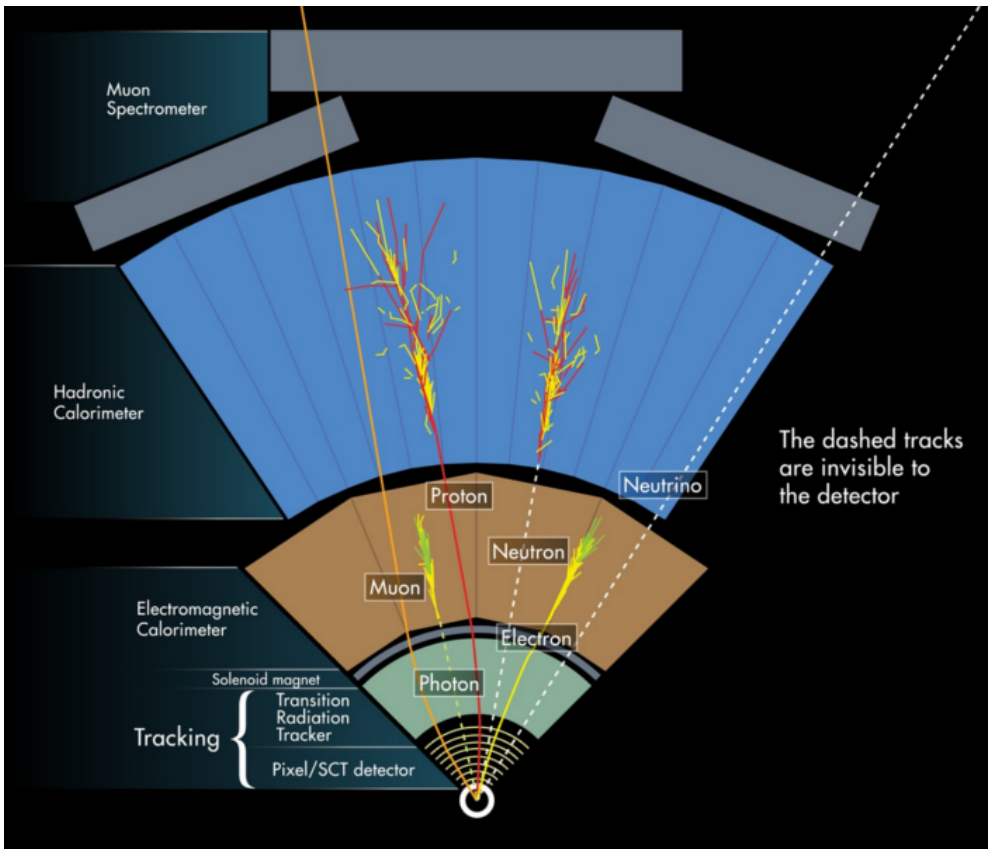

FIGURE 4.1: The signatures of different particles recorded by the ATLAS detector [57].

4.1.2 Identification

The identification step is introduced to make a separation between electrons coming from signal and background processes. This selection is done using electron identification algorithms. As input, these algorithms use electron clusters, the track quality and the shape of the calorimeter shower. Three operating points with increasing background rejection are defined as Loose, Medium, and Tight. These points are inclusive which means that Loose is a subset of Medium, while Medium is a subset of Tight. The identification efficiency of the Loose, Medium and Tight working points for electron candidates with $E_T \approx 25$ GeV is 93%, 89% and 80%, respectively [58]. The tight operating points have worse efficiencies for the identification of electrons but on the other hand have a very low efficiency for mis-identification of jets as electrons.

4.1.3 Isolation

The final step used to discriminate signal from background electrons is the isolation. In this step, the following two discriminating variables are used to reject non-prompt electrons, electrons produced in hadron decays and light hadrons mis-identified as electrons:

- calorimetric isolation energy $E_T^{cone0.2}(\eta, \phi)$ defined as the sum of transverse energy of clusters within a cone of a radius dR=0.2. This variable is illustrated in Figure 4.2.
- track isolation $p_T^{cone0.2}(\eta, \phi)$ defined as the sum of transverse momenta of all tracks inside a cone size of dR=0.2 as illustrated in Figure 4.3.

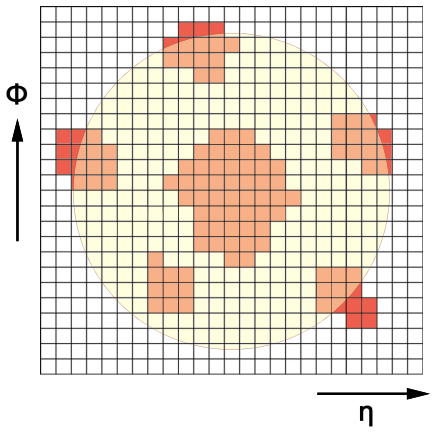

FIGURE 4.2: Illustration of the $E_T^{cone0.2}$ variable. The grid shows the middle EMCal cells in the η and ϕ directions. Clusters (red) that fall into the isolation cone (yellow) are used in the isolation computation.

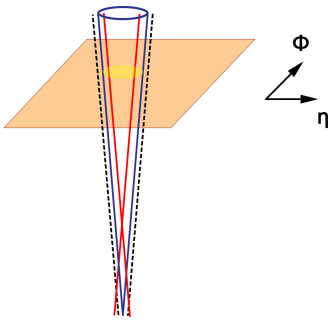

FIGURE 4.3: Illustration of the p_T^{cone} variable. All good tracks located in a cone around objects are selected and shown in red. The black dotted lines show not selected tracks which are too far from the object.

Based on these isolation variables divided by E_T, a variety of selection requirements has been defined to select isolated electrons resulting in working points [58].

4.1.4 Electrons used in this thesis

Two types of electrons are used in this thesis:

- **Baseline electrons**

All electrons selected as the baseline electrons are reconstructed according to the steps discussed above. They have to pass the Loose quality standard. The baseline electrons should be within $|\eta| < 2.47$ and exceed 7 GeV (10 GeV) in p_T for the search for squarks and gluinos (the search for charginos and neutralinos). This type of electrons is used in the calculation of all kinematic variables[1] and of the missing transverse momentum.

- **Signal electrons**

Signal electrons are further required to pass the Tight quality standard with the GradientLoose isolation. This isolation selection is applied on the $E_T^{cone0.2}$ and $p_T^{cone0.2}$ variables in such a way that the isolation efficiency is larger than 95% for electrons with p_T = 25 GeV and 99% for electrons with p_T = 60 GeV [58]. The signal electrons must have p_T > 25 GeV (27 GeV) for the search for squarks and gluinos (the search for charginos and neutralinos). This type of electrons does not contain electrons which do not originate from the collision. In order to remove such electrons, criteria on the transverse and longitudinal components of the impact parameter (IP, see Section 3.2.3) are used. In the ATLAS coordinate system[2], the transverse IP (d_0) is the closest distance of the track to the primary vertex (PV) in the $r-\phi$ projection, while the longitudinal IP (z_0) is defined as the z value on the track that gives a value of d_0. The definitions of d_0 and z_0 with respect to the PV are shown in Figure 4.4 (d_0^{PV} and z_0^{PV}). The signal electrons have to pass the following IP criteria:

- $|\Delta z_0^{PV} \sin\theta| < 0.5$ mm, and
- $|d_0^{PV}\text{significance}| < 5$.

where the d_0^{PV}significance is the track impact parameter significance defined as $d_0^{PV}\text{significance} \equiv \frac{d_0^{PV}}{\sigma_{d_0^{PV}}}$ and $\sigma_{d_0^{PV}}$ is the uncertainty on the reconstructed d_0^{PV}. The signal electrons are used in definitions of signal, control and validation regions.
All requirements made on the electrons can be seen in Table 4.1.

[1] defined in Chapter 6.
[2] illustrated in Figure 3.8.

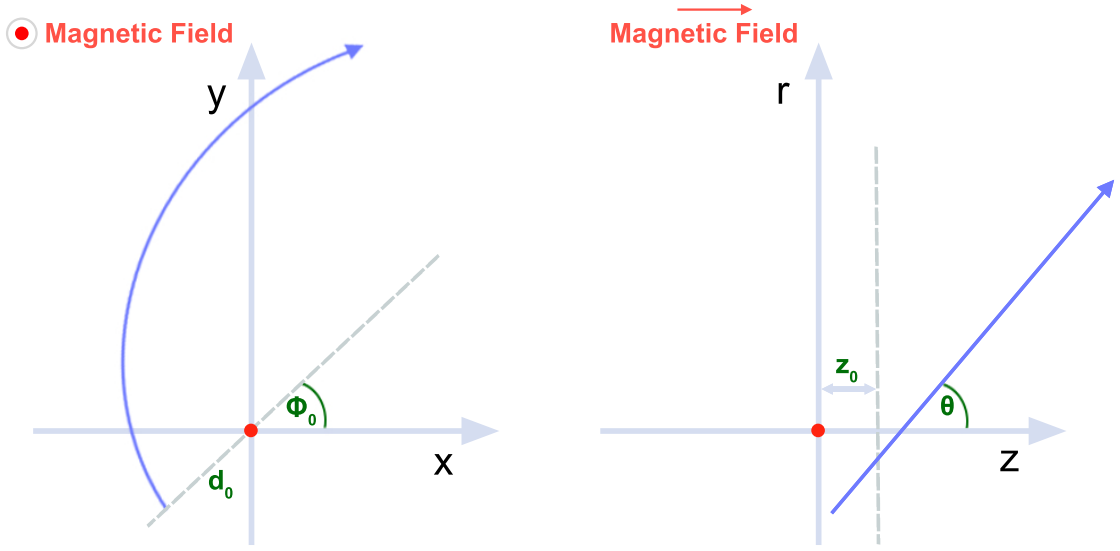

FIGURE 4.4: The definitions of longitudinal and transverse impact parameters. The red dot marks the primary vertex.

Baseline electron	
Kinematics	$p_T > 7$ (10) GeV and $\lvert\eta^{clust}\rvert < 2.47$
Quality	Loose working point
Signal electron	
Kinematics	$p_T > 25$ (27) GeV
Isolation	GradientLoose
IP	$\lvert z_0^{PV}\rvert < 0.5$ mm and $\lvert d_0^{PV}\text{significance}\rvert < 5$

TABLE 4.1: Summary of the electron definition. The criteria are the same for both searches except the p_T criterion which is given in brackets for the search for charginos and neutralinos. The signal selection requirements are applied on top of the baseline selection.

4.2 Muons

Muons traverse the entire ATLAS detector, as indicated in Figure 4.1. They leave a track in the ID and Muon Spectrometer (MS), and little or no energy in the EMCal and hadronic calorimeters.

4.2.1 Reconstruction

The reconstruction of the muons is performed in the ID and MS independently. Then these two measurements are combined to form muon tracks. Depending on which sub-detectors are used in the reconstruction step, the following four types of muons are defined:

- **Combined muons** are reconstructed in the ID and MS independently, then a combined track is formed using a global fit. These muons have the best quality [59].
- **Segment-tagged muons** use ID tracks extrapolated to MS tracks. A track is identified as a muon if it is linked to at least one local segment in the MDT or CSC. This type of muons crosses only one layer of the MS due to the low p_T [59].
- **Calorimeter-tagged muons** are reconstructed without information from the MS. For their reconstruction, an ID track linked to an energy deposit in the calorimeters is used [59].
- **Extrapolated muons** are reconstructed only based on a track in the MS with an additional requirement that the track originates from the interaction point [59].

Collections of muons used in physics analyses are produced after resolving overlaps between the different muon types. If two types of muons have the same ID track, combined muons have a preference, then segment-tagged muons and at the end calorimeter-tagged muons. The overlap with extrapolated muons is solved by studying the track quality [59].

4.2.2 Identification

The identification method uses quality requirements that separate prompt muons with a high efficiency from background muons. Three variables are used in the identification for combined muons [59]:

- q/p significance, defined as:

$$\text{q/p significance} = \frac{\left|\left(q/p_T\right)_{ID} - \left(q/p_T\right)_{MS}\right|}{\sqrt{\sigma^2_{ID} + \sigma^2_{MS}}} \tag{4.1}$$

- ρ, defined as:

$$\rho = \frac{\left|p_T^{ID} - p_T^{MS}\right|}{p_T^{\text{Combined–track}}} \tag{4.2}$$

- the normalised χ^2 of the combined track fit.

Based on them, four working points are defined as: Medium, Loose, Tight and High p_T. They have to satisfy specific needs of different physics analyses such as: small systematic uncertainties, high efficiency, good purity and best resolution in the high p_T region, respectively. All four working points are described below.

- **Medium muons** are combined or extrapolated muons. These muons must have at least three hits in at least two MDT layers (except for tracks in $|\eta| < 0.1$) and the q/p significance less than seven. The medium selection is the default for muons in ATLAS because it minimizes systematic uncertainties [59].

- **Loose muons** are all combined and extrapolated muons that satisfy the medium selection discussed above. The segment-tagged and calorimeter-tagged muons are also included, but they are limited to the region $|\eta| < 0.1$ [59].

- **Tight muons** are combined muons with hits in at least two MS layers. They also need to satisfy the medium selection. The tight selection is designed to maximize the purity of muons by reducing some efficiencies [59].

- **High-p_T muons** are identified from the combined muons. They should satisfy the medium selection and have at least three hits in three MS layers. This requirement of having at least three hits improves the resolution of muons with p_T above 1.5 TeV by around 30% and reduces the reconstruction efficiency by about 20% [59].

4.2.3 Isolation

The muon isolation is used in many physics analyses to reject muons from background processes. The muon isolation variables are the same as for the electron isolation [59].

4.2.4 Muons used in this thesis

Two types of the muons are used in this thesis:

- **Baseline muons**

All muons selected as the baseline muons are reconstructed according to the steps described in Section 4.2.1. They have to pass the Medium quality standard. The baseline muons should be within $|\eta| < 2.7$ and exceed 6 GeV (10 GeV) in p_T for the search for squarks and gluinos (the search for charginos and neutralinos). This type of muons is used in the calculation of all kinematic variables[3] and of the missing transverse momentum.

[3] defined in Chapter 6.

- **Signal muons**

Signal muons are further required to be GradientLoose isolated. The GradientLoose isolation is defined in the same way as for the signal electrons and required to be larger than 95% at 25 GeV and 99% at 60 GeV [59]. The signal muons must have $p_T > 25$ GeV (27 GeV) for the search for squarks and gluinos (the search for charginos and neutralinos). This type of the muons also needs to pass the same IP criteria as the signal electrons:

- $|\Delta z_0^{PV} \sin\theta| < 0.5$ mm, and
- $|d_0^{PV}\text{significance}| < 3$.

The signal muons are used in definitions of signal, control and validation regions.
All requirements made on muons can be seen in Table 4.2.

Baseline muon	
Kinematics	$p_T > 6$ (10) GeV and $\|\eta\| < 2.7$
Quality	Medium working point
Signal muon	
Kinematics	$p_T > 25$ (27) GeV
Isolation	GradientLoose
IP	$\|z_0^{PV}\| < 0.5$ mm and $\|d_0^{PV}\text{significance}\| < 3$

TABLE 4.2: Summary of the muon definitions. All criteria are the same for both searches except the p_T criterion which is given in brackets for the search for charginos and neutralinos. The signal selection requirements are applied on top of the baseline selection.

4.3 Jets

Jets can be defined as collimated sprays of stable particles originating from the fragmentation and hadronization of quarks or gluons which emerge from the interaction point. They are built based on information from the ID and the calorimeters. Figure 4.5 shows a basic illustration of a proton-proton collision with the fragmentation and hadronization of the quarks and gluons resulting in a reconstructed jet.

4.3.1 Reconstruction

The reconstruction of jets is performed in the calorimeter using as inputs energy deposits associated to tracks reconstructed in the ID. The standard

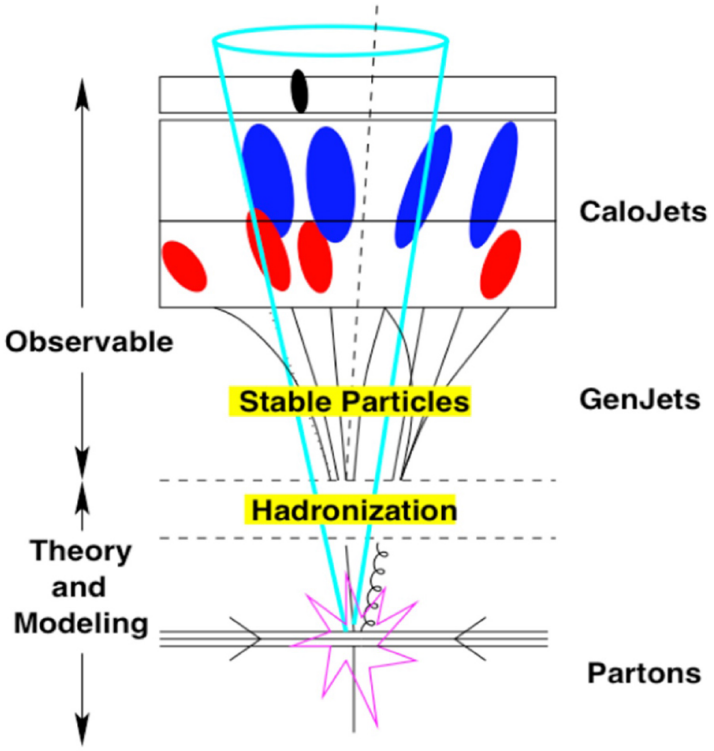

FIGURE 4.5: A proton-proton collision with a particle shower and a reconstructed jet [60].

algorithm for the reconstruction of jets used in ATLAS is called anti-k_T [61]. It uses two distance parameters:

- d_{ij} between two clusters i and j defined by:

$$d_{ij} = \min\left(\frac{1}{p_{T_i}^2}, \frac{1}{p_{T_j}^2}\right) \times \frac{\Delta R_{ij}^2}{R} \tag{4.3}$$

where $p_{T_{i(j)}}$ is the transverse momentum of the clusters i(j), ΔR_{ij} is the angular separation of the two clusters and R is the radius parameter of the algorithm. Typically, R is set to be 0.4.

- d_k for an individual cluster defined as:

$$d_k = \frac{1}{p_{T_k}^2} \tag{4.4}$$

where p_{T_k} is the transverse momentum of the cluster k.

The minimum of all d_{ij} and d_k parameters is calculated. If the minimum is the distance parameter d_{ij} between two clusters then the corresponding clusters i and j are combined into one cluster ij and the minimum of all d_{ij} and d_k parameters are calculated again. When the minimum is the distance parameter d_k for an individual cluster k, then the cluster k is defined to be

a jet and removed from the list of clusters. These steps are repeated with an updated cluster list until all clusters are combined into jets.

4.3.2 Calibration

The goal of the jet calibration is to correct the energy and momentum of jets measured in the calorimeters. This method consists of a few steps described in the following [62].

- **Pile-up corrections**

A jet reconstructed in the calorimeter contains the energy from the hard scattering and the pile-up. Since both processes occur during the same bunch crossing, the origin of the jet needs to be determined. This is not possible with the calorimeter due to a poor pointing resolution. In order to solve this issue, the first step of jet calibration is a pile-up correction.
The pile-up corrections are performed with the jet area technique based on the energy density ρ in the calorimeter [62]. The energy density is defined as the median of the jet p_T divided by its area.

- **Origin correction**

The origin correction is applied to make sure that jets have their origin in the PV instead of the center of the ATLAS detector [62].

- **Jet energy scale and η corrections**

This calibration step corrects the reconstructed jet p_T to the particle-level energy scale and the reconstructed jet η for a bias due to poorly instrumented regions of the calorimeters [62].

- **In situ correction**

The last step of the calibration takes into account differences between data and MC simulation in the jet p_T measurement that originate from different sources such as: physics of jet formation, electromagnetic and hadronic interactions in the detector, pile-up activity, the description of materials used to built the detector, limitations in the simulation of UEs [62].

- **Additional correction due to pile-up**

An important part for many physics analyses is the rejection of reconstructed jets that come from pile-up vertices. For this purpose the Jet Vertex Tagger (JVT) is introduced. The algorithm uses variables which connect non pile-up jets and the PV. For jets with $20 < p_T < 60$ GeV and $\eta < 2.4$, the output of the JVT algorithm is required to be larger than 0.59 [38].

4.3.3 Jets used in this thesis

Two types of the jets are used in this thesis:

- **Baseline jets**

All jets selected as the baseline jets are reconstructed according to the steps discussed above. They should be within $|\eta| < 2.8$ and exceed 20 GeV in p_T. This type of jets is used in the calculation of all kinematic variables[4] and of the missing transverse momentum.

- **Signal jets**

Signal jets are further required to have $p_T > 25$ GeV and pass the JVT requirement. These jets are used in definitions of signal, control and validation regions.
All requirements made on the jets can be seen in Table 4.3.

Baseline jet	
Kinematics	$p_T > 20$ GeV and $\|\eta\| < 2.8$
Signal jet	
Kinematics	$p_T > 25$ GeV
JVT requirement	0.59

TABLE 4.3: Summary of the jet definition. The signal selection requirements are applied on top of the baseline selection.

4.4 b-jets

Jets that originate from the b quark hadronization, called b-jets, are present in many physics processes. Their identification is crucial in separating them from other processes which consist of jets from gluons and light-flavour quarks, and from the c quark fragmentation.
Unique features of the b quarks greatly help to distinguish b-jets from lighter jets. The relatively large mass of b quarks (> 5 GeV) allows their decay products to have higher transverse momenta. The b quarks also have sufficient lifetime[5] to travel a measurable distance before decaying. This leads to the presence of a secondary vertex (SV) displaced from the primary interaction point, and of tracks with a high transverse IP. In case of semi-leptonic b quark decays, the b-jets can be identified by the presence of a lepton (electron or muon) within the jet. The branching ratio of these decays is $\sim 20\%$ including both the direct decay, $b \to W^{-*}X$, $W^{-*} \to l^{-}\overline{\nu_l}$ and the cascade decay $b \to W^{-*}c$, $c \to l^{+}\nu_l X$ [63].

[4] defined in Chapter 6.
[5] Typically, their lifetime is of the order of 1.5 ps.

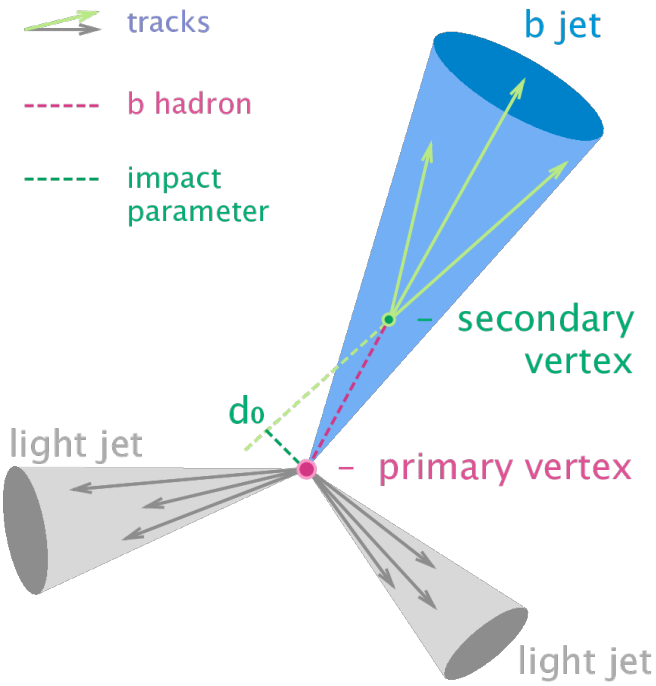

FIGURE 4.6: Illustration of the identification of a jet initiated by a b quark decay [64].

4.4.1 Tagging algorithms

The b-tagging algorithms are so-called b-taggers and are divided according to a main variable used for the tagging:
1) **IP based algorithms** exploit the fact that most of the b quarks produced travel a distance which is measurable with the ID before decaying. There are three algorithms which use impact parameter significances of all tracks in a jet to tag a b-jet [65]:

- IP1D uses the longitudinal impact parameter significances,
- IP2D makes use of the transverse impact parameter significances, and
- IP3D uses both the longitudinal and transverse impact parameter significances, taking advantage of their correlations.

2) **SV tagging algorithms**, called SV taggers, involve explicit reconstruction of a displaced SV in a jet. The reconstruction starts by forming two-track vertices which are displaced from the PV. All tracks from the remaining vertices are combined to single SV. There are two SV taggers which exploit properties of the SV such as the invariant mass of all tracks linked to the vertex, the ratio calculated between the sum of vertex track momenta and the jet energy, and the number of two-track vertices to tag a b-jet [65]:

- SV1 uses the first two variables, while
- SV2 uses all three variables mentioned above.

3) **Decay chain multi-vertex algorithm**, known as JetFitter, studies the topology of b and c quark decays inside a jet to reconstruct a full decay chain.
Outputs from the IP3D, SV1 and JetFitter algorithms are then combined. In the LHC Run II, the combination is done by using a Boosted Decision Tree and the resulting tagging algorithm is called MV2 which is trained with different c-jet/light-jet proportions. MV2c20 is trained with 20% of the c-jets and 80% of the light-jets, while MV2c10 is trained with 10% of the c-jets and 90% of the light-jets.

4.4.2 b-jets used in this thesis

b-jets are tagged using the MV2 tagger algorithm with 10% of the c-jets and 90% of the light-jets rejection (MV2c10). They are further required to be within $|\eta| < 2.5$ and have $p_T > 25$ GeV. Table 4.4 shows all requirements made on the b-jets used in definitions of signal, control and validation regions.

	b-jet
Kinematics	$p_T > 25$ GeV and $\|\eta\| < 2.5$
b-tagger algorithm	MV2c10 @ fixed cut of 77% working point

TABLE 4.4: Summary of the b-jet definition.

4.5 Large-R jets

In the LHC Run II, the higher centre-of-mass energy of 13 TeV opens new a kinematic regime for the production of boosted SM particles or new massive particles which can decay to boosted SM particles. For example, if W, Z and Higgs bosons are boosted, they are produced with substantial momentum and not at rest. This means that their decay products might be sufficiently collimated. If the distance between the decay products gets smaller than the radius of the jet, the decay products can merge as shown in Figure 4.7. This potential merging results in jets with significantly larger radius, so-called large-R jets or fat jets.

Independent of the type of a decaying particle, the angular separation approximately goes as [66]:

$$\Delta R \approx \frac{2m}{p_T} \tag{4.5}$$

where ΔR is defined in Equation 3.8, m and p_T are the mass and transverse momentum of the decaying particle, respectively.

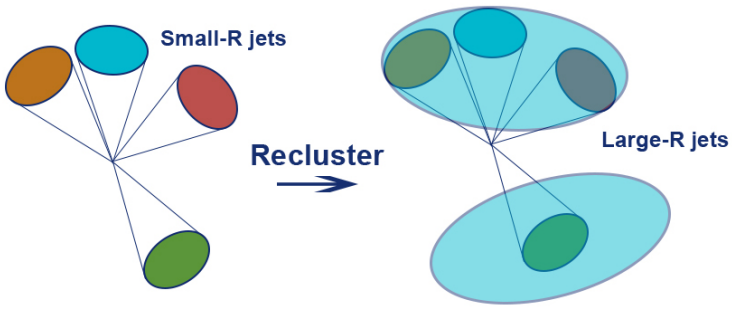

FIGURE 4.7: Illustration of forming the large-R jets from smaller jets.

Usually, the mass of large-R jets, M, is used to separate SUSY signals from SM events. The mass is defined as:

$$M^2 = \left(\sum_i E_i\right)^2 - \left(\sum_i \vec{p}_i\right)^2 \tag{4.6}$$

where E_i and $\vec{p}_i$ are the energy and three-momentum of the i^{th} constituent. The sum is over all jets in an event.
One potential consequence of reconstructing large-R jets is due to contamination; as a large radius size is used to collect all collimated decay products into a single jet, unwanted radiation from beam remnants and overlapping simultaneous proton-proton collisions can also be collected. If this additional radiation is soft, it does not affect the energy of the jet significantly but it could have a large impact on the mass of the large-R jets.
There is a wide range of algorithms defined to remove these effects. The most common algorithm in ATLAS is trimming which removes all sub-constituents from the large-R jets if the p_T fraction, defined as $f = p_T(sub)/p_T(J)$, is less than 5%. This algorithm first takes all particles in a jet with a radius R and reclusters them into sub-jets with a radius R_{sub} where $R_{sub} < R$. The sub-jets which satisfy the condition $p_T^{sub-jet} < f_{cut} \times p_T^{jets}$ are kept and merged to form a trimmed jet. The f_{cut} is the fixed dimensionless parameter [67].

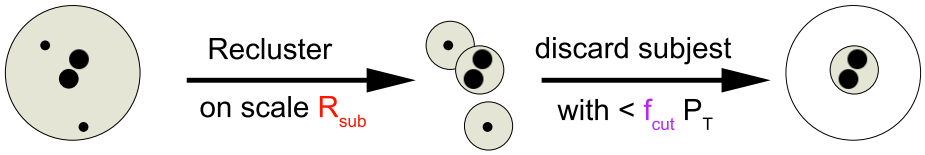

FIGURE 4.8: Illustration of the trimming procedure used to remove the contamination.

4.5.1 Study of large-R jets

The algorithm uses anti-k_T 0.4 jets as inputs to form the large-R jets. Four different values of the radius of the large-R jets have been tested, looking at signal events in which squarks (gluinos) decay to a W/Z/h boson and $\tilde{\chi}_1^0$ via $\tilde{\chi}_1^\pm / \tilde{\chi}_2^0$. Figure 4.9 shows the distributions of the mass of the leading large-R jets for such events with different values of the radius: 0.8 (A), 1.0 (B), 1.2 (C) and 1.4 (D). A clearer signal peak is seen around the mass of W/Z/h boson with the radius of large-R jets with 0.8.

Figure 4.10 compares the four different radius of large-R jets already shown

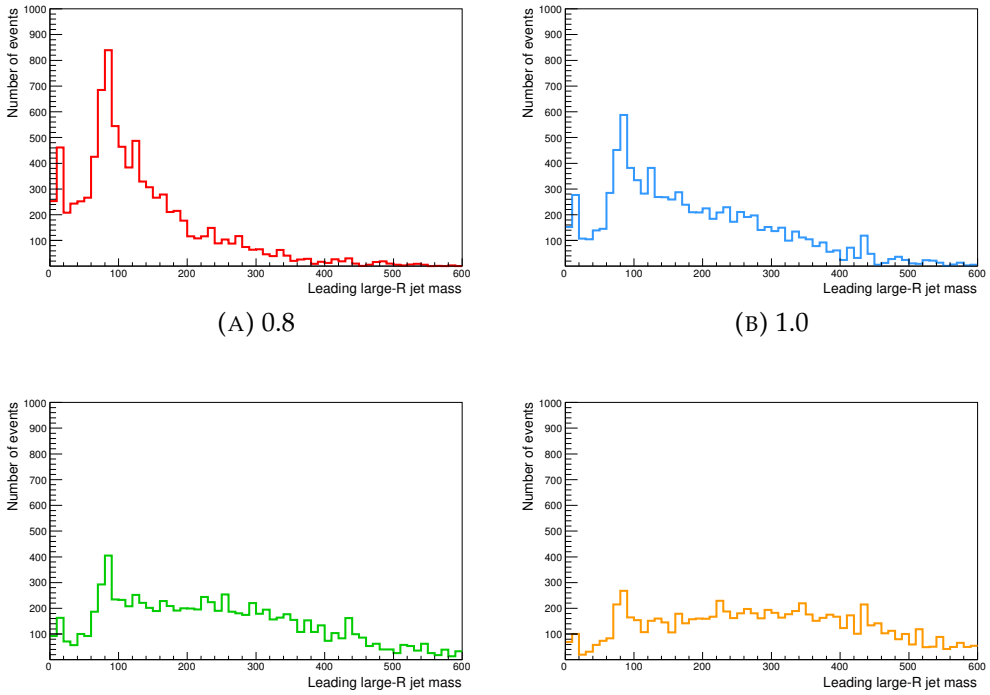

(A) 0.8 (B) 1.0

(C) 1.2 (D) 1.4

FIGURE 4.9: Mass of the leading large-R jet with different values of the radius.

separately in Figure 4.9. The red solid line (0.8) shows a clearer peak around the mass of W/Z/h bosons than the other lines. For these studies, an additional unwanted radiation is removed using the trimming procedure. The recommended values for f_{cut} of 5% and for R_{sub} of 0.3 are applied.

4.6 Overlapping objects

Objects described so far might overlap with other objects due to the fact that most of the reconstruction steps described above are run independently. For this purpose, an overlap removal between objects is used. This method removes objects using the geometrical variable ΔR defined in Equation 3.8.

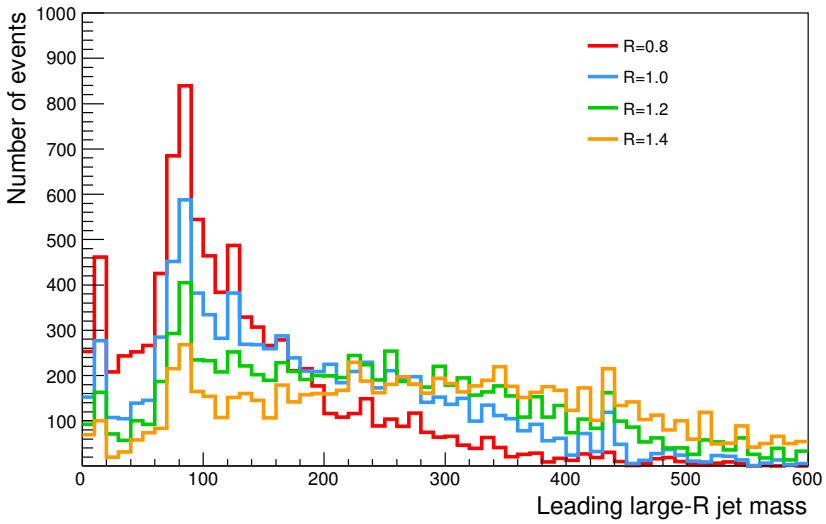

FIGURE 4.10: Comparison between large-R jets with different values of the radius R.

The procedure is the following:

- remove any jet reconstructed near electrons ($\Delta R < 0.2$) due to deposits in the EMCal which can be used for the reconstruction of jets but at the same time they can be identified as coming from electrons. If a jet is tagged as a b-jet, the electron will be removed due to the frequent production of electrons in decays of heavy-flavor jets,
- remove electrons near muons ($\Delta R < 0.01$) due to bremsstrahlung effects from muons followed by a photon conversion into electron pairs,
- remove muons near jets ($\Delta R < \min(0.4, 0.04 + 10\ \text{GeV} / p_T(\mu))$) with JVT > 0.6, $p_T < 50$ and $|\eta| < 2.4$ or jets with more than three tracks with $p_T > 500$ MeV. If a jet is tagged as a b-jet, the muon is kept, and
- discard any jet reconstructed near muons ($\Delta R < 0.2$).

4.7 Missing transverse momentum

Apart from particles which can precisely be measured such as electrons, muons, hadrons, there are particles which are invisible to general purpose detectors like ATLAS. Due to the conservation of momentum, the transverse momenta of all collision products have to sum to zero. The missing transverse momentum (E_T^{miss}) is defined as the negative vector sum of p_T measured in an event. The existence of missing transverse momentum may be indicative of weakly-interacting stable particles. In the SM, these particles are the neutrinos, but in a beyond the SM theory like SUSY, the neutralinos can pass through detectors without any interaction with detector materials and may

result in missing transverse momentum.
The total E_T^{miss} term is defined as:

$$E_T^{miss} = \sqrt{(E_x^{miss})^2 + (E_y^{miss})^2} \tag{4.7}$$

where E_x^{miss} and E_y^{miss} are respectively defined as:

$$E_x^{miss} = -p_x^{jet} - p_x^{electron} - p_x^{muon} - p_x^{photon} - p_x^{soft} \tag{4.8}$$

$$E_y^{miss} = -p_y^{jet} - p_y^{electron} - p_x^{muon} - p_y^{photon} - p_y^{soft} \tag{4.9}$$

In practice, the E_T^{miss} components of an event are calculated independently for each type of baseline objects and for the "soft" term. The soft term takes into account momentum contributions that are not attributed to any of the baseline objects and can be reconstructed using one of the three algorithms: the Calorimeter Soft Term E_T^{miss}, Track E_T^{miss} and the Track Soft Term E_T^{miss}. The Calorimeter Soft Term E_T^{miss} is calorimeter-based: it uses the energy deposits in the calorimeter which are not associated with any reconstructed hard object. The algorithm is very sensitive to pile-up. The Track E_T^{miss} uses momenta of ID tracks and includes tracks emanating from pile-up. The Track Soft Term E_T^{miss} is much more robust, since it excludes tracks from pile-up vertices [68].

4.7.1 Missing transverse momentum used in this thesis

The E_T^{miss} used in this thesis is calculated using baseline electrons, baseline muons, baseline jets, and photons with $p_T > 10$ GeV. Hadronic tau decays are included in the jet component. The soft term is reconstructed with the Track Soft Term E_T^{miss} algorithm.

Chapter 5

Standard Model backgrounds

As discussed in Chapter 2, both searches have exactly one lepton, jets and missing transverse momentum in the final states. However, these final states can also be obtained from several SM processes acting as backgrounds in this thesis. A vital part of searching for supersymmetric particles is a good understanding of these SM processes. This chapter details all SM processes which give the same or similar final states as the SUSY signals considered in this thesis.

5.1 Standard Model backgrounds in the 1 lepton channel

The dominant SM processes contributing to the final state with one lepton, jets and missing transverse momentum are top quark pair production, production of a W boson in association with jets and single top production. Smaller background processes arise from production of a Z boson in association with jets, $t\bar{t}$ production in association with a vector boson or a Higgs boson, WH and ZH productions, diboson and triboson backgrounds. A brief summary of the generators used for each process, together with a few technical details, is given in Section 5.2. Although, multi jet processes have a very high production cross-section this background is negligible due to the one lepton requirement and a hard criterion on the missing transverse momentum.

5.1.1 Top quark pair background

The production of a top quark pair often precisely mimics a final state expected from the SUSY signals. Figure 5.1 shows a $t\bar{t}$ diagram where both top and anti-top quarks decay to a W boson and a b-jet. A final state with one isolated lepton is obtained if one of the W bosons decays to a lepton and a neutrino and the other one to quarks. In this case, the final state will contain one lepton, four jets (not including jets from ISR or FSR) and missing transverse momentum from neutrino. Events where both W bosons decay to a

lepton can contribute to the background, if one of the leptons has not been identified or selected.

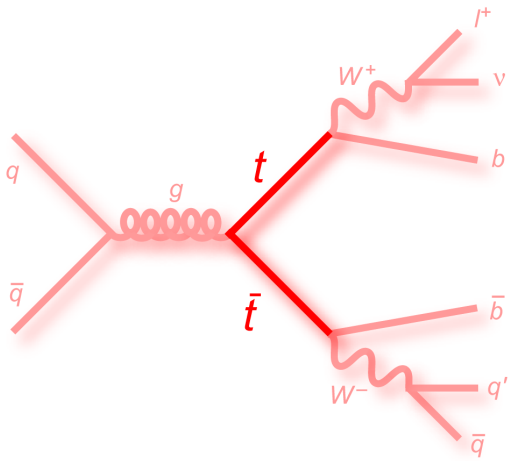

FIGURE 5.1: Feynman diagram for the $t\bar{t}$ production [69].

5.1.2 W+jets background

The production of W bosons produced in association with jets is the second largest background in the 1 lepton channel. A final state with one lepton can be obtained if the W boson decays leptonically. Figure 5.2 shows the production of the W boson with associated jets.

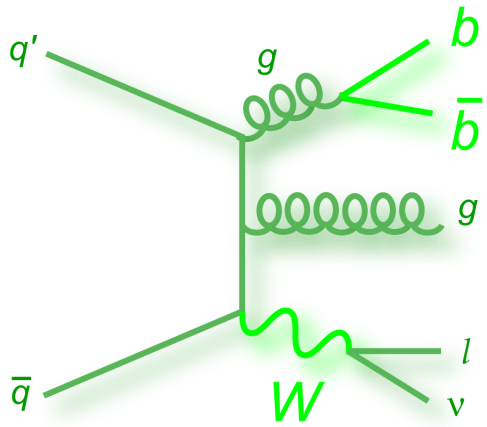

FIGURE 5.2: Feynman diagram for the production of a W boson in association with jets [69].

5.1.3 Single top background

Similarly to $t\bar{t}$ events, a lepton in single top events arrives from a W boson. The production of single top quarks can happen in several ways known as channels. A bottom quark can transform to a top quark and a W boson giving a "t-channel" or an intermediate W boson can decay into a top and an anti-bottom quark giving a "s-channel". The third channel in which a single top quark is produced in association with a W boson is known as a "Wt channel" [70]. Figure 5.3 shows the "t-channel" of the single top production.

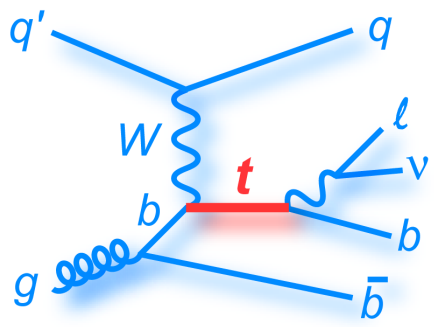

FIGURE 5.3: Feynman diagram of the single top production for the "t-channel" [69].

5.1.4 Smaller backgrounds

Smaller backgrounds have a similar topology as the SUSY signals but with smaller cross-sections. The following processes are treated as the smaller backgrounds in this thesis:

- production of a single Z boson in association with jets,
- production of $t\bar{t}$ background including a vector boson production where a boson could be either a W or Z boson,
- WH and ZH backgrounds,
- production of $t\bar{t}$ with a Higgs boson decaying to two b-jets,
- diboson and triboson backgrounds with W and/or Z bosons.

5.2 MC background samples

MC background samples are generated for each SM process by using the MC generators described in Section 3.4.2. To generate $t\bar{t}$ and single top samples with the t-, s- and Wt production mechanisms, POWHEG-Box interfaced to PYTHIA is used. The SHERPA at the NLO is used to generate W/Z+jets, diboson and tribosons samples. For $t\bar{t}V$ events, MadGraph at the LO is used,

while $t\bar{t}H$ events are generated with MCAtNLO and VH events are produced with PYTHIA. Table 5.1 details the generators used to produce background samples.

Physics process	Generator	Matrix Elements	Cross-section normalisation
$W(\rightarrow e\nu)$ + jets	SHERPA	NLO	NNLO
$Z/\gamma^*(\rightarrow ee)$ + jets	SHERPA	NLO	NNLO
$t\bar{t}$	POWHEG + PYTHIA	NLO	NNLO+NNLL
Single-top (t-, s- and Wt-channels)	POWHEG + PYTHIA	NLO	NNLO
$t\bar{t}$ + W/Z/WW	Madgraph	LO	NLO
WW, WZ and ZZ	SHERPA	NLO	NLO
WWW, WWZ WZZ and ZZZ	SHERPA	NLO	NLO
$t\bar{t}$ + H	aMcAtNlo+Herwigpp	NLO	NLO
WH and ZH	PYTHIA+EvtGen	LO	NLO

TABLE 5.1: Simulated background samples shown with the corresponding generator, matrix element and cross-section normalisation [50, 71–82].

Chapter 6

Kinematic variables

In order to obtain a good separation between the SUSY signal and background events different kinematic variables has been studied, but only the most useful variables are retained for both searches. These kinematic variables are described in this chapter, together with plots showing their discriminating power. The background events are stacked and shown with full color, while the signal models shown with lines are superimposed to show the power of the variables in discriminating different kinematic shapes.

6.1 Transverse mass of lepton and missing transverse energy m_T

The transverse mass of lepton and missing transverse energy is an important kinematic variable for both searches presented in this thesis [83]. It is defined as:

$$m_T = \sqrt{2 \cdot p_T^l \cdot E_T^{miss} \cdot (1 - \cos \Delta\phi(l, E_T^{miss}))} \tag{6.1}$$

using the leading lepton p_T, the missing transverse energy and the azimuthal angle between them.
This variable can suppress one of the most dominant background processes such as the W+jets background. If missing transverse energy comes only from neutrinos in the W decay, the m_T distribution shows a clear kinematic edge at the mass of the W boson[1]. On the other hand, if missing transverse energy comes from neutrinos and the LSPs, m_T has higher values than the mass of the W boson. Figure 6.1 shows the differences in the m_T distribution around the mass of the W boson between the squark and gluino signals, and background events on the left side, and the chargino/neutralino signal and background events on the right side.

[1] m_W=80370±19 MeV [84].

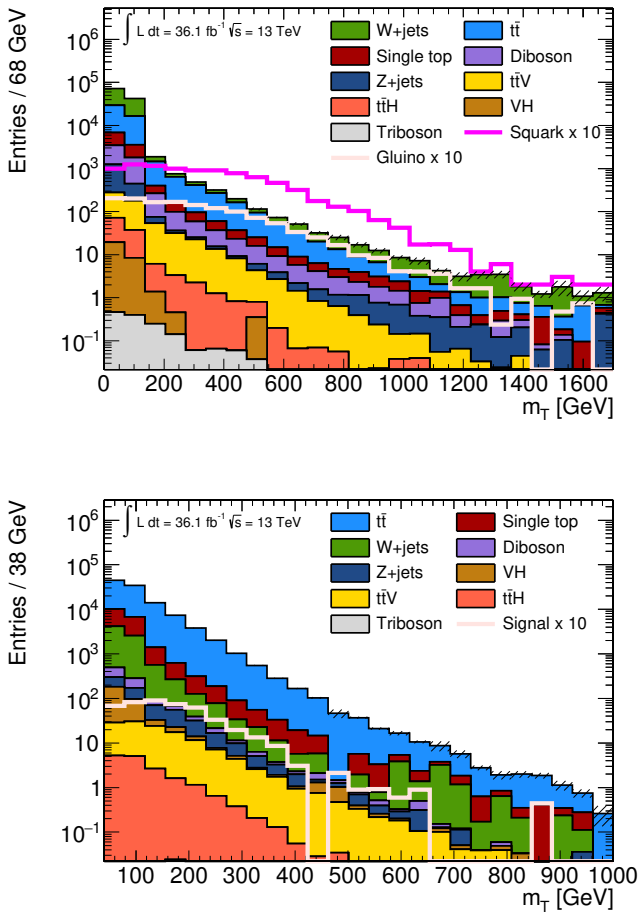

FIGURE 6.1: m_T distribution with the squark and gluino signals after applying a selection of exactly one lepton and at least two jets (top), and with the chargino/neutralino signal after requesting exactly one lepton, two b-jets and two or three jets (bottom).

6.2 Invariant mass of two b-jets m_{bb}

The invariant mass of two b-jets is defined as the sum of the b-jets four-vectors squared:

$$m_{b_1 b_2} = (P_{b_1} + P_{b_2})^2 \tag{6.2}$$

It can also be written as:

$$m_{b_1 b_2} = m_{b_1} + m_{b_2} + 2(E_{b_1} E_{b_2} - |p_{b_1}| \times |p_{b_2}| \times \cos\theta) \tag{6.3}$$

Figure 6.2 shows the difference between the squark and gluino signals, and the background events on the left side, and between the chargino/neutralino signal and the background events on the right side. In both cases, the signal shows a clear peak around the mass of the Higgs boson.

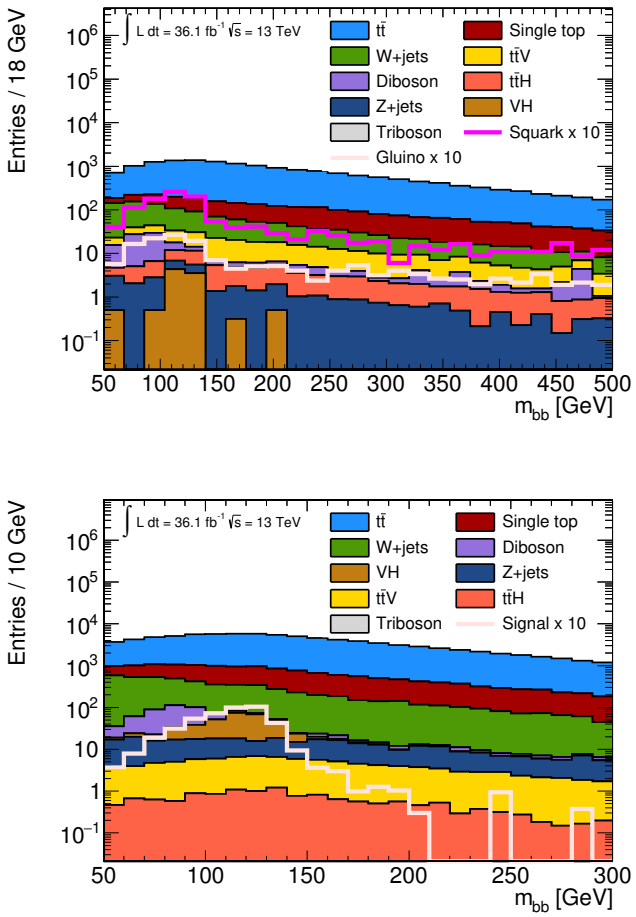

FIGURE 6.2: m_{bb} distribution with the squark and gluino signals after applying a selection of exactly one lepton and at least two jets (top), and with the chargino/neutralino signal after requiring exactly one lepton, two b-jets and two or three jets (bottom).

6.3 Effective mass of lepton, jets and missing transverse energy m_{eff}

The effective mass of lepton, jets and missing transverse energy is the sum of the transverse momentum of the lepton p_T^l, the transverse momenta of all jets p_T^{jet}, and the missing transverse energy [85, 86]:

$$m_{eff} = p_T^l + \sum p_T^{jet} + E_T^{miss} \tag{6.4}$$

This variable is used as a kinematic variable because it often has a good relation to the mass differences between initially produced SUSY particles and the LSP. Figure 6.3 shows the differences in the m_{eff} distribution between the signal and background events, where it is evident that the signal events have

higher values of m_{eff}. The m_{eff} variable is used only in the search for squarks and gluinos.

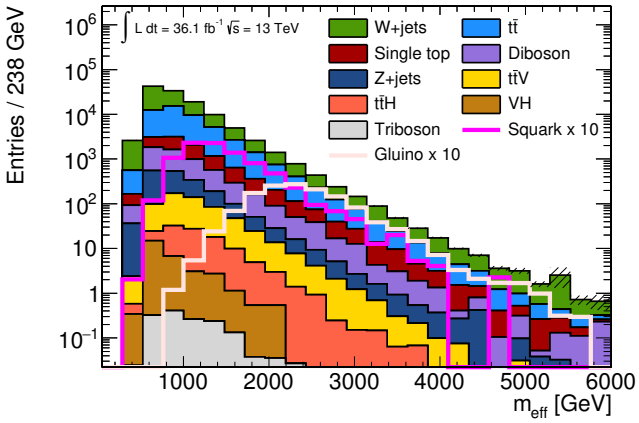

FIGURE 6.3: m_{eff} distribution with the squark and gluino signals after applying a selection of exactly one lepton and at least two jets.

6.4 Aplanarity $\mathcal{A}$

The aplanarity provides information about the shape of events [87]. It uses information on the full momentum tensor of an event, M_{xyz}, that is given through its eigenvalues λ_1, λ_2 and λ_3:

$$M_{xyz} = \sum_i \begin{pmatrix} p_{x_i}^2 & p_{x_i}p_{y_i} & p_{x_i}p_{z_i} \\ p_{y_i}p_{x_i} & p_{y_i}^2 & p_{y_i}p_{z_i} \\ p_{z_i}p_{x_i} & p_{z_i}p_{y_i} & p_{z_i}^2 \end{pmatrix} \tag{6.5}$$

where the sum runs over a lepton and all jets used in the event.
The individual eigenvalues of the tensor in Equation 6.5 are normalized and ordered as $\lambda_1 > \lambda_2 > \lambda_3$. The aplanarity is then defined as:

$$\mathcal{A} = \frac{3}{2}\lambda_3 \tag{6.6}$$

There are three different shapes of an event: linear, planar and aplanar. The SM background events usually have a linear or planar shape as shown in Figure 6.4. Generally, it means that most of the momentum activity in an event is concentrated in a plane. On the other hand, since a SUSY particle decays to two heavy particles which are usually produced approximately at rest, they tend to decay uniformly in all directions as shown in Figure 6.5. Due to this,

SUSY events have an aplanar shape with a large value of aplanarity. Figure 6.6 shows a difference in shape for the signal and SM background events. This variable is used only in the search for squarks and gluinos.

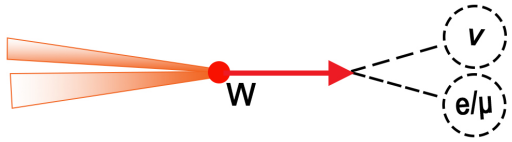

FIGURE 6.4: The shape of the aplanarity for the SM background events.

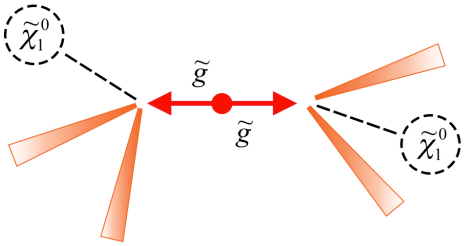

FIGURE 6.5: The shape of the aplanarity for the SUSY events.

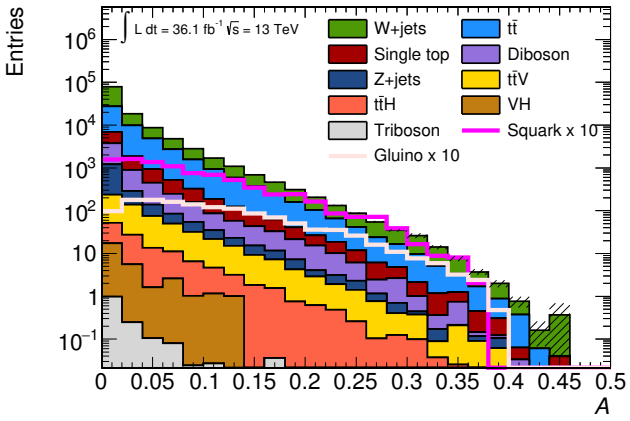

FIGURE 6.6: Aplanarity distribution with the squark and gluino signals after applying a selection of exactly one signal lepton and at least two jets.

6.5 Contransverse mass of two b-jets m_{CT}

The contranverse mass of two b-jets is designed to give information about the kinematic configuration of visible objects. It is defined as [88]:

$$m_{CT} = \sqrt{2 \cdot p_T^{b_1} \cdot p_T^{b_2} \cdot (1 + \cos\Delta\phi(b_1, b_2))} \tag{6.7}$$

using the p_T of two b-jets and the angle between them.
The m_{CT} variable can be reconstructed from the four-momenta of the two visible objects in an event showing a kinematic edge. For $t\bar{t}$ background events, the value of this endpoint is given by [88]:

$$m_{CT}^{max} = \frac{m_t^2 - m_W^2}{m_t} \sim 136 \text{ GeV} \tag{6.8}$$

where the mass of the top quark is 173.1±0.6 GeV [89].
Events with larger mass splittings between two SUSY states in the decay chain can be produced with large values of m_{CT}. Therefore, m_{CT} can be used as a kinematic variable to separate signal from background events.
Figure 6.7 shows the differences in the m_{CT} distribution between the signal and background events. This variable is used only in the search for charginos and neutralinos.

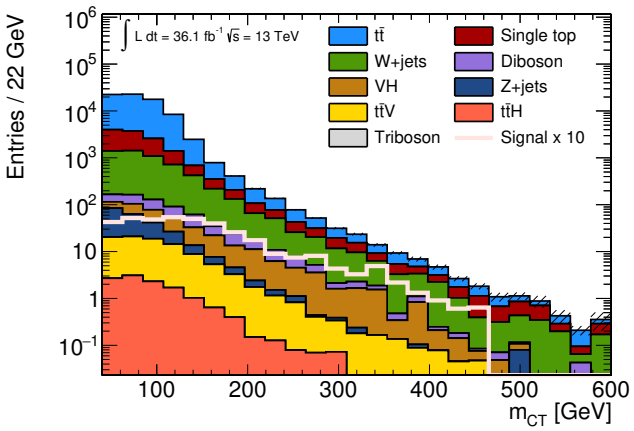

FIGURE 6.7: m_{CT} distribution with the chargino/neutralino signal after applying a selection of exactly one lepton, two b-jets and two or three jets.

Chapter 7

Analysis strategy

Although the SUSY search program at ATLAS targets a wide range of different signal scenarios and final states, most analyses follow a similar analysis strategy. The goal is to select events consistent with the SUSY signal with a high efficiency while suppressing the SM backgrounds. The kinematic variables defined in Chapter 6 are employed to discriminate the SUSY signal from the SM backgrounds. After the event selection, a precise estimation of the remaining SM background is very important. This chapter describes the general analysis strategy used in many SUSY searches including both searches presented in this thesis [90].

7.1 Signal regions

Signal regions (SRs) are defined to have a high contribution from a SUSY signal and a low contamination from SM predictions. They are designed based on signal kinematic features using various selection criteria. The SRs might be divided into further sub-regions to capture the kinematic shape of a particular signal.

7.1.1 Optimization strategies

An optimization procedure is performed to find suitable SRs. A good SR should be characterized by a high significance, defined as:

$$Z = \frac{s}{\sqrt{b + (\sigma_b)^2}} \tag{7.1}$$

where Z is the significance, s and b are the number of expected signal and background events, respectively and σ_b is the systematic uncertainty of the total background. In the optimization procedure, it is requested that the SR contains at least two background events in order to reduce the statistical uncertainty and avoid unphysical results.

7.2 Control regions

Control regions (CRs) are defined to be enriched with one specific SM background process. They are designed to be as kinematically close to the SRs as possible, but orthogonal to them. This is done by changing one or two of the SR selection criteria as shown in Figure 7.1. The signal contamination in the CRs is negligible. Each dominant background has its own CR, and CRs belonging to the same SR are orthogonal to each other.

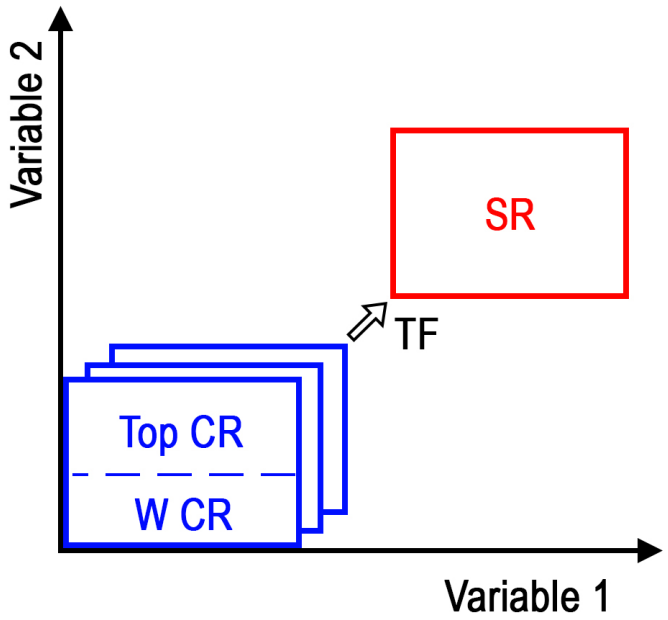

FIGURE 7.1: Schematic view of the SR with the multiple CRs. The SR is defined by selection criteria on variables 1 and 2. Both criteria are reverted to define the CRs.

The number of estimated background events in a SR, for the SM background of interest k, $N_{SR}^{estimated(k)}$, is given by:

$$N_{SR}^{estimated(k)} = \mu_k \times N_{SR}^{MC^k} \tag{7.2}$$

where μ_k is the normalisation factor obtained in the fit to data and defined as:

$$\mu_k = \frac{N_{CR}^{data} - N_{CR}^{MC^{additional-background}}}{N_{CR}^{MC^k}} \tag{7.3}$$

If $\mu_k \approx 1$, the simulated number of events agrees well with the number of events observed in data.

Based on Equations 7.2 and 7.3, the transfer function between the CR and SR for the background k can be written as:

$$TF_{CR\to SR} = \frac{N_{SR}^{MC^k}}{N_{CR}^{MC^k}} \tag{7.4}$$

Detailed background estimation techniques for each search are described in dedicated sections.

7.3 Validation regions

The next important component of the analysis strategy is the validation of the background estimates in the SR. For this purpose, one or more validation regions (VRs) are defined. They are designed by reverting one of two or more criteria which have been used for the SR definitions with respect to the CR selection. A schematic view of an analysis strategy with one SR, and multiple CRs and VRs is shown in Figure 7.2.

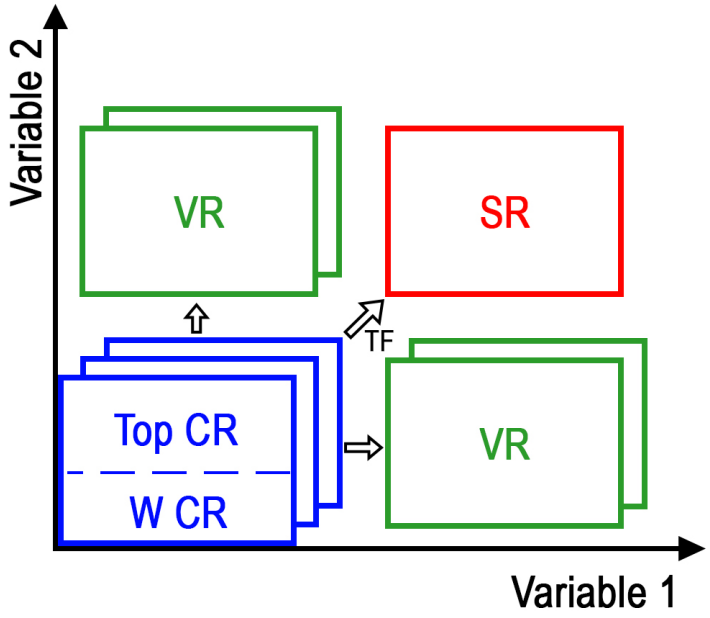

FIGURE 7.2: Schematic view of the SR with the multiple CRs and VRs. The VRs are defined by inverting some of the SR selection criteria.

The number of estimated background events in the VR can be found in a similar way as in a SR using:

$$N_{VR}^{estimated(k)} = \mu_k \times N_{VR}^{MC^k} \tag{7.5}$$

If there is a large disagreement between the observed and predicted number of events in the VRs, the SR must not be unblinded. Additional studies have to be done in order to better understand the disagreement. Only in case when a satisfactory agreement between the observed and predicted number of events in all VRs is found, the background predictions are extrapolated into the SR and compared to the observed data. In general, this step is called "unblinding" or "opening the box".

Chapter 8

Statistical apparatus

The searches presented in this thesis use a software tool for statistical data analysis called HistFitter in order to obtain the background normalization factors and to check if any potential excess of observed events over the SM predictions is statistically significant. HistFitter is based on the packages RooStats and HistFactory [90–94]. This chapter gives the mathematical background of this tool.

8.1 Likelihood function

The general likelihood function used in this thesis can be written as [90]:

$$\begin{aligned} L\left(\mathbf{n}, \boldsymbol{\theta^0} \mid \mu, \mathbf{b}, \boldsymbol{\theta}\right) &= P_{SR} \times P_{CR} \times C_{syst} \\ &= P\left(n_S \mid \lambda_S\left(\mu, \mathbf{b}, \boldsymbol{\theta}\right)\right) \times \prod_{i \epsilon CR} P\left(n_i \mid \lambda_i\left(\mu, \mathbf{b}, \boldsymbol{\theta}\right)\right) \times C_{syst}\left(\boldsymbol{\theta^0}, \boldsymbol{\theta}\right) \end{aligned} \tag{8.1}$$

where:

- P is the Poisson distribution which depends on the number of observed events in the SR, n_S, or CR, n_i.
- λ_S and λ_i are the Poisson expectations depending on the background prediction $\mathbf{b}$, the nuisance parameters [1] $\boldsymbol{\theta}$, the normalization factors for background processes μ_p and the signal strength parameter μ.
- C_{syst} are PDFs for auxiliary measurements which constrain systematics uncertainties and depends on $\boldsymbol{\theta}$ and $\boldsymbol{\theta^0}$.
- $\boldsymbol{\theta^0}$ are introduced due to variations of $\boldsymbol{\theta}$ and present the central values of the auxiliary measurements around $\boldsymbol{\theta}$.

The profile likelihood ratio is defined as [93]:

$$\lambda(\mu) = \frac{L\left(\mu, \hat{\hat{\boldsymbol{\theta}}}\right)}{L\left(\hat{\mu}, \hat{\boldsymbol{\theta}}\right)} \tag{8.2}$$

[1] A nuisance parameter is used to describe systematics uncertainties.

where $\hat{\mu}$ and $\hat{\boldsymbol{\theta}}$ maximize the Likelihood, while $\hat{\hat{\boldsymbol{\theta}}}$ maximizes the Likelihood for a fixed μ.

8.2 Test statistic

A test statistic is defined using the profile likelihood ratio from Equation 8.2 as [93]:

$$t_\mu = -2\ln\lambda(\mu) \tag{8.3}$$

The p-value gives the probability of obtaining an outcome of a statistical test at least as extreme as the observed outcome. Using the test statistic, this implies [93]:

$$p_\mu = \int_{t_{\mu,obs}}^{\infty} f(t_\mu \mid \mu) dt_\mu \tag{8.4}$$

where $f(t_\mu \mid \mu)$ is the PDF of the test statistic t_μ given for a fixed value of μ. The integral extends from the observed value of the test statistic to infinity. The p-value is related to the significance Z:

$$Z = \Phi^{-1}(1-p) \tag{8.5}$$

where Φ is the quantile of the standard Gaussian distribution.
Figure 8.1 illustrates the relation between the p-value, the observed t_μ and the significance Z. The significance larger then 3 ($Z > 3$) points to the evidence of new physics, whereas the significance of at least 5 (this corresponds to the p-value of 2.87×10^{-7}) indicates a discovery [93].

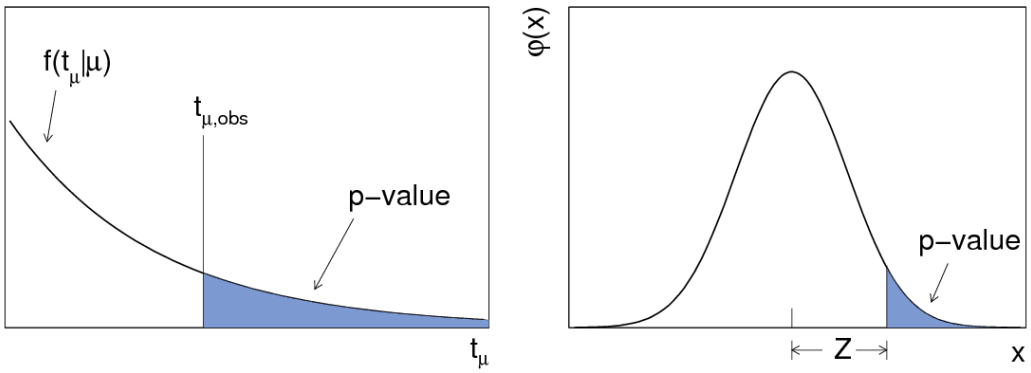

FIGURE 8.1: Illustration of the relation between the p-value, the test statistic t_μ and the significance Z [93].

8.3 Fit strategies

The fit strategies used in this thesis are defined as the background-only fit, the model-independent signal fit and the model-dependent signal fit. They are described in the following.

8.3.1 Background-only fit

The background-only fit strategy is used to estimate the total background in SRs and VRs without incorporating signal contributions in the CRs. The fit is performed simultaneously in a set of orthogonal CRs assuming that no signal is present in the CRs. The input parameters of the Likelihood fit are the number of observed events in each CR, MC background estimates and systematic uncertainties, while the fit parameters are the normalization factors of the SM processes.

8.3.2 Model-independent signal fit

The model-independent signal fit or discovery fit is used to evaluate whether the number of observed data in a SR is compatible with the SM prediction only. In a discovery test, any signal contamination in the CRs is assumed to be negligible and the test statistic q_0 is defined for μ=0 as [93]:

$$q_0 = \begin{cases} -2\ln\lambda(0) & \text{if} \quad \hat{\mu} \geq 0 \\ 0 & \text{if} \quad \hat{\mu} < 0 \end{cases} \tag{8.6}$$

The p-value is calculated using the test statistic q_0 as [93]:

$$p_0 = \int_{q_{0,\text{obs}}}^{\infty} f(q_0 \,|\, 0) dq_0 \tag{8.7}$$

where $f(q_0 \,|\, 0)$ is the PDF of the test statistic q_0 given for the fixed value of μ=0.

8.3.3 Model-dependent signal fit

The model-dependent signal fit or exclusion fit is used if the discovery test fails to reject the background-only hypothesis. In an exclusion test, a specific signal hypothesis with a fixed signal strength is tested and a signal contamination in the CRs is taken into account. The modified test statistic q_μ is given by [93]:

$$q_\mu = \begin{cases} -2\ln\lambda(\mu) & \text{if} \quad \hat{\mu} \leq \mu \\ 0 & \text{if} \quad \hat{\mu} > \mu \end{cases} \tag{8.8}$$

where the signal strength is imposed to be $\mu = 1$ in this thesis.
The p-value defined in Equation 8.4 is given by:

$$p_\mu = \int_{q_{\mu,\text{obs}}}^{\infty} f(q_\mu \,|\, \mu) dq_\mu \tag{8.9}$$

where $f(q_\mu \mid \mu)$ is the PDF of the test statistic q_μ assuming μ=1.

8.4 CL_s technique

The signal is excluded using the CLs technique defined as [94]:

$$CL_s = \frac{p_1}{1 - p_0} \tag{8.10}$$

where p_1 and p_0 are the p-values calculated using Equation 8.9 for $\mu = 1$ and Equation 8.7 for $\mu = 0$. If $CL_s < 0.05$, a specific signal hypothesis is excluded at 95% Confidence Level (CL).

Chapter 9

Search for squarks and gluinos decaying to W/Z/h bosons

This chapter presents the search for squarks and gluinos decaying to W, Z or h bosons (the WZh model for short) described in Section 2.5.1. A slightly different supersymmetric model in which squarks and gluinos decay to only W bosons has been performed by the ATLAS collaboration and the latest result is reported in [95]. The WZh model has been introduced to cover production of squarks and gluinos decaying to W/Z/h bosons instead only to W bosons.

The first section describes a construction of the WZh model and a baseline event selection including a trigger strategy. Afterwards, the analysis strategy is detailed and the obtained sensitivity has been compared with a reinterpretation of the published analysis on squarks and gluinos decaying to only W bosons. At the end of this chapter, future prospects and a possibility of using large-R jets are discussed.

9.1 Construction of the WZh model

The WZh simplified model in which the pair-produced squarks (gluinos) decay through either $\tilde{\chi}_1^{\pm}$ or $\tilde{\chi}_2^0$ to W/Z/h bosons has been designed to explore boson-tagging techniques as well as final states including b-jets.
In this model, the masses of $\tilde{\chi}_1^{\pm}$ and $\tilde{\chi}_2^0$ are assumed to be equal. The masses of squarks (gluinos) and $\tilde{\chi}_1^{\pm}/\tilde{\chi}_2^0$ are chosen with respect to the variable x defined as:

$$x \equiv \frac{m_{\tilde{\chi}_1^{\pm}} - m_{\tilde{\chi}_1^0}}{m_{\tilde{q}(\tilde{g})} - m_{\tilde{\chi}_1^0}} \tag{9.1}$$

In order to ensure that $\tilde{\chi}_1^{\pm}/\tilde{\chi}_2^0$ can decay to an on-shell Higgs boson, the minimum value of the variable x has to satisfy the condition:

$$\Delta m = m_{\tilde{\chi}_1^{\pm}/\tilde{\chi}_2^0} - m_{\tilde{\chi}_1^0} \geq 130\text{GeV}$$

The mass of $\tilde{\chi}_1^0$ is fixed to be 60 GeV.
Branching ratios (BRs) of squarks, gluinos, $\tilde{\chi}_1^{\pm}$ and $\tilde{\chi}_2^0$ are motivated by possible pMSSM (phenomenological Minimal Supersymmetric Standard Model) scenarios, which is a two-dimensional subspace of the 19 parameters [96, 97]:

$\tan\beta$	the ratio of the VEVs of the two Higgs doublet fields
$\lvert\mu\rvert$	the higgsino mass parameter
M_1, M_2, M_3	the bino, wino and gluino mass parameters
M_A	the mass of the pseudoscalar Higgs boson
$m_{\tilde{q}}, m_{\tilde{u}_R}, m_{\tilde{d}_R}, m_{\tilde{l}}, m_{\tilde{e}_R}$	first/second generation sfermion masses
$m_{\tilde{Q}}, m_{\tilde{t}_R}, m_{\tilde{b}_R}, m_{\tilde{L}}, m_{\tilde{\tau}_R}$	third generation sfermion masses
A_t, A_b, A_τ	third generation trilinear couplings

The calculation of BRs is done separately for the squark and gluino case. The parameters from the pMSSM scenario are set in the package SUSY-HIT, which is used for the calculation of BRs [98, 99].

In the squark case, the first and second generation of squarks are assumed to be lighter than gluinos and their masses are set to 1.1 TeV [100]. The value of 1.1 TeV is chosen because it is the minimum excluded value of squark masses at the LHC (at the time of the construction of this model). The third generation squarks and gluinos are effectively decoupled by fixing their mass to 4 TeV. The other parameters are set to be M_A= 4 TeV, tan β = 10, A_t = A_b = A_τ = 4 TeV. Three scenarios with M1 = 100 GeV, M2 = 500 GeV and μ = 2000 GeV, and all possible permutations have been explored. The total BR to the W, Z and h bosons obtained from decays of left-handed squarks and right-handed squarks are shown in Figures 9.1 and 9.2, respectively. The total BRs to Z and h bosons are similar in the three combinations for the left-handed squarks case and the two combinations for the right-handed squarks case, while the total BR to W bosons is about two times larger than to Z or h bosons in the mentioned combinations.

In the gluino case, masses of the gluinos are set to be 1.8 TeV according to the latest result published by the ATLAS collaboration at time of the construction of this model [100]. The squarks in all generations are assumed to be heavier than gluinos and are decoupled by setting their masses to 4 TeV. The other parameters are set to be M_A= 4 TeV, tan β = 10, A_t = A_b = A_τ = 4 TeV. The same scenarios as above of M1, M2 and μ together with all six permutations have been tested. The total BRs to the W, Z and h bosons for each permutation obtained from decays of gluinos are shown in Figure 9.3. The total BRs to Z and h bosons are similar in the four combinations while the total BR to W bosons is about two times larger in the same combinations.

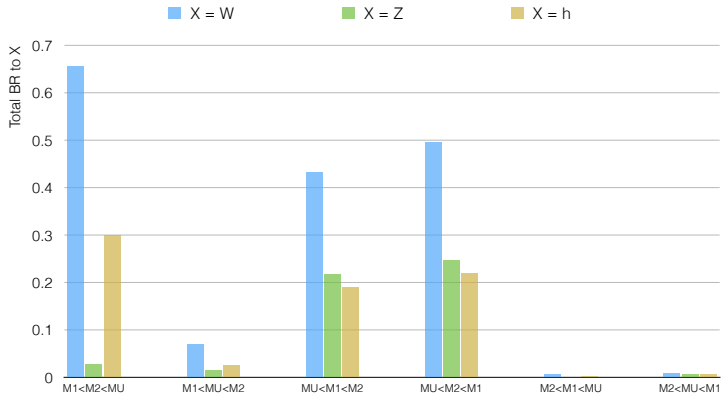

FIGURE 9.1: Total BRs to the W, Z and h bosons obtained from decays of left-handed squarks.

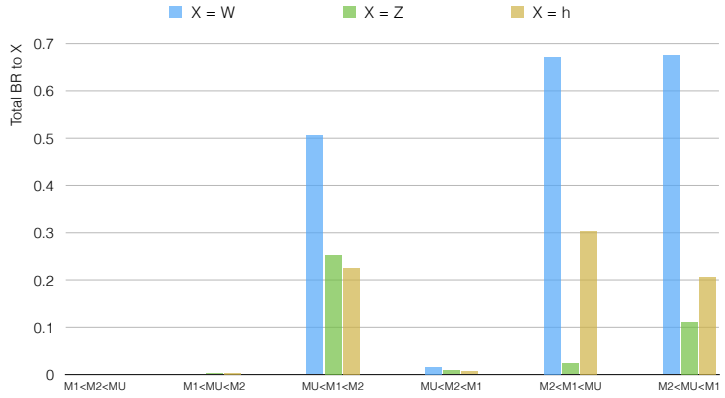

FIGURE 9.2: Total BRs to the W, Z and h bosons obtained from decays of right-handed squarks.

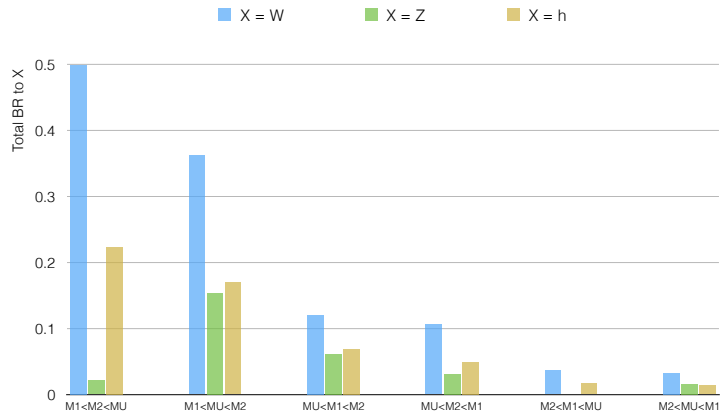

FIGURE 9.3: Total BRs to the W, Z and h bosons obtained from decays of gluinos.

Since the combination in which the BR to W boson is about two times larger then the BR to Z or h boson appears a few times for the squark and gluino cases, the model is constructed in such a way. Figures 9.4 and 9.5 show the squark and gluino decays, respectively, with the chosen BRs.

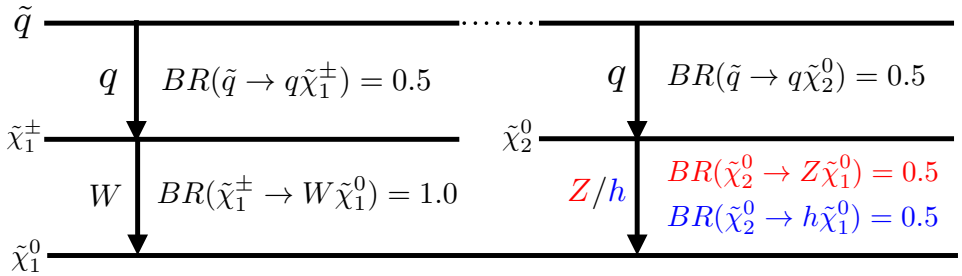

FIGURE 9.4: Decay chain of squarks with the chosen BRs.

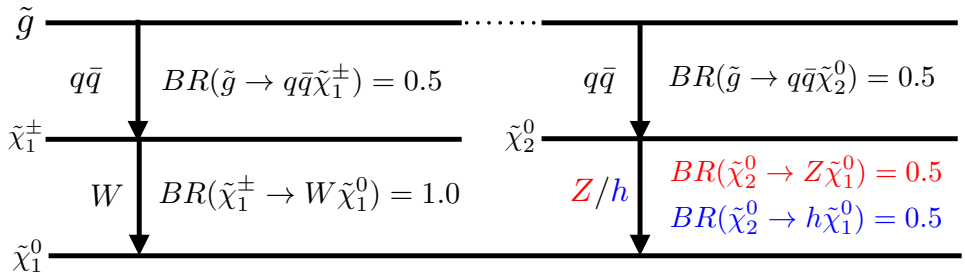

FIGURE 9.5: Decay chain of gluinos with the chosen BRs.

9.2 Dataset and Monte Carlo samples

This search uses a dataset recorded at the center-of-mass energy of 13 TeV with an integrated luminosity of 36.1 fb^{-1}.
Signal samples are generated with MadGraph interfaced to PYTHIA for both cases. Figure 9.6 shows the signal grid for the squark case (left) and gluino case (right). Both grids have 72 signal points shown as red dots. Since the aim is to extend the parameter space with respect to the published analysis [95], the gluino grid has more signal points with higher gluino masses.

9.3 Baseline selection

The baseline selection includes data quality checks, a trigger selection and further preselection criteria based on the signal topology. All of these criteria are described in this section.

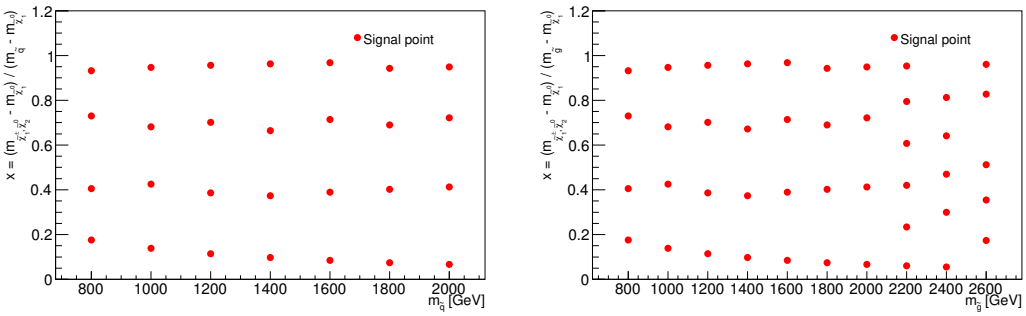

FIGURE 9.6: Two-dimensional signal grid in the $m_{\tilde{q}(\tilde{g})}$ - x plane for the squark case (left) and the gluino case (right).

9.3.1 Data quality check

All events are required to pass several data quality checks to keep only high quality events from proton-proton collisions, collected during optimal operation of the LHC and of ATLAS:

- **Data quality**: all events obtained from stable beams delivered by the LHC when the ATLAS detector is operating with all sub-detectors are given in a "Good Run List (GRL)". For the search presented in this thesis only events which have been marked as good in the GRL are used.
- **Data corruption**: incomplete events can appear due to problems in the trigger and/or data acquisition system. Also events which fall into an inactive area of the LAr and Tile calorimeter, can give a source of fake missing transverse momentum. All these events are vetoed.
- **Primary vertex**: vertices from proton-proton collisions are reconstructed based on information from the Inner Detector. Only events with at least two reconstructed primary vertices are used for this search.
- **Cosmic muon**: muons from cosmic rays can enter the detector and precisely mimic the trajectory of a muon obtained from a proton-proton collision. In order to remove these cosmic muons, all events which contain a muon with $|d_0^{PV}| > 0.2$ mm or $|z_0^{PV}| > 1$ mm are rejected.
- **Bad muon**: all events which contain badly reconstructed muons are vetoed. A muon is considered as badly reconstructed if $\sigma(q/p)/(q/p) > 0.2$, where q is the charge of the muon.
- **Bad jet**: events with bad jets are rejected. A bad jet could come from cosmic-ray showers, detector effects and/or problems which appear due to the quality of the LHC beams.

9.3.2 Trigger strategy

The dataset used is collected using missing transverse momentum (E_T^{miss}) triggers with different thresholds during the data taking period 2015 - 2016. Table 9.1 shows the values of the thresholds at the L1 and the HLT, and how much integrated luminosity was collected with the thresholds.

Period	HLT threshold [GeV]	L1 threshold [GeV]	Integrated luminosity [fb^{-1}]
2015	70	50	3.2
2016 A-D3	90	50	6.1
2016 D4-F1	100	50	5.5
2016 F2-	110	50	21.7

TABLE 9.1: Summary of the E_T^{miss} triggers used in this search.

The turn-on curves[1] of the E_T^{miss} trigger efficiency as a function of the offline E_T^{miss} are shown in Figure 9.7. They have been extracted using data collected by single lepton (electron or muon) triggers as references and an offline criterion on the lepton (electron or muon) transverse momentum of > 27 GeV. All turn-on curves have been divided into the electron and muon channels, and a selection of exactly one lepton and at least two jets is applied before extracting the trigger efficiency. Since the lowest requested criterion on E_T^{miss} is 250 GeV in this analysis as shown in Section 9.4, the turn-on curves show that the trigger is fully efficient beyond this value.

9.3.3 Preselection criteria

After the trigger requirements, the events are further selected by applying additional criteria, which are called preselection criteria:

Lepton criterion, N_{lep}: the search presented in this chapter requests either a signal electron or a signal muon. If the squarks (gluinos) decay via $\tilde{\chi}_1^{\pm}$ to a W boson and $\tilde{\chi}_1^0$, then one lepton (+ missing transverse momentum) arises from the leptonic decay of the W boson. However, if the squarks (gluinos) decay via $\tilde{\chi}_2^0$ to a Z or h boson and $\tilde{\chi}_1^0$, then the origin of the lepton depends on the Z or h decays. Figure 9.8 shows the lepton origin after requesting exactly one signal lepton (electron or muon). The origin of the

[1] A trigger efficiency curve can be separated into three parts. The first part has low values of E_T^{miss} and the trigger cannot record any events in this part due to the higher trigger requirement. In the second part, the efficiency curve which is called turn-on goes from an efficiency of zero to the maximum efficiency for a considered trigger. In the third part, the trigger is maximally efficient and this region is called plateu.

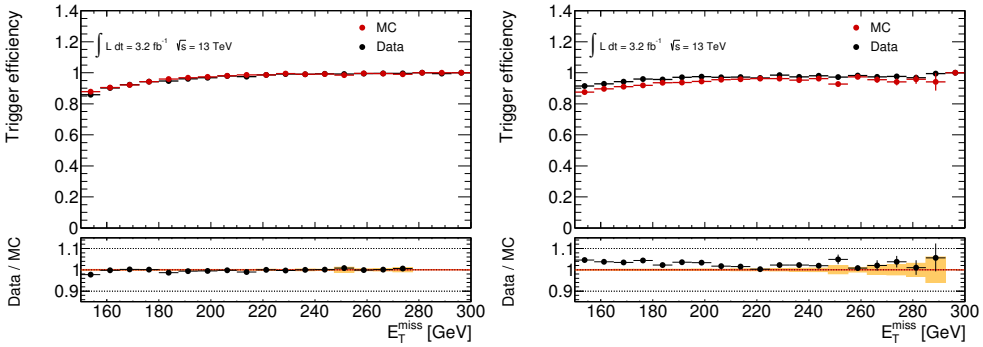

e channel, 70 GeV μ channel, 70 GeV

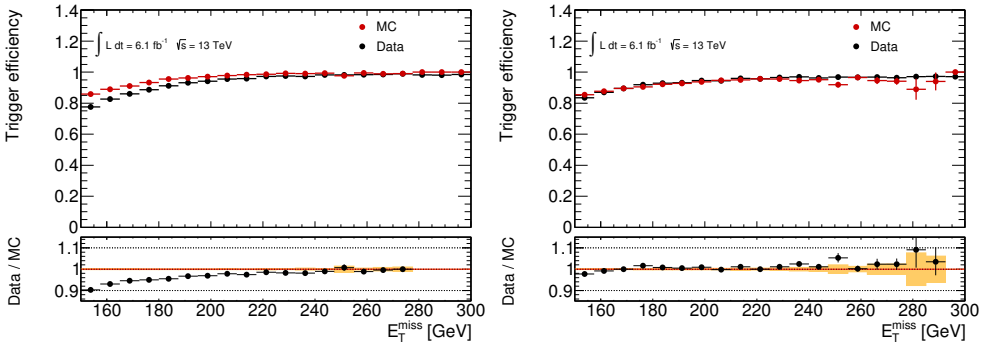

e channel, 90 GeV μ channel, 90 GeV

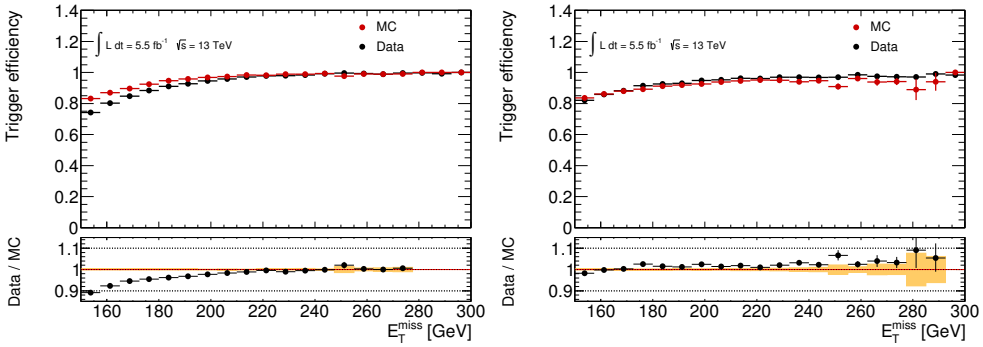

e channel, 100 GeV μ channel, 100 GeV

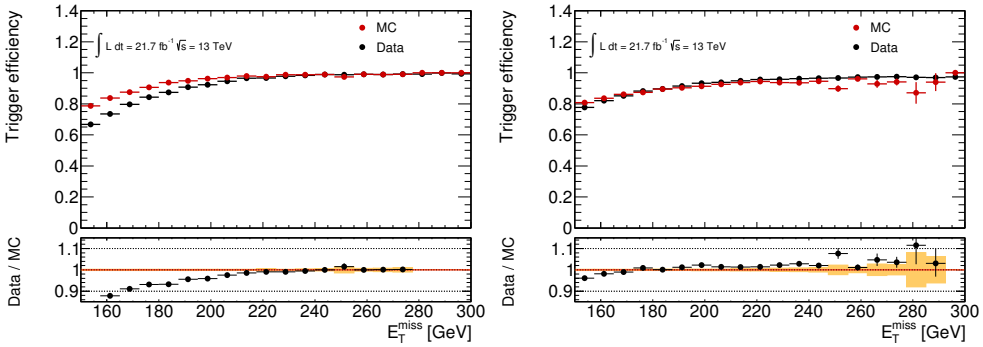

e channel, 110 GeV μ channel, 110 GeV

FIGURE 9.7: Trigger efficiencies in data and in MC simulated $t\bar{t}$ events as a function of E_T^{miss} plotted for the E_T^{miss} triggers listed in Table 9.1. The trigger efficiencies have been divided into the electron (left) and muon (right) channels. The $t\bar{t}$ process is used because it is the dominant background in this search.

lepton is in 87% of the cases a W boson, in 3% (10%) of the cases a Z (h) boson. This is expected because exactly one lepton can be obtained from a W decay. In case of Z and h decays, two leptons are mostly expected but they can also contribute to the final state with one lepton if one of them has not been identified or selected.

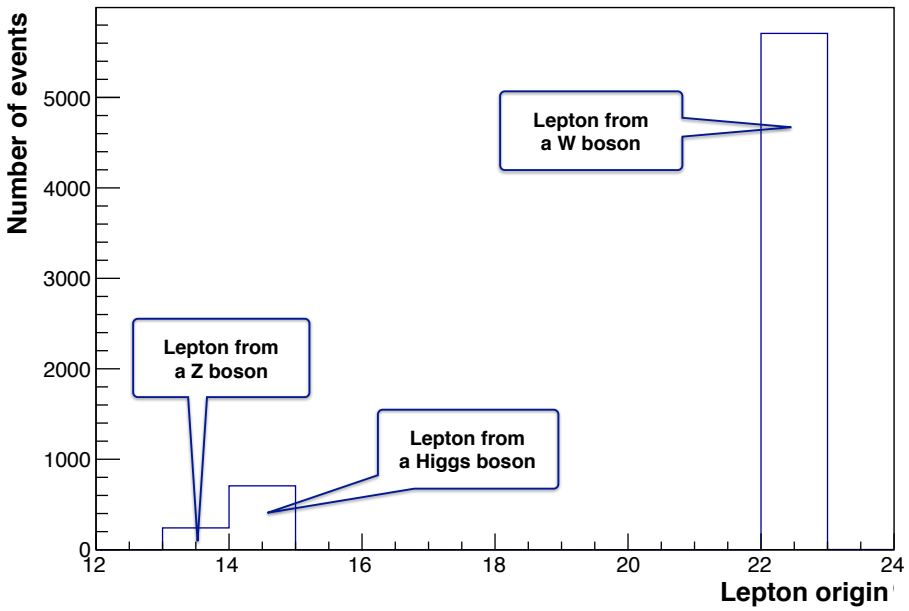

FIGURE 9.8: The lepton origin from W, Z and h bosons. The X-axis shows the Monte Carlo numbers of parent particles: 13 - Z boson, 14 - Higgs boson and 22 - W boson.

Criterion on the jet multiplicity including b-jets: as already discussed, this search allows a different number of jets including jets from b-quarks in the final state. In order to select typical events for the signal and reduce as many background events as possible, any accepted event is required to contain at least two jets.

9.4 Analysis strategy

The optimisation strategy has been performed for the events that pass the baseline selection using the kinematic variables defined in Chapter 6. In order to cover different scenarios of mass splittings between $\tilde{q}(\tilde{g})$, $\tilde{\chi}_1^{\pm}/\tilde{\chi}_2^0$ and $\tilde{\chi}_1^0$ three SRs are defined as: signal region compressed (SRC), signal region intermediate (SRI) and signal region boosted (SRB).

The SRC provides sensitivity to scenarios known as "compressed scenarios" where $m_{\tilde{\chi}_1^{\pm}/\tilde{\chi}_2^0}$ is close to $m_{\tilde{\chi}_1^0}$. In this scenario, the signal events are

expected to have a soft p_T lepton, larger values of m_{eff} and of aplanarity due to the large mass splittings between $\tilde{q}(\tilde{g})$ and $\tilde{\chi}_1^{\pm}/\tilde{\chi}_2^0$.

The SRI covers scenarios in which $m_{\tilde{\chi}_1^{\pm}/\tilde{\chi}_2^0}$ are chosen to be mid-way between $\tilde{q}(\tilde{g})$ and $\tilde{\chi}_1^0$. In this scenario, known as "intermediate scenario", the signal events have similar characteristics as in the compressed scenario but a harder lepton spectrum.

The SRB is designed for scenarios where $m_{\tilde{q}(\tilde{g})}$ is close to $m_{\tilde{\chi}_1^{\pm}/\tilde{\chi}_2^0}$. This scenario is called "boosted scenario", because the W/Z/h boson produced in the decay of $\tilde{\chi}_1^{\pm}/\tilde{\chi}_2^0$ is significantly boosted. Due to the boosted W/Z/h boson the signal events have a high-p_T lepton and larger values of m_T.
A schematic overview of all scenarios is sketched in Figure 9.9, while the whole grid with all three SRs is illustrated in Figure 9.10.

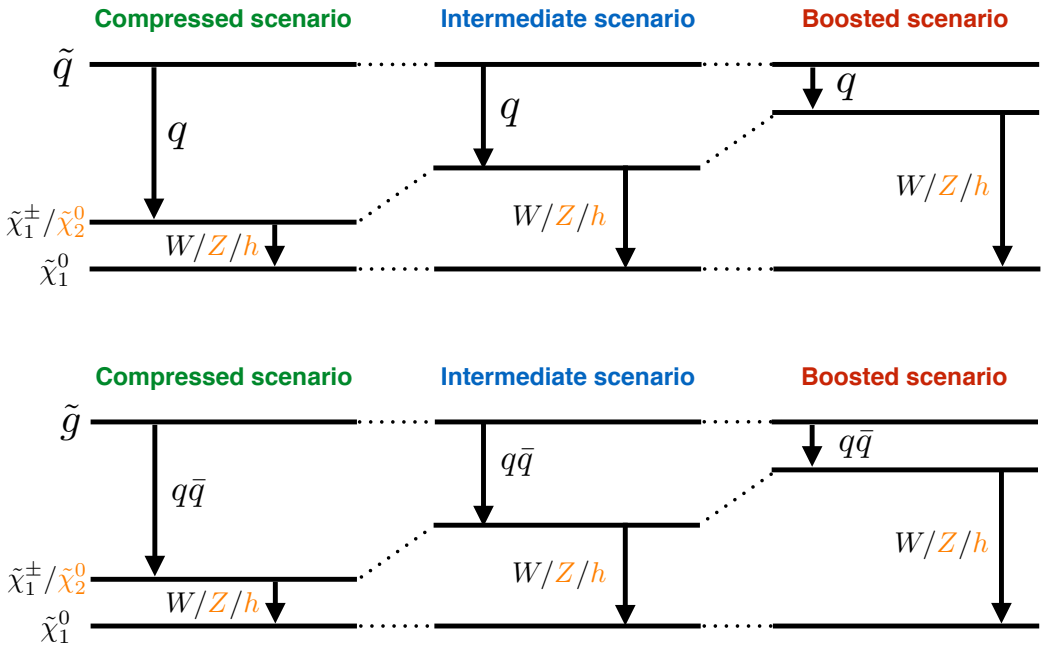

FIGURE 9.9: Decay chains of squarks (top) and gluinos (bottom) considered in this search. A decay of $\tilde{\chi}_2^0$ to Z or H boson (+ $\tilde{\chi}_1^0$) is shown in orange. The vertical distance indicates mass differences between sparticles.

Representative signal points have been chosen in all three scenarios. The significance Z defined in Equation 7.1 is calculated for each representative signal point using the following optimization scan:

N_{jets}	[2,3,4,5,6,7,8]
E_T^{miss} [GeV]	[200, 250, 300, 350, 400, 450, 500]
m_T [GeV]	[100, 125, 150, 175, 200, 225, 250, 275, 300, 325, 350, 375, 400, 425]
m_{eff} [GeV]	[600, 800, 1000, 1200, 1400, 1600, 1800, 2000, 2200]
Aplanarity	[0, 0.01, 0.02, 0.03, 0.04, 0.05, 0.06, 0.07]
E_T^{miss}/m_{eff}	[0., 0.1, 0.2, 0.3, 0.4]

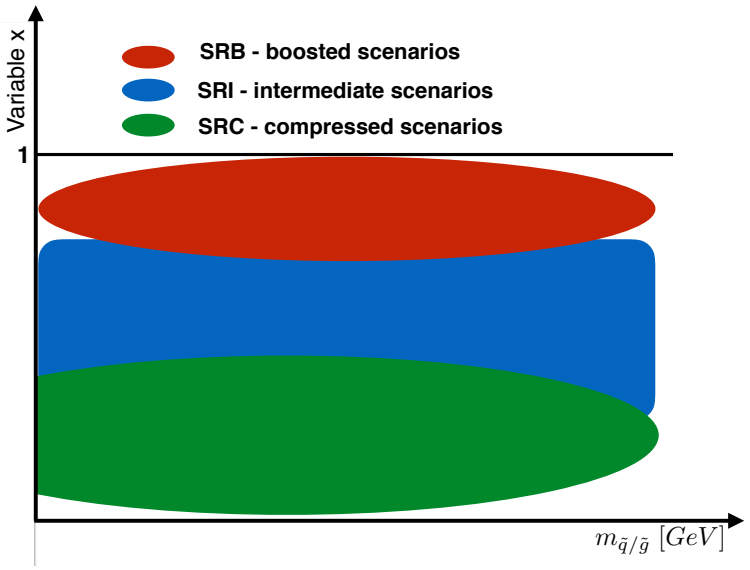

FIGURE 9.10: Schematic overview of the three SRs in the $m_{\tilde{q}(\tilde{g})}$ - variable x plane. The variable x is defined in Equation 9.1.

The selections with the highest significance for each representative signal point have been checked with so-called N-1 plots. The N-1 plots show the key kinematic variables for representative signal points and all background processes after applying all selection criteria minus the plotted quantity. Figures 9.11 to 9.13 show the N-1 plots with the key kinematic variables for the compressed, intermediate and boosted scenarios, respectively. Three squark representative signal points from each scenario are shown on the left side, while the gluino representative signal points are shown on the right side. The bottom pad shows the expected significance. The final SRs have been chosen by averaging the expected significance obtained from the N-1 plots between different representative signal points in each scenario.

Table 9.2 shows the final SR selections for the squark and gluino cases.

	Squark case			Gluino case		
	SRC	SRI	SRB	SRC	SRI	SRB
N_{jets}	2	3	4	3	5	3
E_T^{miss} [GeV]	500	500	250	250	300	250
m_T [GeV]	125	125	425	125	200	425
m_{eff} [GeV]	2200	1600	1600	2000	2000	1800
E_T^{miss}/m_{eff}	–	–	0.4	–	–	0.3
Aplanarity	0.07	0.07	–	0.07	0.06	–

TABLE 9.2: The SR selections for the squark and gluino case.

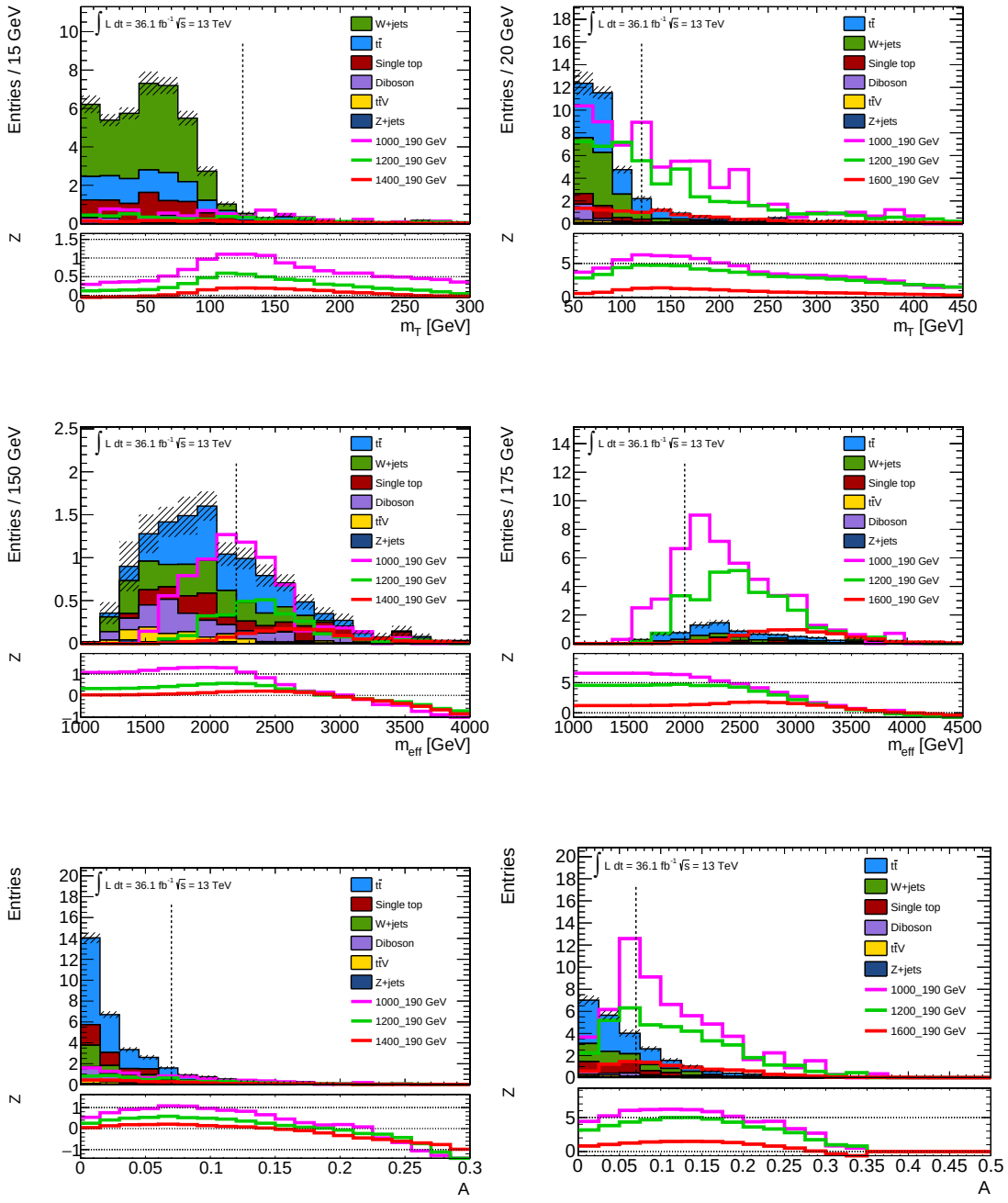

FIGURE 9.11: The N-1 plots for three representative signal points and all background processes as a function of m_T, m_{eff} and aplanarity after applying the SRC selection minus the plotted variable. The squark representative signal points are shown on the left side, while the gluino representative signal points are shown on the right side. All representative signal points are taken from the compressed spectra. The bottom pad shows the expected significance.

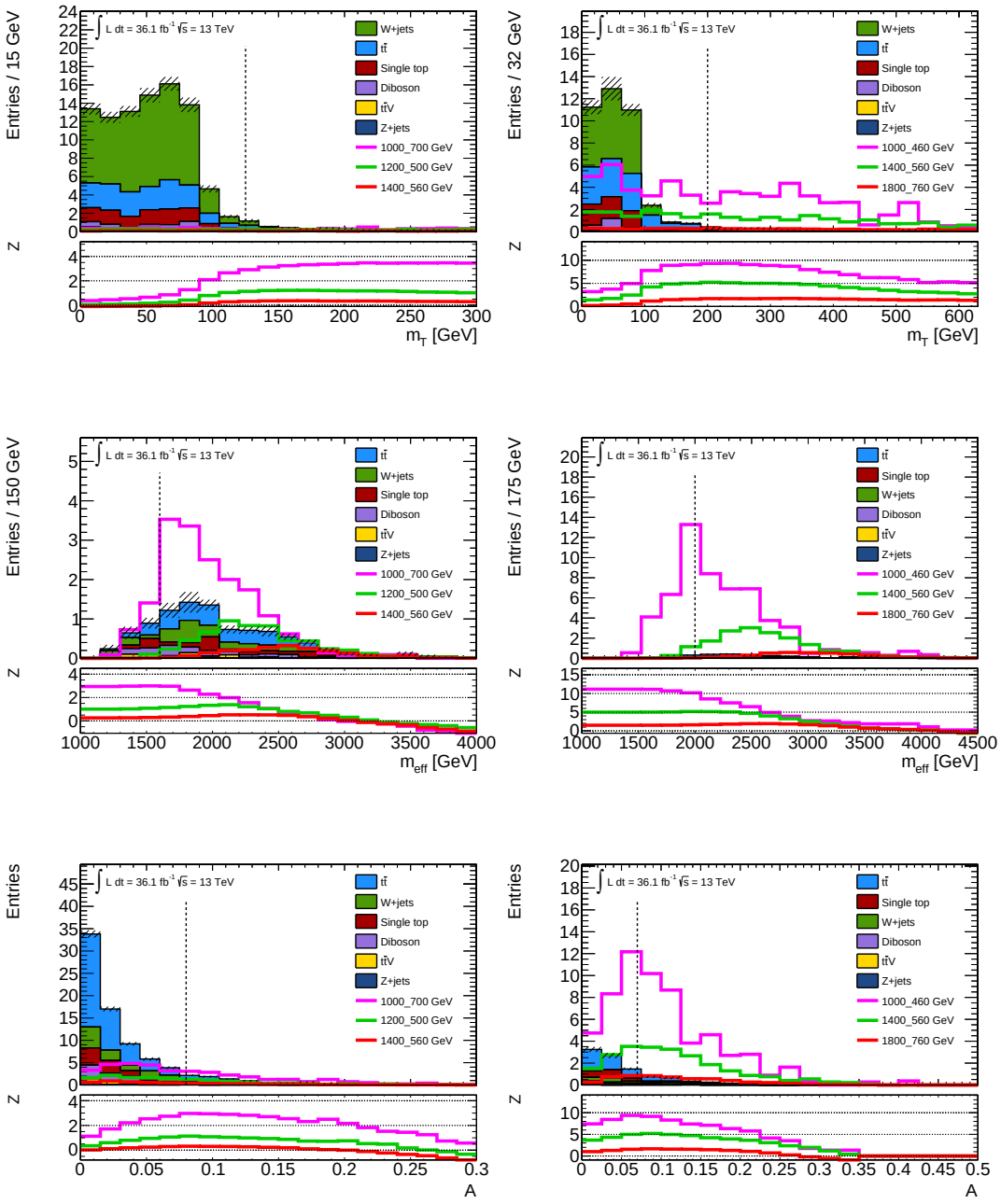

FIGURE 9.12: The N-1 plots for three representative signal points and all background processes as a function of m_T, m_{eff} and aplanarity after applying the SRI selection minus the plotted variable. The squark representative signal points are shown on the left side, while the gluino representative signal points are shown on the right side. All representative signal points are taken from the intermediate spectra. The bottom pad shows the expected significance.

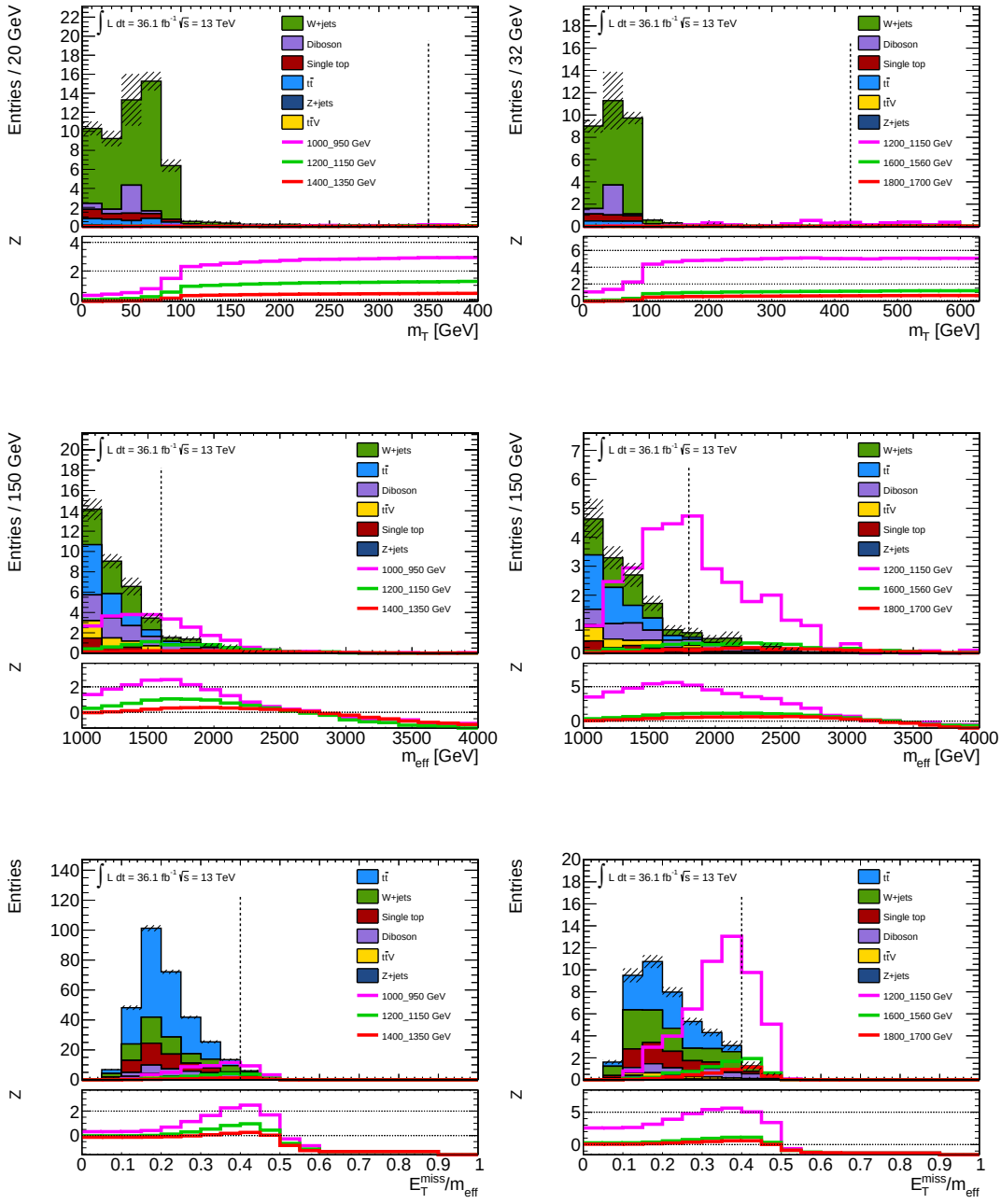

FIGURE 9.13: The N-1 plots for three representative signal points and all background processes as a function of m_T, m_{eff} and E_T^{miss}/m_{eff} after applying the SRB selection minus the plotted variable. The squark representative signal points are shown on the left side, while the gluino representative signal points are shown on the right side. All representative signal points are taken from the boosted spectra. The bottom pad shows the expected significance.

The 2 σ sensitivity projections obtained using the SR selections are shown in Figure 9.14 for the squark case and in Figure 9.15 for the gluino case. In the squark case, the SRB covers the middle part of the grid up to $m_{\tilde{q}}$ = 1200 GeV, the SRI shows the sensitivity for the signal points with $m_{\tilde{q}}$ from 800 GeV to 1100 GeV and the x values from 0.65 to 0.85. The last SRC does not show any sensitivity. In the gluino case, all three SRs cover the middle part of the grid up to $m_{\tilde{g}}$ = 1750 GeV.

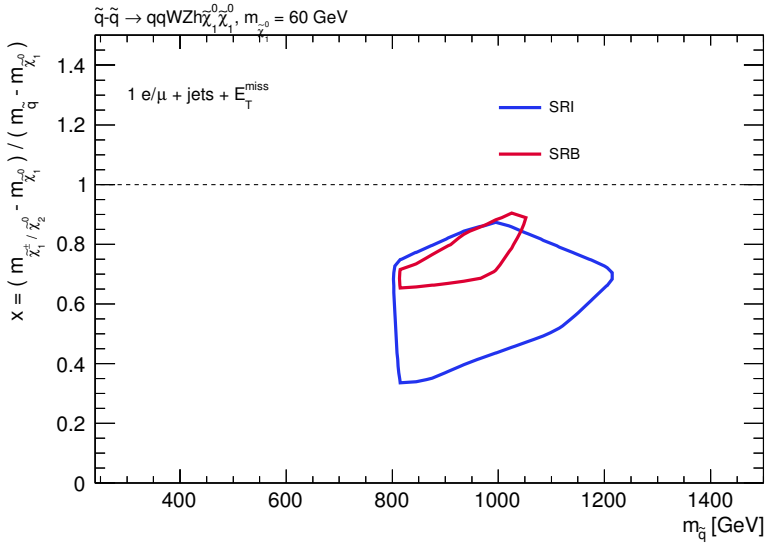

FIGURE 9.14: The sensitivity projection obtained by using the SR selections from Table 9.2 for the squark case.

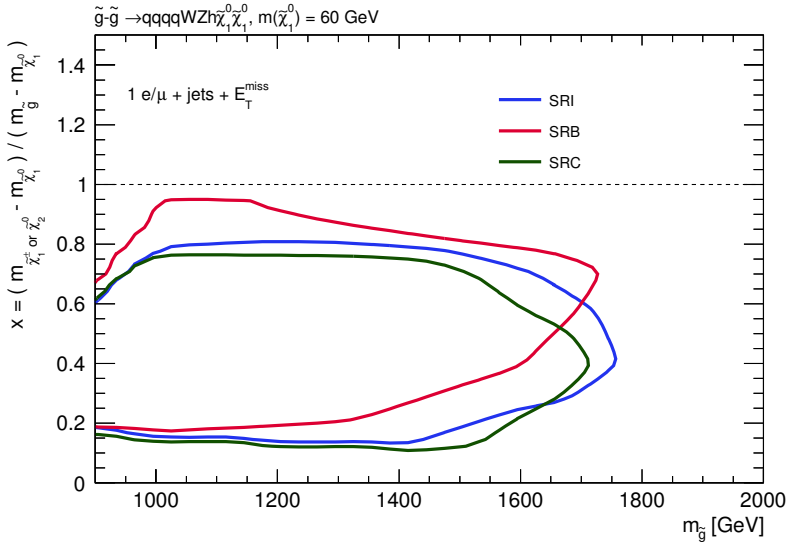

FIGURE 9.15: The sensitivity projection obtained by using the SR selections from Table 9.2 for the gluino case.

Due to the existence of the h boson, the WZh model was used to explore variables defined with the b-jets. Such variables are m_{bb} and m_{CT} introduced in Chapter 6. These two variables have been added to the optimization scan above and the significance have been calculated for the same representative signal points. However, the selections with the highest significance obtained from the optimization scan show a very low sensitivity. The variables defined with the b-jets are not useful for this model because many signal events contain exactly one or no b-jet. Figure 9.16 shows the signal events after requesting at least one baseline lepton and at least two baseline jets. On the X-axis are shown additional requirements.

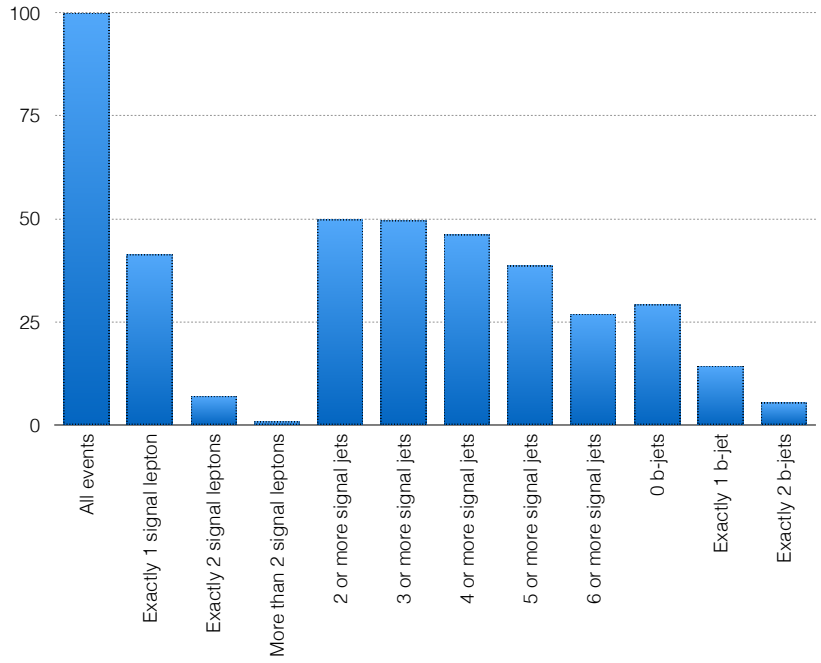

FIGURE 9.16: Number of the signal events with the different requirements.

9.5 Search for squarks and gluinos decaying to two W bosons

The search for squarks and gluinos decaying to two W bosons has been performed by the ATLAS collaboration using the data recorded during the LHC Run I [101] and II [95, 102]. This section presents the latest published analysis by the ATLAS experiment [95] with the purpose of testing it on the WZh model.

In the squark case, the squark decays to the lightest chargino and one SM quark $\tilde{q} \to q\tilde{\chi}_1^{\pm}$, then the chargino decays to the W boson and the LSP as

shown in Figure 9.17 (left). In the gluino case, the gluino decays to the lightest chargino and two SM quarks $\tilde{g} \to q\bar{q}\tilde{\chi}_1^{\pm}$. The decay chain of chargino is the same as in the squark case (Figure 9.17 right). The LSP is assumed to be the lightest neutralino.

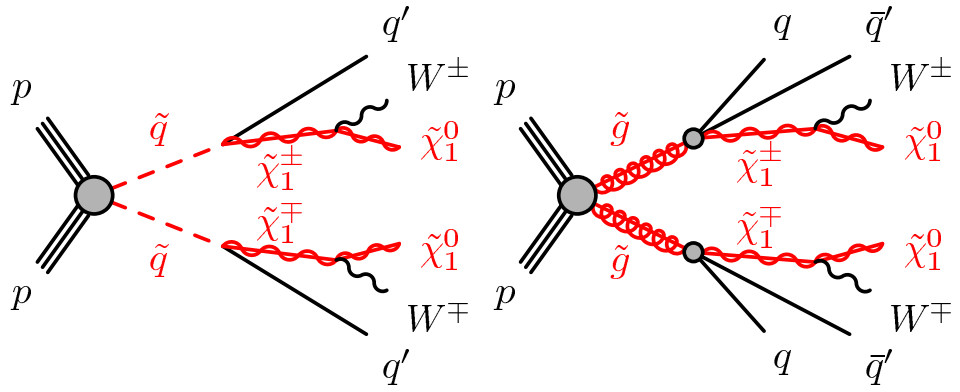

FIGURE 9.17: The decay chain of squarks (left) and gluinos (right) to W bosons [95].

In this model, one of the W boson decays to one lepton (electron or muon) and missing transverse momentum, while the second one decays hadronically. The final state consists of one lepton (electron or muon), several jets depending on the initial SUSY particles ($\tilde{q}/\tilde{g}$) and missing transverse momentum from neutrino(s) and neutralinos.

The search for squarks and gluinos decaying to two W bosons is performed using SUSY simplified models. In both cases, the masses of squarks (gluinos), the lightest chargino and the lightest neutralino are free parameters, while other sparticles which do not participate in the interactions are decoupled by setting them to high masses. Depending on the free parameters, two different model parameterizations are explored. Both models contain the variable x defined in Equation 9.1.

In the first model, the masses of squarks (gluinos) and the variable x are free parameters, while the mass of the lightest neutralino is set to be 60 GeV. In the second model, the masses of squarks (gluinos) and the lightest neutralino are free parameters, while the mass of the lightest chargino is set by fixing x to 0.5.

9.5.1 Analysis strategy

To cover as much parameter space as possible, the four SRs are designed using the variables defined in Chapter 6 [95]. They are marked as 2J, 4J low-x, 4J high-x and 6J according to the minimum number of jets required. The SRs are optimized by binning in b-veto/b-tag and m_{eff} in the model dependent signal fit, where a simultaneous fit is performed over 28 bins of all four SRs. The dominant SM backgrounds originate from top quark production ($t\bar{t}$ and single top) and W+jets production. These backgrounds are estimated in dedicated CRs. For each SR, two types of the CRs labeled TR for the top quark

background and WR for the W+jets background are designed in each bin of m_{eff}. The TR and WR have the same selection except the b-jet requirement. The TR requests at least one jet originating from a b quark, while the WR vetoes this type of jets. The extrapolation from the CRs to the SRs has been validated in dedicated VRs. They are designed to be kinematically close to the SR and use the same binning in m_{eff} as the SRs.

The 2J SR focuses on scenarios with small mass differences between $\tilde{q}(\tilde{g})$, $\tilde{\chi}_1^{\pm}$ and $\tilde{\chi}_1^0$, and a small p_T of the decay products. Selected events have one lepton (electron or muon) with a minimum p_T of 7 (6) GeV for the electron (muon) and at least two jets. The maximum p_T is determined as $p_T <$ minimum $(5 \cdot N_{jets}, 35)$ GeV. A schematic overview of the 2J SR together with all CRs and VRs is illustrated in Figure 9.18. The CRs (TR and WR) are designed by reverting the m_T and E_T criteria with respect to the SR selection. Two VRs labeled as VR m_T and VR E_T are defined by inverting either m_T or E_T.

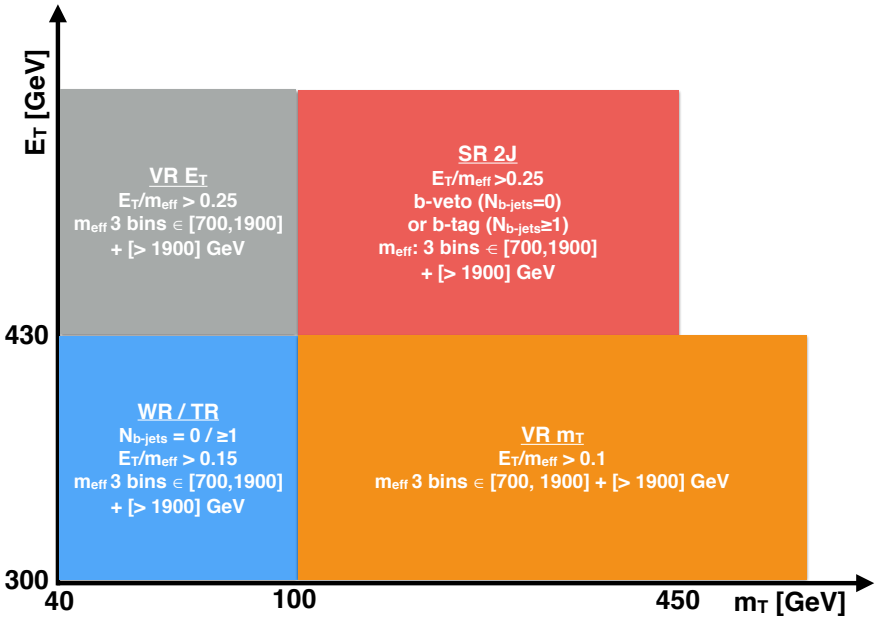

FIGURE 9.18: The definitions of the 2J SR, CRs and VRs. All selections include exactly one lepton (electron or muon) with a minimum p_T of 7 (6) for the electron (muon) and the maximum $p_T <$ minimum $(5 \cdot N_{jets}, 35)$ GeV, and at least two jets.

The 4J low-x SR is designed to cover scenarios with small differences between $m_{\tilde{\chi}_1^{\pm}}$ and $m_{\tilde{\chi}_1^0}$, and a fixed mass of the lightest neutralino at 60 GeV. Selected events have a high jet activity leading to higher m_{eff} and larger aplanarity. A schematic overview of the 4J low-x SR together with all CRs and VRs is shown in Figure 9.19. The CRs denoted by TR and WR are designed with respect to the SR selection and the b-jet requirement. Two VRs labeled as VR Aplanarity and VR Hybrid are defined by inverting either aplanarity or m_T.

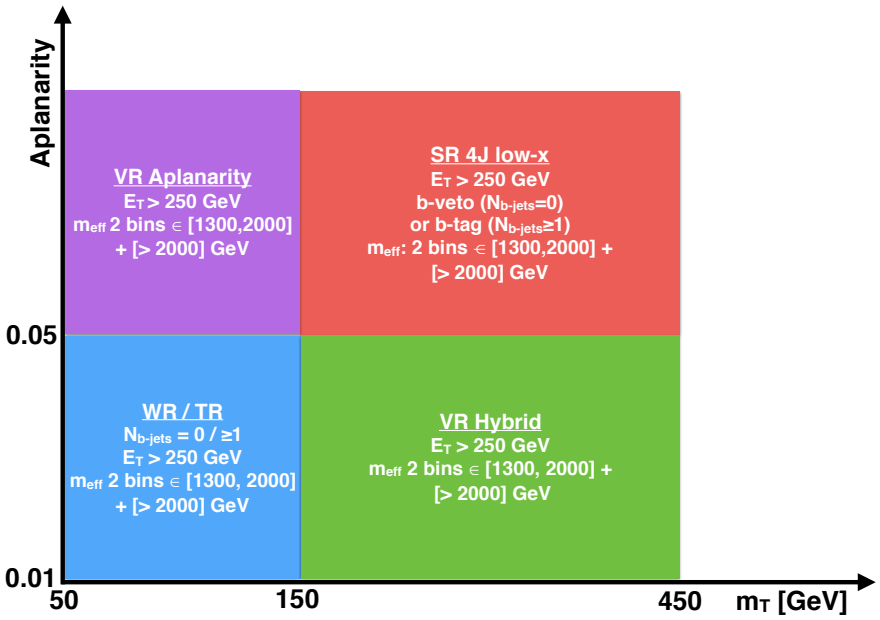

FIGURE 9.19: The definitions of the 4J low-x SR, CRs and VRs. All selections include events containing exactly one lepton (electron or muon) with the p_T of 35 GeV, and 4 or 5 jets.

The 4J high-x SR targets scenarios with small differences between $m_{\tilde{q}(\tilde{g})}$ and $m_{\tilde{\chi}_1^\pm}$, and a fixed mass of the lightest neutralino at 60 GeV. The small differences between $m_{\tilde{q}(\tilde{g})}$ and $m_{\tilde{\chi}_1^\pm}$ lead to significantly boosted W bosons which result in a high-p_T lepton and larger m_T. Figure 9.20 shows a schematic overview of the 4J high-x SR together with all CRs and VRs. Two CRs (TR and WR) and three VRs (VR Aplanarity, VR m_T and VR Hybrid) are designed by reverting aplanarity and/or m_T.

The 6J SR focuses on scenarios with large masses of sparticles. Selected events have exactly one high-p_T lepton (electron or muon) and six or more signal jets. The 6J strategy also includes two CRs (TR and WR) defined based on the b-jet requirement, and two VRs (VR Aplanarity and VR m_T) designed by inverting either aplanarity or m_T. Figure 9.21 shows a schematic overview of the 6J SR together with all CRs and VRs.

9.5.2 Results

The final results of the search for squarks $\tilde{q} \to qqW^\pm W^\pm \tilde{\chi}_1^0 \tilde{\chi}_1^0$ and for gluinos $\tilde{g} \to q\bar{q}qq\bar{W}^\pm W^\pm \tilde{\chi}_1^0 \tilde{\chi}_1^0$ are shown in Figures 9.22-9.25. The figures show the number of observed events in all SRs and VRs compared to the SM estimations. No significant excess of data over the SM estimation is found in any region.

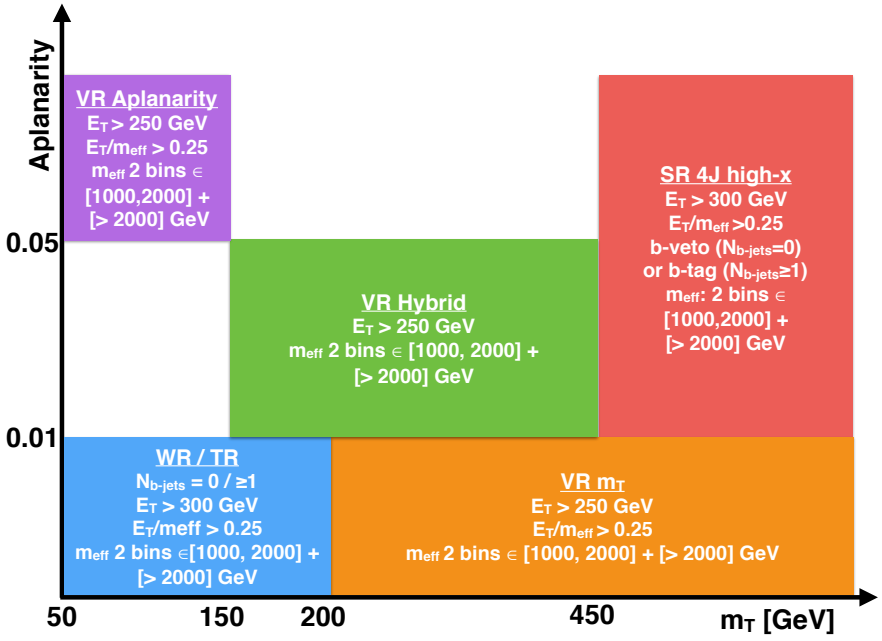

FIGURE 9.20: The definitions of the 4J high-x SR, CRs and VRs. All selections include exactly one lepton (electron or muon) with the p_T of 35 GeV, and 4 or 5 jets.

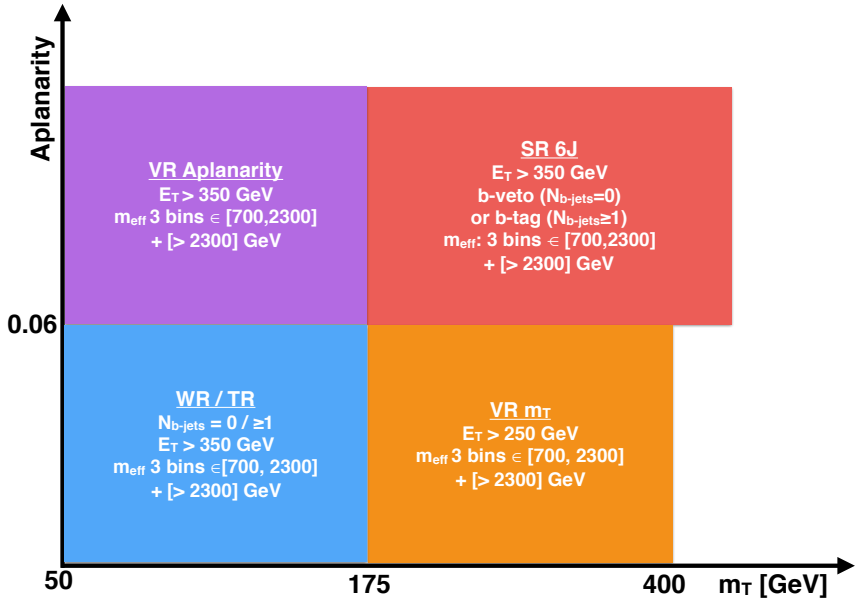

FIGURE 9.21: The definitions of the 6J SR, CRs and VRs. All selections include exactly one lepton (electron or muon) with the p_T of 35 GeV and at least 6 jets.

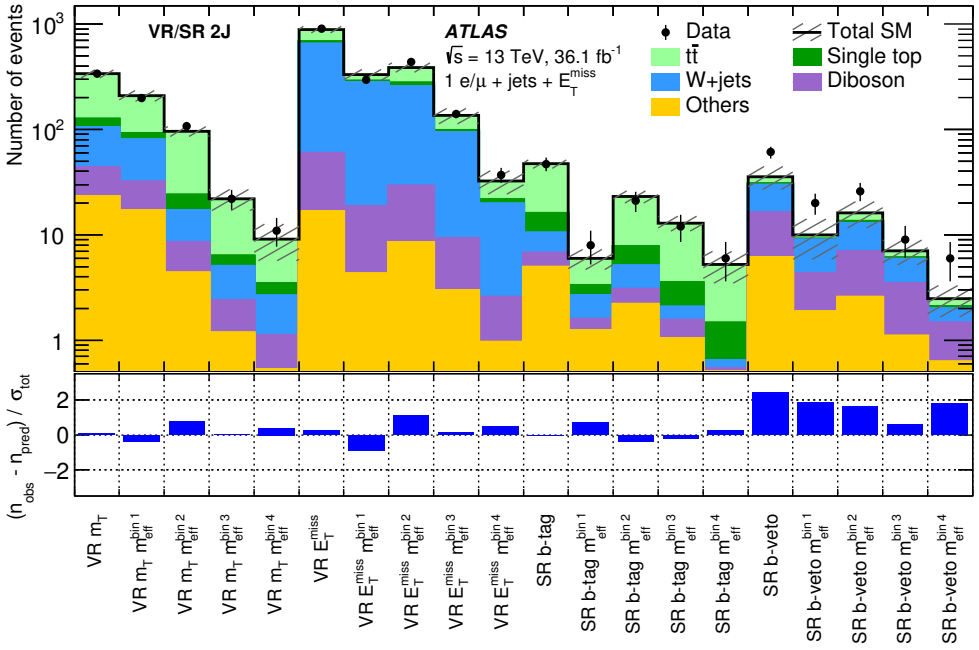

FIGURE 9.22: The observed and expected yields in the 2J SR and corresponding VRs [95].

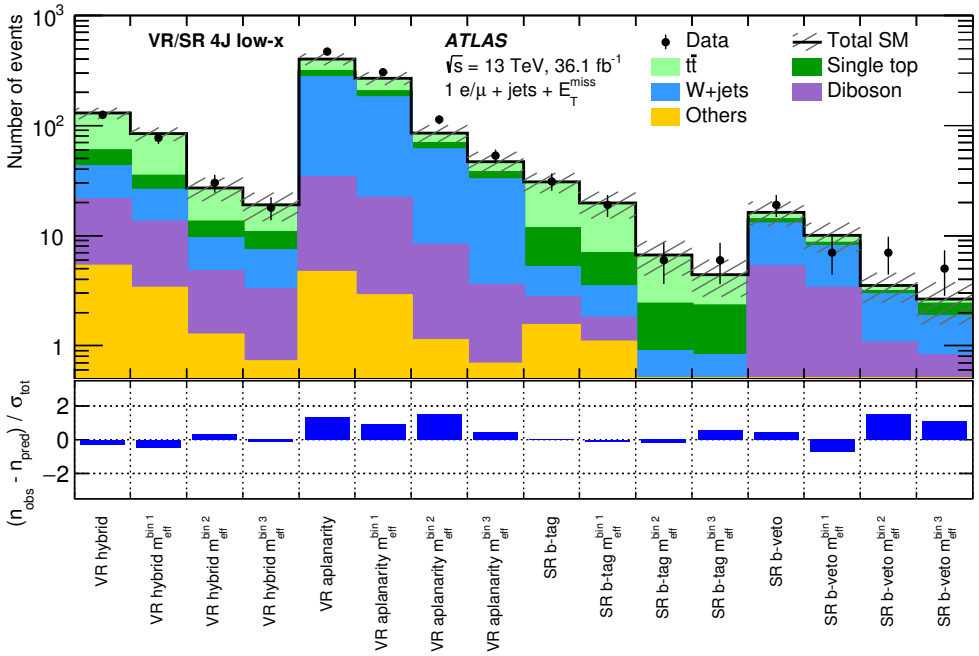

FIGURE 9.23: The observed and expected yields in the 4J low-x SR and corresponding VRs [95].

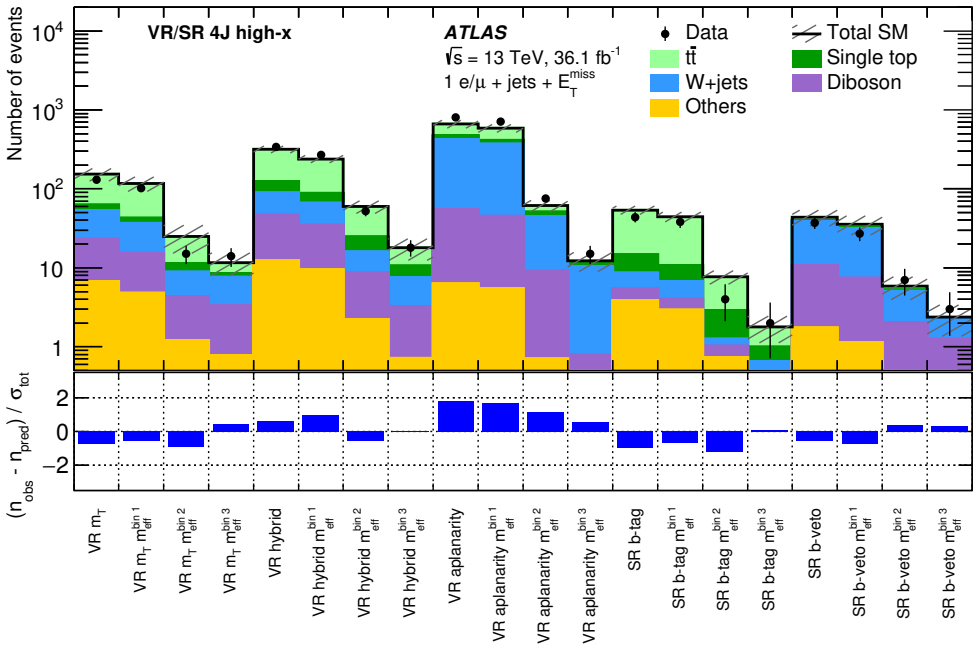

FIGURE 9.24: The observed and expected yields in the 4J high-x SR [95].

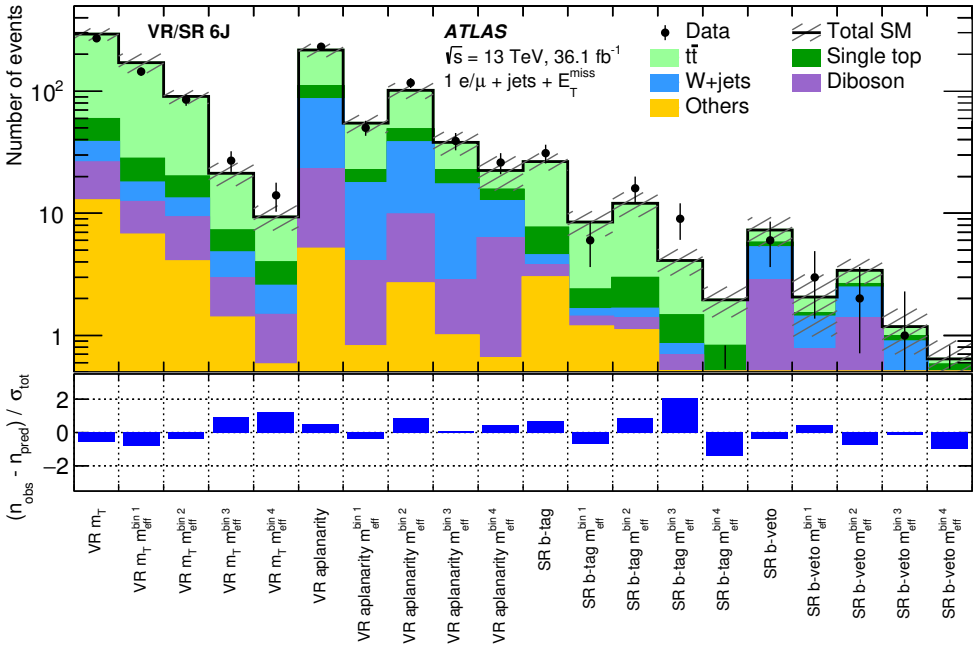

FIGURE 9.25: The observed and expected yields in the 6J SR [95].

9.5.3 Reinterpretation of the published analysis

The analysis strategy detailed in Section 9.5.1 is used for an exclusion limit interpretation on the $\tilde{q}\tilde{q} \rightarrow qqWZh\tilde{\chi}_1^0\tilde{\chi}_1^0$ and $\tilde{g}\tilde{g} \rightarrow q\bar{q}q\bar{q}WZh\tilde{\chi}_1^0\tilde{\chi}_1^0$ simplified models. The exclusion limits are derived using the model-dependent fit which is performed simultaneously in the CRs and SRs, taking into account all systematic uncertainties with their correlations. The results are shown in Figures 9.26 and 9.27 for $\tilde{q}\tilde{q}$ and $\tilde{g}\tilde{g}$ pair production, respectively. The 95% CL observed limits and the $\pm 1\sigma$ variation on this limit due to the theoretical signal production cross-section are shown as the red solid line and red dotted lines, respectively. The 95% CL expected limits and the $\pm 1\sigma$ variation on the limit are shown with a black dashed line and a yellow error band. Masses up to 1.3 TeV are excluded for squark pair production and up to 2 TeV for gluino pair production.

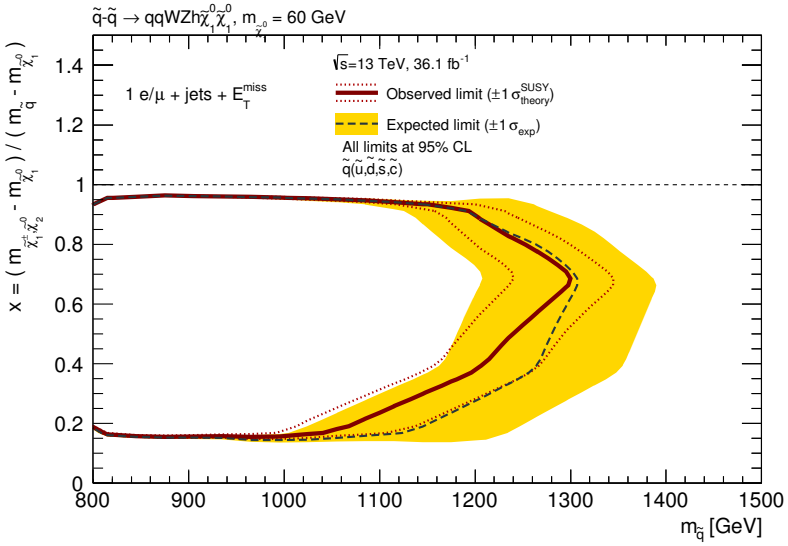

FIGURE 9.26: Exclusion limits for the $\tilde{q}\tilde{q} \rightarrow qqWZh\tilde{\chi}_1^0\tilde{\chi}_1^0$ simplified model. The observed limits and the $\pm 1\sigma$ variation on this limit are shown with the red solid line and red dotted lines, respectively. The expected limit and the $\pm 1\sigma$ variation are shown using the black dashed line with the yellow error band.

9.5.4 Comparison of strategies

The SR selections presented in Section 9.4 are optimized for discovery. These SRs have been chosen with respect to the highest significance for each representative signal point and they are not orthogonal.

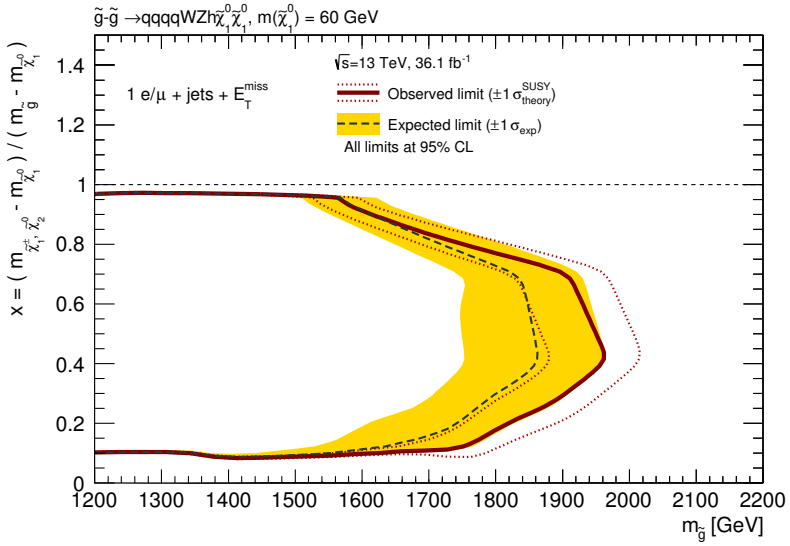

FIGURE 9.27: Exclusion limits for the $\tilde{g}\tilde{g} \rightarrow q\bar{q}q\bar{q}WZh\tilde{\chi}_1^0\tilde{\chi}_1^0$ simplified model. The observed limits and the $\pm$ 1σ variation on this limit are shown with the red solid and two red dotted lines, respectively. The expected limit and the $\pm$ 1σ variation are shown using the black dashed line with the yellow error band.

On the other hand, the SR selections presented in Section 9.5.1 are designed to provide the best exclusion limit and they are orthogonal[2].

9.6 Future prospects

During the LHC Run II, the LHC machine should deliver a luminosity of 150 fb^{-1} [103]. In the next period of the LHC running, known as the LHC Run III, additional 150 fb^{-1} are expected [103]. After the LHC Run III, a new project known as HL-LHC (High-Luminosity LHC) is planned to be active. The aim of this project is to improve the LHC performance in order to increase discovery potentials. The HL-LHC will try to provide a total integrated luminosity of 3000 fb^{-1} [103]. Figure 9.28 shows the LHC program until 2025 schematically.

The higher center-of-mass energy in the LHC Run II affects the productions of the SM particles with significant Lorenz boost and allows usage of the large-R jets introduced in Section 4.5. In order to maximize the sensitivity reach and cover a part of the parameter space in which the variable x is close to 1, the search for squarks and gluinos decaying to W/Z/h bosons has been also performed using the large-R jets. The mass of the large-R jets defined

[2]SRs can be optimized either for discovery or exclusion. If a SR is optimized for discovery it must have a high significance. On the other hand, if a SR is optimized for exclusion then the SR selection has higher signal acceptance but also more background events.

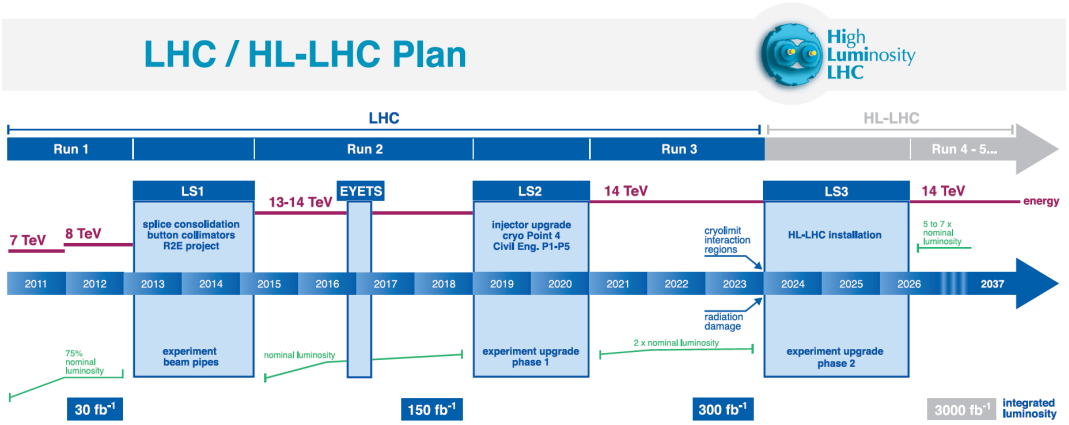

FIGURE 9.28: The LHC plan until 2025 with the centre-of-mass energy of collisions shown with red lines and an integrated luminosity shown in green lines [104].

in Equation 4.6 is added on the top of the optimization scan used in Section 9.4. The significance is calculated for each combination from the optimization scan using three representative signal points taken from the boosted spectra. The selections with the highest significance for both cases are taken as potential SR selections. These potential SR selections have been checked with the significance of N-1 plots. Figure 9.29 shows the N-1 plots of the main kinematic variables for the squark case (left) and the gluino case (right). The bottom pad shows the expected significance. The final SR selections are obtained by averaging the expected significance in the N-1 plots and are reported in Table 9.3.

Variable	SR - Squark	SR - Gluino
N_{jets}	3	4
E_T^{miss} [GeV]	250	250
m_T [GeV]	350	350
m_{eff} [GeV]	1600	2000
E_T^{miss}/m_{eff}	0.3	0.4
Aplanarity	0.01	0.01
M [GeV]	120	120

TABLE 9.3: The boosted SR selection for the squark pair production (the second column) and the gluino pair production (the third column).

Figure 9.30 (A and B) shows the sensitivity projection for the squark and gluino cases, respectively, obtained with the SR selection detailed in Table 9.3. The black line corresponds to the sensitivity of 2 σ. The SRs with the

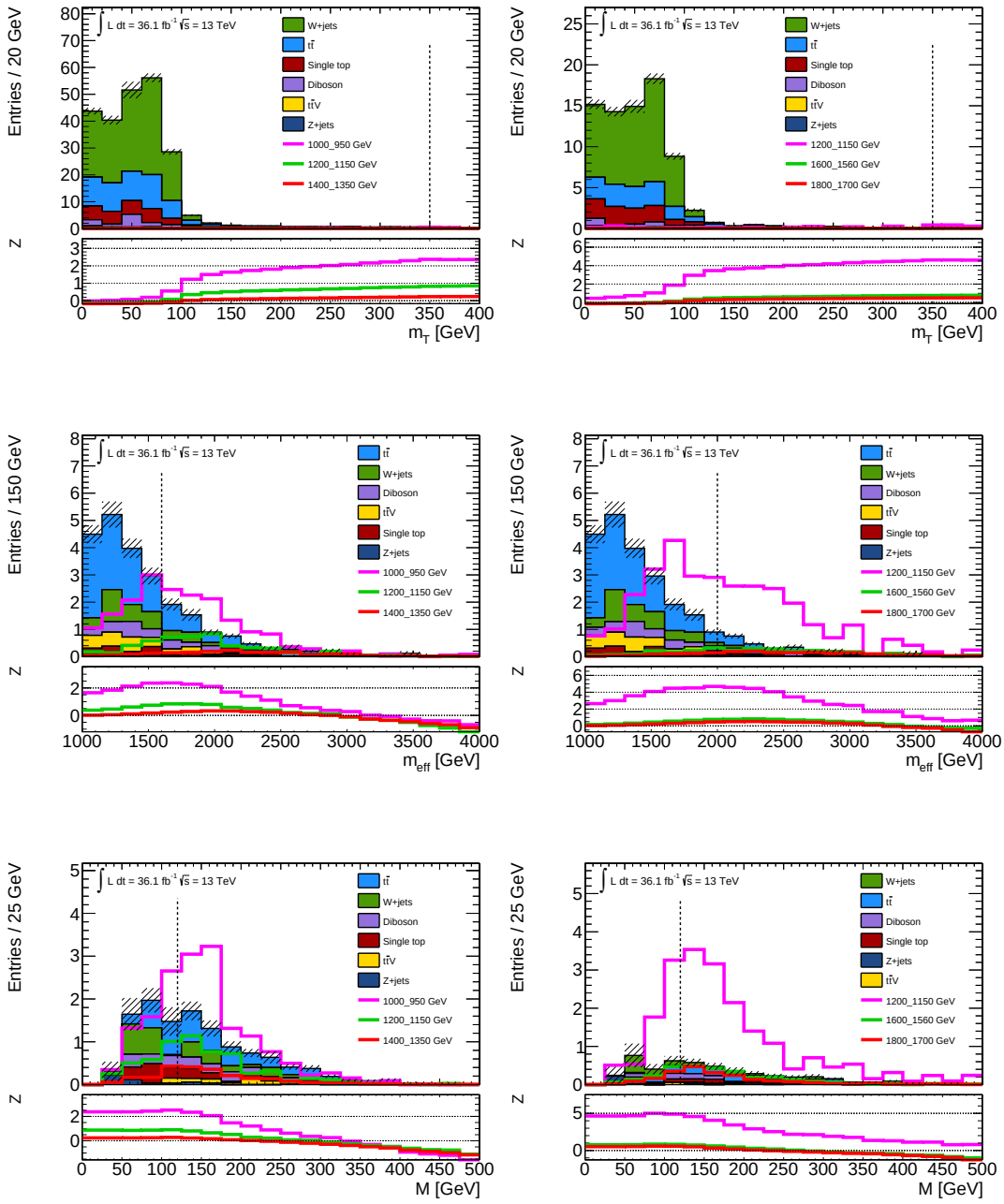

FIGURE 9.29: The N-1 plots for three representative signal points and all background processes as a function of m_T, m_{eff} and M (mass of the large-R jets) after applying the boosted SR selection minus the plotted variable. The squark representative signal points are shown on the left side, while the gluino representative signal points are shown on the right side. All representative signal points are taken from the boosted spectra. The bottom pad shows the expected significance.

large-R jets (the boosted SRs) cover the boosted part of parameter space with large mass splittings between $\tilde{\chi}_1^{\pm}/\tilde{\chi}_2^0$ and $\tilde{\chi}_1^0$ as expected.
In additional, the sensitivity projections for the integrated luminosities of 120 fb^{-1} (C and D) and 150 fb^{-1} (E and F) are reported for the squark (left) and gluino (right) pair production. As shown in the figure, the higher integrated luminosity in the LHC Run II will significantly extend the current sensitivity reach.

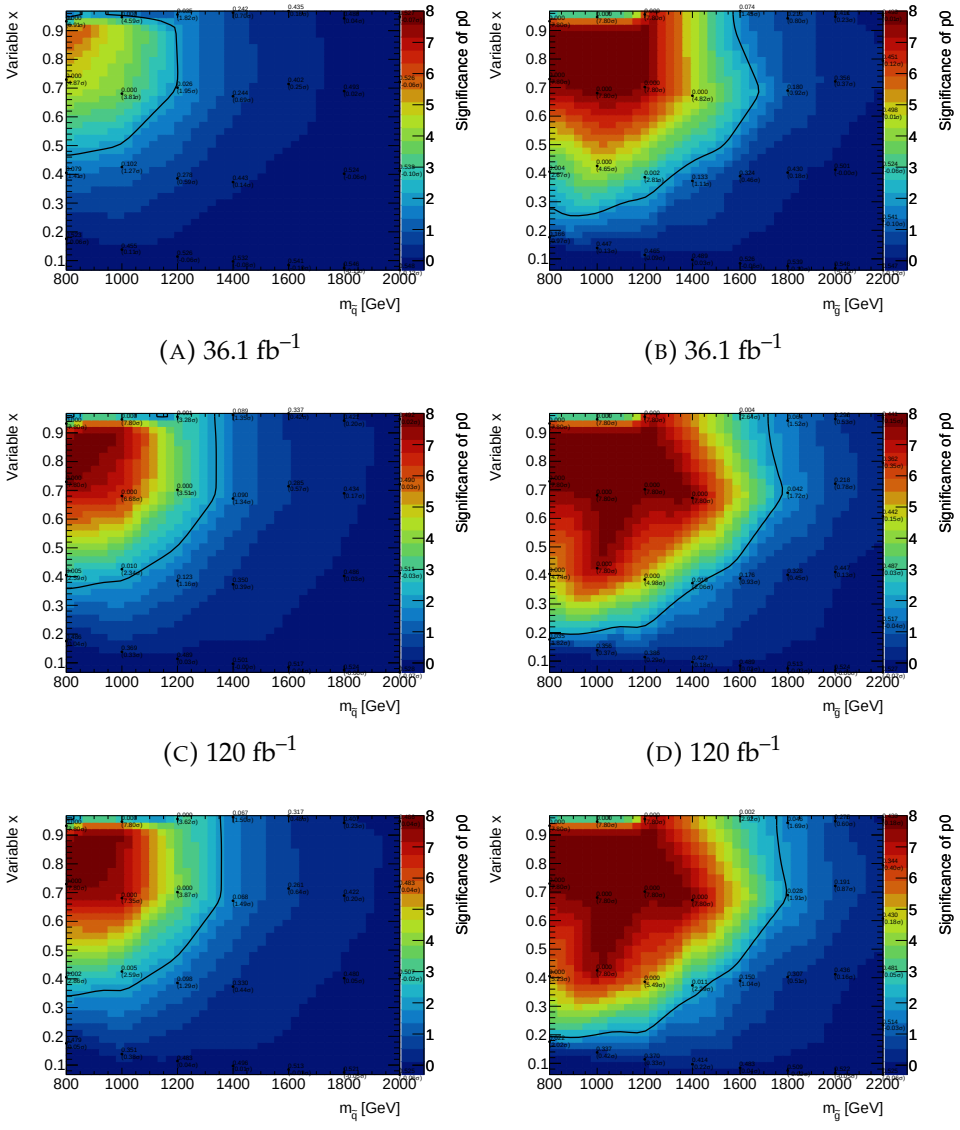

(A) 36.1 fb^{-1} (B) 36.1 fb^{-1}

(C) 120 fb^{-1} (D) 120 fb^{-1}

(E) 150 fb^{-1} (F) 150 fb^{-1}

FIGURE 9.30: The 2 σ sensitivity projections obtained using the boosted SR selection for the squark (left) and gluino (right) pair production.

Chapter 10

Search for charginos and neutralinos decaying to W and h bosons

This chapter presents the search for the lightest chargino $\tilde{\chi}_1^{\pm}$ and the next-to-lightest neutralino $\tilde{\chi}_2^0$ decaying via W and h bosons to final states with exactly one lepton, two b-jets and missing transverse momentum, described in Section 2.5.2. First, a motivation for this search with the result obtained during the LHC Run I is given. Afterwards, a common event selection including trigger studies is described. This is followed by a description of the full analysis strategy. Finally, the uncertainties on the measurement in data and MC are discussed, and the result of the analysis is shown.

10.1 Motivation

The same final state was explored with the dataset recorded by the ATLAS detector at the centre-of-mass energy of 8 TeV corresponding to the integrated luminosity of 20.3 fb^{-1} [105]. Since the observed events in data were found to be consistent in all SRs, the results were used to set exclusion limits on the masses of $\tilde{\chi}_1^{\pm}/\tilde{\chi}_2^0$. Figure 10.1 shows the 95% CL exclusion limits in the $m_{\tilde{\chi}_1^{\pm}/\tilde{\chi}_2^0} - m_{\tilde{\chi}_1^0}$ plane of the simplified model, where $m_{\tilde{\chi}_1^{\pm}/\tilde{\chi}_2^0}$ up to 150 GeV are excluded for $m_{\tilde{\chi}_1^0}$=0 GeV [105].

The production cross-section of $\tilde{\chi}_1^{\pm}/\tilde{\chi}_2^0$ is largely increased at the higher centre-of-mass energy of 13 TeV during the LHC Run II. Figure 10.2 compares the cross-sections at the centre-of-mass energy of 8 and of 13 TeV. For a $\tilde{\chi}_1^{\pm}/\tilde{\chi}_2^0$ with mass of 500 GeV, it increases by a factor of 8 from 5.7 fb^{-1} to 46.4 fb^{-1}.

As discussed above, the previous search was performed using 20.3 fb^{-1} of proton-proton collision. The larger integrated luminosity in 2015 and 2016 improves the signal sensitivity by a factor 1.8.

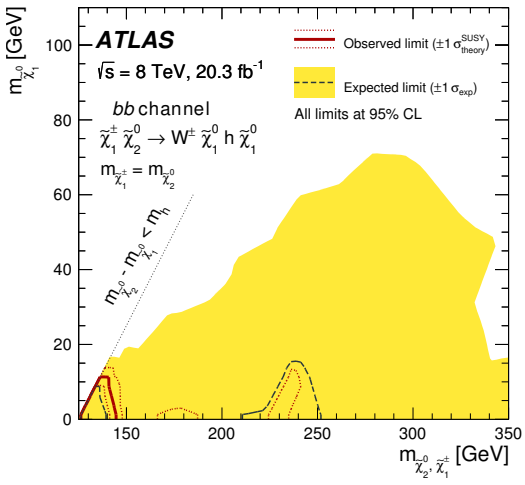

FIGURE 10.1: The red solid and blue dashed lines show the observed and expected 95% CL exclusion limits respectively, in the mass plane of $m_{\tilde{\chi}_1^\pm,\tilde{\chi}_2^0}$ vs. $m_{\tilde{\chi}_1^0}$ obtained in the LHC Run I [105].

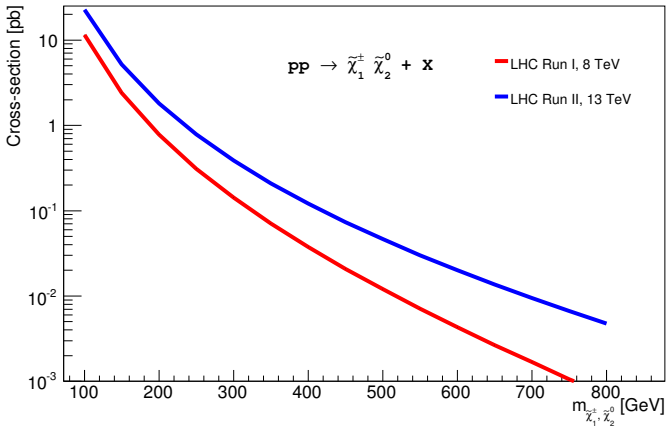

FIGURE 10.2: The cross-section comparison between the centre-of-mass energy of 8 and of 13 TeV for the production of $\tilde{\chi}_1^\pm/\tilde{\chi}_2^0$+X, where X indicates particles from ISR).

10.2 Dataset and Monte Carlo samples

This search uses the same dataset as the search for squarks and gluinos discussed in Chapter 9.
Signal events are generated using the MadGraph generator at the LO matrix element interfaced with Pythia in order to simulate the parton shower, the fragmentation and UEs.
Slepton, squarks and gluinos do not participate in the interactions and they are set to be very massive and decoupled. The masses of $\tilde{\chi}_1^\pm/\tilde{\chi}_2^0$ and $\tilde{\chi}_1^0$ are

only free parameters. Figure 10.3 shows the two-dimensional grid built by varying the masses of $\tilde{\chi}_1^{\pm}/\tilde{\chi}_2^0$ and $\tilde{\chi}_1^0$.

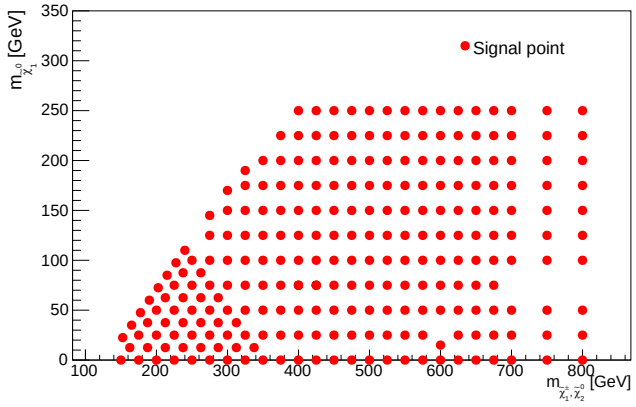

FIGURE 10.3: Two-dimensional signal grid in the $m_{\tilde{\chi}_1^{\pm},\tilde{\chi}_2^0}$-$m_{\tilde{\chi}_1^0}$ plane. Each red point shows one signal point.

10.3 Baseline selection

The baseline selection includes the same data quality checks as the previous search described in Section 9.3.1, a corresponding trigger selection and pre-selection criteria based on the signal topology. All of these criteria which significantly reduce the background events are described in this section.

10.3.1 Trigger strategy

The dataset used in this search is collected using the same missing transverse momentum (E_T^{miss}) triggers as the search for squarks and gluinos, listed in Table 9.1. The turn-on curves of the E_T^{miss} triggers have been extracted in the same way as for the previous search and are shown as a function of E_T^{miss} in Figure 10.4. A selection of exactly one lepton, two b-jets, two or three jets and m_T>100 GeV is applied before extracting the trigger efficiency. In order to better estimate the trigger efficiency, the last bin presents a range from 180 to 300 GeV. A starting point of 180 GeV has been taken due to the selection criteria on E_T^{miss} in VRs discussed in Section 10.6. The turn-on curves show that the triggers are not fully efficient at the plateau, especially in the muon channel. A correction factor for MC which corrects trigger efficiencies to data needs to be used. Studies to provide such a factor have been performed but due to very poor statistics the correction factor could not be determined. Instead, an uncertainty of 4% is applied to all events in order to account for small differences in the efficiency of E_T^{miss} triggers between data and MC observed in the figure.

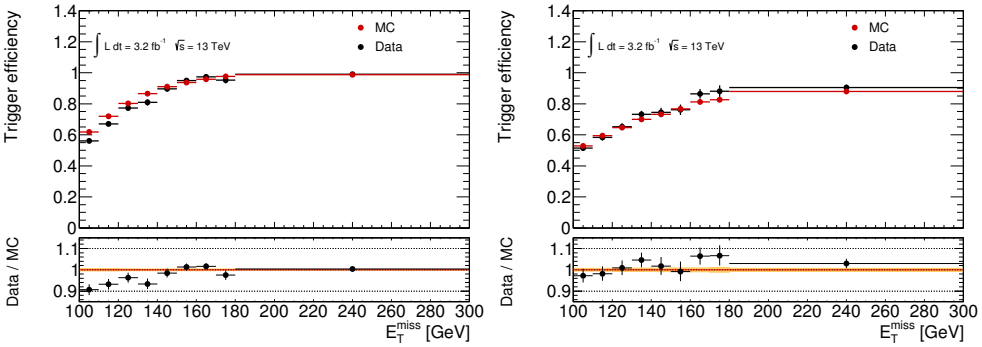

e channel, 70 GeV

μ channel, 70 GeV

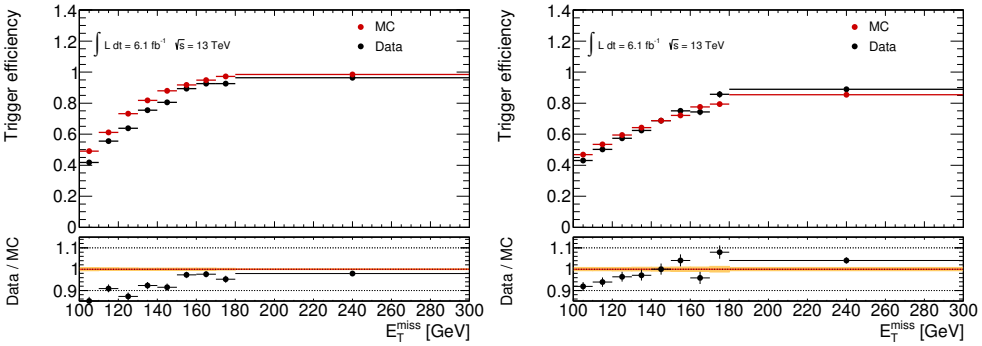

e channel, 90 GeV

μ channel, 90 GeV

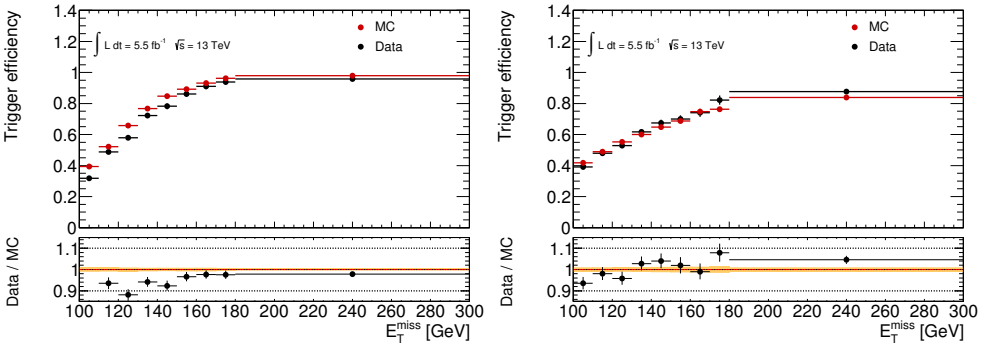

e channel, 100 GeV

μ channel, 100 GeV

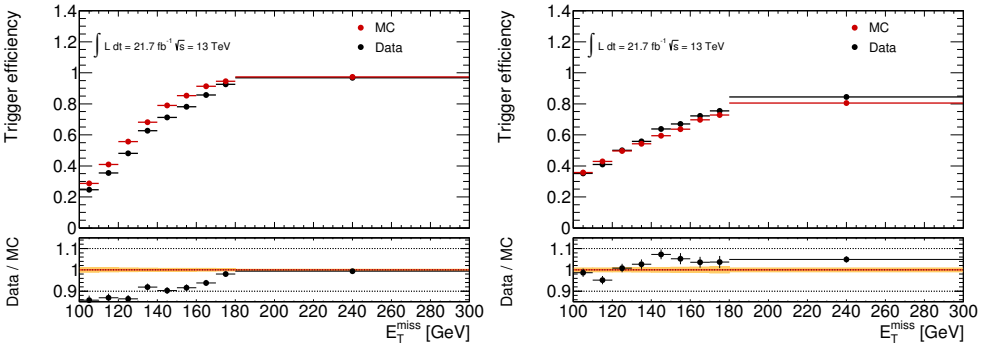

e channel, 110 GeV

μ channel, 110 GeV

FIGURE 10.4: Trigger efficiencies of data and MC simulated $t\bar{t}$ events as a function of E_T^{miss} plotted for the E_T^{miss} triggers listed in Table 9.1. The $t\bar{t}$ process is used because it is the dominant background in this search. The trigger efficiencies have been divided into the electron (left) and muon (right) channels.

10.3.2 Preselection criteria

The preselection criteria are applied to all events that pass the trigger requirements. The main aim of these criteria is to select typical events for the considered signal:

Lepton criterion, N_{lep}: the search for charginos and neutralinos requests either a signal electron or a signal muon in the final state. Events which contain a second lepton (electron or muon) are vetoed.

Criterion on the b-jet multiplicity, N_{b-jets}: as discussed in Section 2.5.2, this search only takes into account the $H \rightarrow b\bar{b}$ decay mode. According to this fact, any event accepted is required to contain exactly two jets originating from b quarks with $p_T > 25$ GeV each.

Criterion on the jet multiplicity, N_{jets}: this search requests two or three jets in the final state in order to account for possible jets in the signal events which could come from ISR and/or FSR processes. Figure 10.5 shows the number of jets after requesting exactly one lepton, where is evident that the request of two or three jets significantly reduces $t\bar{t}$ events.

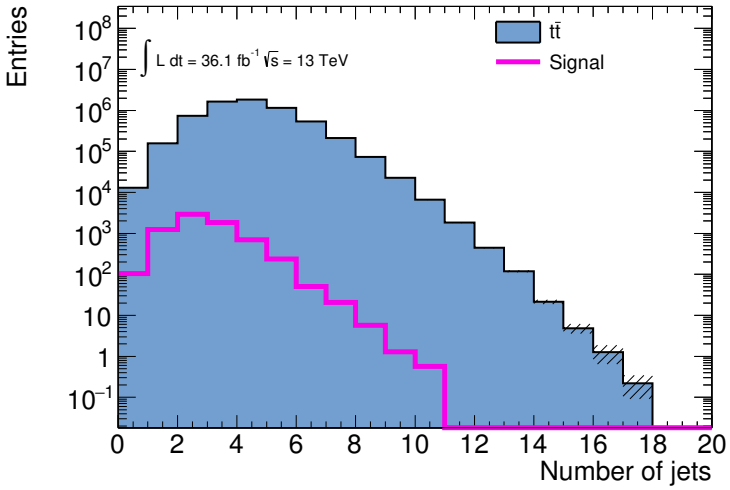

FIGURE 10.5: Number of jets in the signal and $t\bar{t}$ events after requesting exactly one lepton.

10.4 Signal region optimization

The signal region optimization is performed with the aim to provide a good coverage in the $m_{\tilde{\chi}_1^+,\tilde{\chi}_2^0}$ - $m_{\tilde{\chi}_1^0}$ parameter space. In order to cover as much parameter space as possible three SRs are designed as: SR low mass (SRLM), SR medium mass (SRMM) and SR high mass (SRHM). The SRLM is designed

to cover scenarios with small mass splittings between $\tilde{\chi}_1^{\pm}/\tilde{\chi}_2^0$ and $\tilde{\chi}_1^0$, while the SRHM targets large mass splittings between $\tilde{\chi}_1^{\pm}/\tilde{\chi}_2^0$ and $\tilde{\chi}_1^0$. The SRMM is introduced to be a compromise between these two approaches. A schematic overview of all three SRs is given in Figure 10.6.

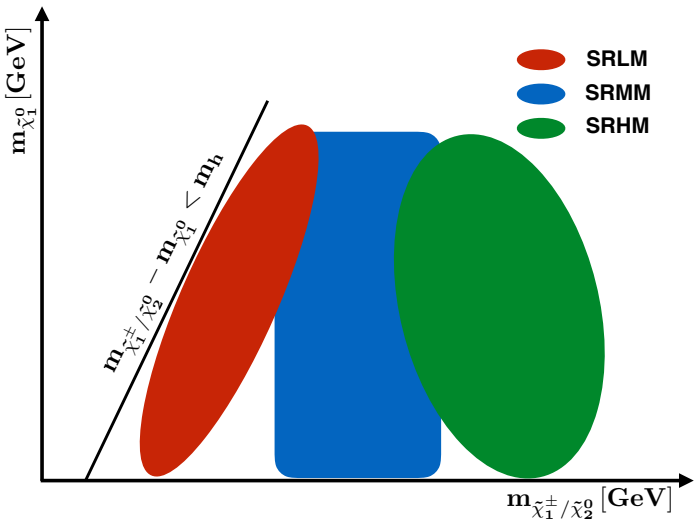

FIGURE 10.6: Schematic overview of all three SRs in the $m_{\tilde{\chi}_1^{\pm}/\tilde{\chi}_2^0}$-$m_{\tilde{\chi}_1^0}$ parameter space.

The optimization procedure follows all steps described in Section 7.1 and uses only the MC simulated events. A systematic uncertainty of 25% is taken as an estimate of systematic uncertainties on the total background. The variables used in the SR definition are m_{bb}, m_{CT}, m_T and E_T^{miss} described in Chapter 6.

Since $H \to b\bar{b}$ is a fully reconstructable resonance and manifests itself as a narrow peak in the m_{bb} distribution (see Section 6.2), m_{bb} is not included in the optimization scan. The shape of the signal peak is fitted by using a Crystal Ball function which consists of a Gaussian core portion and a power law tail defined as [106]:

$$f(x;\alpha,n,\bar{x},\sigma) = N\cdot\begin{cases} e^{-\frac{1}{2}\left(\frac{x-\bar{x}}{\sigma}\right)^2} & \text{for} \quad \frac{x-\bar{x}}{\sigma} > -\alpha \\ \left(\frac{n}{|\alpha|}\right)^n e^{-\frac{|\alpha|^2}{2}} \left(\frac{n}{|\alpha|} - |\alpha| - \frac{x-\bar{x}}{\sigma}\right)^{-n} & \text{for} \quad \frac{x-\bar{x}}{\sigma} \leq -\alpha \end{cases} \tag{10.1}$$

where x is a Higgs boson mass of 125 GeV, α and n are the power law parameters, $\bar{x}$ is the mean of the Gaussian core, σ is the standard deviation of the

Gaussian core and N is the normalization factor [107] defined as:

$$N^{-1} = \sigma \cdot \left[\frac{n}{|\alpha|} \frac{1}{n-1} \cdot e^{\left(-\frac{|\alpha|^2}{2}\right)} + \sqrt{\frac{\pi}{2}} \left(1 + e^{\left(\frac{|\alpha|}{\sqrt{2}}\right)}\right) \right] \tag{10.2}$$

The fit is performed for eight signal points taken from different parts of the parameter space. Figure 10.7 shows the results of the fit after applying the preselection criteria, $E_T^{miss} > 40$ GeV and $m_T > 40$ GeV. As indicated in Figure 10.7, the most probable value of 120 GeV with a width of 15 GeV has been found. This value indicates that the position of the signal peak in the m_{bb} spectrum is shifted by 5 GeV. There are two effects which can explain this shift. As already mentioned, the signal events could have two or three additional jets which could come from ISR and/or FSR processes. Since these jets are not included in the reconstruction of the Higgs resonance they can shift the peak downwards by a couple of percent. The second effect is related to a semi-leptonic decay of b-jet which results in one lepton and neutrino. The energies of the b-jet decay products are not included in the jet reconstruction and shift the peak towards lower values.
For the SR selections the signal peak with its width obtained from the fit is used (105 GeV - 135 GeV).

The m_{CT} variable has an endpoint around 136 GeV for $t\bar{t}$ events as discussed in Section 6.5. In order to suppress as many background events as possible and still keep a good statistics, a selection criterion of 160 GeV is applied in all SRs. The search is then performed for higher values of the m_{CT} distribution.

Since the selection criteria on m_{bb} and m_{CT} have been fixed due to the kinematics of the W and h bosons, the optimization scan runs only over different values of E_T^{miss} and of m_T.

The E_T^{miss} variable is particularly powerful in reducing the background events while keeping a good fraction of the signal events. Due to the presence of three undetected particles (one neutrino from a W boson and two $\tilde{\chi}_1^0$), the signal events have higher values of E_T^{miss} than the background events.

Figure 10.8 shows the m_T distributions for three representative signal points taken from different parts of the parameter space. Since the kinematics of these three signal points are different, this variable is used to design three SRs.

The results of the optimization scan including the preselection criteria, the fixed criteria on m_{bb} and m_{CT} are reported in Table 10.1.

In order to have the best significance, the criteria on m_T and E_T^{miss} obtained from the optimization scan have been cross-checked with the two-dimensional distributions of m_T vs. E_T^{miss} for all dominant backgrounds and five signal points, shown in Figure 10.9. Due to small mass splittings between $\tilde{\chi}_1^{\pm}/\tilde{\chi}_2^0$ and $\tilde{\chi}_1^0$, the m_T and E_T^{miss} distributions for these signal points are expected to be smaller than for the signal points with medium and large mass

splittings between $\tilde{\chi}_1^{\pm}/\tilde{\chi}_2^0$ and $\tilde{\chi}_1^0$ and therefore more similar to the background processes. On the other hand, the signal points with medium and large mass splittings between $\tilde{\chi}_1^{\pm}/\tilde{\chi}_2^0$ and $\tilde{\chi}_1^0$ have higher values of m_T and E_T^{miss} than the background events as shown in the figure.

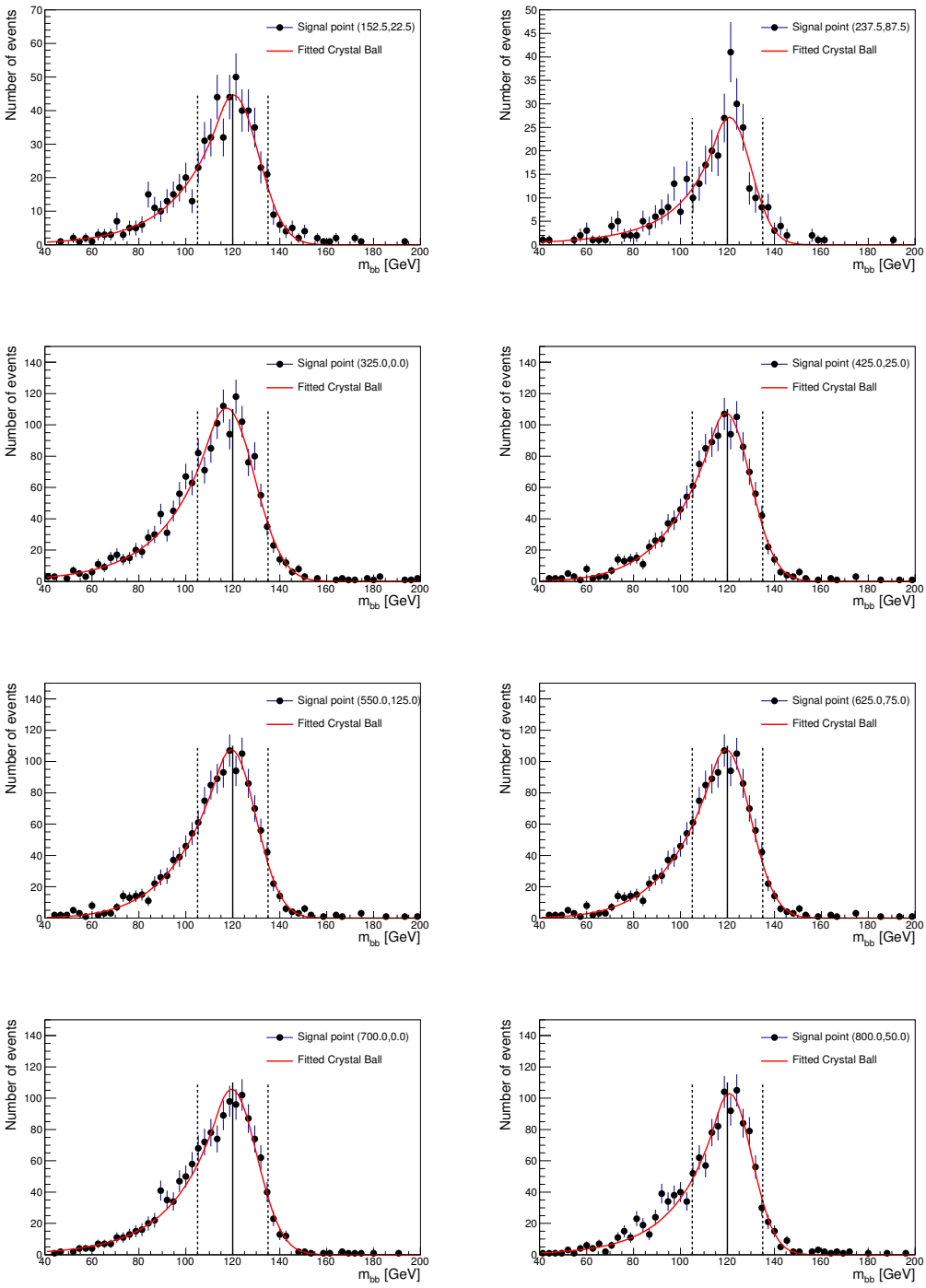

FIGURE 10.7: The shape of the signal peak (black dots) fitted with the Crystal Ball function (solid red line) in a region with the baseline criteria, E_T > 40 GeV and m_T >40 GeV.

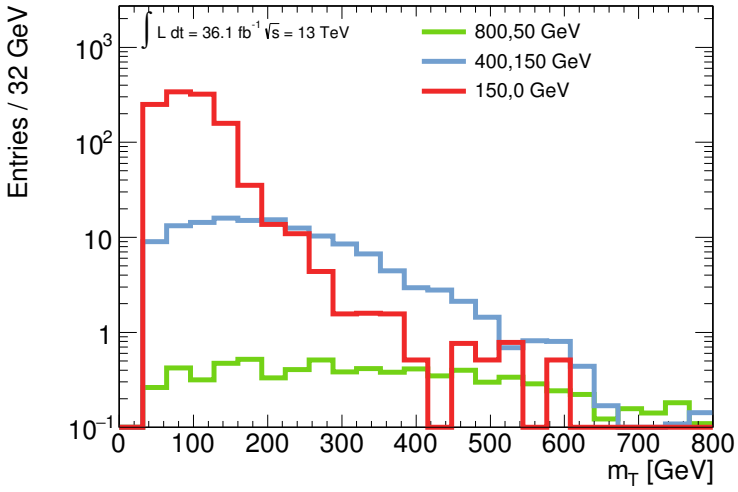

FIGURE 10.8: m_T distribution of three representative signal points with different mass splittings between $\tilde{\chi}_1^{\pm}/\tilde{\chi}_2^0$ and $\tilde{\chi}_1^0$.

Variable	**Preselection**		
N_{lep}	1		
$N_{b\text{–}jets}$	2		
N_{jets}	2 or 3		
	SRLM	**SRMM**	**SRHM**
m_{bb} [GeV]	[105 - 135]		
m_{CT} [GeV]	> 160		
m_T [GeV]	[100 - 140]	[140 - 200]	> 200
E_T^{miss} [GeV]	> 200		

TABLE 10.1: Summary of the SR definitions.

Figure 10.10 shows the two-dimensional distributions of m_T vs. E_T^{miss} for the dominant backgrounds and the same signal points as above after applying the preselection criteria, and the fixed criteria on m_{bb} and m_{CT}. The red lines correspond to the SR selections which drastically reduce the background events with minimal signal losses for the signal points with medium and large mass splittings between $\tilde{\chi}_1^{\pm}/\tilde{\chi}_2^0$ and $\tilde{\chi}_1^0$. Since the signal points with small splittings between $\tilde{\chi}_1^{\pm}/\tilde{\chi}_2^0$ and $\tilde{\chi}_1^0$ have similar m_T vs. E_T^{miss} distributions in comparison to the backgrounds, the lower criterion on m_T of 100 GeV is used in the SRLM to suppress the dominant backgrounds.

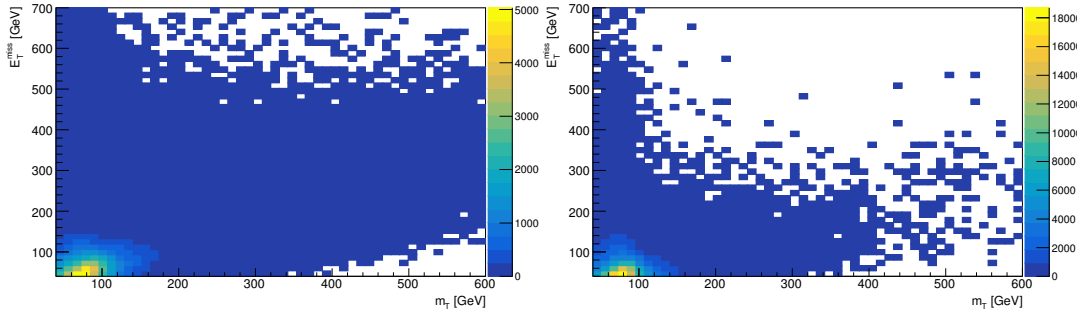

$t\bar{t}$ W+jets

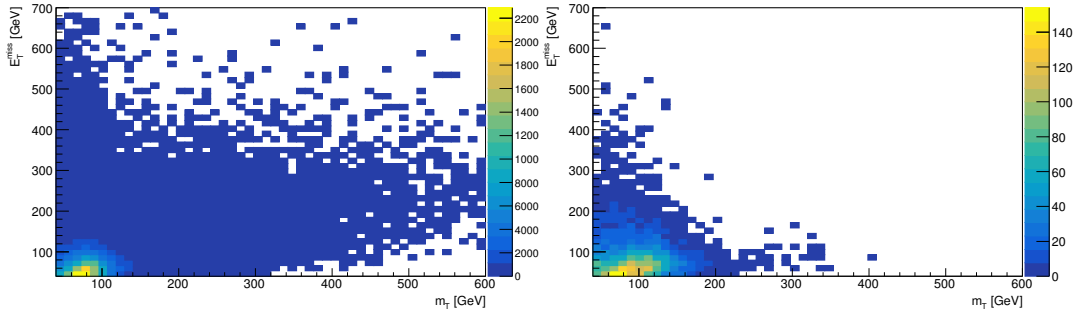

Single top Signal: 152; 22.5 GeV

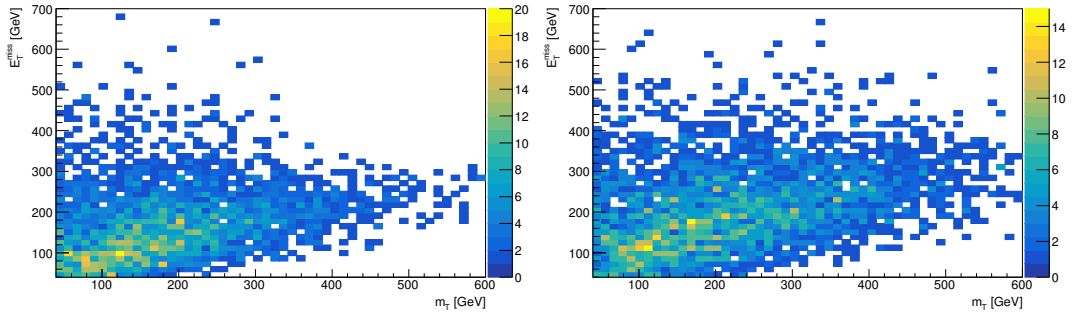

Signal: 325; 0 GeV Signal: 425; 25 GeV

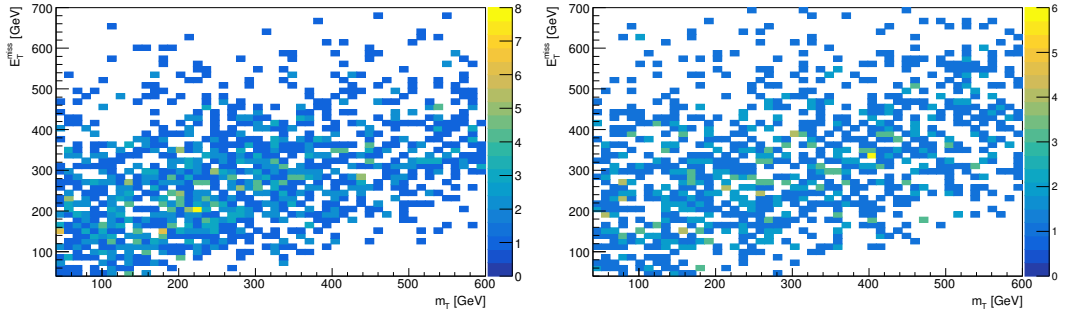

Signal: 625; 75 GeV Signal: 800; 50 GeV

FIGURE 10.9: Two-dimensional distributions of m_T and E_T^{miss} after applying the baseline criteria for all dominant backgrounds and five signal points.

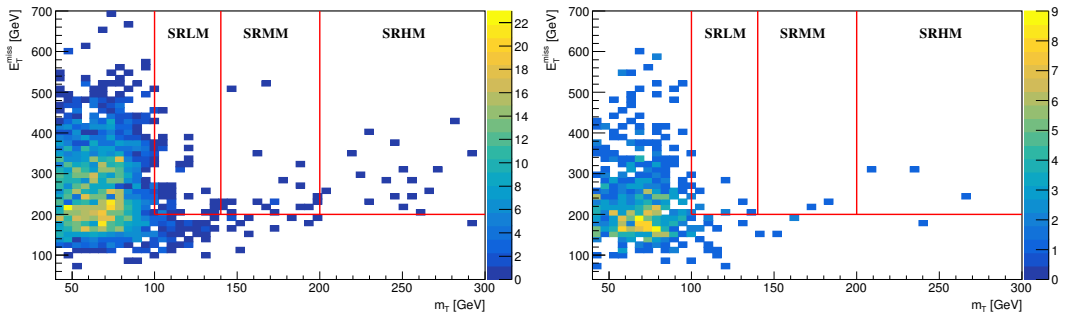

$t\bar{t}$ W+jets

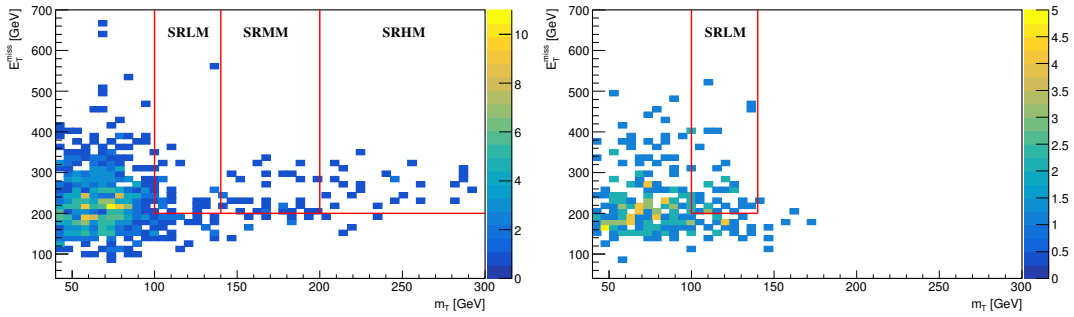

Single top Signal: 152; 22.5 GeV

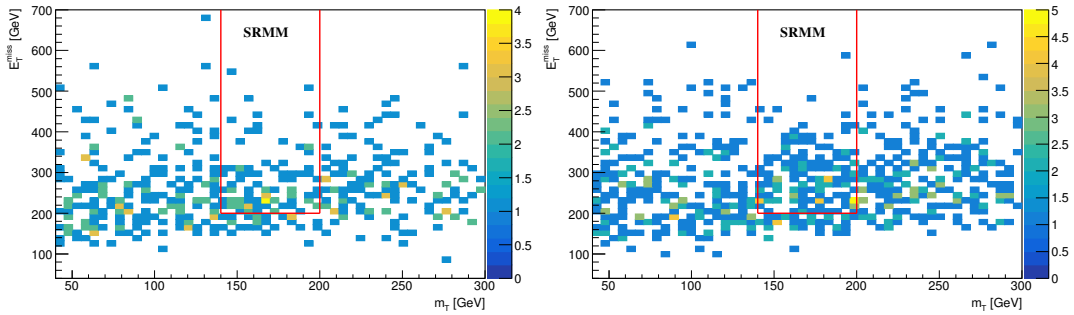

Signal: 325; 0 GeV Signal: 425; 25 GeV

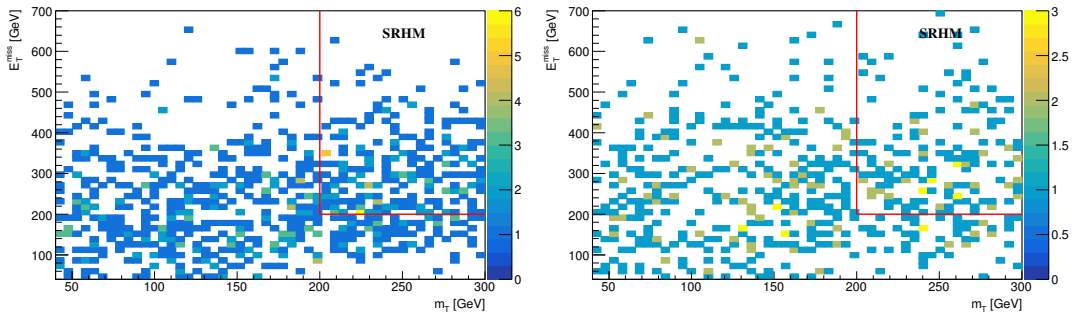

Signal: 625; 75 GeV Signal: 800; 50 GeV

FIGURE 10.10: Two-dimensional distributions of m_T and E_T^{miss} after applying the baseline criteria, $105 < m_{bb} < 135$ GeV and $m_{CT} > 160$ GeV for all dominant backgrounds and five signal points. The red lines correspond the SR selections.

The separation between the signal and background events has further been investigated with N-1 plots. These plots show the key kinematic variables for three signal points and all background processes after applying all selection criteria minus the plotted quantity as shown in Figures 10.11 to 10.13. The bottom pad shows the expected significance. Since the m_{bb} and m_{CT} variables have not been optimized in the optimization scan, the conclusion on some optimized criteria may slightly differ from Table 10.1.

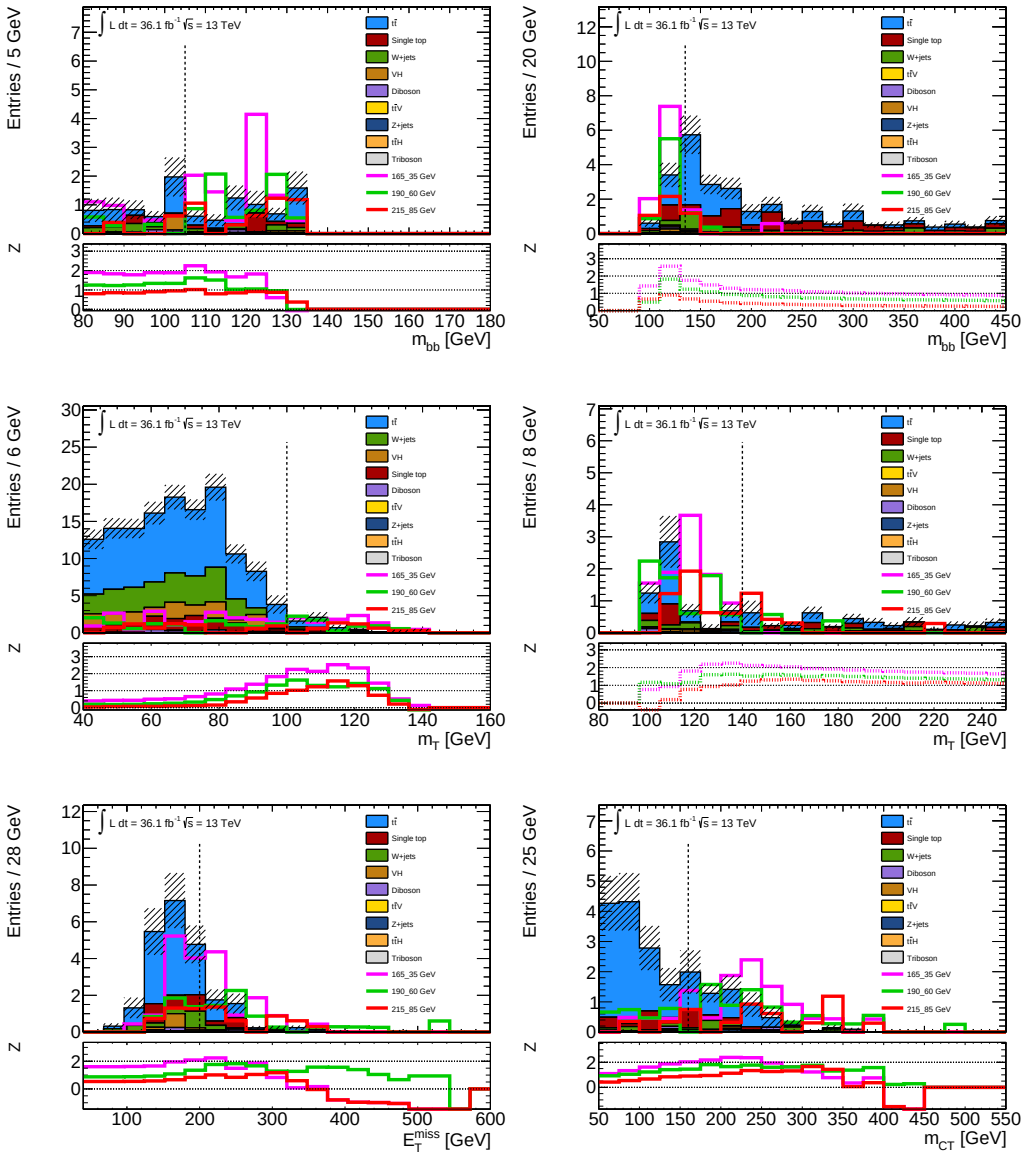

FIGURE 10.11: The N-1 plots for three signal points and all background processes after applying the SRLM selection minus the plotted variable. The signal points are taken from the parameter space with small mass splittings between $\tilde{\chi}_1^{\pm}/\tilde{\chi}_2^0$ and $\tilde{\chi}_1^0$. The bottom pad shows the expected significance.

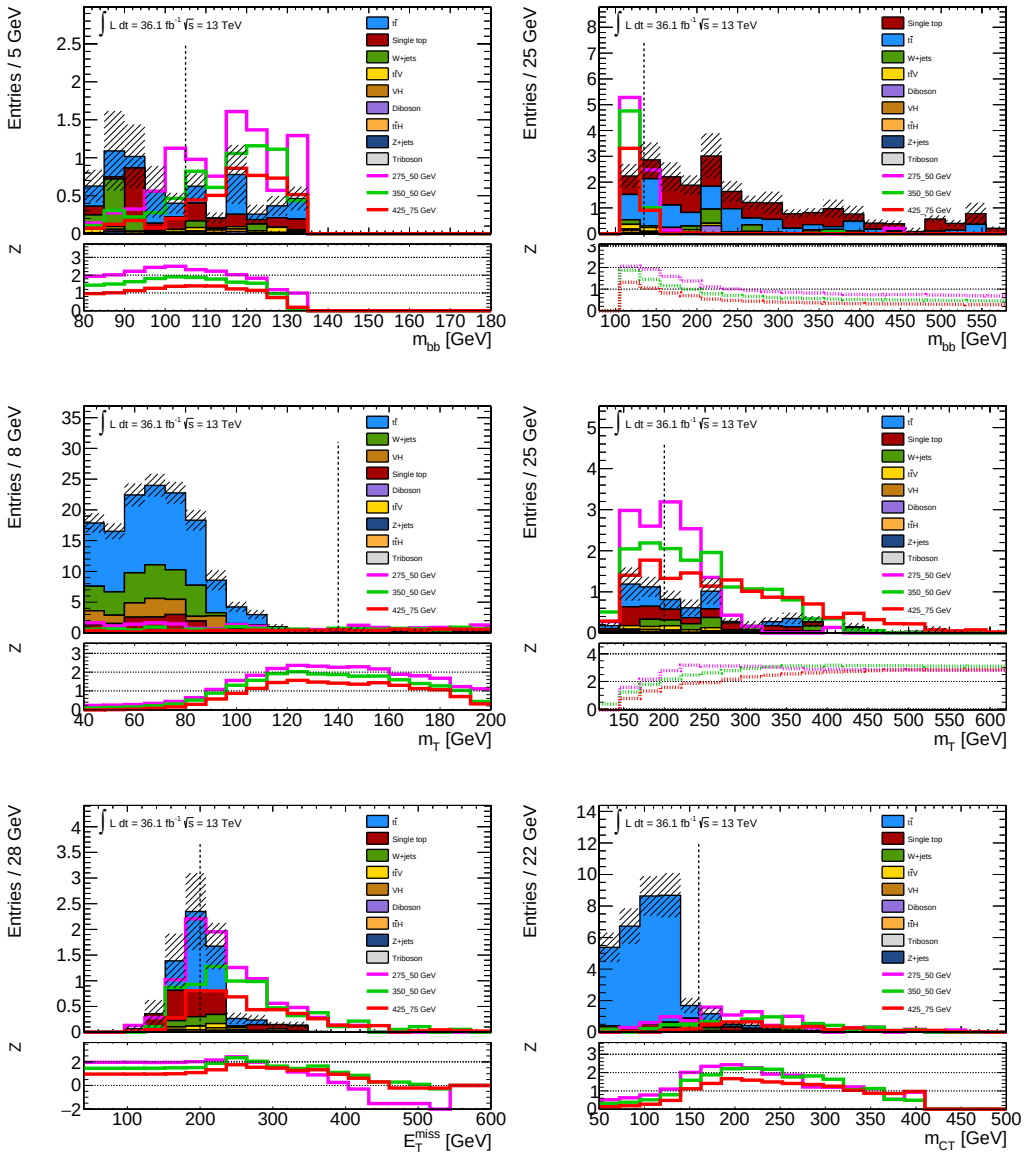

FIGURE 10.12: The N-1 plots for three signal points and all background processes after applying the SRMM selection minus the plotted variable. The signal points are taken from the middle part of the $m_{\tilde{\chi}_1^\pm/\tilde{\chi}_2^0}$ - $m_{\tilde{\chi}_1^0}$ parameter space. The bottom pad shows the expected significance.

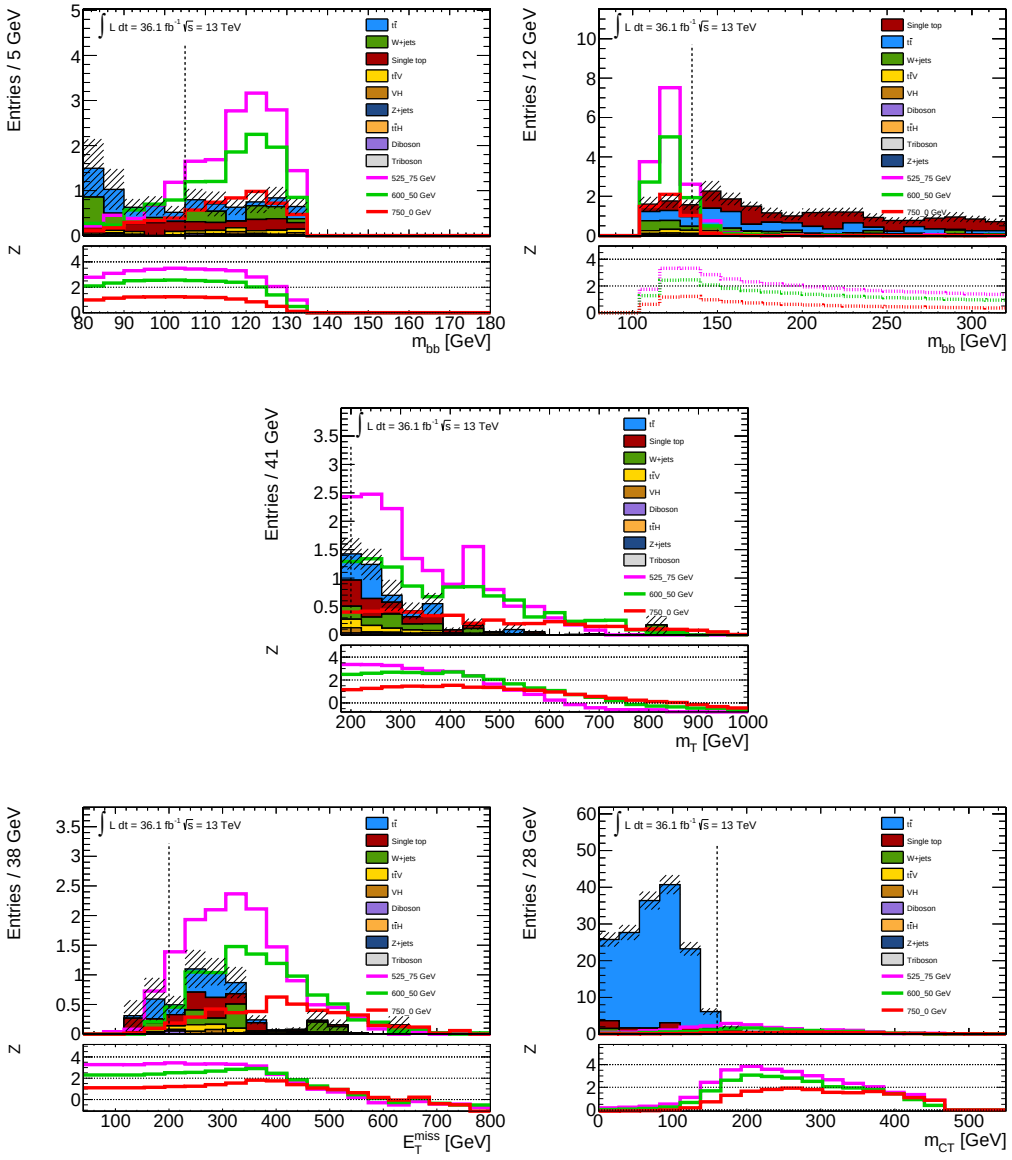

FIGURE 10.13: The N-1 plots for three signal points and all background processes after applying the SRHM selection minus the plotted variable. The signal points are taken from the parameter space with large mass splittings between $\tilde{\chi}_1^{\pm}/\tilde{\chi}_2^0$ and $\tilde{\chi}_1^0$. The bottom pad shows the expected significance.

The 2 σ sensitivity projections obtained using the SR selections detailed in Table 10.1 for each SR are shown in Figure 10.14. The good sensitivity reach is found in the $m_{\tilde{\chi}_1^\pm/\tilde{\chi}_2^0}$ - $m_{\tilde{\chi}_1^0}$ parameter space with middle and large mass splittings between $\tilde{\chi}_1^\pm/\tilde{\chi}_2^0$ and $\tilde{\chi}_1^0$. The lower sensitivity is observed in the $m_{\tilde{\chi}_1^\pm/\tilde{\chi}_2^0}$ - $m_{\tilde{\chi}_1^0}$ parameter space with small mass splittings between $\tilde{\chi}_1^\pm/\tilde{\chi}_2^0$ and $\tilde{\chi}_1^0$ as expected due to the similar kinematics between the signal and background events.

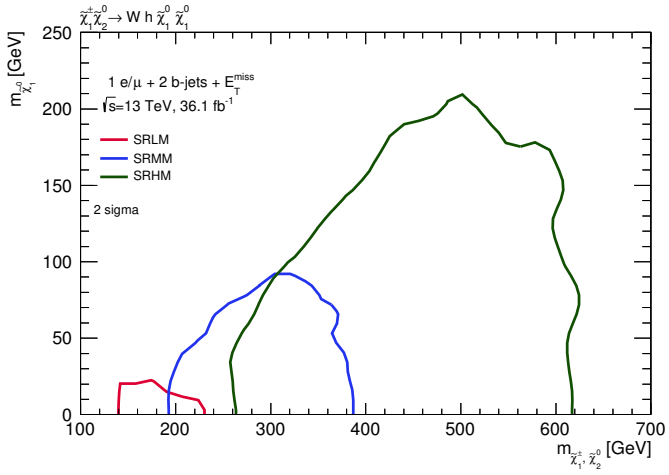

FIGURE 10.14: Sensitivity projection obtained using all three SR definitions.

The SRs are designed to be orthogonal to each other and can be combined. Figure 10.15 shows the 2 σ sensitivity projection obtained combining all three SRs.

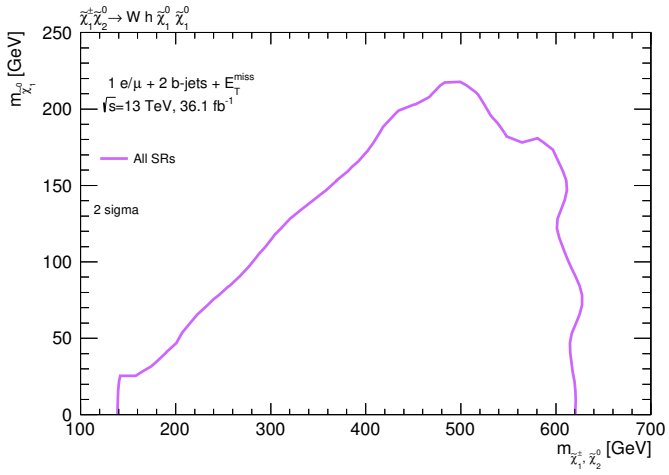

FIGURE 10.15: Sensitivity projection obtained combining all three SRs.

10.5 Background estimation

As discussed, the dominant background contributions in the SRs are due to $t\bar{t}$, W+jets and single top production. Three CRs enriched in $t\bar{t}$ events (TCRLM, TCRMM and TCRHM) have been designed to be kinematically close and at the same time statistically independent to the SRs. The orthogonality is ensured by reverting the selection on m_{CT} ($m_{CT} < 160$ GeV) and m_{bb} ($50 =< m_{bb} <= 105$ GeV or $m_{bb} >= 135$ GeV). The selection criteria on m_T and E_T^{miss} are the same as in the SR selections. The composition of the TCRLM, TCRMM and TCRHM is shown respectively in Figure 10.16, for all backgrounds. The dominant backgrounds are shown separately, while the smaller background processes are grouped into one category and are shown as "Others". The contribution of the $t\bar{t}$ background is about 82% in the TCRLM, 91% in the TCRMM and 93% in the TCRHM.

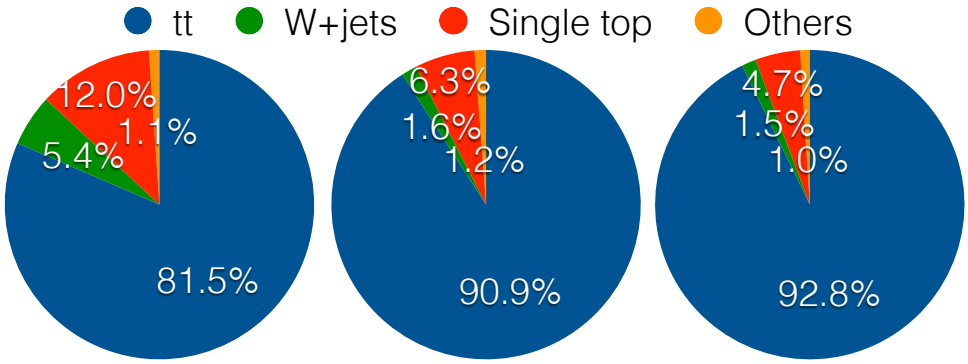

FIGURE 10.16: Composition of the TCRLM (left), TCRMM (middle) and TCRHM (top). The dominant background processes are shown separately, while the smaller background processes are grouped into one category and shown as "Others".

The signal contamination is found to be below 5% in all three TCRs as shown in Figure 10.17.

Figures 10.18 to 10.20 show the main kinematic distributions of data with black dots and the MC background processes with colored stacks in the TCRLM, TCRMM and TCRHM, respectively. The middle pad shows data/MC comparisons and the bottom pad shows contributions of each background. The dominant backgrounds are normalized to data using the normalization factors listed in Table 10.5 and only statistical uncertainties are considered. A reasonable agreement is found within the statistical uncertainties.

A region enriched in W+jets events named WCT has been designed with $m_T < 100$ GeV and $m_{bb} < 80$ GeV due to kinematics of the W boson. The selection on m_{bb} has been chosen to maximise the purity of the W+jets events, but retains enough statistics to study the background modelling. The selection criteria on m_{CT} and E_T^{miss} are the same as in the SR selections.

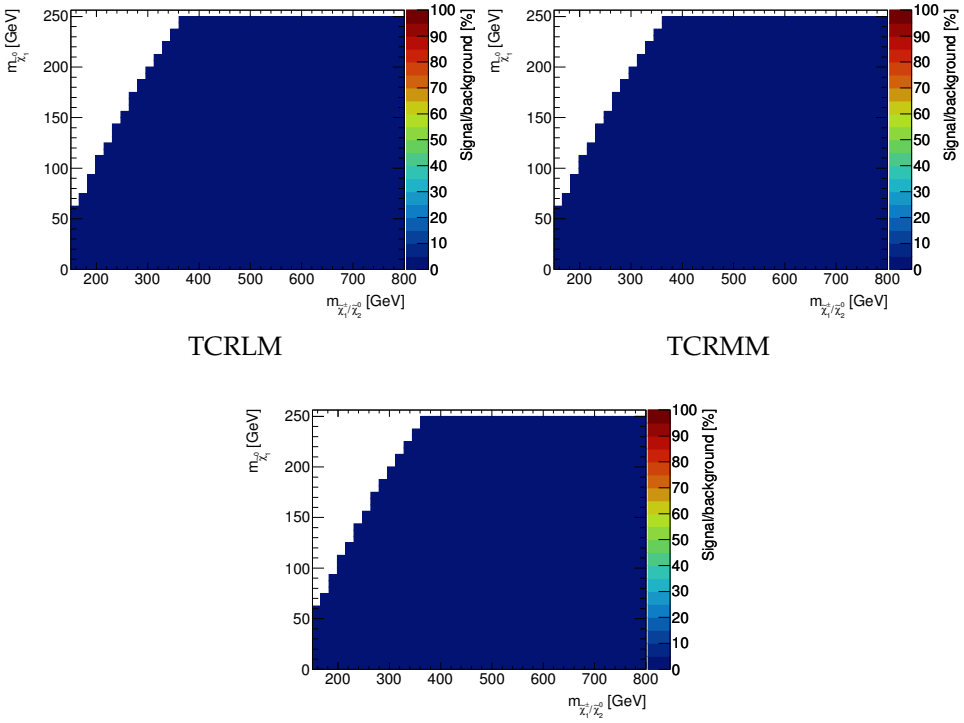

FIGURE 10.17: Signal contaminations in the TCRLM, TCRMM and TCRHM, respectively.

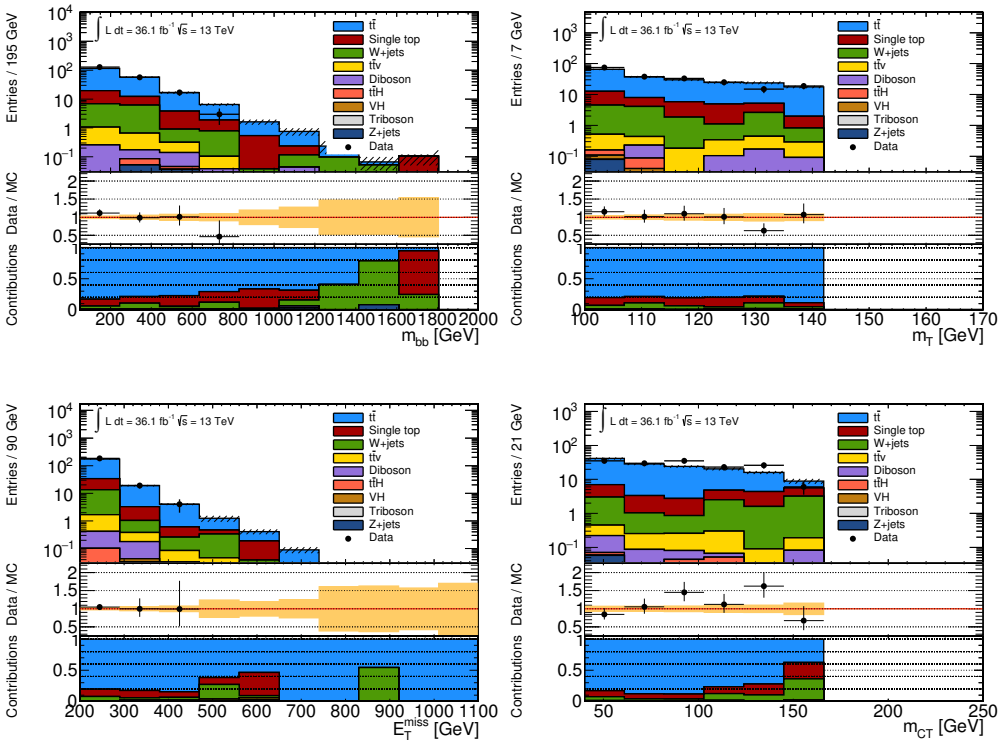

FIGURE 10.18: Data and MC comparison in the TCRLM.

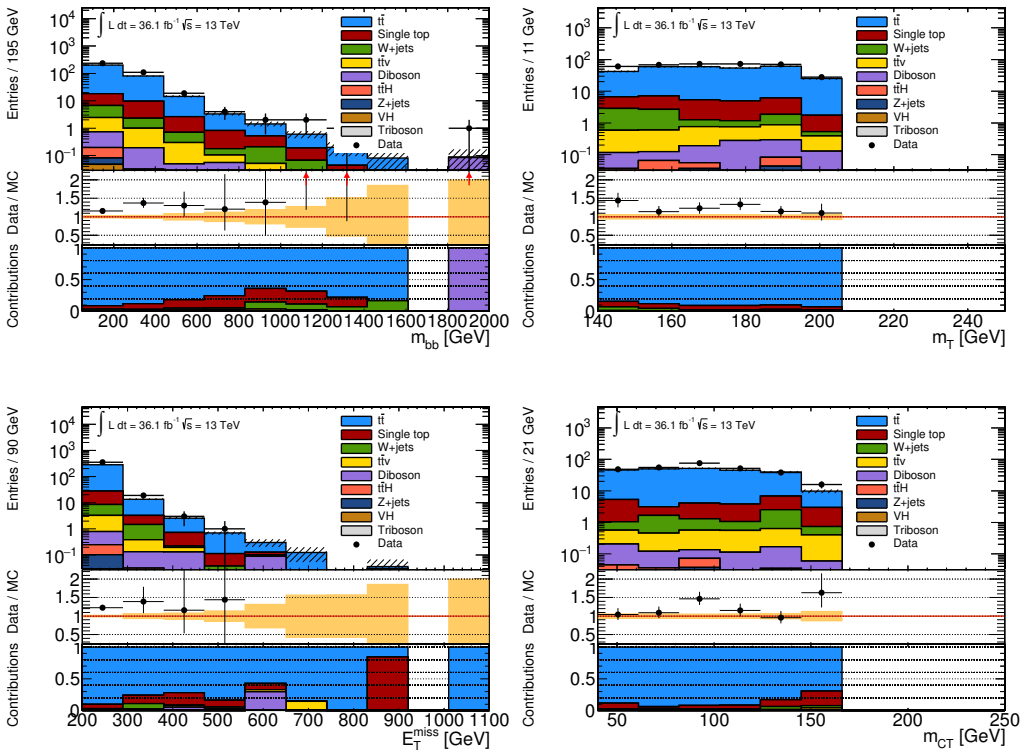

FIGURE 10.19: Data and MC comparison in the TCRMM.

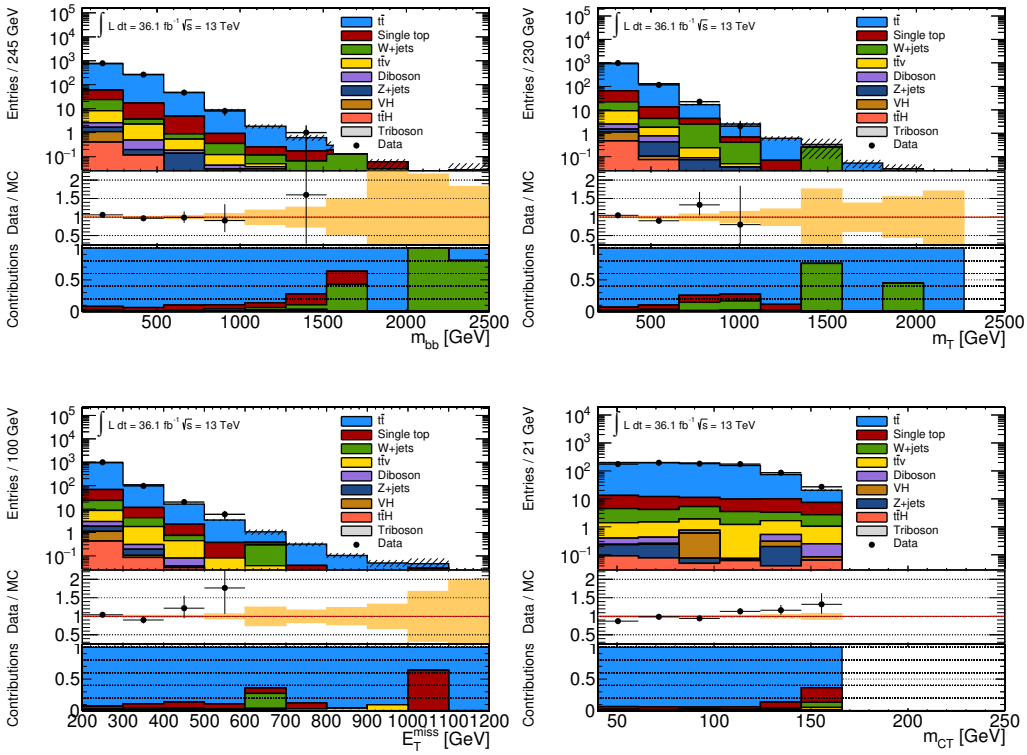

FIGURE 10.20: Data and MC comparison in the TCRHM.

Figure 10.21 shows the expected background contribution (left) and the signal contamination (right) in the WCR. The contribution of the W+jets events is 61.6%, while the signal contamination is less than 5%.

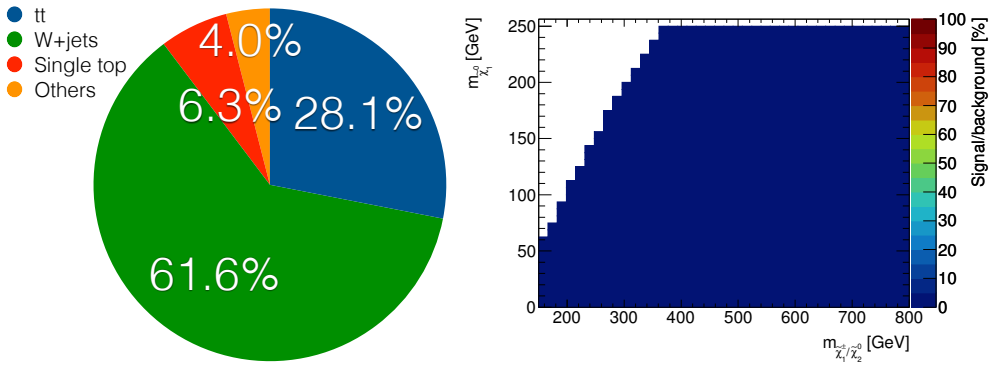

FIGURE 10.21: Composition of the WCR showing the background contribution (left) and the signal contamination (right). The dominant backgrounds are shown separately, while the smaller background processes are shown together as "Others".

Figure 10.22 shows the main kinematic distributions of data and the MC background processes in the WCR. The middle pad compares data with the expected backgrounds, while the bottom pad shows contributions of each background. The dominant backgrounds are normalized to data by applying the normalization factors listed in Table 10.5. The statistical uncertainties are only considered and a resonable agreement is observed within the statistical uncertainties.

The last CR enriched in single top events is called STCR. It is designed to use a high value of m_{bb} ($m_{bb} > 195$ GeV). In order to have enough statistics, values of m_T beyond 100 GeV are used. The selection criteria on m_{CT} and E_T^{miss} are the same as in the SR selections. Figure 10.23 shows the compositions of the STCR. The signal contamination in the STCR is about 5%, while the contribution of the single top events is 50.6%.

Figure 10.24 shows the main kinematic distributions of data and the expected backgrounds in the STCR. The middle pad shows the ratio between data and the expected backgrounds, while the bottom pad shows contributions of each background. The dominant backgrounds are normalized to data using the normalization factors listed in Table 10.5 and only the statistical uncertainties are considered. Overall reasonable agreement is observed within the statistical uncertainties.

The summary of all CRs including the preselection criteria is reported in Table 10.2.

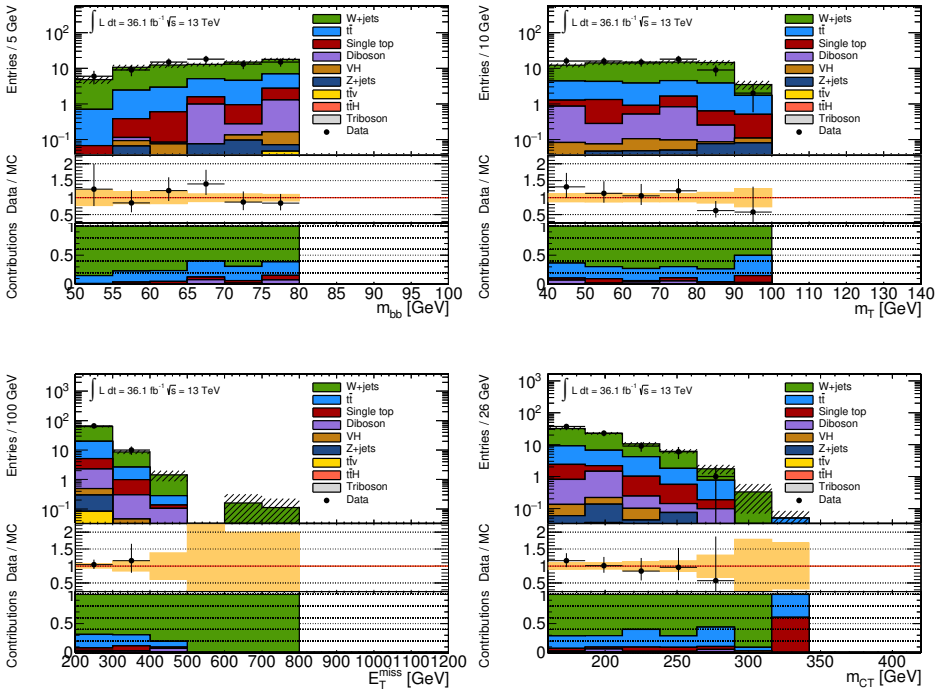

FIGURE 10.22: Data and MC comparison in the CRW.

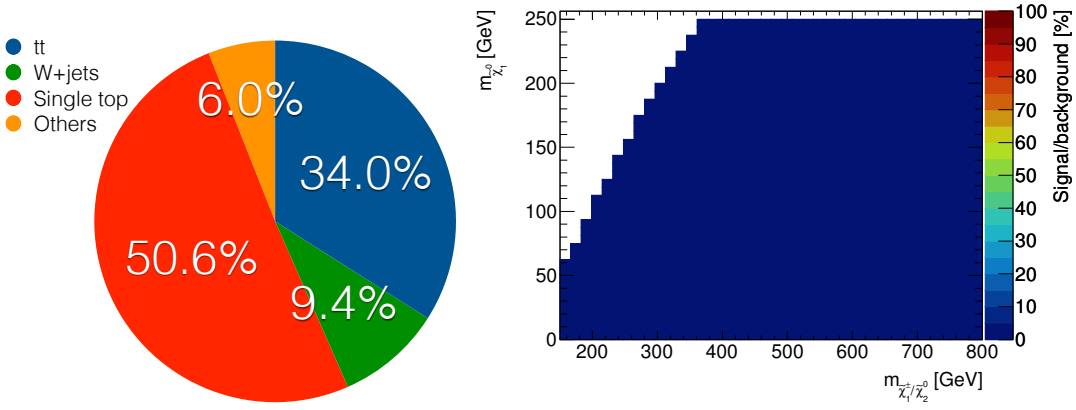

FIGURE 10.23: Composition of the STCR showing the background contribution (left) and the signal contamination (right). The dominant backgrounds are shown separately, while the smaller background processes are shown together as "Others".

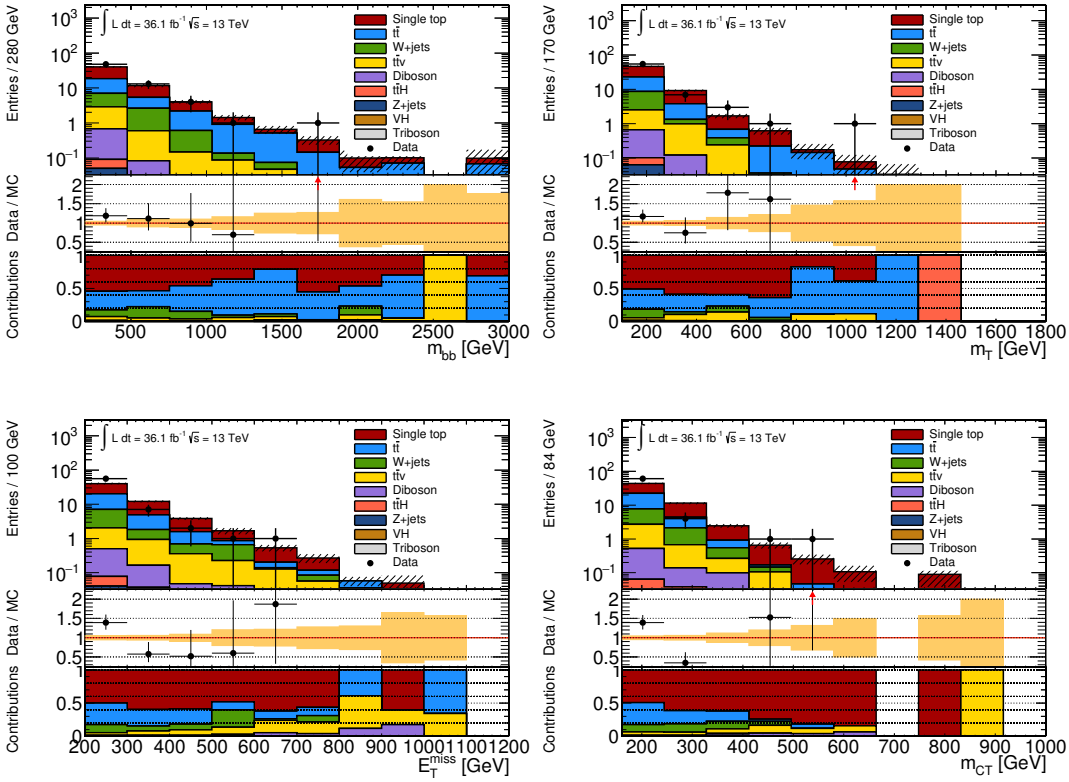

FIGURE 10.24: Data and MC comparison in the STCR.

Variable	**Preselection**				
N_{lep}	1				
N_{b-jets}	2				
N_{jets}	2 or 3				
	TCRLM	**TCRMM**	**TCRHM**	**WCR**	**STCR**
m_{bb} [GeV]	[50 - 105] or >= 135			< 80	> 195
m_{CT} [GeV]	< 160			> 160	
m_T [GeV]	[100 - 140]	[140 - 200]	> 200	[40 - 100]	> 100
E_T^{miss} [GeV]	> 200				

TABLE 10.2: Summary of all CR definitions.

10.6 Validation of the procedure

In order to validate the background estimations, two types of VRs are designed depending on the m_{bb} value. Both types consist of three VRs designed with different m_T criteria as done for the TCRs and the SRs. The first type of the VRs is known as "ON" due to the criterion on m_{bb} which includes the peak of the Higgs boson mass and its width (the same m_{bb} criterion as in the SRs). The three VRs belonging to the ON type are labeled as $VRLM_{ON}$, $VRMM_{ON}$ and $VRHM_{ON}$ with respect to the criteria on m_T. The selection on m_{CT} stays inverted as in the TCRs and the selection on E_T^{miss} is the same as in all CR and SR definitions. The second type of the VRs uses the mass sidebands in m_{bb} meaning that the selection on m_{bb} is inverted. These VRs are called "OFF" and are labeled as $VRLM_{OFF}$, $VRMM_{OFF}$ and $VRHM_{OFF}$ with respect to the selection on m_T. The selection on E_T^{miss} of 180 GeV is applied to keep the signal contamination within acceptable limits. The selection on m_{CT} is the same as in the WCR, STCR and all SRs.

All VRs are summarized in Table 10.3 together with the preselection criteria.

Variable	**Preselection**					
N_{lep}	1					
N_{b-jets}	2					
N_{jets}	2 or 3					
	Type I VRs			**Type II VRs**		
	$\mathbf{VRLM_{ON}}$	$\mathbf{VRMM_{ON}}$	$\mathbf{VRHM_{ON}}$	$\mathbf{VRLM_{OFF}}$	$\mathbf{VRMM_{OFF}}$	$\mathbf{VRHM_{OFF}}$
m_{bb} [GeV]	[105 - 135]			< [50 - 95] or [145 - 195]		
m_{CT} [GeV]	< 160			> 160		
m_T [GeV]	[100 - 140]	[140 - 200]	> 200	[100 - 140]	[140 - 200]	> 200
E_T^{miss} [GeV]	> 200			> 180		

TABLE 10.3: Summary of all VR definitions.

Figures from 10.25 to 10.30 show the main kinematic distributions of data with black dots and the expected backgrounds with colored stacks in the $VRLM_{ON}$, $VRMM_{ON}$, $VRHM_{ON}$, $VRLM_{OFF}$, $VRMM_{OFF}$ and $VRHM_{OFF}$, respectively. The dominant backgrounds are normalized to data by applying the normalization factors listed in Table 10.5 and only the statistical uncertainties are taken into account. The middle pad compares data with the expected backgrounds, while the bottom pad shows the background contributions. Overall reasonable agreement is observed within the statistical uncertainties.

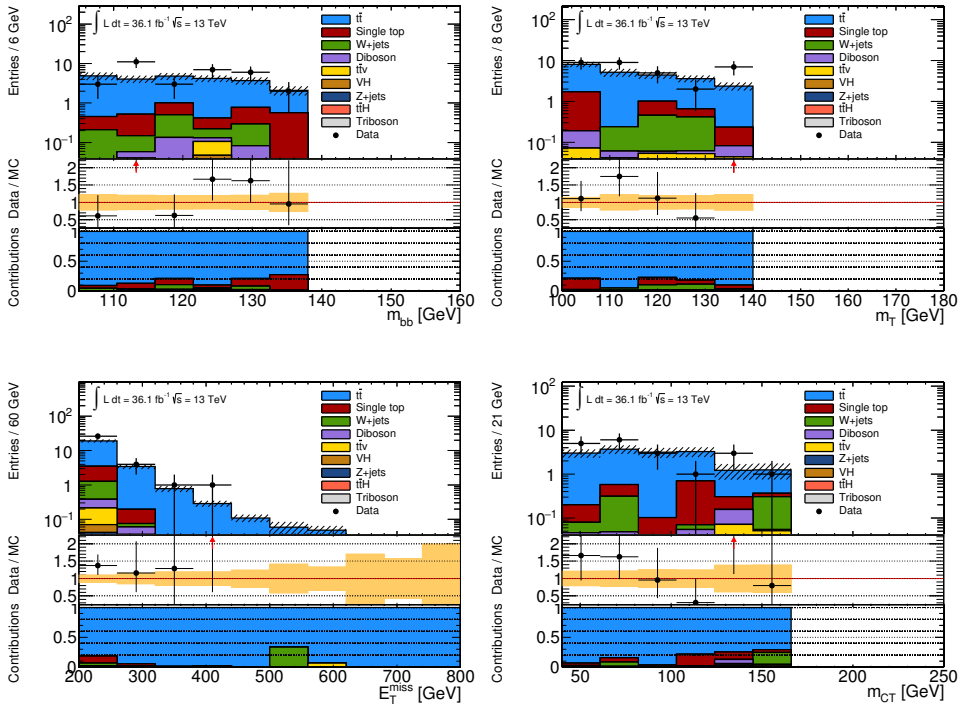

FIGURE 10.25: Main kinematic distributions of data and the SM predictions in the VRLM$_{ON}$.

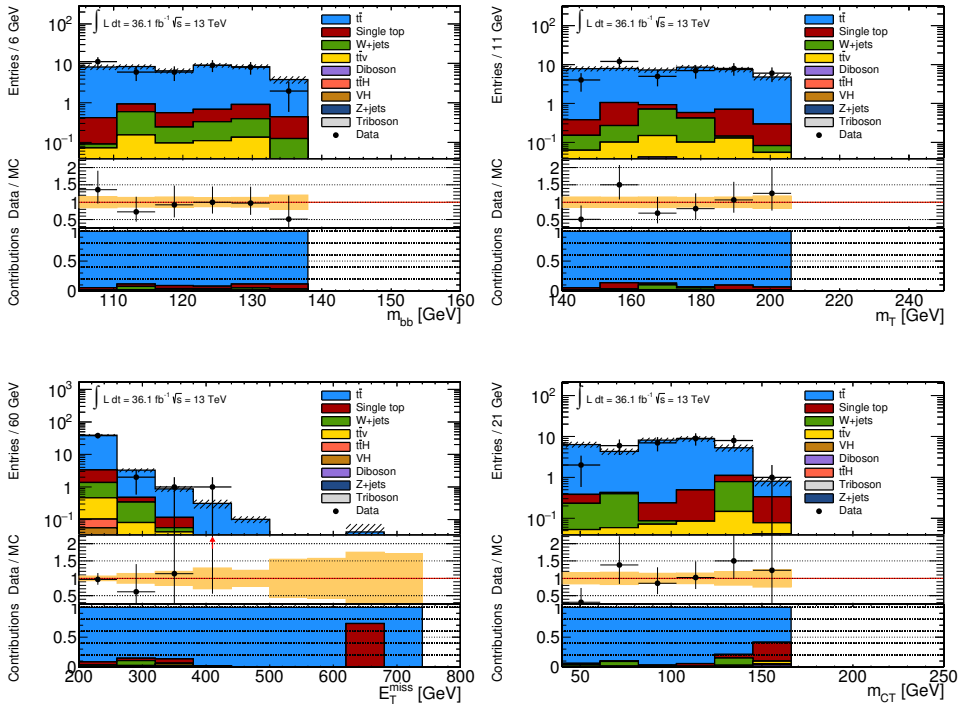

FIGURE 10.26: Main kinematic distributions of data and the SM predictions in the VRMM$_{ON}$.

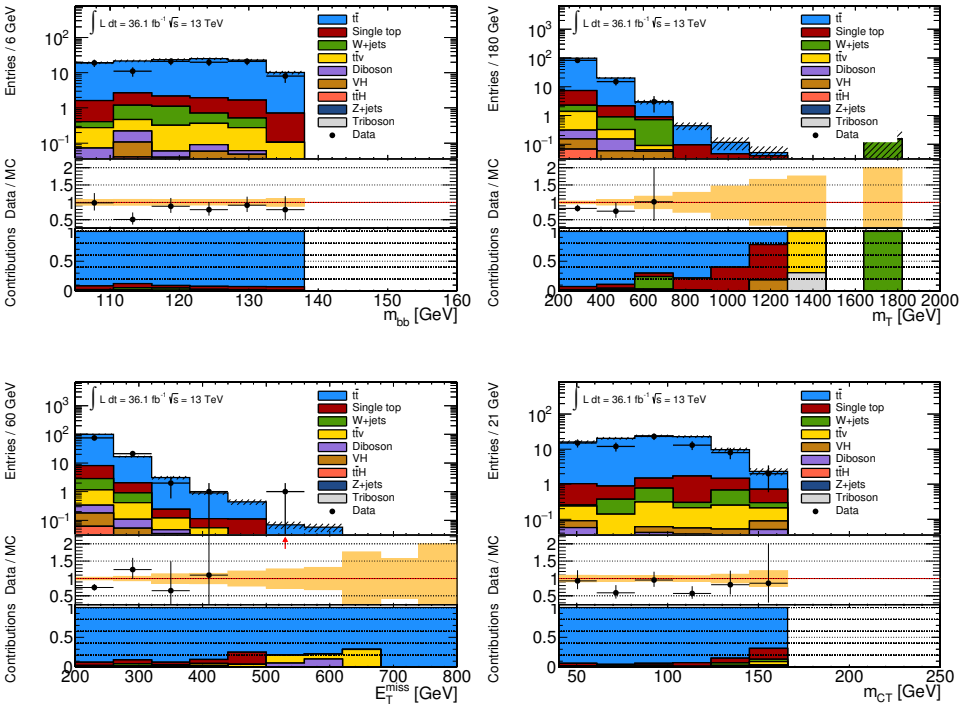

FIGURE 10.27: Main kinematic distributions of data and the SM predictions in the VRHM_{ON}.

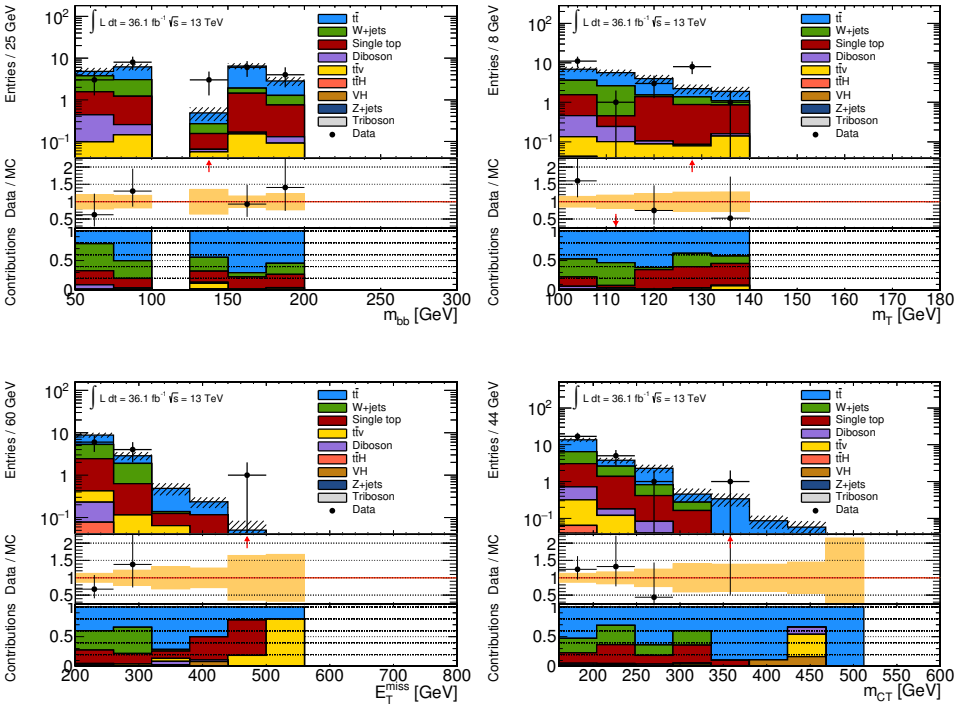

FIGURE 10.28: Main kinematic distributions of data and the SM predictions in the VRLM_{OFF}.

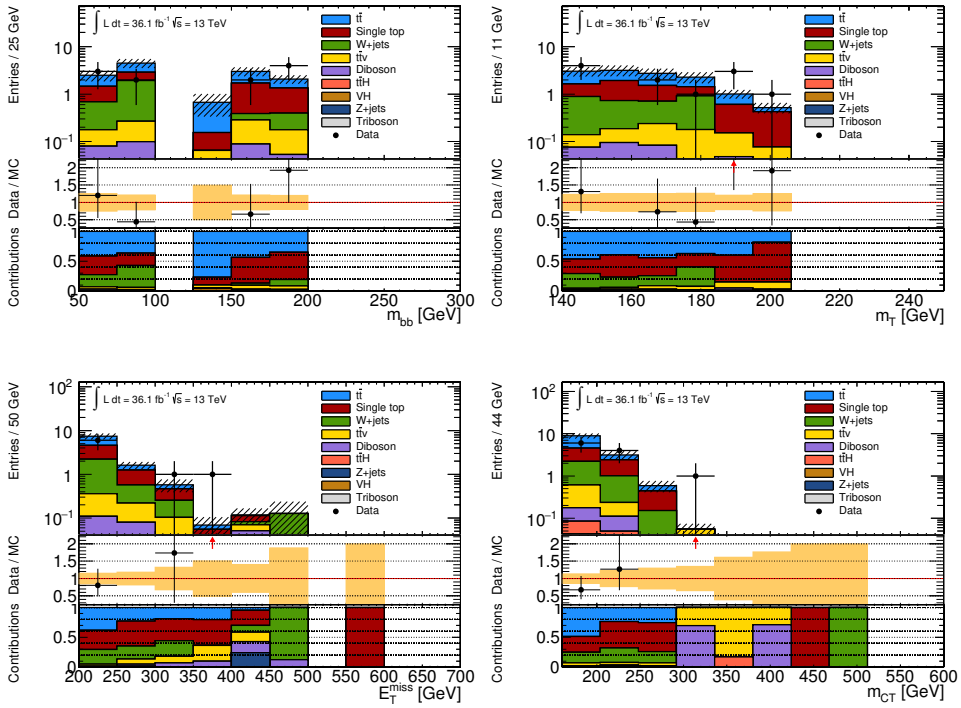

FIGURE 10.29: Main kinematic distributions of data and the SM predictions in the VRMM$_{\text{OFF}}$.

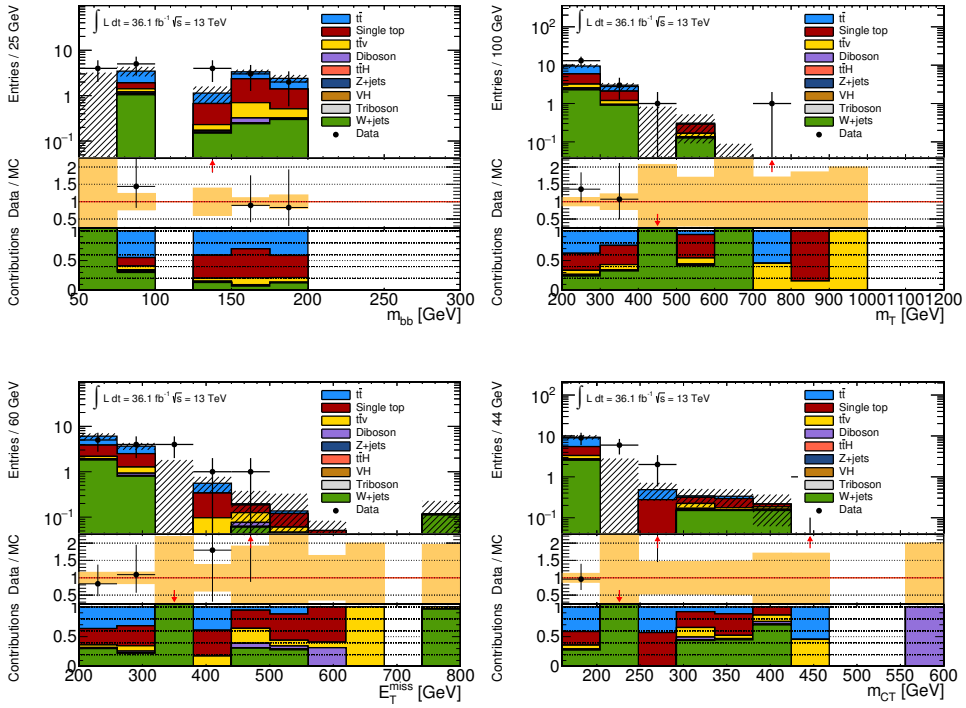

FIGURE 10.30: Main kinematic distributions of data and the SM predictions in the VRHM$_{\text{OFF}}$.

Figure 10.31 shows the signal contaminations in the VRs. The signal contamination is less than 20% in all VRs except the $VRHM_{OFF}$ where a bit higher signal contamination of 25% is observed.

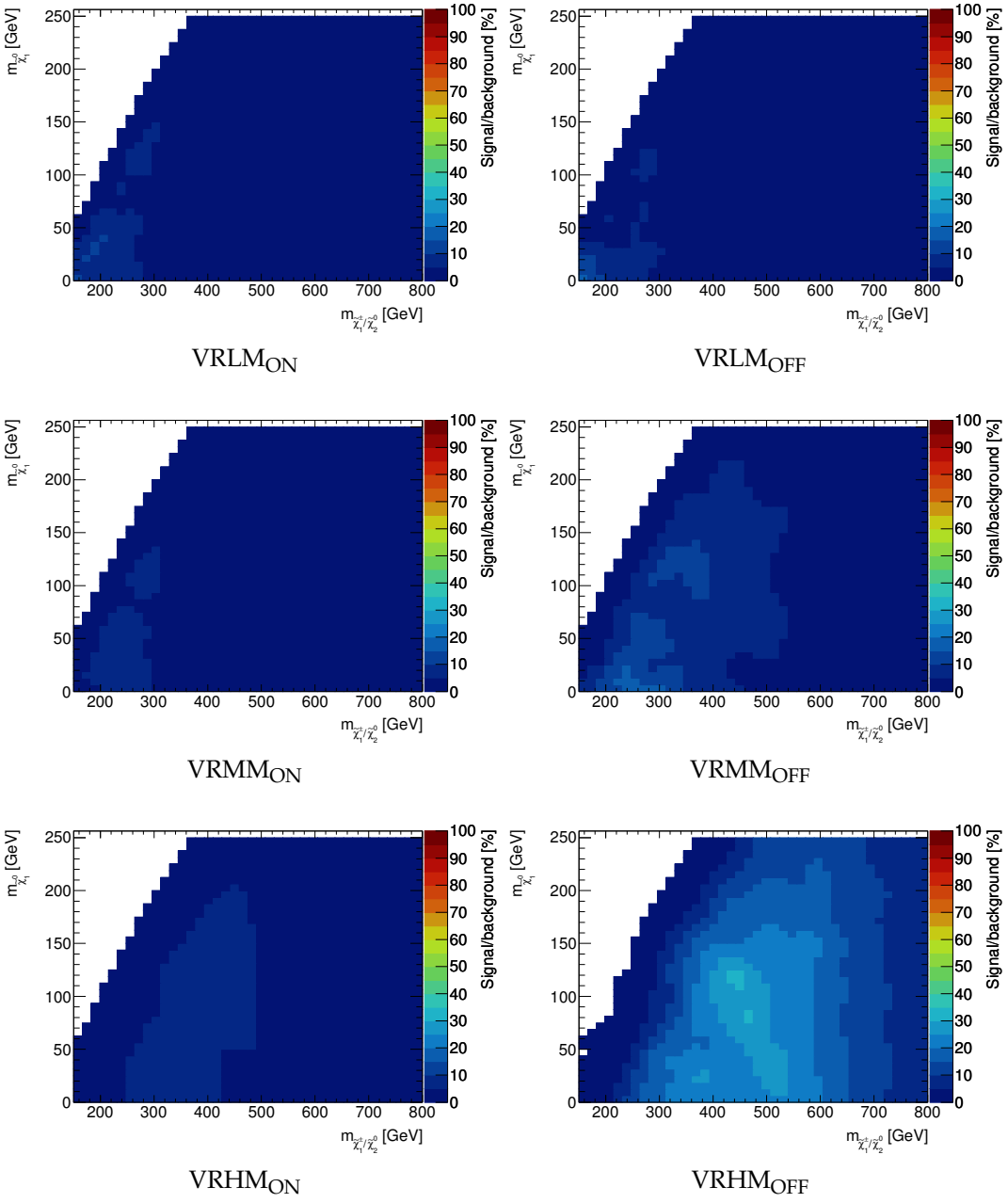

FIGURE 10.31: Signal contamination in all VRs.

The full analysis strategy which includes 3 SRs, 5 CRs and 6 VRs is illustrated in Figure 10.32.

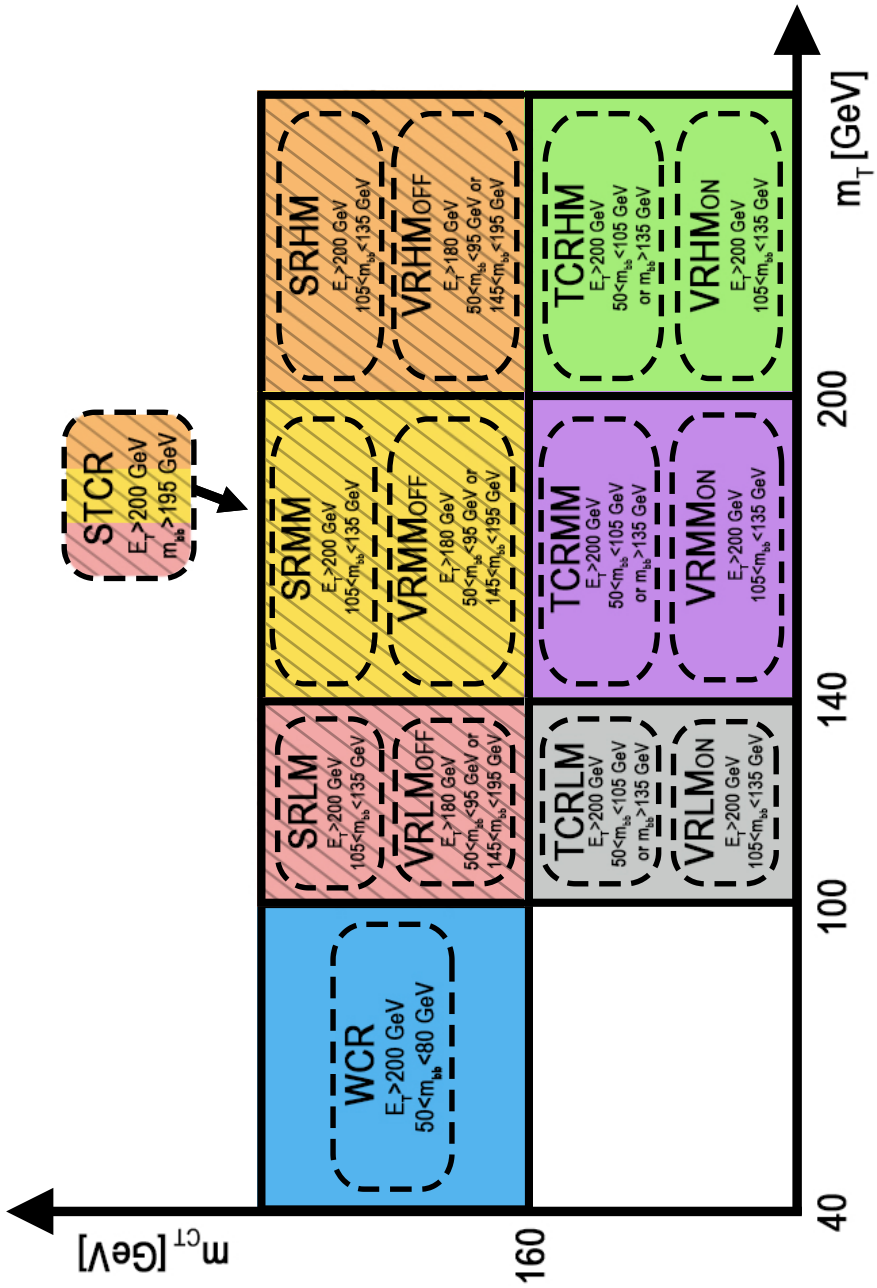

FIGURE 10.32: Schematic overview of all SRs, CRs and VRs in the m_T-m_{CT} plane. STCR control region overlaps the SR and VR_{OFF} regions, but it is orthogonal to them because of the m_{bb} > 195 GeV criterion.

10.7 Systematic uncertainties

Systematic uncertainties are connected to the background estimates, the signal modeling and cross-sections. They affect the predicted background event yields in the SRs, CRs and VRs, and the TFs used for the extrapolation of the SM estimates from the CRs to the SRs. The systematic uncertainties can be divided into experimental and theoretical uncertainties.

10.7.1 Experimental systematic uncertainties

Experimental systematic uncertainties consist of all detector related systematics. They are estimated by varying the calibrations described in Chapter 4 and are discussed in the following.

- **Electron systematic uncertainty**

Electron systematic uncertainties come from the reconstruction, identification and isolation procedures. They are determined by using a Tag-and-Probe method and samples of $Z \rightarrow ee$ and $J/\Psi \rightarrow ee$ decays. In both cases, a selection criterion is applied on one of two decay electrons. That electron is called "tag". The second electron from the decay, called "probe", is used for the efficiency measurements. For electrons with low p_T (from 7 to 20 GeV) $J/\Psi \rightarrow ee$ events are used, while electrons with $p_T > 15$ GeV are covered by $Z \rightarrow ee$ decays [58]. In the overlapping bin 15-20 GeV, events from both decays are combined [58].

- **Muon systematic uncertainty**

There are two types of uncertainties associated to muons. The first type presents the efficiency uncertainties which come from the reconstruction, identification and isolation criteria. The second type consists of the statistical and systematic uncertainties in the measurement. Both types are determined with a Tag-and-Probe method using $Z \rightarrow \mu\mu$ events [59].

- **Jet systematic uncertainty**

The Jet Energy Scale (JES) uncertainty describes the uncertainty on jet kinematic measurements after the calibration step discussed in Section 4.3. It is the dominant uncertainty and applied to all jets with $p_T > 15$ GeV and $|\eta| < 4.5$ [108]. The Jet Energy Resolution (JER) uncertainty is similar to the JES, but it describes the uncertainty on the energy resolution. The JER is estimated by smearing reconstructed jet energies to a Gaussian distribution [109].

- **b-jet systematic uncertainty**

The uncertainty on the b-tagging efficiency is evaluated using different samples for each algorithm and different configurations for the combined algorithm MV2 [110, 111].

- **MET systematic uncertainty**

Apart from the uncertainties on the reconstructed objects, there is one more uncertainty related to the soft term described in Section 4.7. This uncertainty is determined using Z($\rightarrow$ ll)+jets events by making a comparison between the expected and observed momentum profile of soft terms [68].

- **Pile-up systematic uncertainty**

An uncertainty on the pile-up contribution is obtained by scaling the average number of interactions per crossing in MC by 10%.

- **Luminosity systematic uncertainty**

An uncertainty of 3.2% on the integrated luminosity is used [112].

- **Trigger systematic uncertainty**

The uncertainty of 4% is applied to all events as discussed in Section 10.3.1.

10.7.2 Theoretical systematic uncertainties

Theoretical systematic uncertainties consist of uncertainties which come from the MC estimates. They are usually evaluated using different MC samples with respect to the nominal MC samples listed in Table 5.1.

Signal uncertainties: the uncertainty on the signal production cross-sections is estimated using two PDF sets together with variations on the renormalisation and factorisation parameters.

Top pair and single top background uncertainties: the uncertainties on the $t\bar{t}$ and single top MC samples are evaluated as uncertainties on the transfer factors which are used for the extrapolation between the CRs and SRs, or VRs. The sources of the uncertainties considered are:

- **Hard Scattering**: the difference of the predictions between POWHEG interfaced to PYTHIA and SHERPA is used to evaluate the systematic uncertainties for the MC $t\bar{t}$ samples. For the single top samples the predictions of POWHEG interfaced to PYTHIA are compared to MadGraph interfaced to PYTHIA.
- **Hadronisation/Fragmentation model**: the predictions of POWHEG interfaced to the two different parton shower algorithms PYTHIA and HERWIG are compared.
- **Scale variations and additional radiation**: the predictions of POWHEG are compared with variable shower radiation.
- **Interference (Wt-channel)**: the difference between the predictions of POWHEG interfaced to PYTHIA is compared to MadGraph interfaced to PYTHIA.

W+jets background uncertainties: the uncertainties on the W+jets background are evaluated as uncertainties on the transfer factor. The uncertainties due to the PDF set are estimated by comparing to other PDF sets. The uncertanties due to the renormalisation, factorisation and resummation scales are evaluated by varying these scales up down by factors of 0.5 and 2, while the uncertainties on the CKKW scale are derived by varying the thresholds from 15 GeV to 30 GeV.

Other background uncertainties: for the Z+jets background, the same sources of uncertainties need to be considered as for W+jets. Since the Z+jets background is a small background in this search, the uncertainties are calculated on the yields in the SRs and not on the transfer factors. For the diboson samples only an uncertainty on the cross-section is applied, while the uncertainties on the $t\bar{t}V$ samples include uncertainties on the scale and PDF.

10.8 Results

The background estimates in the CRs and VRs are shown in Table 10.4. The observed events are found to be in a good agreement with the SM predictions in the CRs, while the observed events in the VRs agree with the SM predictions within the uncertainties. The normalization factors evaluated in the fit are given in Table 10.5.

CR	**TRLM**	**TRMM**	**TRHM**	**WR**	**STCR**
Observed events	192	359	1115	72	65
Fitted bkg events	192 ± 14	359 ± 19	1115 ± 34	72 ± 9	65 ± 8

$\mathbf{VR_{ON}}$	$\mathbf{VRLM_{ON}}$	$VRMM_{ON}$	$VRHM_{ON}$
Observed events	29	41	100
Fitted bkg events	23 ± 9	54 ± 24	131 ± 22

$\mathbf{VR_{OFF}}$	$\mathbf{VRLM_{OFF}}$	$\mathbf{VRMM_{OFF}}$	$\mathbf{VRHM_{OFF}}$
Observed events	24	10	18
Fitted bkg events	22 ± 7	13.9 ± 3.3	10.3 ± 3.4

TABLE 10.4: Observed events and background fit results for the CRs and VRs. The total uncertainties include both statistical and systematic sources.

The final results of the search for $\tilde{\chi}_1^{\pm}\tilde{\chi}_2^0$ decaying to $W^{\pm}\tilde{\chi}_1^0 h\tilde{\chi}_1^0$ are given in Table 10.6, which shows the number of observed and expected events in all three SRs. The total uncertainties include both statistical and systematic sources. As shown in the table, the fitted SM estimations are 5.7±2.3 in the

μ_{TLM}	μ_{TMM}	μ_{THM}	μ_{W}	μ_{ST}
1.02 ± 0.14	1.10 ± 0.11	0.89 ± 0.04	1.26 ± 0.18	1.18 ± 0.18

TABLE 10.5: The normalization factors.

SRLM and 4.6±1.2 in the SRHM, while 6 and 5 events are observed, respectively, resulting in a good agreement between data and the SM expectations. The deviation of about 2 σ is found in the SRMM, where 2.8±1.0 events are expected while 7 events are observed.

SR	**SRLM**	**SRMM**	**SRHM**
Observed events	6	7	5
Fitted bkg events	5.7 ± 2.3	2.8 ± 1.0	4.6 ± 1.2

TABLE 10.6: Observed events and background fit results for the SRLM, SRMM and SRHM. The total uncertainties include both statistical and systematic sources.

Figure 10.33 shows the number of observed and expected events in all regions considered in this search. As discussed above, the good agreement is found in all CRs and VRs.

The largest deviation between the observed and expected events of 2 σ observed in the SRMM has been cross-checked with N-1 plots. Figures 10.34 to 10.36 show the distributions of observed data, the SM predictions and two simulated signal points as a function of the main kinematic variables m_T, m_{bb}, E_T^{miss}, and m_{CT} for all events passing the SRLM, SRMM and SRHM criteria, respectively minus the plotted variable. The "Others" category contains the contributions from the production of the Z boson in association with jets, triboson backgrounds, the VH production and $t\bar{t}$ events including the H boson production. Some differences between the observed events and the SM predictions are observed in the m_T distribution. However, careful checks of the main kinematic distributions in all three SR selections lead to the conclusion that no statistically significant excess has been observed.

The main kinematic distributions after applying all the SRLM, SRMM and SRHM criteria, respectively are shown in Figures from 10.37 to 10.39. The "Others" category contains the same contributions as in the N-1 plots.

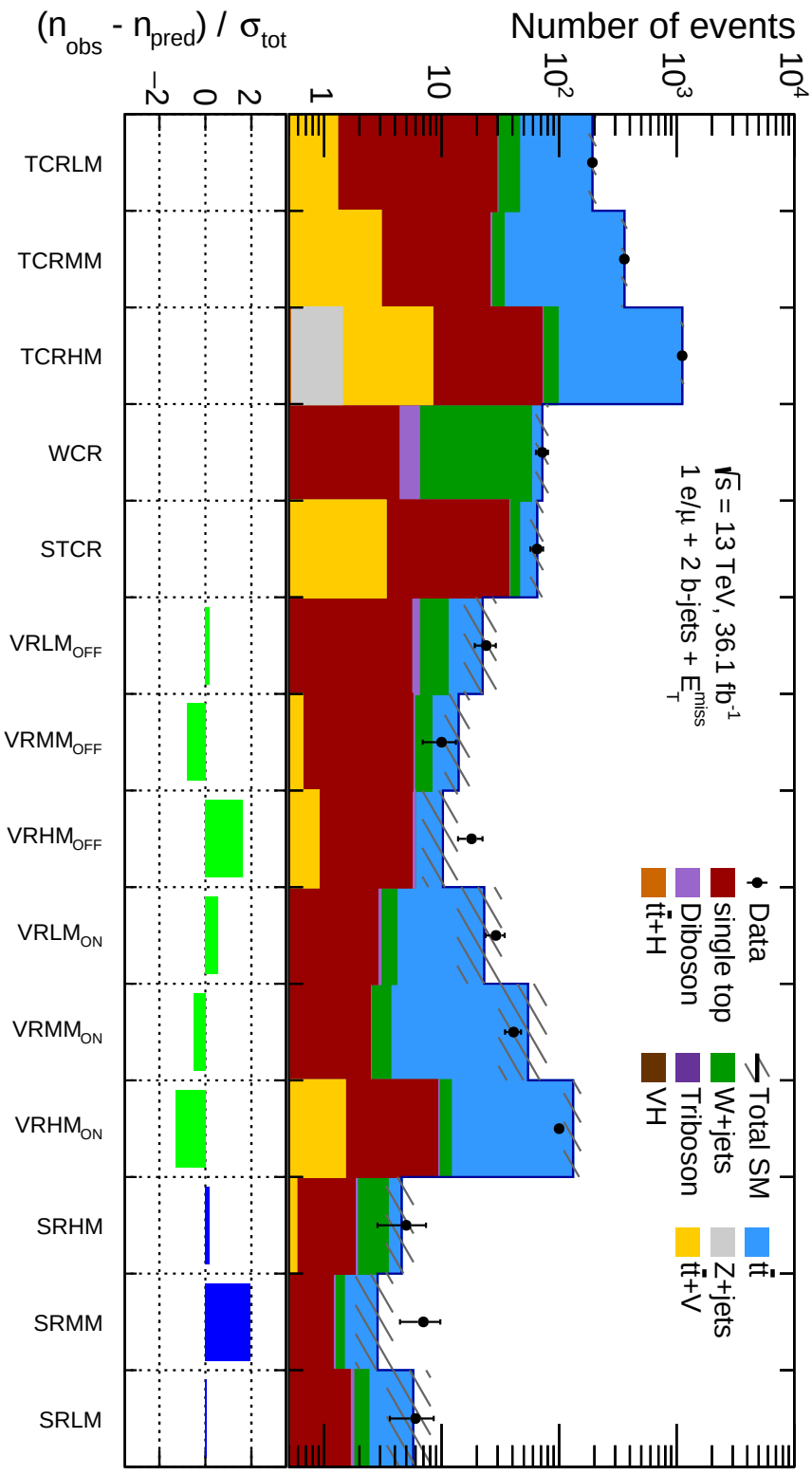

FIGURE 10.33: Distributions of observed data and the SM predictions for all regions.

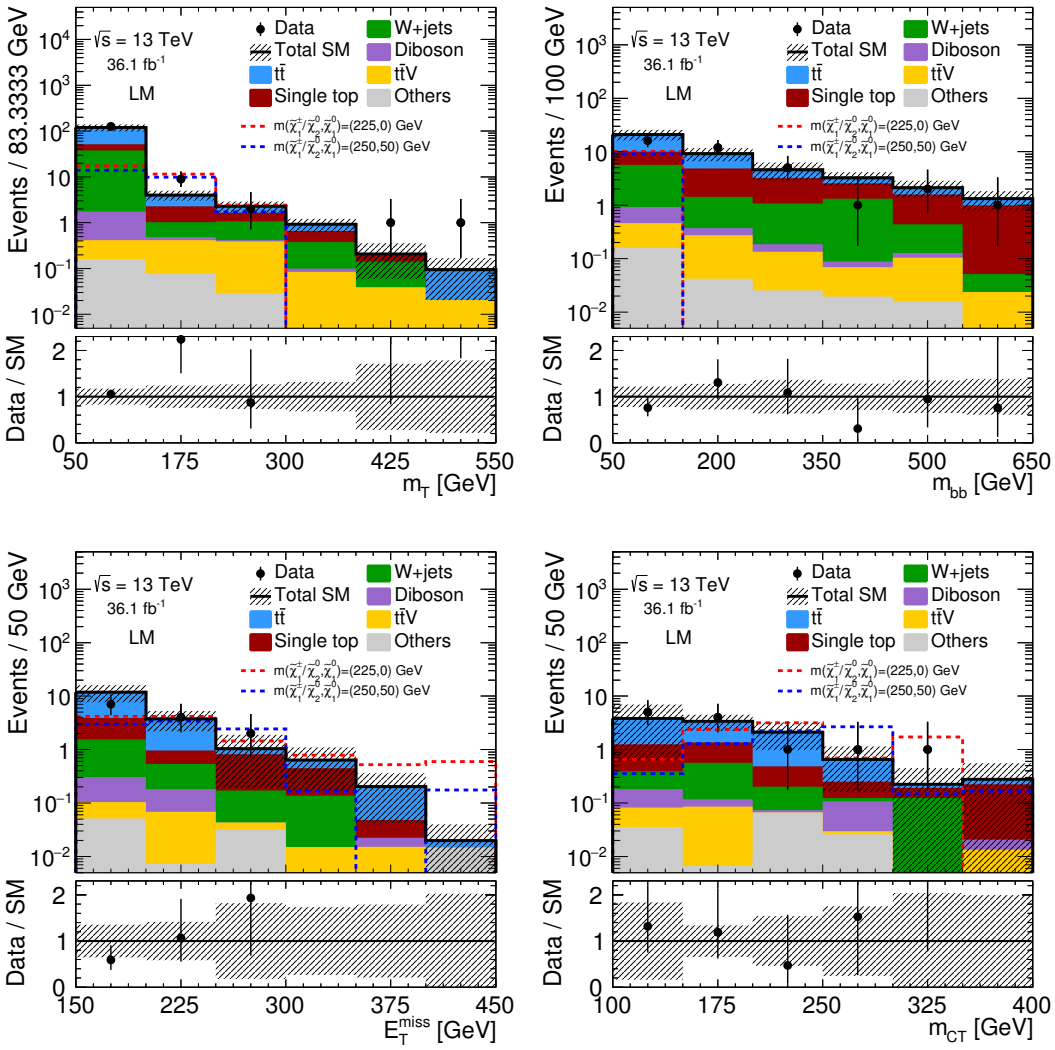

FIGURE 10.34: Distributions of observed data, the SM predictions and two signal points as a function of m_T, m_{bb}, E_T^{miss} and m_{CT} for all events passing the SRLM criteria minus the plotted variable. The signal points are $m_{\tilde{\chi}_1^\pm/\tilde{\chi}_2^0,\tilde{\chi}_1^0}$ = (225, 0) GeV and $m_{\tilde{\chi}_1^\pm/\tilde{\chi}_2^0,\tilde{\chi}_1^0}$ = (250, 50) GeV. The uncertainty bands include both statistical and systematic uncertainties. The "Others" category contains the contributions from the Z+jets, triboson, VH and $t\bar{t}H$ backgrounds.

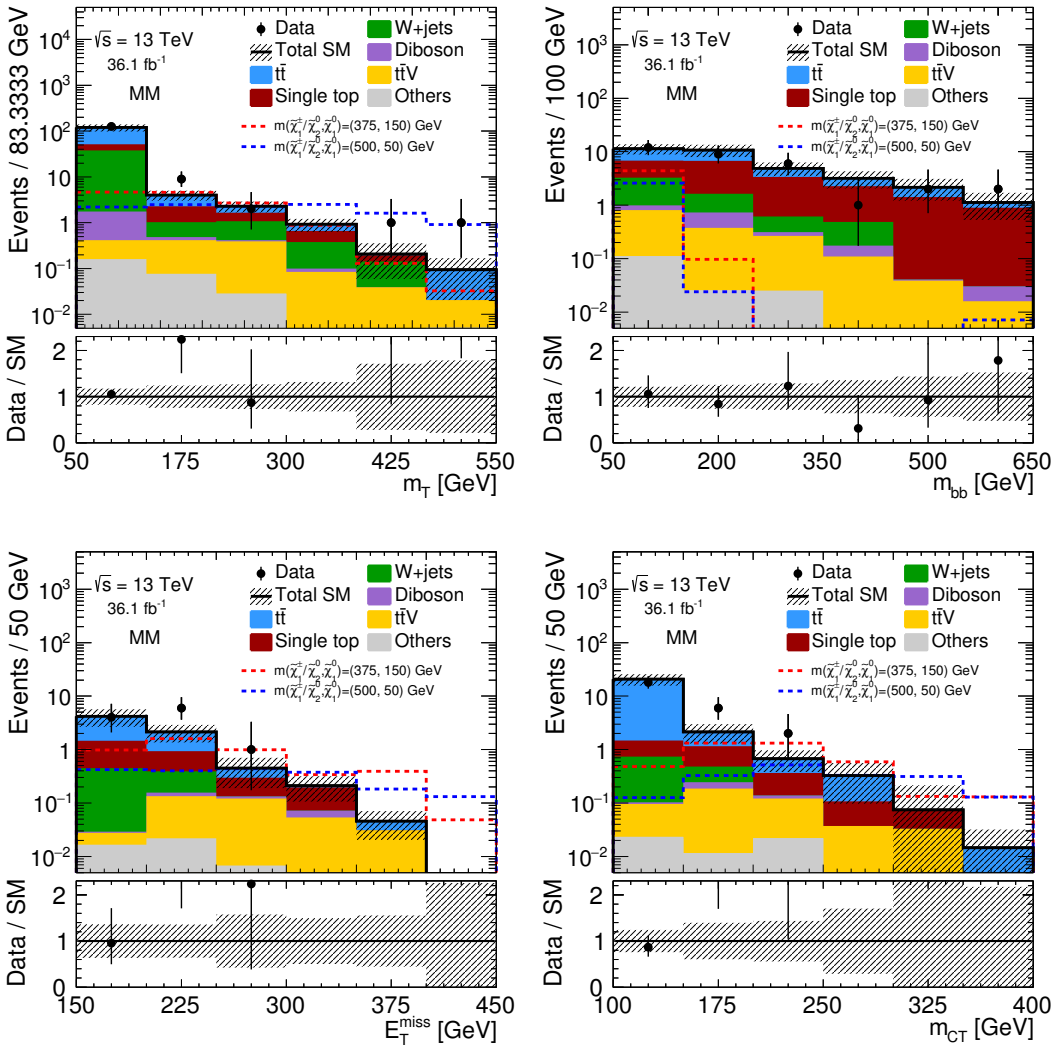

FIGURE 10.35: Distributions of observed data, the SM predictions and two signal points as a function of m_T, m_{bb}, E_T^{miss} and m_{CT} for all events passing the SRMM criteria minus the plotted quantity. The signal points are $m_{\tilde{\chi}_1^\pm/\tilde{\chi}_2^0,\tilde{\chi}_1^0}$ = (375, 150) GeV and $m_{\tilde{\chi}_1^\pm/\tilde{\chi}_2^0,\tilde{\chi}_1^0}$ = (500, 50) GeV. The uncertainty bands include statistical and systematic uncertainties. The "Others" category contains the contributions from the Z+jets, triboson, VH and $t\bar{t}H$ backgrounds.

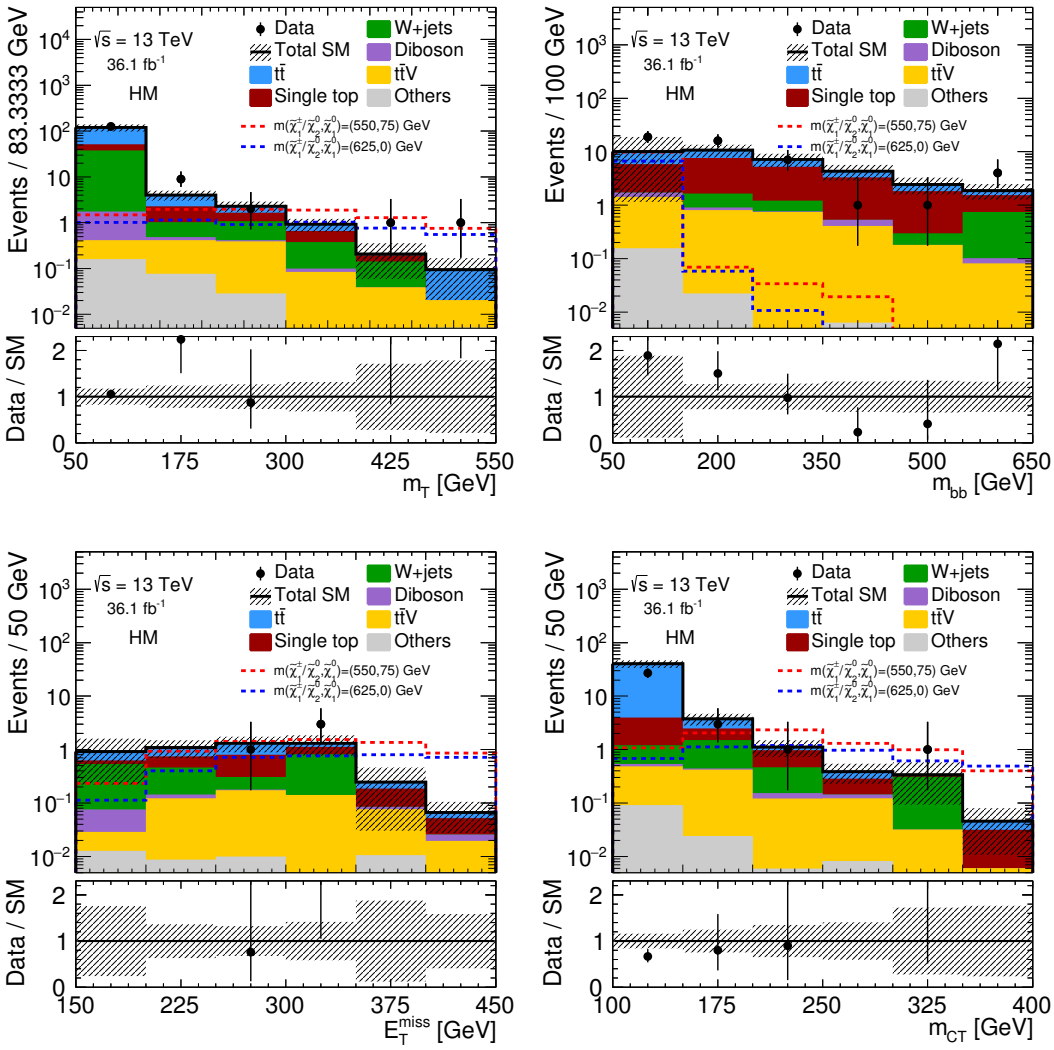

FIGURE 10.36: Distributions of observed data, the SM predictions and two signal points as a function of m_T, m_{bb}, E_T^{miss} and m_{CT} for all events passing the SRHM criteria minus the plotted variable. The signal points shown are $m_{\tilde{\chi}_1^\pm/\tilde{\chi}_2^0,\tilde{\chi}_1^0}$ = (550, 75) GeV and $m_{\tilde{\chi}_1^\pm/\tilde{\chi}_2^0,\tilde{\chi}_1^0}$ = (625, 0) GeV. The uncertainty bands include statistical and systematic uncertainties. The "Others" category contains the contributions from the Z+jets, triboson, VH and $t\bar{t}H$ backgrounds.

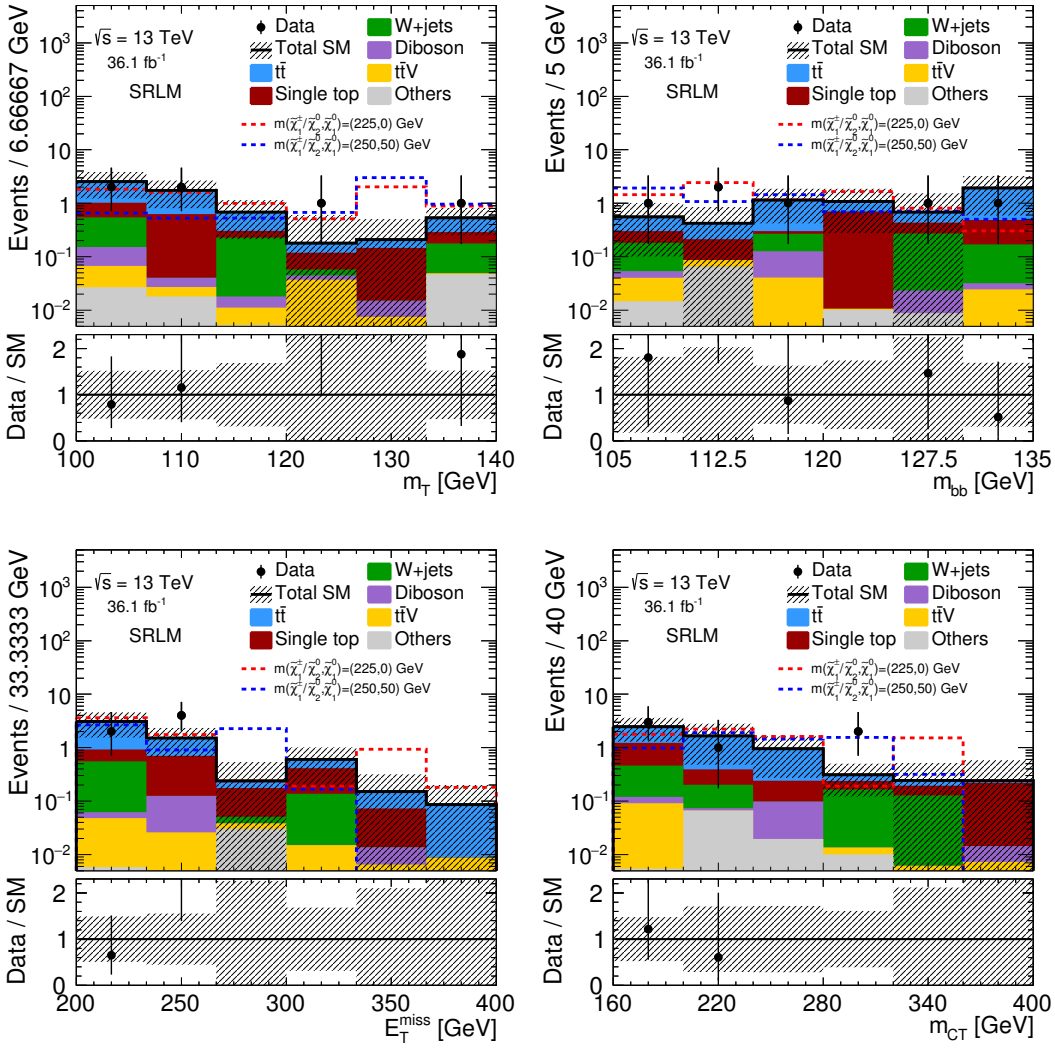

FIGURE 10.37: Distributions of observed data, the SM predictions and two signal points in the SRLM as a function of m_T, m_{bb}, E_T^{miss} and m_{CT}. The signal points plotted are $m_{\tilde{\chi}_1^\pm/\tilde{\chi}_2^0,\tilde{\chi}_1^0}$ = (225, 0) GeV and $m_{\tilde{\chi}_1^\pm/\tilde{\chi}_2^0,\tilde{\chi}_1^0}$ = (250, 50) GeV. The uncertainty bands include both statistical and systematic uncertainties. The "Others" category contains the contributions from the Z+jets, triboson, VH and $t\bar{t}H$ backgrounds.

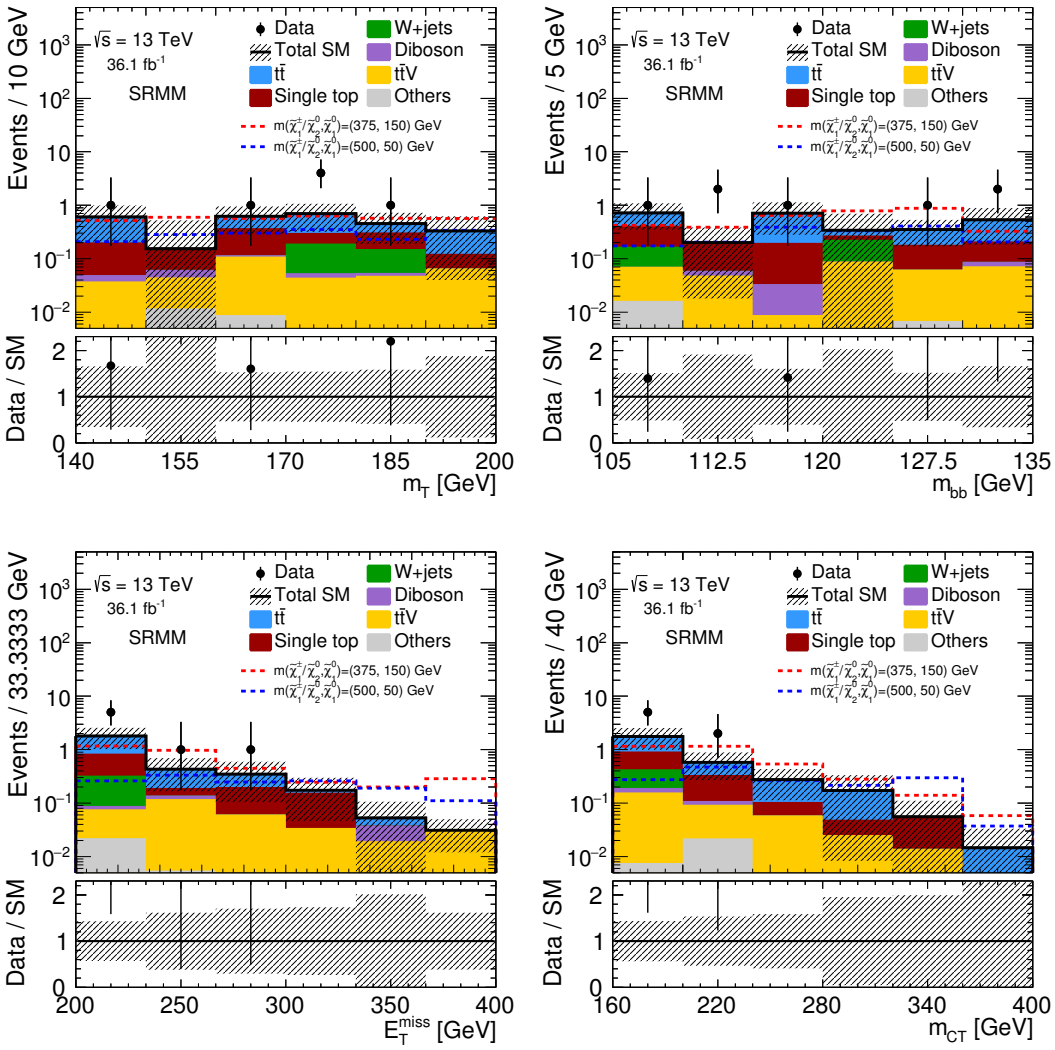

FIGURE 10.38: Distributions of observed data, the SM predictions and two signal points in the SRMM as a function of m_T, m_{bb}, E_T^{miss} and m_{CT}. The signal points plotted are $m_{\tilde{\chi}_1^\pm/\tilde{\chi}_2^0,\tilde{\chi}_1^0}$ = (375, 150) GeV and $m_{\tilde{\chi}_1^\pm/\tilde{\chi}_2^0,\tilde{\chi}_1^0}$ = (500, 50) GeV. The uncertainty bands include both statistical and systematic uncertainties. The "Others" category contains the contributions from the Z+jets, triboson, VH and $t\bar{t}H$ backgrounds.

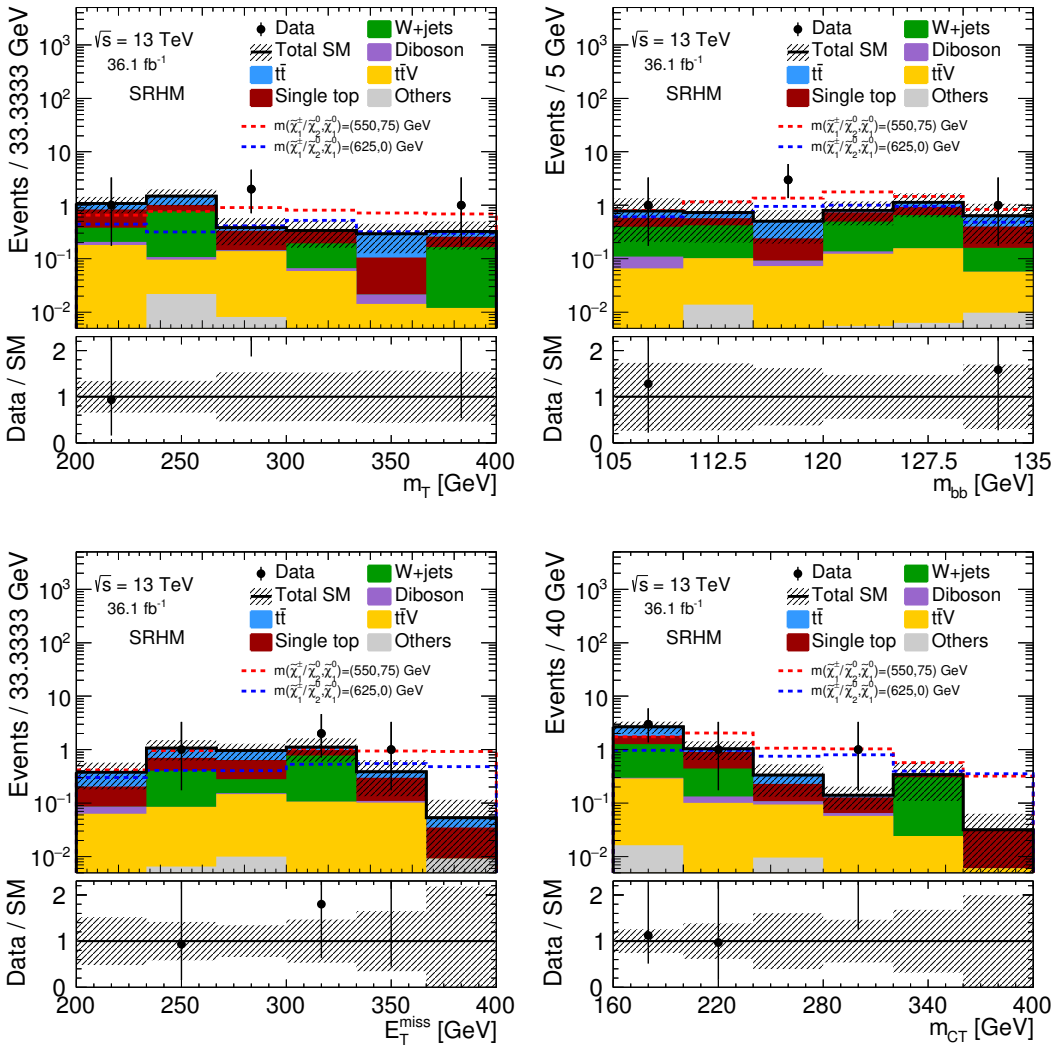

FIGURE 10.39: Distributions of observed data, the SM predictions and two signal points in the SRHM as a function of m_T, m_{bb}, E_T^{miss} and m_{CT}. The signal points plotted are $m_{\tilde{\chi}_1^\pm/\tilde{\chi}_2^0,\tilde{\chi}_1^0}$ = (550, 75) GeV and $m_{\tilde{\chi}_1^\pm/\tilde{\chi}_2^0,\tilde{\chi}_1^0}$ = (625, 0) GeV. The uncertainty bands include both statistical and systematic uncertainties. The "Others" category contains the contributions from the Z+jets, triboson, VH and $t\bar{t}H$ backgrounds.

The total systematic uncertainty in all regions considered in this search is reported in Table 10.7. It ranges from 3.01% in the TCRHM to 43.85% in the $VRMM_{ON}$. The largest uncertainties in the $VRMM_{ON}$ originate from the theoretical uncertainties on the $t\bar{t}$ background and amount to more than 36%. In all regions, the theoretical uncertainties on the $t\bar{t}$ background are dominant.

Uncertainty of channel	**SRLM**	**SRMM**	**SRHM**
Total background expectation	5.73	2.85	4.57
Total background systematic	±2.32 [40.40%]	±1.0 [35.02%]	±1.20 [26.26%]
Uncertainty of channel	**TCRLM**	**TCRMM**	**TCRHM**
Total background expectation	192.00	359.00	1115.00
Total background systematic	±14.00 [7.29%]	±19.17 [5.34%]	±33.59 [3.01%]

Uncertainty of channel	**WCR**	**STCR**
Total background expectation	72.00	65.00
Total background systematic	±8.76 [12.17%]	±8.08 [12.42%]

Uncertainty of channel	$\mathbf{VRLM_{ON}}$	$\mathbf{VRMM_{ON}}$	$\mathbf{VRHM_{ON}}$
Total background expectation	23.00	54.34	131.33
Total background systematic	±9.42 [40.95%]	±23.83 [43.85%]	±21.63 [16.47%]
Uncertainty of channel	$\mathbf{VRLM_{OFF}}$	$\mathbf{VRMM_{OFF}}$	$\mathbf{VRHM_{OFF}}$
Total background expectation	22.34	13.94	10.26
Total background systematic	±6.84 [30.60%]	±3.31 [23.76%]	±3.41 [33.21%]

TABLE 10.7: Total statistical and background systematic uncertainties for all regions. The percentages show the uncertainty relative to the total expected background.

10.9 Interpretation

Since the event yields observed in data are compatible with the SM predictions in all SRs, the results are interpreted as an exclusion limit for the $\tilde{\chi}_1^{\pm}\tilde{\chi}_2^0 \rightarrow W^{\pm}\tilde{\chi}_1^0 h\tilde{\chi}_1^0$ simplified model. The exclusion limits are derived by using the model-dependent fit described in Section 8.3.3, and the overall signal strength is assumed to have only positive values. The fit is performed simultaneously in the CRs and SRs, taking into account the systematic uncertainties and their correlations in the different regions. The result is shown in Figure 10.40, where the black dashed and red solid lines represent the 95% CL expected and observed limits, respectively. The yellow band around the expected limit shows the effect of the $\pm 1\sigma$ variation on the limit. The two

dotted red lines around the observed limit represent the $\pm 1\sigma$ variation on this limit due to the theoretical signal production cross-section. The gray area shows the observed limit from the previous search performed with 20.3 fb^{-1} at the center-of-mass energy of 8 TeV [105]. The exclusion limit from the LHC Run I is significantly improved by the increase in statistics and center-of-mass energy. As shown in the figure, the masses of $\tilde{\chi}_1^{\pm}\tilde{\chi}_2^0$ are excluded up to 550 GeV. This limit is valid only in case when $m_{\tilde{\chi}_1^0} = 0$ GeV. This is an important observation. Although the masses of $\tilde{\chi}_1^{\pm}\tilde{\chi}_2^0$ are excluded up to 550 GeV there is not any exclusion for a high mass of $\tilde{\chi}_1^0$. A part close to the diagonal remains difficult to reach due to increased background predictions and increased systematic uncertainties. This part could be a possible hiding place for supersymmetric particles considered in this chapter.

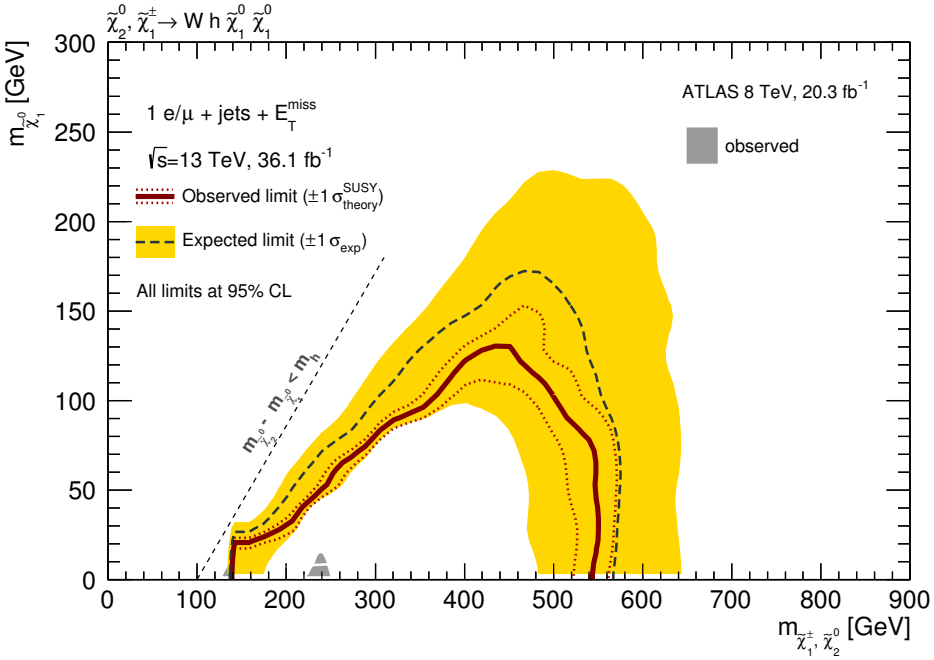

FIGURE 10.40: Exclusion limits for the $\tilde{\chi}_1^{\pm}\tilde{\chi}_2^0 \rightarrow W^{\pm}\tilde{\chi}_1^0 h\tilde{\chi}_1^0$ simplified model. The red solid and the two red dotted lines show the observed limits and the $\pm 1\sigma$ variation on this limit due to the theoretical signal production cross-section, respectively. The black dashed line with the yellow error band show the expected limit and the effect of the $\pm 1\sigma$ variation on the limit. The result obtained with data recorded during the LHC Run I is shown as the gray area.

Chapter 11

Conclusion

This thesis presents two searches for supersymmetric particles in events with exactly one lepton (electron or muon), jets and missing transverse momentum. Both searches use proton-proton collisions delivered by the Large Hadron Collider (LHC) at the centre-of-mass energy of 13 TeV in 2015 and 2016. The searches are performed on the dataset recorded by the ATLAS detector with an integrated luminosity of 36.1 fb^{-1}.

The search for squarks and gluinos decaying to W/Z/h bosons was explored using variables such as N_{jet}, m_T, m_{eff}, E_T^{miss}, E_T^{miss}/m_{eff}, and aplanarity. The sensitivity of this analysis has been compared with a reinterpretation of a published analysis on squarks and gluinos decaying to two W bosons. Additionally, the analysis is performed using variables sensitive to the Higgs boson, but due to the strong b-jet requirement such variables cannot improve the sensitivity. However, the sensitivity reach can be maximized in the boosted part of the parameter space with small mass splittings between $\tilde{q}(\tilde{g})$ and $\tilde{\chi}_1^{\pm}/\tilde{\chi}_2^0$ using jets with a large radius.

The search for charginos and neutralinos decaying to W and h bosons was performed with three signal regions covering different mass splittings between $\tilde{\chi}_1^{\pm}/\tilde{\chi}_2^0$ and $\tilde{\chi}_1^0$. A background strategy was developed where dominant backgrounds were normalized and validated in dedicated regions. The observed events in data have been found to be consistent with the Standard Model (SM) predictions in all three signal regions. The results are interpreted as exclusion limits on masses of $\tilde{\chi}_1^{\pm}/\tilde{\chi}_2^0$, where masses of $\tilde{\chi}_1^{\pm}/\tilde{\chi}_2^0$ up to 550 GeV are excluded at 95% Confidence Level. The LHC Run I limits are significantly improved due to higher production cross-sections, the increased integrated luminosity and the improvements of the particle reconstruction.

Although there is not any concrete experimental evidence for supersymmetric particles in the dataset recorded by the ATLAS detector in 2015 and 2016 with the integrated luminosity of 36.1 fb^{-1}, supersymmetry remains among the most popular SM extensions due to its elegant solutions to many of the open issues in the SM. The full LHC dataset will significantly increase the current sensitivity and might provide hints to the new physics phenomena beyond the SM. The next discovery in these field can be a key to our

understanding of particle physics.

Appendix A

Study of missing transverse momentum trigger recommendations for physics analyses

The studies described in this section are motivated by the searches for supersymmetric particles presented in this thesis, especially with the search for charginos and neutralinos decaying to W and h bosons. As already discussed both searches use the missing transverse momentum (E_T^{miss}) triggers, but these triggers are not fully efficient for the search for charginos and neutralinos (see Section 10.3.1). This search as well as many others need correction factors to correct the E_T^{miss} trigger efficiency obtained from the MC simulation to data. This chapter describes studies performed with the aim to provide such factors which are called scale factors.

A.1 Methods to estimate scale factors

A.1.1 Data and simulated samples

The studies presented here use the dataset recorded by the ATLAS detector at the centre-of-mass energy of 13 TeV with an integrated luminosity of 21.7 fb^{-1} and MC samples. Since these studies are based on the searches for supersymmetric particles with one isolated lepton in the final states, only dominant SM processes such as $t\bar{t}$ and W + jets are considered. These processes are merged and are treated as one MC process.

A.1.2 Event selections

The event selection starts with the one lepton (electron or muon) requirement because both searches presented in this thesis require either one electron or

one muon. This requirement allows the calculation of scale factors separately for the electron and muon channels.
Due to kinematics of the MC process ($t\bar{t}$ + W+jets) a b-tagging requirement is also applied resulting in two selections: b-tag and b-veto. The b-tag selects only events with at least one b-jet, while the b-veto vetoes such events. Other requirements on the number of b-jets (= 2, $\geq$ 2, =3, $\geq$ 3, ...) significantly reduce statistics and cannot be applied. This issue is already reported in Section 10.3.1 and is a reason why the scale factor has not been provided for the search for charginos and neutralinos decaying to W and h bosons.
After the one lepton and b-tagging requirements, the events are further select by applying the following criteria:

p_T^{l1}	[30-40, 40-50, 50-60, 60-70, 70-80] GeV
m_T	[<30, 30-40, 40-50, 50-60, 60-70] GeV
N_{jets}	[2, 3, 4, 5, 6]
3 jets + $p_T^{j1=2=3}$	[30, 40, 50, 60, 70] GeV

These criteria are chosen to make these studies more general and cover different parts of parameter space:

- **Criterion on the lepton** p_T^{l1}: this criterion starts from 30 GeV because one lepton usually arises from a W boson decay and have a high p_T.
- **Criterion on** m_T: the criterion on this variable goes from 0 GeV to 70 GeV due to kinematic of a W boson.
- **Criteria on jets (**N_{jets} **and 3 jets +** $p_T^{j1=2=3}$**)**: these criteria consider all possible jets which could come from squark or gluino decays.

A.1.3 Strategy

The performance of the triggers is not well modelled in the MC simulated data as can be seen in Figures 9.7 and 10.4. Both figures show that the trigger efficiencies in data and MC are not 100% comparable. The differences can be taken into account by applying a scale factor to all MC events which passed the trigger. The scale factor (SF) is defined as:

$$SF = \frac{\epsilon_{data}}{\epsilon_{MC}} \tag{A.1}$$

where ϵ_{data} and ϵ_{MC} are the trigger efficiency measured in data and the efficiency of the MC simulated trigger, respectively. Both efficiencies are calculated as the number of events which passed the trigger, divided by the number of all events considered.
The studies consider only the E_T^{miss} trigger with the HLT threshold of 110 GeV. As reported in Table 9.1, this trigger has collected events grouped in datasets with an integrated luminosity of 21.7 fb^{-1} (60% of all events used in this thesis).

A.2 Results

This section presents results obtained by using Equation A.1 and the selections detailed in Section A.1.2 for the E_T^{miss} trigger with the HLT threshold of 110 GeV. Figure A.1 shows the scale factors in the electron channel after requesting exactly one electron and vetoing b-jets for the different p_T^{l1} (A)/m_T (B)/N_{jets} (C)/3 jets + $p_T^{j1=j2=j3}$ (D) selections. Considering only a part from 180 GeV[1], the different values of the scale factor can be observed. Their values go from 0.93 to 0.97. Figure A.2 shows the scale factors in the electron channel after requesting the same selections as above and at least one b-jet. The scale factors are ordered in the same way as in the previous figure. Looking at the part of interest (from 180 GeV) the scale factors have the values from 0.92 to 0.98, except for the 3 jets + $p_T^{j1=j2=j3}$ selection where they look pretty similar.

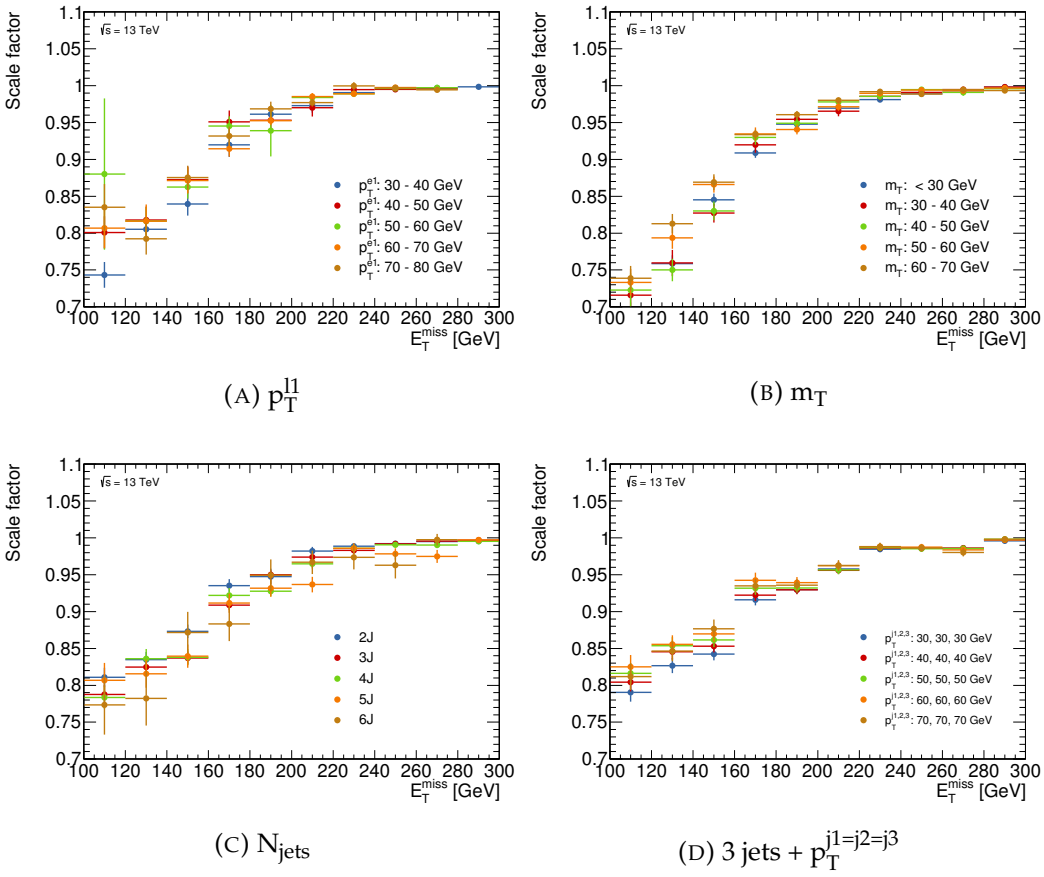

(A) p_T^{l1} (B) m_T

(C) N_{jets} (D) 3 jets + $p_T^{j1=j2=j3}$

FIGURE A.1: Scale factors calculated by using Equation A.1 in the electron channel after requesting exactly one electron and vetoing b-jets.

[1] A starting point of 180 GeV has been taken due to the VR selections in the search for charginos and neutralinos.

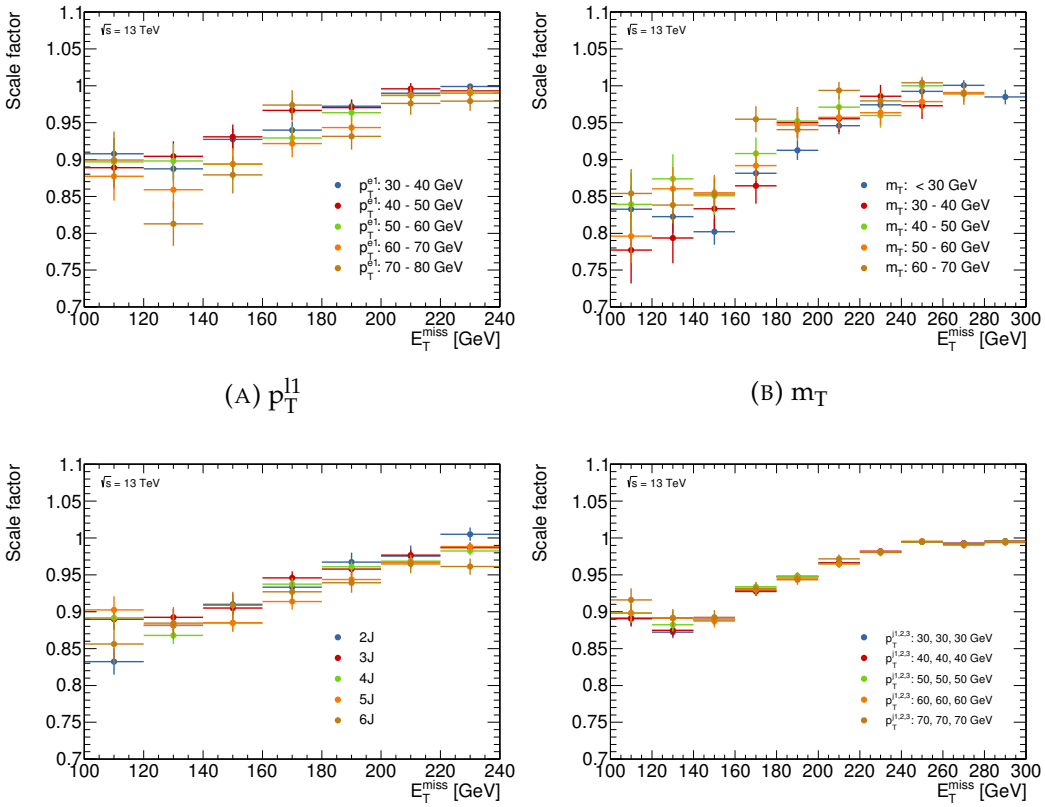

(A) p_T^{l1} (B) m_T

(C) N_{jets} (D) 3 jets + $p_T^{j1=j2=j3}$

FIGURE A.2: Scale factors calculated by using Equation A.1 in the electron channel after requesting exactly one electron and at least one b-jet.

Figures A.3 and A.4 show the scale factors after requesting the same selections as above but in the muon channel. The b-veto requirement is shown in Figure A.3, while the b-tag in Figure A.4. The scale factors in the muon channel look better then in the electron channel. Their values go from 0.96 to 1 for both the b-jet requirements (b-veto and b-tag). The selections as 3 jets + $p_T^{j1=j2=j3}$ and m_T give the scale factors with the value of 1. The E_T^{miss} trigger efficiency in the muon channel is expected to be different from the E_T^{miss} trigger efficiency obtained in the electron channel because the E_T^{miss} used in these studies is calculated with the contribution from baseline muons as described in Section 4.7.1. The differences between the electron and muon channel can be partly recovered by computing the E_T^{miss} without the contribution from baseline muons[2].

[2] At the L1, only information from the calorimeters is available. At the HLT, tracking information from the inner detector is available while information from the muon spectrometer is not.

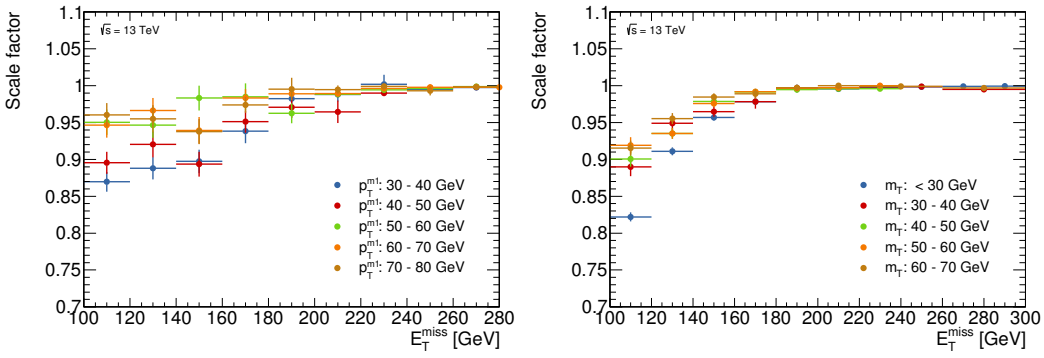

(A) p_T^{l1} (B) m_T

(C) N_{jets} (D) 3 jets + $p_T^{j1=j2=j3}$

FIGURE A.3: Scale factors calculated by using Equation A.1 in the muon channel after requesting exactly one muon and vetoing b-jets.

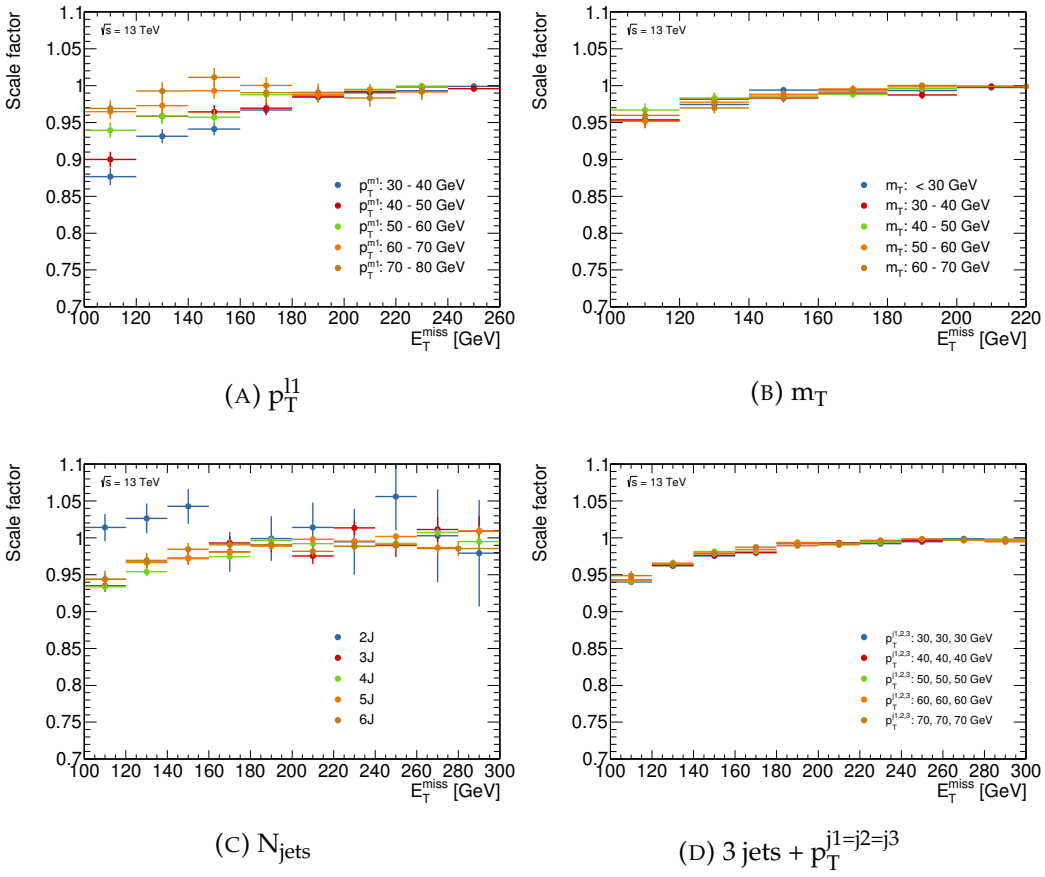

(A) p_T^{l1} (B) m_T

(C) N_{jets} (D) 3 jets + $p_T^{j1=j2=j3}$

FIGURE A.4: Scale factors calculated by using Equation A.1 in the muon channel after requesting exactly one muon and at least one b-jet.

A.3 Fit function

In order to remove bias caused by the binning the scale factors shown in Section A.2 have been modeled by the error function with the following parameterization:

$$\Phi(E_T^{miss}) = \frac{p_0}{2} \cdot \left[1 + \mathrm{erf}\left(\frac{E_T^{miss} - p_1}{p_2} \right) \right] \tag{A.2}$$

where $\Phi(E_T^{miss})$ is the probability that an event with a certain value of E_T^{miss} passes the trigger, p_0 is the height of the plateau, p_1 is the effective threshold and p_2 is the standard deviation of the Gaussian.
Different choices of initial parameters have been tested with the aim to find as good a fit as possible. The results obtained after an optimisation of the initial parameters are shown in Figures A.5-A.8. The order of results is the same as before. Overall the fit function describes the scale factors well, but the unique scale factor can be provided. As already discussed in Section A.2, some differences between the different selections can be observed leading to a conclusion that the scale factors are dependent of event topology.

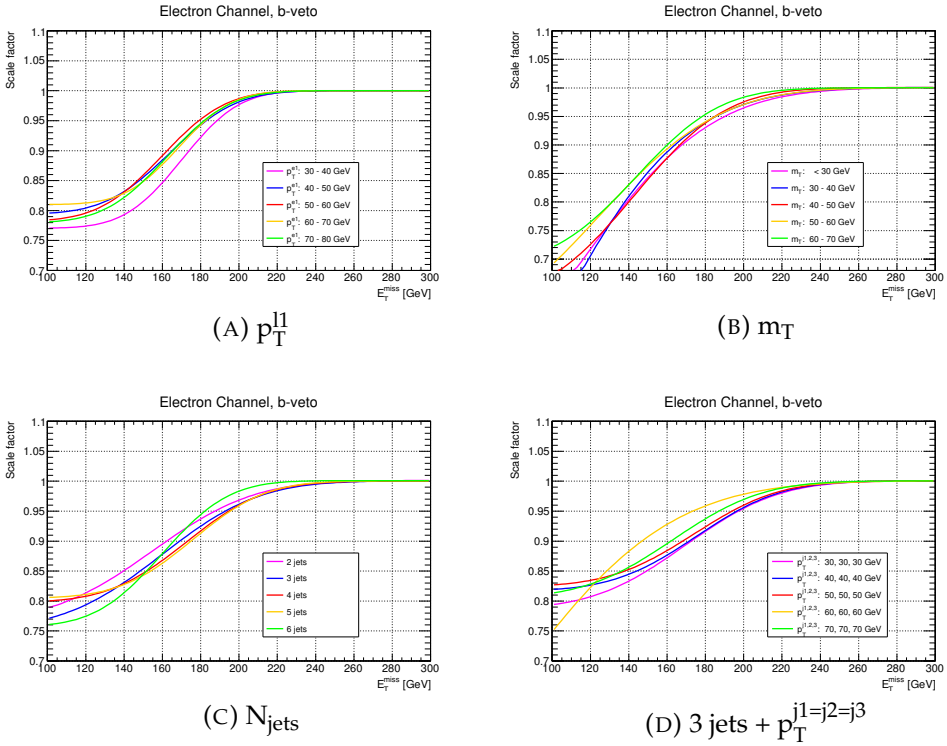

(A) p_T^{l1} (B) m_T

(C) N_{jets} (D) 3 jets + $p_T^{j1=j2=j3}$

FIGURE A.5: Scale factors obtained by using the error function A.2 in the electron channel after vetoing b-jets.

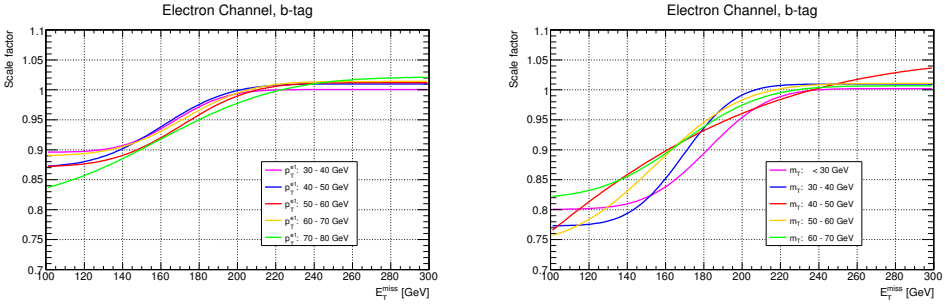

(A) p_T^{l1}

(B) m_T

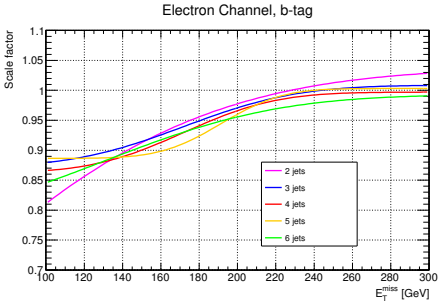

(C) N_{jets}

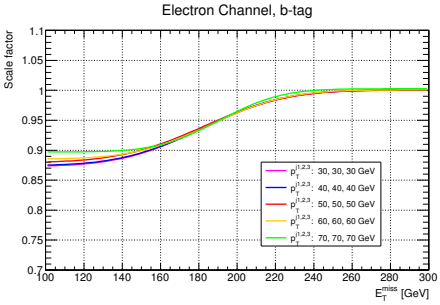

(D) 3 jets + $p_T^{j1=j2=j3}$

FIGURE A.6: Scale factors obtained by using the error function A.2 in the electron channel after requesting at least one b-jet.

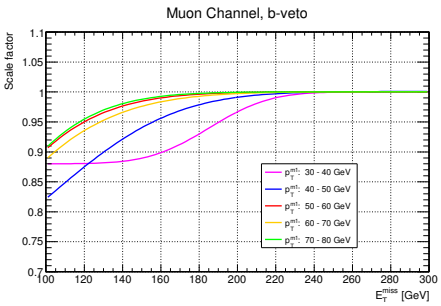

(A) p_T^{l1}

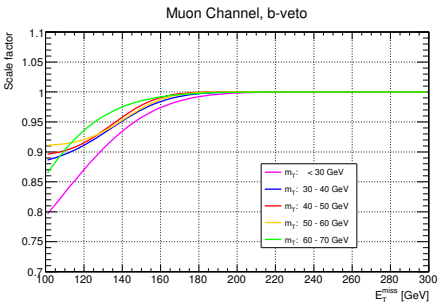

(B) m_T

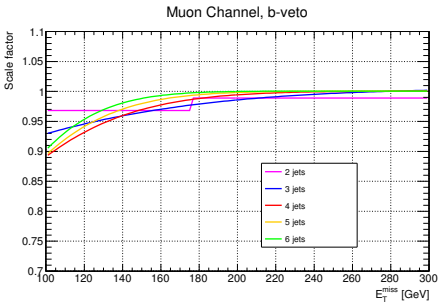

(C) N_{jets}

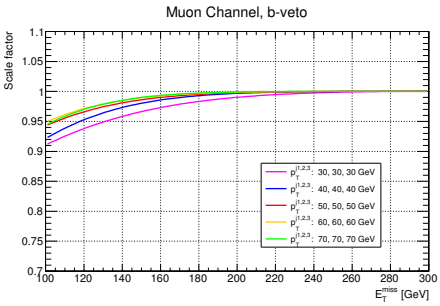

(D) 3 jets + $p_T^{j1=j2=j3}$

FIGURE A.7: Scale factors obtained by using the error function A.2 in the muon channel after vetoing b-jets.

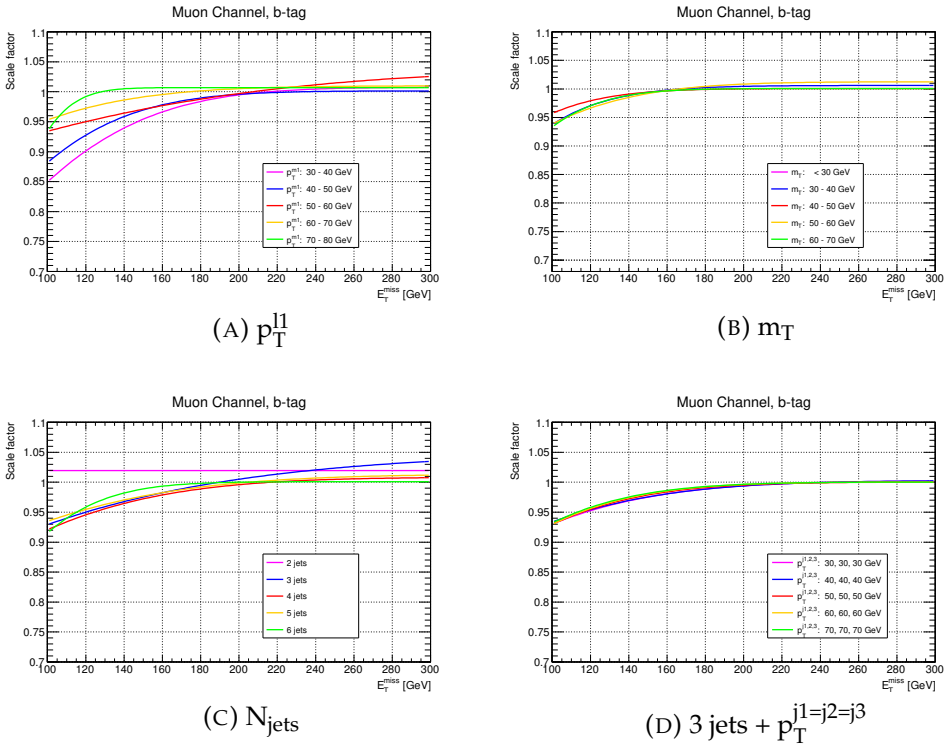

(A) p_T^{l1} (B) m_T

(C) N_{jets} (D) 3 jets + $p_T^{j1=j2=j3}$

FIGURE A.8: Scale factors obtained by using the error function A.2 in the muon channel after requesting at least one b-jet.

A.4 Conclusion

This chapter presents the studies performed with the aim to provide an unique scale factor for all analyses in ATLAS. The studies have been motivated by the searches for supersummetric particles in events with one isolated lepton presented in this thesis. The different selection criteria have been applied in order to make these studies more general. The unique scale factor for all physics analyses in ATLAS cannot be determined because the scale factors are dependent of event topology.

Bibliography

[1] W. N. Cottingham. "An Introduction to the Standard Model of Particle Physics". *CAMBRIDGE, 2nd edition* (2007).

[2] D. V. Schroeder M. E. Peskin. "An Introduction To Quantum Field Theory". *Avalon Publishing* (1995).

[3] The ATLAS Collaboration. "Observation of a new particle in the search for the Standard Model Higgs boson with the ATLAS detector at the LHC". *Phys.Lett. B716, arXiv:1207.7214* (2012).

[4] The CMS Collaboration. "Observation of a new boson at a mass of 125 GeV with the CMS experiment at the LHC". *Phys. Lett. B 716, arXiv:1207.7235* (2012).

[5] *Standard Model*. Website. URL: https://sciencesprings.wordpress.com/2016/05/13/from-physicsworld-parallel-universe-search-focuses-on-neutrons/standard-model/.

[6] K.A. Olive et al. (Particle Data Group). "Review of Particle Physics". *Chinese Physics C 38, 090001* (2014).

[7] A. Pich. "QUANTUM CHROMODYNAMICS". *arXiv:hep-ph/9505231* (1995).

[8] D. Griffiths. "Introduction to Elementary Particles". *WILEY-VCH, 2nd edition* (2008).

[9] *The Higgs Mechanism*. Website. URL: http://yichen.me/sandbox/HZZIntroduction/#/goldenchannel-higgs.

[10] The ATLAS Collaboration. "Summary of several Standard Model total production cross section measurements" (Public plot). URL: https://atlas.web.cern.ch/Atlas/GROUPS/PHYSICS/CombinedSummaryPlots/SM/.

[11] Stephen P. Martin. "A Supersymmetry Primer". *arXiv:hep-ph/9709356* (2016).

[12] The Plank Collaboration. "Planck 2015 results I, Overview of products and scientific results". *arXiv:1502.01582* (2015).

[13] *Supersymmetry*. Website. URL: http://www.hephy.at/en/research/theoretical-physics/supersymmetry/.

[14] The Super-Kamiokande Collaboration. "The Super-Kamiokande detector". *Nucl.Instrum.Meth. A501* (2003).

[15] M. Miura. "Search for Nucleon Decay in Super-Kamiokand". *Nuclear and Particle Physics Proceedings: Vol. 273–275, p516-521* (2016).

[16] D. I. Kazakov. "Beyond the Standard Model (In Search of Supersymmetry)". *arXiv:hep-ph/0012288* (2000).

[17] *Nobel Prizes*. Website. URL: https://www.nobelprize.org/nobel_prizes/physics/laureates/2004/phypub4highen.jpg.

[18] D. Alves et al. "Simplified Models for LHC New Physics Searches". *arXiv:1105.2838* (2012).

[19] C. Borschensky et al. "Squark and gluino production cross sections in pp collisions at $\sqrt{s}$ = 13, 14, 33 and 100 TeV". *Eur.Phys.J. C74 no.12, 3174 arXiv:1407.5066 [hep-ph] MS-TP-14-25, CERN-PH-TH-2014-137, TTK-14-13* (2014).

[20] C. Patrignani et al. (Particle Data Group). "STATUS OF HIGGS BOSON PHYSICS". *Chin. Phys. C, 40, 100001* (2016).

[21] L. Evans and P. Bryant. "LHC Machine". *JINST 3 S08001* (2008).

[22] The ATLAS Collaboration. "Proceedings of the ECFA-CERN workshop". *CERN-84-10-V-1, ECFA-84-85, CERN-YELLOW-84-10-V-1* (1984).

[23] *Large Hadron Collider*. URL: http://graphics.latimes.com/media/towergraphics/towercard-03b958fc-41c1-4a95-b037-05e50b77282f.jpg.

[24] *CERN experiments*. Website. URL: https://home.cern/about/experiments.

[25] The CMS Collaboration. "The CMS experiment at the CERN LHC". *JINST 3 S08004* (2008).

[26] The LHCb Collaboration. "The LHCb Detector at the LHC". *JINST 3 S08005* (2008).

[27] The ALICE Collaboration. "The ALICE experiment at the CERN LHC". *JINST 3 S08002* (2008).

[28] The LHCf Collaboration. "The LHCf detector at the CERN Large Hadron Collider". *JINST 3 S08006* (2008).

[29] The TOTEM Collaboration. "The TOTEM Experiment at the CERN Large Hadron Collider". *JINST 3 S08007* (2008).

[30] V. Mitson et al. The MoEDAL Collaboration. "The MoEDAL experiment at the LHC: status and results". *arXiv:1703.07141v2* (2017).

[31] *Future Timeline*. Website. URL: http://www.futuretimeline.net/blog/images/55-lhc.jpg.

[32] *Cern accelerator complex*. Website. URL: https://en.wikipedia.org/wiki/Proton_Synchrotron#/media/File:Cern-accelerator-complex.svg.

[33] A. Hoecker. "Physics at the LHC Run-2 and Beyond". *arXiv:1611.07864* (2016).

[34] *The Proton Synchrotron*. Website. URL: https://home.cern/about/accelerators/proton-synchrotron.

[35] R. Bruce et al. "LHC RUN 2: RESULTS AND CHALLENGES". *ISBN 978-3-95450-178-6 14* (2016).

[36] O. S. Brüning et al. "LHC design report". *CERN-2004-003-V1* (2004).

[37] The ATLAS Collaboration. "Luminosity Public Results Run 2" (Public results). URL: https://twiki.cern.ch/twiki/bin/view/AtlasPublic/LuminosityPublicResultsRun2.

[38] The ATLAS Collaboration. "Performance of pile-up mitigation techniques for jets in pp collisions at sqrt(s)=8 TeV using the ATLAS detector". *arXiv:1510.03823v2 [hep-ex]* (2016).

[39] The ATLAS Collaboration. "The ATLAS experiment at the CERN Large Hadron Collider". *JINST 3 S08003* (2008).

[40] E. Daw. "Lecture 7 - Rapidity and Pseudorapidity" (2012). URL: http://www.hep.shef.ac.uk/edaw/PHY206/Site/2012_course_files/phy206rlec7.pdf.

[41] *Pseudorapidity*. Website. URL: https://en.wikipedia.org/wiki/Pseudorapidity#/media/File:Pseudorapidity2.png.

[42] The BaBar Collaboration. "Dalitz plot analysis". *arXiv:1011.4190* (2010).

[43] The ATLAS Collaboration. "Performance of the ATLAS trigger system in 2015". *Eur. Phys. J. C, arXiv:1611.09661* (2017).

[44] The ATLAS Collaboration. "Performance of the ATLAS Trigger System in 2010". *arXiv:1110.1530v2* (2010).

[45] The ATLAS Collaboration. "2015 start-up trigger menu and initial performance assessment of the ATLAS trigger using Run-2 data". *ATL-DAQ-PUB-2016-001* (2015).

[46] The ATLAS Collaboration. "Trigger Menu in 2016". *ATL-DAQ-PUB-2017-001* (2017).

[47] The ATLAS Collaboration. "ATLAS TDAG System, Techical Desig Report". *CERN-LHCC-2013-018, ATLAS-TDR-023-2013* (2013).

[48] The ATLAS Collaboration. "Electron performance measurements with the ATLAS detector using the 2010 LHC proton-proton collision data". *arXiv:1110.3174v2 [hep-ex]* (2011).

[49] *Monte Carlo simulation*. Website. URL: http://scholarpedia.org/article/File:MonteCarloSchematic.jpeg.

[50] T. Gleisberg et al. "Event generation with SHERPA 1.1". *arXiv:0811.4622* (2009).

[51] P. Nason. "A New Method for Combining NLO QCD with Shower Monte Carlo Algorithms". *arXiv:hep-ph/0409146* (2004).

[52] S. Frixione et al. "Matching NLO QCD computations with Parton Shower simulations: the POWHEG method". *arXiv:0709.2092* (2007).

[53] S. Alioli et al. "A general framework for implementing NLO calculations in shower Monte Carlo programs: the POWHEG BOX". *arXiv:1002.2581* (2010).

[54] T. Sjostrand et al. "PYTHIA 6.4 Physics and Manual". *arXiv:hep-ph/0603175* (2006).

[55] J. Alwall et al. "The automated computation of tree-level and next-to-leading order differential cross sections, and their matching to parton shower simulations". *arXiv:1405.0301* (2014).

[56] *Tier centres*. Website. URL: http://wlcg-public.web.cern.ch/tier-centres.

[57] *ATLAS detector*. Website. URL: http://collider.physics.ox.ac.uk/img/layers.png.

[58] The ATLAS Collaboration. "Electron efficiency measurements with the ATLAS detector using the 2015 LHC proton-proton collision data". *ATLAS-CONF-2016-024* (2016).

[59] The ATLAS Collaboration. "Muon reconstruction performance of the ATLAS detector in proton-proton collision data at $\sqrt{s}$=13 TeV". *Eur. Phys. J. C 76: 292, arXiv:1603.05598* (2016).

[60] R. Atkin. "Review of jet reconstruction algorithms" (2015). URL: J. Phys.:Conf.Ser.645012008.

[61] Matteo Cacciari and Gavin P. Salam. "The anti-kt jet clustering algorithm". *arXiv:0802.1189v2 [hep-ph]* (2008).

[62] The ATLAS Collaboration. "Jet energy scale measurements and their systematic uncertainties in proton-proton collisions at $\sqrt{s}$=13 TeV with the ATLAS detector". *arXiv: 1703.09665* (2015).

[63] the DELPHI Collaboration et al. The ALEPH Collaboration ().

[64] *b-tagging*. Website. URL: https://en.wikipedia.org/wiki/B-tagging.

[65] The ATLAS collaboration. "Optimisation of the ATLASb-tagging performance for the 2016 LHC Run". *ATL-PHYS-PUB-2016-012* (2016).

[66] The ATLAS Collaboration. "Performance of jet substructure techniques for large-R jets in proton-proton collisions at $\sqrt{s}$ = 7 TeV using the ATLAS detector". *JHEP 1309 (2013) 076, arXiv:1306.4945 [hep-ex]* (2013).

[67] D. Krohn et al. "Jet Trimming". *arXiv:0912.1342* (2010).

[68] The ATLAS Collaboration. "Expected performance of missing transverse momentum reconstruction for the ATLAS detector at $\sqrt{s}$ = 13 TeV". *ATL-PHYS-PUB-2015-023* (2008).

[69] *Useful Diagrams of Top Signals and Backgrounds*. Website. URL: https://www-d0.fnal.gov/Run2Physics/top/top_public_web_pages/top_feynman_diagrams.html.

[70] D. Gillberg. "Discovery of Single Top Quark Production". *arXiv:0906.0523* (2009).

[71] A. Mitov M. Czakon. "Top++: a program for the calculation of the top-pair cross-section at hadron colliders". *arXiv:1112.5675* (2014).

[72] N. Kidonakis. "Two-loop soft anomalous dimensions for single top quark associated production with a W^- or H^-". *arXiv:1005.4451* (2010).

[73] P. Kant et al. "HATHOR for single top-quark production: Updated predictions and uncertainty estimates for single top-quark production in hadronic collisions". *arXiv:1406.4403* (2015).

[74] S. Hoeche T. Gleisberg. "Comix, a new matrix element generator". *arXiv:0808.3674* (2008).

[75] F. Cascioli et al. "Scattering Amplitudes with Open Loops". *arXiv:1111.5206* (2012).

[76] F. Krauss S. Schumann. "A parton shower algorithm based on Catani-Seymour dipole factorisation". *arXiv:0709.1027* (2008).

[77] S. Hoeche et al. "QCD matrix elements + parton showers: The NLO case". *arXiv:1207.5030* (2013).

[78] R. Ball et al. "Parton distributions for the LHC Run II". *arXiv:1410.8849* (2015).

[79] R. Gavin et al. "FEWZ 2.0: A code for hadronic Z production at next-to-next-to-leading order". *arXiv:1011.3540* (2011).

[80] The ATLAS collaboration. "Monte Carlo Generators for the Production of a W or Z/γ Boson in Association with Jets at ATLAS in Run 2". *ATL-PHYS-PUB-2016-003* (2016).

[81] The ATLAS collaboration. "Modelling of the $t\bar{t}H$ and $t\bar{t}V$ (V=W,Z) processes for $\sqrt{s}$=13 TeV ATLAS analyses". *ATL-PHYS-PUB-2016-005* (2016).

[82] The ATLAS collaboration. "Multi-Boson Simulation for 13 TeV ATLAS Analyses". *ATL-PHYS-PUB-2016-002* (2016).

[83] D. Tovey. "Transverse mass and invariant mass observables for measuring the mass of a semi-invisibly decaying heavy particle". *arXiv:1008.3837* (2010).

[84] The ATLAS collaboration. "Measurement of the W-boson mass in pp collisions at $\sqrt{s}$=7 TeV with the ATLAS detector". *arXiv:1701.07240* (2017).

[85] I. Hinchliffe et al. "Precision SUSY measurements at CERN LHC". *Phys. Rev. D 55, 5520* (1997).

[86] D. Tovey. "Measuring the SUSY Mass Scale at the LHC". *arXiv:hep-ph/0006276* (2000).

[87] C. Chen. "New approach to identifying boosted hadronically-decaying particle using jet substructure in its center-of-mass frame". *arXiv:1112.2567v3* (2012).

[88] D. Tovey. "On measuring the masses of pair-produced semi-invisibly decaying particles at hadron colliders". *arXiv:0802.2879* (2008).

[89] C. Patrignani et al.(Particle Data Group). "QUARKS". *Chin. Phys. C, 40, 100001* (2016).

[90] M. Baak et al. "HistFitter software framework for statistical data analysis". *arXiv:1410.1280* (2014).

[91] K. Cranmer et al. "HistFactory:A tool for creating statistical models for use with RooFit and RooStats". *CERN-OPEN-2012-016* (2012).

[92] D. Kirkby W. Verkerke. "The RooFit toolkit for data modeling". *arXiv: physics/0306116* (2003).

[93] G. Cowan et al. "Asymptotic formulae for likelihood-based tests of new physics". *arXiv:1007.1727* (2013).

[94] A. Read. "Presentation of search results: The CL(s) technique". *J.Phys. G28 (2002) 2693-2704* (2002).

[95] The ATLAS Collaboration. "Search for squarks and gluinos in events with an isolated lepton, jets, and missing transverse momentum at $\sqrt{s}$ = 13 TeV with the ATLAS detector". *arXiv:1708.08232* (2017).

[96] A. Djouadi et al. "The Minimal Supersymmetric Standard Model: Group Summary Report". *arXiv:hep-ph/9901246* (1999).

[97] C.F. Berger et al. "Supersymmetry Without Prejudice". *arXiv:0812.0980* (2008).

[98] A. Djouadi et al. *Program Package SUSY-HIT - SU(spect)-S(deca)Y-H(decay)-I(n)Terface*. Website. URL: https://www.itp.kit.edu/~maggie/SUSY-HIT/.

[99] A. Djouadi et al. "Decays of Supersymmetric Particles: the program SUSY-HIT (SUspect-SdecaY-Hdecay-InTerface)". *arXiv:hep-ph/0609292* (2006).

[100] The ATLAS Collaboration. "Search for squarks and gluinos in events with an isolated lepton, jets, and missing transverse momentum at $\sqrt{s}$ = 13 TeV with the ATLAS detector". *ATL-COM-PHYS-2016-904* (2016).

[101] The ATLAS Collaboration. "Search for squarks and gluinos in events with an isolated lepton, jets and missing transverse momentum at $\sqrt{s}$ = 8 TeV with the ATLAS detector". *J. High Energy Phys. 116, arXiv:1501.03555* (2015).

[102] The ATLAS Collaboration. "Search for gluinos in events with an isolated lepton, jets and missing transverse momentum at $\sqrt{s}$ = 13 TeV with the ATLAS detector". *arXiv:1605.04285* (2016).

[103] G. Apollinari et al. "High Luminosity Large Hadron Collider HL-LHC". *arXiv:1705.08830* (2017).

[104] *High Luminosity Large Hadron Collider*. Website. URL: https://hilumi-lhcds.web.cern.ch/about/hl-lhc-project.

[105] The ATLAS Collaboration. "Search for direct pair production of a chargino and a neutralino decaying to the 125 GeV Higgs boson in $\sqrt{s} = 8$ TeV pp collisions with the ATLAS detector". *arXiv:1501.07110* (2015).

[106] S. Das. "A simple alternative to the Crystal Ball function". *arXiv:1603.08591* (2016).

[107] T. Skwarnicki. "A study of the radiative CASCADE transitions between the Upsilon-Prime and Upsilon resonances". *ISSN 0418-9833, DESY-F31-86-02, DESY-F-31-86-02* (1986).

[108] The ATLAS Collaboration. "Jet energy scale and its systematic uncertainty in proton-proton collisions at sqrt(s)=7 TeV with ATLAS 2011 data". *ATLAS-CONF-2013-004* (2013).

[109] The ATLAS Collaboration. "Jet energy resolution and selection efficiency relative to track jets from in-situ techniques with the ATLAS Detector Using Proton-Proton Collisions at a Center of Mass Energy $\sqrt{s} = 7$ TeV". *ATLAS-CONF-2010-054* (2010).

[110] The ATLAS Collaboration. "Performance of b-jet identification in the ATLAS experiment". *INST 11 P04008* (2016).

[111] The ATLAS Collaboration. "Calibration of the performance of b-tagging for c and light-flavour jets in the 2012 ATLAS data". *ATLAS-CONF-2014-046* (2014).

[112] The ATLAS Collaboration. "Luminosity determination in pp collisions at $\sqrt{s} = 8$ TeV using the ATLAS detector at the LHC". *arXiv:1608.03953* (2016).

Acknowledgements

Many people have contributed to my PhD studies over the past few years and I would like to thank all of them.

First and foremost, I would like to thank Prof. Dr. Dorothee Schaile for giving me the opportunity to make my PhD in the LMU ATLAS group. I am also very thankful for all her support and useful discussions regarding my thesis.

I would like to thank Prof. Dr. Martin Faessler for being the second corrector of this thesis and for all useful comments. I would also like to thank Prof. Dr. Hans Böhringer, Prof. Dr. Thomas Kuhr, Prof. Dr. Wolfgang Dünnweber and Prof. Dr. Harald Lesch for being my doctorate committee.

I would like to express my sincere thanks to Dr. Jeanette Lorenz, first of all, for supporting me during the hard time and for encouraging me to apply for the PhD studies at the Ludwig-Maximilians University. I am also deeply thankful for her mentoring and useful comments regarding my thesis.

Special thanks go to the rest of the LMU ATLAS group for making Garching such a great working place. It was pleasure to work with ALL OF YOU, especially with Dr. Nikolai Hartmann who always has made the hard work seems easier.

I would like to express my deepest thanks to Dr. Fabiola Gianotti, Dr. Peter Jenni, Dr. Martine Bosman and CERN HR James Purvis for choosing me to be an ATLAS PhD Grant recepient and supporting me during the hard time. I appreciate very much everything they have done for me.

Prof. Dr. Dragica Knežević deserves very special thanks for all her support during my studies and very useful advice.

I would like to give special thanks to Dr. Valerio Dao, Dr. Ljiljana Simić, Dr. Antun Balaž and Petar Bokan for being with me during the hard time and for all their support.

My deep thanks go to my landlady Mrs. Susanna Mayer for always creating a very friendly and pleasant atmosphere in her home.

I have been lucky to be a member of the Inclusive 1L and EWK 1L2b teams. Thanks a lot all members for the productive discussions and friendly atmosphere. Special thanks go to Dr. Monica D'Onofrio, Dr. Alberto Cervelli, Dr. Da Xu, Dr. Valentina Tudorache, Dr. Matthew Gignac and Dr. Tomoyuki Saito.

During my long-term stays at CERN, I had an opportunity to meet one amazing person Dr. Lily Morvaj. An even bigger thank you goes to her for continuous support and teaching me all the stuff. I am so blessed to have such a great friend. I also would like to thank ALL MY FRIENDS for providing support and friendship that I needed.

Finally, and most importantly, I would like to express my heartfelt gratitude to my parents Milena and Radmilo for their love and for encouraging me to follow my dreams. My brother Darko has been my best friend throughout my life. Big thanks to him for all support, strength and belief. I would also like to thank his wife Tamara for all her love and support. I LOVE YOU!